Mechanistic studies into the intermolecular Pauson-Khand reaction using a combined statistical, spectroscopic and theoretical approach.

Theo Tanner

PhD

University of York

Chemistry

December 2023

Abstract

In this study, the mechanism of the Pauson-Khand Reaction (PKR) has been investigated, with a particular focus on understanding the underpinning factors influencing regioselectivity in the intermolecular PKR process. To address the challenges which arise from the difficulties in observing or isolating intermediates of the PKR, this study has involved the application of a range of techniques which shed new light on the mechanistic behaviour exhibited by substrates possessing appropriate structural features which are underrepresented in PKRs. A statistical approach has been used to examine regioselectivity effects imposed by electronically polarised internal alkynes. A multicomponent linear regression model was constructed to link DFT-calculated parameters to PKR regiochemical outcomes, allowing for the identification of outliers which highlighted unusual regioselectivity for substrates with 2-heterocyclic groups. Exclusion of cases with this functionality enabled an accurate predictive ability for unseen testing data. Additionally, the errors in the predicted regioselectivities by the model for the excluded cases allowed for the inference of a chemical feature-activity relationship, which has been hypothesised to influence the mechanism. Further exploration of these hypothesised mechanistic effects was undertaken through *in-situ* IR spectroscopy studies of a model system incorporating one of the substrates identified as a model outlier. Observation of the cobalt-carbonyl IR bands in the reaction mixture allowed for the identification of a complexation method dependency on the initial post-decarbonylation equilibrium. Observation of new cobalt carbonyl bands in PKR revealed that a monometallic ionic speciation pathway needed to be considered and investigated. The mechanistic significance of the proposed speciation was further investigated by the construction of a full potential energy surface for a range of possible pathways following cleavage of the Co-Co bond. The findings suggest that intermolecular PKRs involve both bimetallic and monometallic intermediates. The latter is akin to other metal-mediated reaction mechanisms proposed for Pd and Rh. The nature of the interaction between the metal centres and the alkyne was further probed by ultrafast photochemical methods. The use of dimolybdenum(I) cyclopentadienyl tetracarbonyl alkyne analogues of dicobalt(0) hexacarbonyl-alkyne complexes allowed for the observation of long-lived photoproducts, which allowed for ultrafast post carbonyl photolysis study of a PKR-like system, and highlighted the effect of alkyne orbital character on photolysis pathways.

List of Contents

List of Figures

List of Tables

List of Schemes

Acknowledgements

Before anybody else, I want to thank my supervisors, John, Jason and Ian for all of the guidance and support they have given me during my time working with you. Your patience, kindness and wisdom have been a massive factor in allowing me to not just complete my PhD studies, but to enjoy them as well. I could not have asked for a better team to be working with while conducting this work, and I feel like I have learned so much from the vast breadth of knowledge across the field that you are able to bring to discussions.

The research presented in this work would not be able to exist without the support of the technical teams in the department and elsewhere. I would like to thank Heather Fish, Karl Heaton and the team at the CLF for their help in running, maintaining and training me on the instruments which have enabled me to do most of the work detailed in this thesis. I would also like to thank Adrian Whitwood, for teaching me everything I know from his vast knowledge of crystallography. I already miss the XRD service, and I count being a part of it as one of the highlights of my time as a PGR at York.

I have been very fortunate during my time here to be at the intersection of two large and friendly research groups, and I've been able to make a lot of amazing connections here which I will treasure for many years to come. I want to thank you all for making my time here so much fun, always being there when I needed to talk through some ideas, giving me suggestions and above all making my time here something really special. There are too many of you to do justice to on this page, but I will always remember the times we shared together, the Yorktoberfests, Browns comas, Burns suppers, cryptic crosswords, Charles trips and Magic games.

I would like to thank my family for all of their support during my study. You have always believed in me and let me know that I am able to do anything if I put my mind to it, and I want you to know that the confidence which that has instilled in me has been instrumental in allowing me to complete this work.

And finally, Megan, I want to thank you so much. Your kind words and common sense have always been the things which have kept me going when times were tough. You have always been in my corner and backing me up, and your support means the world to me. Thank you so much for always being there for me and making me happier than ever.

Author’s Declaration

I declare that this thesis is a presentation of original work, and I am the sole author. All work was conducted in the University of York or the Rutherford Appleton Laboratory, Harwell between October 2019 and December 2023. This work has not previously been presented for a degree or other qualification at this University or elsewhere. All sources are acknowledged as references.

Theo Tanner

December 2023

Chapter 1: General Introduction

1.1. The discovery of the Pauson-Khand reaction

The Pauson-Khand reaction (PKR) refers to the coupling of an alkene, alkyne and carbon monoxide to form a five-membered cyclopentenone ring (Scheme 1). This formal [2+2+1] cycloaddition represents a route to the synthesis of highly substituted and functionally complex molecules in a single step, by the annulation of substituted reagents.

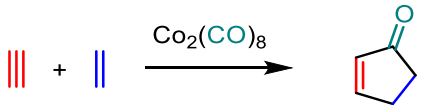

Scheme 1 - A simplified schematic of the Pauson-Khand reaction, showing the origin of ring components in the cyclopentenone product.

The discovery leading to the modern PKR was made by Ihsan Khand, a researcher working under the direct supervision of Prof. Peter Pauson at the University of Strathclyde in the 1970s. The first allusion to the chemistry later to become the PKR can be found in a communication published in 1971.[1] While investigating the reactivity of cobalt-alkyne complexes (**1**) with norbornadiene (**2**) to form cyclopentadienyl cobalt complexes, the authors noted that these reagents also had the capacity to form organic carbonyl products derived from a combination of norbornadiene, acetylene and carbon monoxide. The product of the breakdown of the cobalt-alkyne complex was found to be dependent on the reaction solvent. When dimethoxyethane (DME[a]) was used as the solvent, the expected retro Diels-Alder was observed, giving the cyclopentadienyl cobalt complex **3**. However, when hydrocarbon solvents such as benzene, toluene or mesitylene were used, the formation of carbonyl products was seen, alongside the solvent-complexed form of $Co_4(CO)_9$ (**4**) (Scheme 2).

[a] A full table of all abbreviations used in this document can be found in Appendix 8

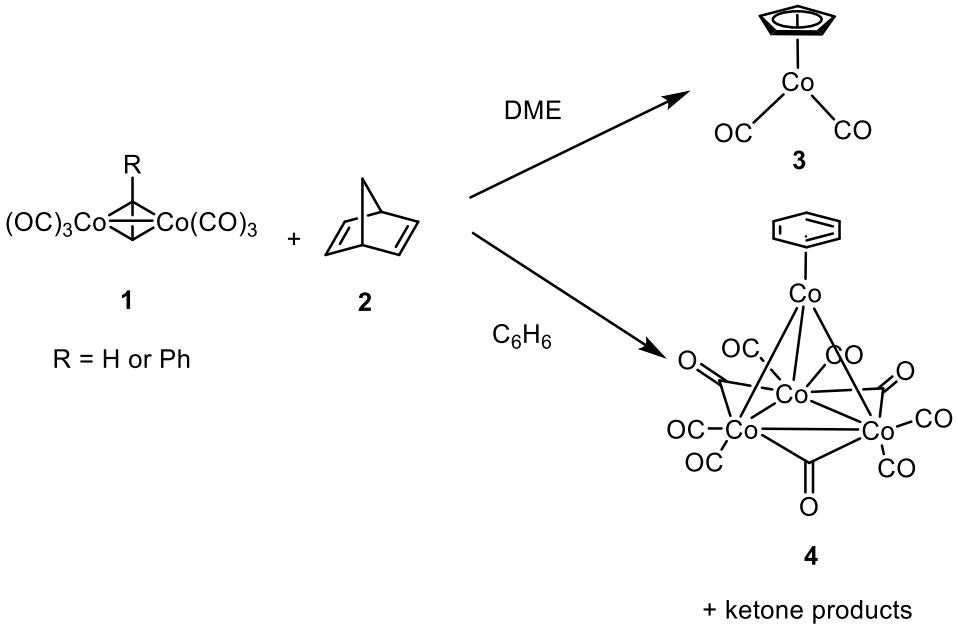

Scheme 2 - Initial observations by Pauson and Khand of the effect of solvent on organometallic and organic products formed by the reaction of cobalt-alkyne complexes with norbornadiene.

While this observation of unexpected reactivity was not explored further in the 1971 publication, Khand, Pauson and colleagues quickly produced a follow-up investigation which was published in 1973.[2] In this work, the scope of the reaction was further explored, and the exact identity of its products were assigned. The authors found that the coupling of the cobalt-alkyne complex, norbornadiene and a carbonyl ligand from the complex yielded a cyclopentenone ring (**6)**. This reaction was shown to be possible for a range of alkyne substituents and in several solvents. Through the use of ^{1}H NMR spectroscopy and comparison with *bona fide* samples of the proposed products, the exact structure and stereochemistry of the resulting cyclopentenones could be confidently assigned. It was observed that in all cases the *exo*-adduct of the norbornadiene was formed, and that when an unsymmetrical alkyne was used the larger substituent was found situated α to the carbonyl group in the cyclopentenone ring (Scheme 3). The authors also briefly detail a catalytic preparation of the cyclopentenones, using various substoichiometric amounts of cobalt carbonyl. While many facets of the reaction were not well understood, it was clear that this serendipitous discovery had revealed a novel synthetic methodology for ring formation using (initially) stoichiometric cobalt.

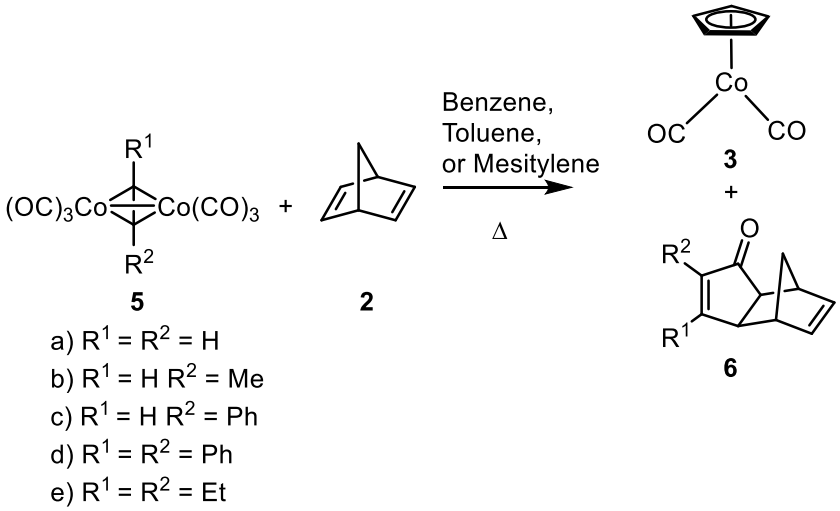

Scheme 3 - Further observations into the reactivity of cobalt-alkyne complexes with norbornadiene, and a range of substrates (a-e) which were found to form cyclopentenone products.

1.2. Discovery of the intramolecular PKR

While the first reported instances of the PKR were intermolecular in nature, it was soon reported that the cobalt-mediated ring forming reaction could be observed in the cases of long-chain enynes, in an intramolecular ring formation. These transformations, which form bicyclic rings, represented a major development in the capabilities of the PKR. Schore and co-workers[3] noted that while yields in the intermolecular system using norbornadiene are generally good, the yields when using unstrained alkenes can vary greatly, and tend to be lower. The authors demonstrate that the use of PK coupling conditions on 1,6 and 1,5 enynes is able to produce fused bicyclic (6,5) and (5,5) bicyclic ring systems respectively (Scheme 4). The authors reported that milder conditions are required for the intramolecular PKRs relative to the intermolecular process using similar substrates. Furthermore, the intramolecular process obviates the need for a strained alkene, allowing even non-cyclic alkenes to react in moderate yields.

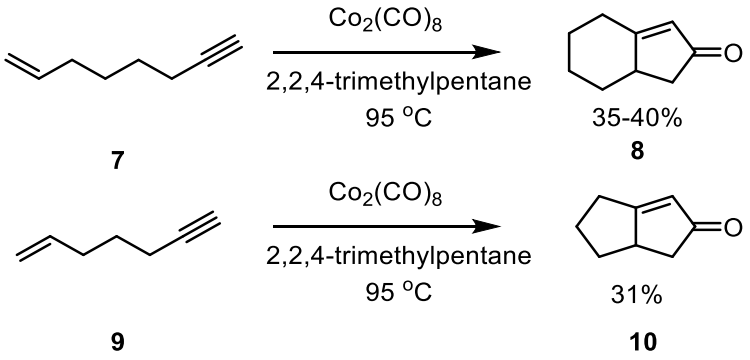

Scheme 4 - Schore and co-workers demonstration of the ability of the PKR to form bicyclic rings from enynes.

The power of this approach is clearly stated by the authors: this synthetic method represents a route to the formation of fused bicyclic rings from straight chains in a single step, without having to first generate a single ring. This novel method of bicyclic ring construction facilitated the rapid and efficient production of precursors suitable for application in complex molecular synthesis, such as in natural products.

1.3. The mechanism of the PKR

The mechanism of the PKR has been a subject of intense scrutiny and study from shortly after the reaction's discovery to the modern day. This section will focus on the major advances in mechanistic understanding of the cobalt-mediated PKR. For in-depth discussion of the understanding of mechanistic factors governing regioselectivity in the intermolecular PKR, see section 2.1.3.

The first proposed full mechanism of the PKR was put forward by Magnus in 1985. Magnus' interest in the PKR was piqued two years earlier, in 1983.[4] At that time, Exon and Magnus had reported a continuation of Schore's reports of bicyclic ring formation from enynes, showing the synthesis of a late-stage precursor to the antitumor agent coriolin. The authors reported that for the PKR to be suitable for the synthesis of natural products, stereoselectivity was vital. The authors showed that a stereoselective synthesis using PKR methodology is indeed possible, but the diastereomeric excess (*de*) present in the product distribution can vary widely as a function of the pendant alkyne substituent. A trimethylsiliyl group attached to the alkyne terminus was found to give an almost nine-fold increase in *de* over a methyl group in the same position.

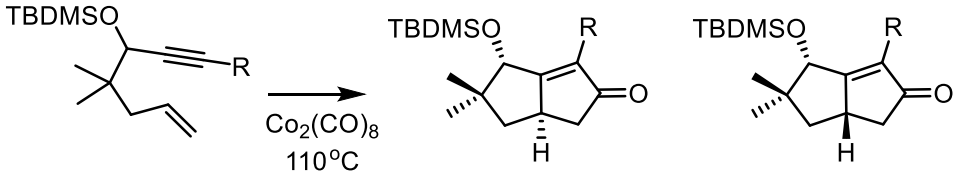

11 **12** **13**

TBDMSO ≡ 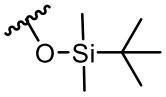

R	12	13
$SiMe_3$	26	1
Me	3	1

Scheme 5 - Synthesis of coriolin precursor by Magnus and Exon, showing de *ratio as function of substituent R*

The authors at the time noted that they were unable to determine the mechanism behind this selectivity, and that speculation would be largely without meaning in the absence of a clear

mechanistic hypothesis. Therefore, in 1985, Magnus revisited the topic from a more mechanistic perspective.[5] Preparing a range of substituted enynes bearing substituents of varying steric character, the authors attempted to rationalise the previously observed effect of the alkyne terminal group on stereospecificity.

Working from the isolable cobalt-alkyne complex, Magnus proposed that the first step of the reaction is the oxidative addition of the alkene to the cobalt centre, forming a five-membered cobaltacycle. In the case of the substrate **11** which Magnus had observed previously, two possible intermediates can be formed from this ring formation (Scheme 6):

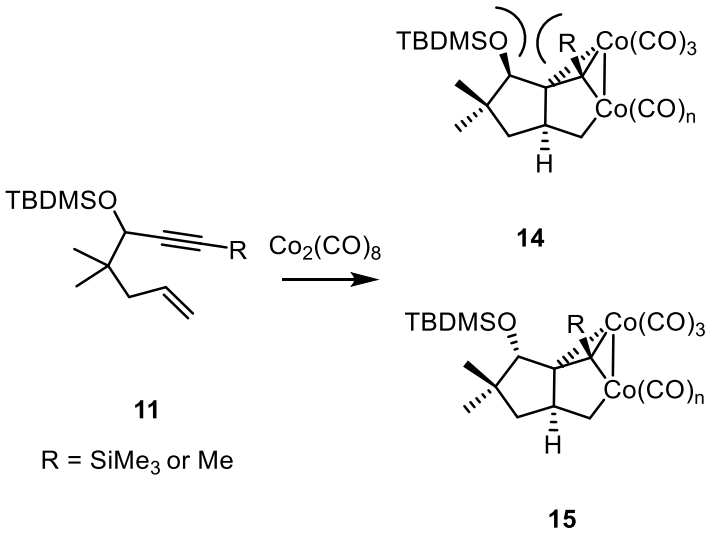

Scheme 6 - Proposed intermediates which give rise to stereoselectivity in the PKR as proposed by Magnus and Principe.

The ring formation step is able to form either of diastereoisomers **14** and **15**. The authors noted that there likely to be an unfavourable steric interaction between the alkyne substituent and the TBDMS group in intermediate **14**. This steric interaction disfavouring the pathway following from this state is consistent with the enhanced stereoselectivity displayed by bulkier alkyne substituents, which would maximise this steric clash. Following this formation, Magnus and Principe proposed that migratory insertion of a carbonyl ligand from the cobalt centre gives a six-membered ring (**16**).

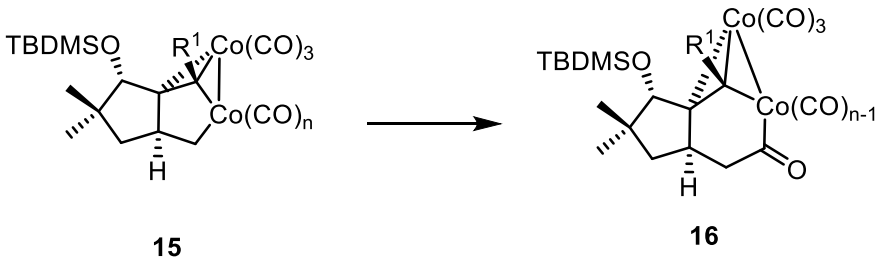

Scheme 7 - Migratory insertion of a carbonyl ligand into a Co-C bond, giving a six-membered cobaltacycle.

This transformation is followed by the reductive elimination of the cobalt atom from the ring, generating the cyclopentenone double bond with the cobalt co-ordinated. Finally, dissociation of the dicobalt species gives the product:

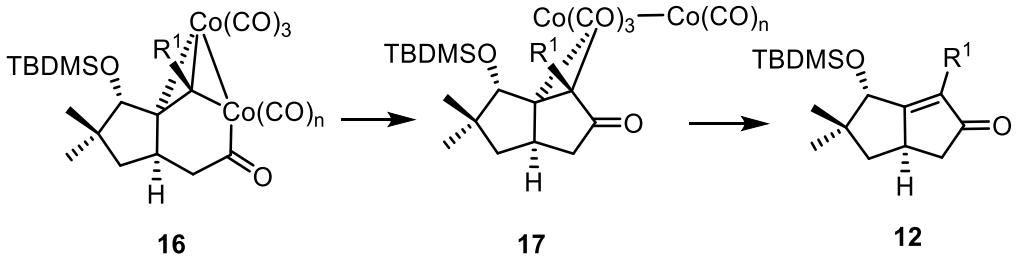

*Scheme 8 - Reductive elimination of cobalt followed by dissociation of the dicobalt species to give the final cyclopentenone product **12.***

Magnus and Principe proposed that this mechanism can explain their stereochemical observations, on the basis of the stability of intermediates like **14** and **15**. The authors demonstrate that they are able to use this model to predict the stereochemistry of a range of substituted enynes.

The Magnus mechanism was soon adopted as the accepted mechanism for the PKR, and a general intermolecular mechanistic pathway was proposed (Scheme 9). The mechanism begins with the dinuclear cobalt-alkyne complex (**I**), which undergoes ligand substitution between a carbonyl and the alkene to form **II**, an alkene-coordinated pentacarbonyl species, a step which is implied but not explicitly referenced in Magnus' 1985 work. From intermediate **II**, the reaction undergoes the oxidative addition to form the cobaltacycle **III**, insertion of a carbonyl to give six-membered cobaltacycle **IV**, and finally elimination and dissociation of the cobalt complex to form **V** and **VI** respectively.

While Magnus and Principe did not discuss in detail the coordination environment at the cobalt following cobaltcycle formation and carbonyl insertion, the generalised form of the Magnus mechanism models the coordination of a free CO to the cobalt centre following each of these

steps. This leads to the overall process being imbalanced in terms of CO, with a net consumption of one equivalent of CO per reaction. In a catalytic setting, where the reaction is undertaken under an atmosphere of CO, the source of this additional equivalent is obvious. However, when in a stoichiometric setting, it is unclear from where the CO which coordinates arises. It may be that the CO arises from a scavenging pathway, where free CO which has been evolved by other molecules of the cobalt-alkyne hexacarbonyl complex is taken up by the reactive intermediates. Alternatively, in the stoichiometric system other Lewis bases may take the role of the CO, coordinating to the cobalt centre.

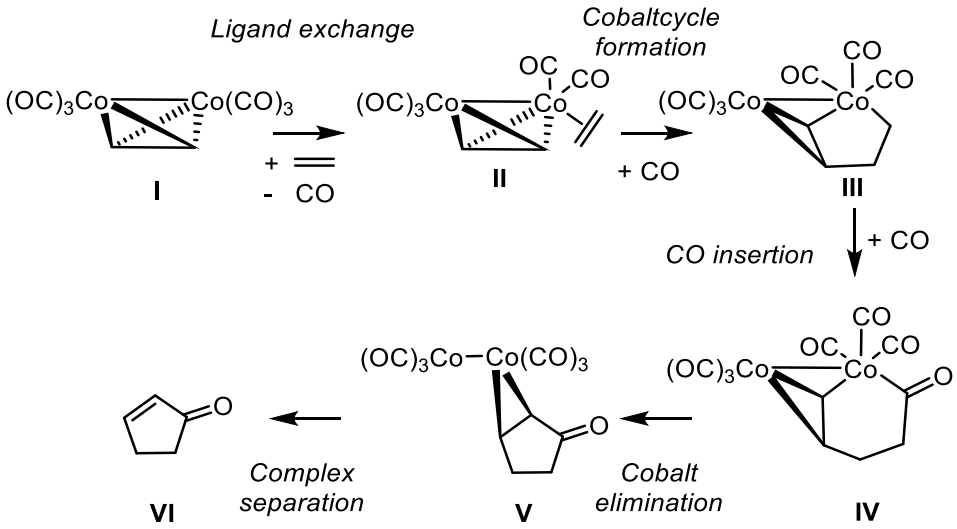

Scheme 9 - The general form of the Magnus mechanism for an intermolecular PKR between ethyne and ethene.

While this mechanistic theory gained popularity quickly, little information could be gathered to provide further supporting evidence for the proposed pathway. Crucially, the intermediates **II** to **V** could not be isolated or observed using traditional tools for mechanistic investigations. Due to this limitation, following the publication of the Magnus mechanism most subsequent investigations focused on the product distribution of PKRs with a given substrate (similar to Magnus' own approach). In 1998, Krafft reported two methods of probing the mechanism by focusing on the cobaltacycle formation in the **II** → **III** step of the pathway. Firstly, Krafft identified that co-ordinating groups on the alkene confer an increased yield and an excellent regioselectivity.[6] Noting that when a non-heteroatomic straight-chain alkene is used (**18**, Scheme 10, top), the yield is generally poor, with an even regioisomeric split between the two possible alkene substituent positions in the final product, Krafft showed that the use of N or S substituted alkenes (e.g. **22**) provide a general increase in yield, and a notable increase in selectivity for the

cyclopentenone bearing the alkene substituent for the α position relative to the carbonyl (**24,** Scheme 10, bottom).

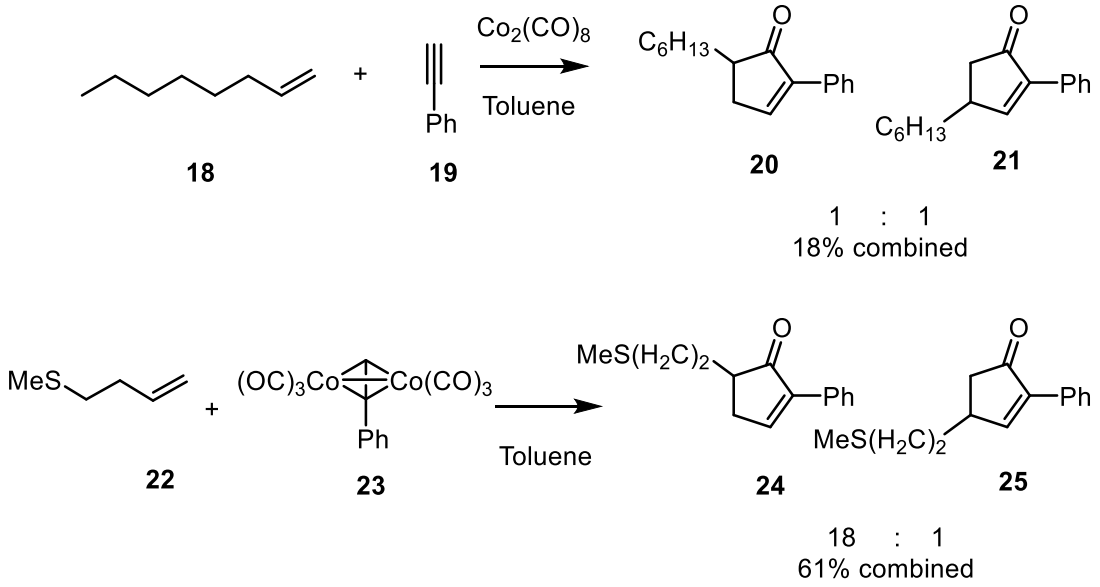

Scheme 10 - Krafft's demonstration of increased yield and selectivity with heteroatom-containing alkenes[6]

Krafft suggested that the observed effects arose from a coordinating alkene enabling the substrate to act as a bidentate ligand, with the heteroatom also coordinating to the cobalt atom (Scheme 11). This coordination in turn orients the unsubstituted side of the alkene towards the alkyne, biasing insertion to occur at the unsubstituted position. This in turn leads to the heteroatomic-substituted group being selective for the α position of the ring.

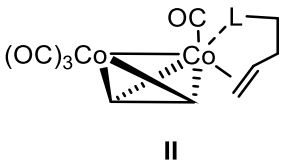

II

Scheme 11 - Krafft's model of the bidentate binding of heteroaromatic alkenes to the cobalt centre.

Krafft highlighted how the key factor in the efficacy of this approach was the length of the carbon tether chain between the alkene and the heteroatom, as expected in a chelation model and through consideration of the Thorpe-Ingold effect. Krafft and Juliano later examined this in more detail,[7] examining the effects of changing the linker length, or the introduction of a second heteroatom to the chain, providing a *pseudo*-tridentate binding capability in the alkene-coordinated intermediate **II**. The authors noted from their observations that the introduction of this second binding group does not necessarily impart greater reactivity than the singly-heterosubstituted alkene can provide.

In a related investigation, Krafft examined the effect of the steric character of alkene substituents on regioselectivity.[8] PKRs of alkenes bearing sterically bulky substituents with a range of internal and terminal alkynes revealed a strong regioselectivity for the cyclopentenone α position by the bulky alkene substituent. The reaction of **27** with **28b** was, for instance, fully selective for **29b** (Scheme 12).

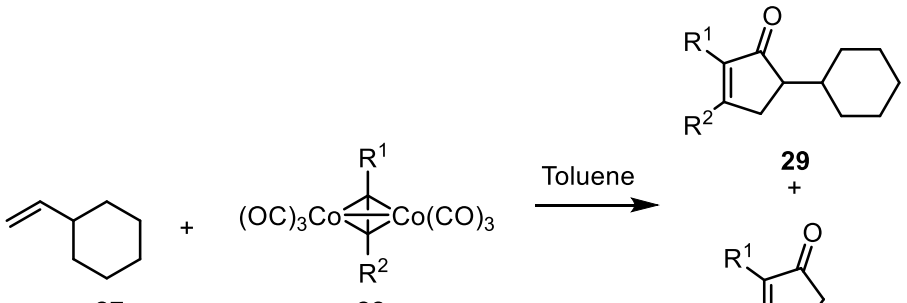

28	R^1	R^2	29	30
a	Ph	H	2.5	1
b	Ph	Me	1	0
c	Me	Me	1	0

Scheme 12 - Example of regioselectivity imparted by sterically bulky alkene substituents, as observed by Krafft.[8]

This propensity for the larger alkene substituent to be found adjacent to the carbonyl in the final product supports Magnus' mechanistic proposal, as the alkene will be more likely to insert in a manner which would place the less sterically congested side (*i.e.* the terminal carbon) adjacent to the alkyne.

Krafft and co-workers consolidated their understanding of directing effects in the intermolecular PKR,[9] providing a seminal study which greatly increased the utility of the intermolecular PKR for the synthesis of natural product precursors and other complex functionalised molecules by providing access to regiochemical control. Throughout the course of their investigation, Krafft and colleagues used the Magnus mechanism to rationalise their findings. Indeed, the predictions generated from the consideration of the Magnus intermediates agreed well with the observed chemical behaviour, providing support for the initial mechanistic proposal. Further advances from this approach soon followed, when Krafft and co-workers were able to isolate the pentacarbonyl CO-loss product of a cobalt complex of thiadiolane-substituted enyne **31**, namely **33** (Scheme 13).

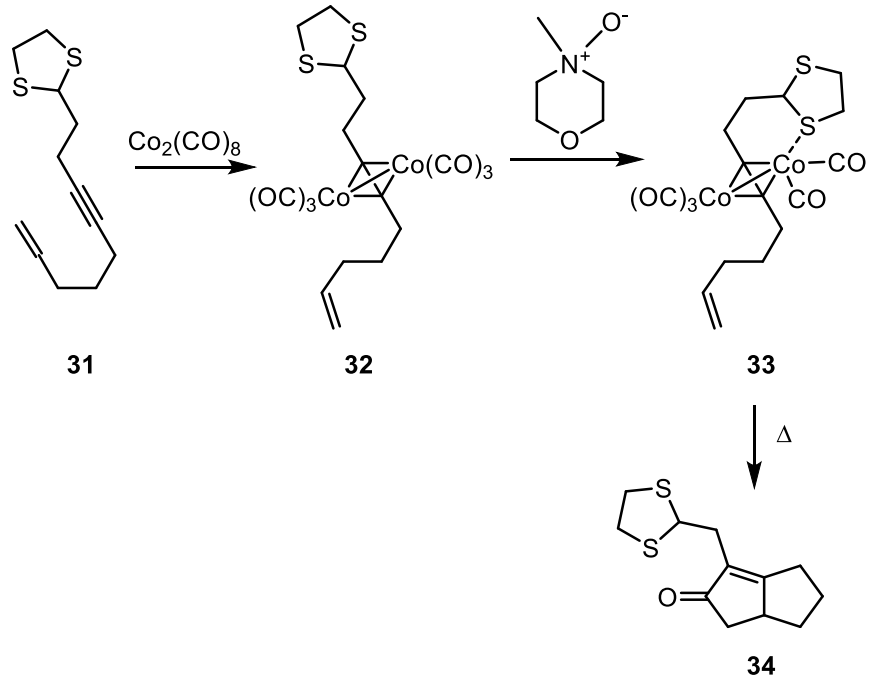

Scheme 13 - Preparation of a pentacarbonyl intermediate as performed by Krafft and colleagues, and subsequent reactivity to form the expected cyclopentenone.

The cobalt complex of **31**, **32**, was activated by N-methylmorpholine N-oxide promotion (for further discussion of promotion in the PKR, see sections 1.5 and 3.1.2) and CO-loss complex **33** was observed by NMR spectroscopic analysis. Treatment of complex **33** with heat yielded cyclopentenone **34**.

The first computational investigation into the PKR was performed by Yamanaka and Nakamura in 2001.[10] Considering ethyne and ethene as the reagents, a computational study examined the energies of the postulated Magnus intermediates, and the transition states between them (B3LYP/631LAN) (Figure 1). The theoretical study shed some light on the difficulty in observing or isolating intermediates of the PKR. Yamanaka and Nakamura found that the most significant energy barrier in the reaction is the initial dissociation of a CO ligand to form the pentacarbonyl dicobalt alkyne complex, **CP2**. Following this step, the subsequent states all lie on a steeply energy-negative gradient, implying fast interconversion between these states to form the product. As such, any intermediate from **II** to **V** would be highly unstable in the reaction, and quickly and irreversibly yield the product **VI**. At a similar time, Pericas and co-workers performed a similar study, again examining the reaction between ethyne and ethene.[11] This investigation too revealed that CO dissociation was the rate-determining step in the reaction, and that while the ring formation of the initial coordinatively unsaturated cobaltacycle (**CP3 → CP4)** is

essentially thermoneutral, a high degree of stabilisation is conferred by the coordination of a further carbonyl ligand, restoring the coordinative saturation of the cobalt centre and giving **CP5**.

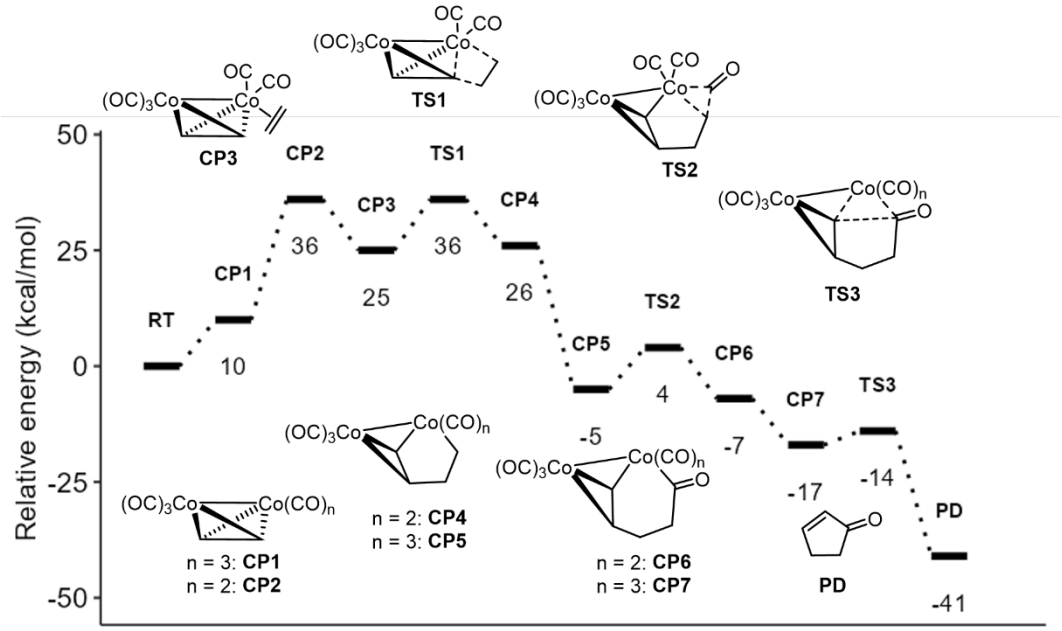

*Figure 1 - Potential energy surface (B3LYP/631LAN) of the PKR from reactants (**RT**) to products (**PD**) as calculated by Nakamura and Yamanaka.*

Pericas and co-workers reported that electron-rich substrates, such as ynamines, would theoretically promote CO loss efficiently, with the calculations estimating that the barrier to dissociation of CO from a dimethylaminoacetylene cobalt complex lies 10 kcal mol^{-1} lower than that of the propyne complex (Scheme 14 – top). The authors attributed this to the transfer of electron density from the nitrogen lone pair into the carbon-cobalt bond, promoting CO loss via an anomeric interaction (Scheme 12 – bottom).

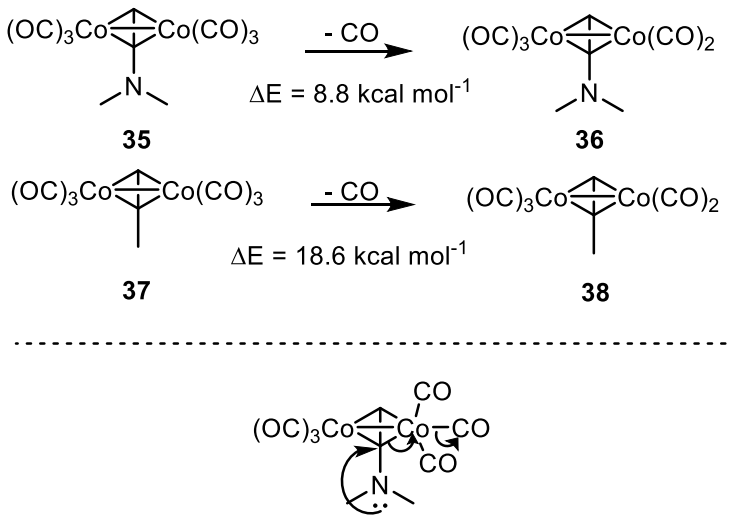

Scheme 14 - Top: the difference in energy barrier to CO dissociation displayed by the cobalt complexes dimethylamenoacetylene and propyne. (VWN/PW91xc)
Bottom: The proposed interaction of the nitrogen lone pair to promote CO dissociation

Following the results of these calculations, the authors attempted to experimentally verify their computational predictions of the relative reactivity of the two complexes. As cobalt complexes of ynamines had not previously been reported, a synthetic method for their preparation was developed.[12] It was found that the resulting ynamines were indeed prone to CO dissociation, requiring their storage under a CO atmosphere at low temperatures.

As would be expected from their propensity to lose CO spontaneously, the cobalt-ynamine complexes were highly active in the PKR, with examples undergoing reactions with norbornadiene at -21°C. However, the high level of reactivity towards norbornadiene was not replicated with other cyclic alkenes. Pericas and colleagues reported that the same substrate failed completely to react at room temperature with cyclohexene. This observation highlighted that while CO dissociation is often the rate-determining step of the pathway, it is not the sole condition which must be met to ensure the formation of PKR products. The authors explored the difference in reactivity between norbornadiene and cyclohexene in more depth and attributed the observed discrepancy to the difference in ring strain. Alkenes displaying a highly strained ring (such as cyclopropene) would display higher reactivity than those with less strained rings (such as cyclohexene). The authors attributed this behaviour to the release of ring strain in the cobaltacycle forming step; a highly-strained ring lends additional exothermicity to this transformation. Later, further investigations into the effect of alkene ring strain on activity were performed by Gimbert and co-workers (described in section 1.4).

Gimbert, Greene and co-workers applied electrospray ionisation (ESI) mass spectrometry (MS) to cobalt-alkyne complexes to examine the early events in the PKR.[13] The study utilised the power of gas-phase ionisation to study reactive intermediates, which can allow for the observation of sensitive intermediates which would not normally be stable for sufficient time to permit detection. By ionisation in the gas phase, tandem MS techniques can study reaction products in the gas phase without interference from other sources. The authors prepared a bis(diphenylphosphino)methane (DPPM) ligated analogue of complex **I** in the Magnus mechanistic pathway (**39**), to allow for accessible ionisation by loss of a proton from the methylene backbone to form the $[M-H]^-$ ion.

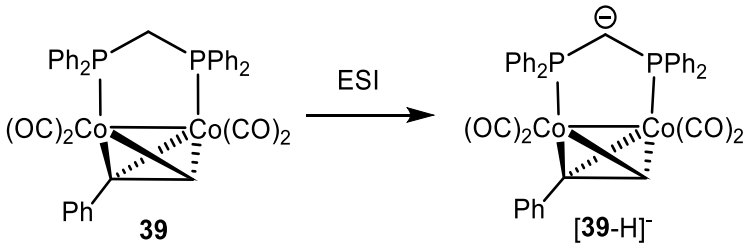

*Scheme 15 - Electrospray ionisation of **35** to form the deprotonated ion*

Complex [**39-H**]$^-$ was demonstrated to be readily formed using ESI-MS conditions, being observed in the mass spectrum (negative mode) alongside CO-dissociated fragment ions [(**39**-H)-CO]$^-$, [(**39**-H)-2CO]$^-$ and [(**39**-H)-3CO]$^-$. The anionic species was selectively transferred to a collision cell and reacted in the gas phase with norbornene. No collision-activated reaction (CAR) adduct was detected for the combination of [(**39**-H)]$^-$ with norbornene, implying that the fully substituted complex could not form an associative complex with norbornene. An ion at *m/z* 781 was detected, which could be assigned to either the alkene coordinated intermediate **41** or the alkene insertion product prior to further CO association, **42** (the two forms are isomers of one another) (Scheme 16). To further probe the origin of the complex at this mass ion peak, and whether the CO/norbornene exchange was direct or indirect, the [(**39**-H)-CO]$^-$ was selected and reacted with norbornene in the same manner, again providing the peak at *m/z* 781. The formation of this peak in the absence of [(**39**-H)]$^-$ showed that it was highly likely that the peak at *m/z* 781 was formed by the [(**39**-H)-CO]$^-$ species.

To assign the identity of the observed peak, DFT calculations (B3LYP/LANL2DZ*) were used to calculate the relative energies of truncated analogues the two possible cobalt-alkyne-norbornene complexes (**41** and **42**). The analogue of **42** was found to lie significantly lower (22 kcal mol^{-1}) in energy than the alkene-coordinated complex, implying that the observed peak

likely corresponded to **42**. Overall, this investigation highlighted a key piece of mechanistic information about the Magnus mechanism: carbonyl/alkene exchange must proceed *via* a dissociative process, with an intermediate coordinatively unsaturated pentacarbonyl cobalt species formed prior to alkene coordination. The authors noted that these findings are in agreement with Yamanaka and Nakamura's inability to locate an energetically-accessible transition state for the direct carbonyl/alkene exchange formed *via* an associative pathway.

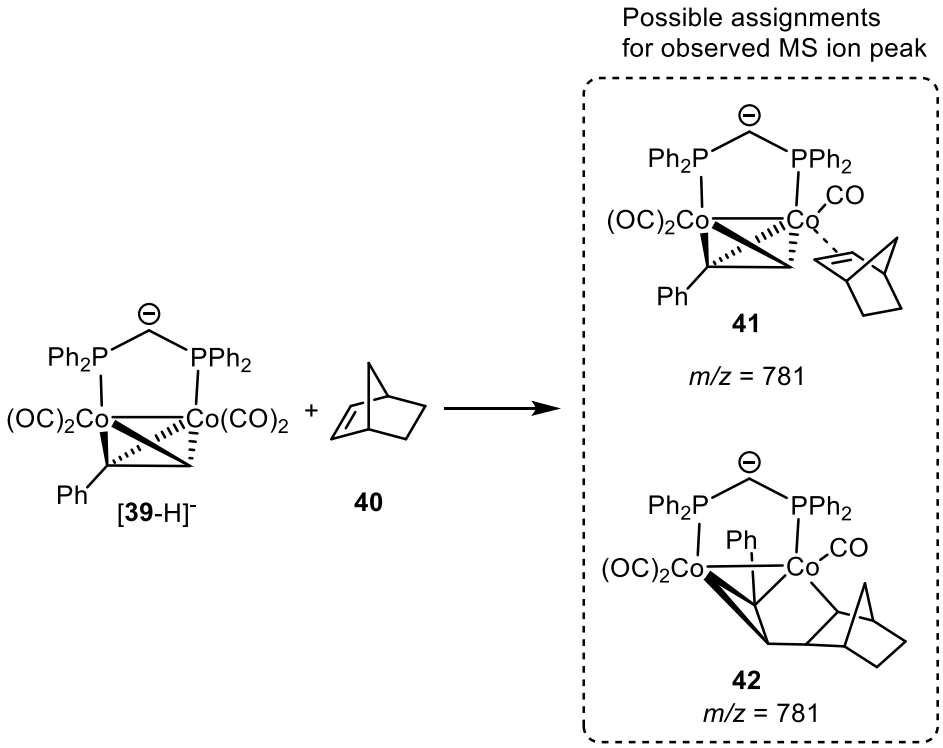

Scheme 16 - The possible assignments of the peak at m/z *781 from the Collision-Activated Reaction (CAR) of [**39**-H]⁻ with norbornene (**36**)*

The authors did not ascertain whether the reaction of **39** under PKR conditions would yield cyclopentenone product. Laschat and co-workers have demonstrated that cobalt complexes featuring bridging bidentate phosphines were inactive to reaction with norbornene using NMO promotion (for discussion of NMO promotion in the PKR, see section 1.5).[14] As such, it is understood that the presence of bidentate phosphines can have an inhibitory effect to PKR reactivity, a factor not discussed in this investigation by Gimbert and Greene.

The first example of an isolated and characterised alkyne/alkene coordinated cobalt pentacarbonyl complex was reported in 2007 by Evans and McGlinchey.[15] The authors prepared the cobalt complex of dibenzocycloheptene-substituted alkene **43**, and found that alongside the expected cobalt-alkyne complex **44**, the pentacarbonyl complex **45** was also able to be isolated

in 15% yield (Scheme 17). Single-crystal X-ray diffraction (SCXRD) studies confirmed the structures of both **44** and **45**, showing that the now vacant coordination site in **45** is occupied by the coordinated alkene portion of **43**. The SCXRD structures showed that the cycloheptene rings in **44** and **45** adopt boat configuration, placing the double bond in a position where it can readily coordinate to the cobalt centre. The authors commented on the thermal instability of **44**, which is found to readily undergo decarbonylation and formation of **45**. This decarbonylation (which is usually energetically demanding and thus the rate determining step of the reaction) is likely assisted by the presence of a tethered coordinating alkene moiety.

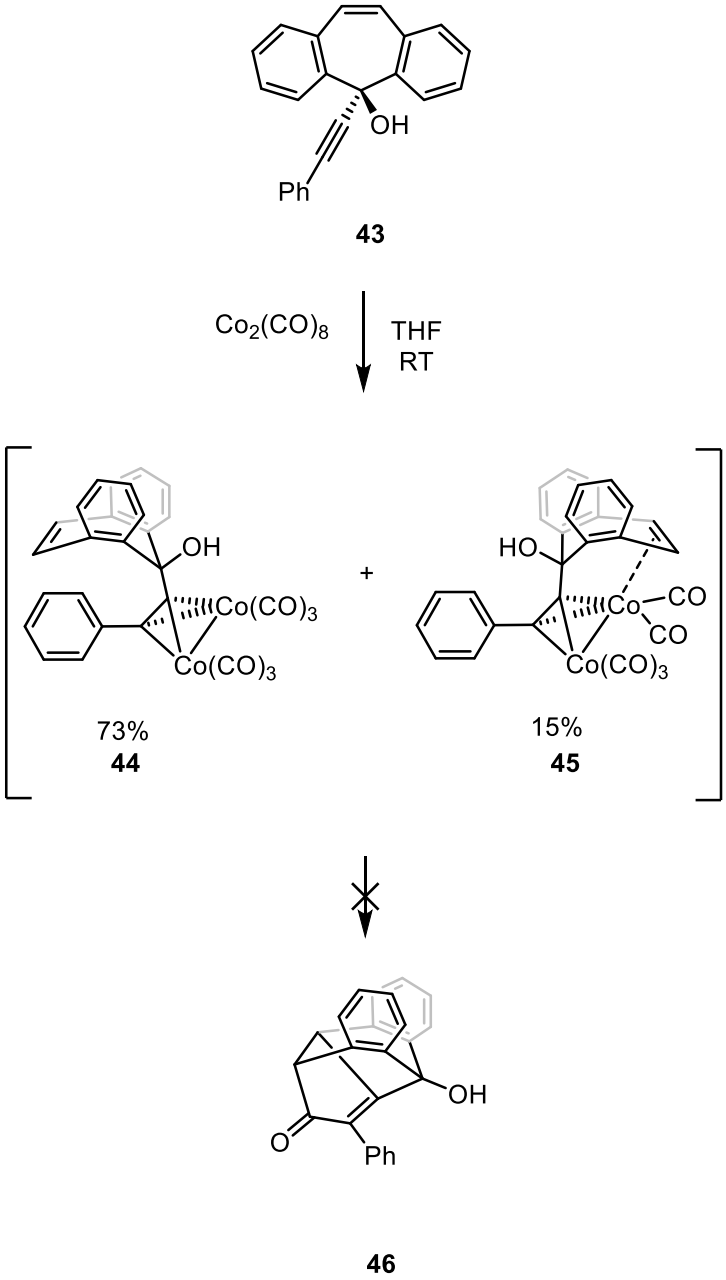

Scheme 17 - Observation of a cobalt-alkyne-alkene complex by Evans, McGlinchey and co-workers, and the expected structure of the unformed cyclopentenone product.[15]

Further heating of complex **45**, however, did not yield cyclopentenone **46**. The lack of conversion to the final PK product was put down to two factors. Firstly, the nature of the coordination of the alkene, and the length of the tether between the alkene and the alkyne, forces the groups about the $Co(CO)_2$(alkene) centre to adopt a staggered conformation relative to the $Co(CO)_3$ centre. This disrupts the normally assumed geometry of alkene-coordinated intermediates, which are thought to form eclipsed conformers with the alkene inserting from the axial position (see section 2.1.3 for further discussion of the influence of alkene coordination and insertion sites).

The displacement away from the eclipsed geometry renders the axial position inaccessible, and may result in the alkene being unable to undergo insertion and cobaltacycle formation. The second rationalisation for the lack of conversion to product is the high degree of ring strain present in cyclopentenone **46**. which may cause later mechanistic steps to be highly energetically demanding.

The characterisation of complex **45** represented the first structural elucidation of a cobalt-alkene-alkyne coordination complex as a Magnus-type intermediate, providing a major advance in the understanding of the PKR mechanism.

Riera, Verdaguer and co-workers used a similar approach to access a cobalt-alkyne-alkene complex utilising a similar dibenzocycloheptene skeleton for the alkene, but in an intermolecular capacity, with a chelating PPh_2 group attached to the cycloheptene ring. The authors reasoned that if the cause of the lack of insertion to form the cyclopentenone product observed by Evans and McGlinchey was the distortion of the eclipsed configuration adopted by the groups about the two cobalt centres, an intermolecular reaction (which employs no tether between alkyne and alkene to influence geometry) should resolve this issue. Similarly, the final product, **50** would not be expected to experience the same steric strain as **46** (Scheme 17). Alkene **47** was converted into the BH_3 protected analogue (**47-BH_3**), and reacted with **48**. The coordinated alkene complex **49** was isolated and characterised by SCXRD. The X-ray diffraction structure confirmed that alkene **47** was capable of acting as a bidentate ligand when coordinating to the cobalt. Furthermore, the complex retains the eclipsed geometry of the cobalt ligands, with the alkene and phosphorus occupying equatorial and axial sites respectively.

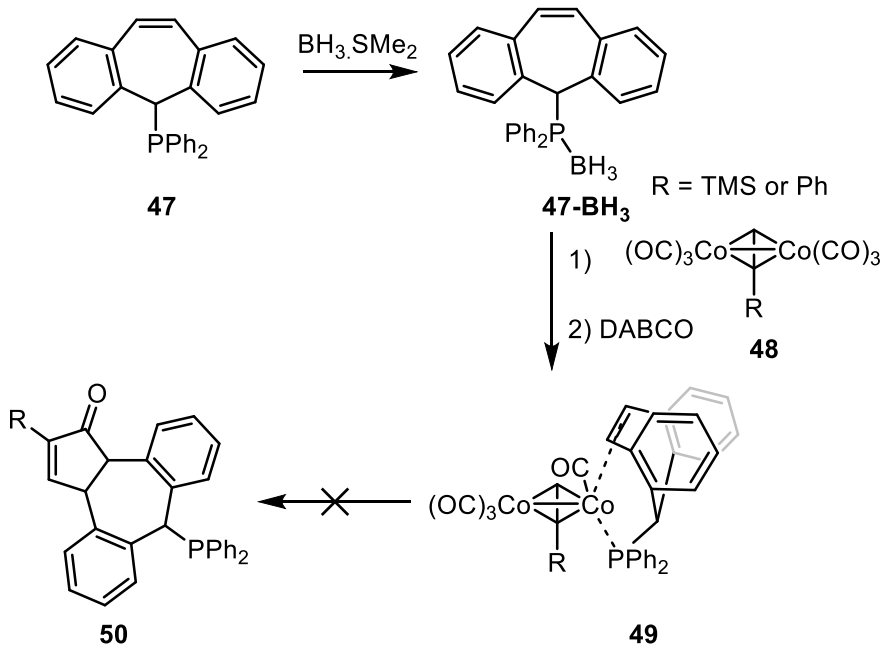

Scheme 18 - The use of a phosphine-alkene ligand to observe cobalt alkyne-alkene complexes, as performed by Verdaguer, Riera and co-workers.

The authors noted that the barrier to rotation for complexes such as **49** are thought to be easily overcome, and that the axial position should be accessible for insertion of the alkene to continue the Magnus mechanistic pathway. However, conversion to the cyclopentenone **50** was not observed, regardless of alkyne substituent or promotion method (thermal or amine N-oxide). The authors proposed that this may be due to the presence of a phosphine ligand bound to the cobalt centre. This was explored further by use of a nonhindered linear alkene bearing a diphenylphosphine group. When these were reacted with a cobalt-phenylacetylene complex, the phosphine-coordinated pentacarbonyl species could be isolated and characterised, but no alkene-coordinated species were detected. Promotion of the phosphine-coordinated species gave the expected cyclopentenone, leading the authors to conclude that the presence of the phosphine was not the causative factor for the lack of reactivity of complex **49**. The authors attributed the lack of reactivity displayed with **49** to the level of activity of the alkene in the insertion step. The authors used DFT (B3LYP/6-31G*) to show that the insertion of the dibenzocycloheptene moiety is notably less energetically favourable than that of a "traditional" intermolecular PKR alkene such as norbornene (+20.8 kcal mol^{-1} relative energy). This sizeable energy difference was suggested to arise from the breaking of conjugation between the two benzene rings fused to the cycloheptene which would occur upon cyclisation. This observed lack of reactivity highlights once again that while the CO-dissociation step is often rate determining,

the alkene must be capable of undergoing the insertion step once coordinated in order to produce PK products.

Gimbert and Greene later revisited their MS studies of the mechanism, intending to examine the source of the carbonyl group which is incorporated into the cyclopentenone ring.[16] Using the cobalt complex of the cationic alkyne moiety N-methyl-N-propargylpyrrolidinium (**51**), mechanistically relevant intermediates could be detected using MS techniques (Scheme 19). A similar approach had earlier been applied by McIndoe and co-workers, who had prepared a range of PKR precursors bearing quarternary ammonium centres, for reaction monitoring by MS methods.[17]

ESI-MS ionisation of **51** led to the detection of fragment ion **52**, the CO-loss product. When ion **52** was selectively subjected to a collision activated reaction (CAR) with norbornene, an ion with *m/z* 476 was detected. As **53** and **54** are isomers of one another, this newly formed ion could correspond to either, or a mix of both. The ion at *m/z* 476 was further selected and a submitted to a CAR with CO, forming an ion peak at *m/z* 504, corresponding to **55** or **56**. An expected ion peak at *m/z* 532, corresponding to **57**, was not observed, despite DFT calculations predicting **57** to have relatively high stability. A peak at *m/z* 246, for the cyclopentenone product **58**, was however observed.

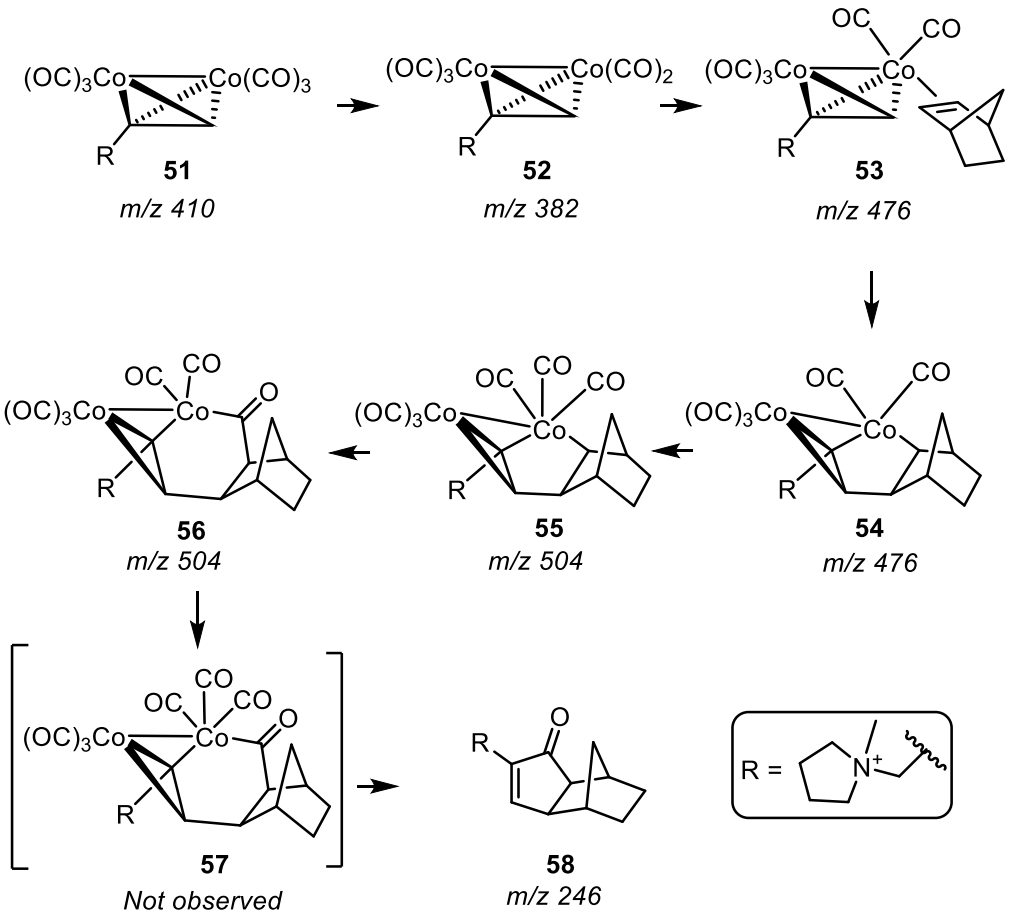

Scheme 19 - Structures of the intermediates observed by ESI-MS as reported by Gimbert, Greene and co-workers.[16]

When the ion at *m/z* 476 (**53** or **54**) was selected for collision-induced dissociation (CID), product **58** was not observed, implying that saturated coordination is required for CO insertion and subsequent complex separation.

Following these observations, isotopically labelled ^{13}CO was used as the collision gas. The incorporation of ^{13}C in the intermediates was not uniform across the intermediates. Intermediate **51** saw a shift to *m/z* 411, due to incorporation of one labelled carbonyl group via carbonyl-norbornene exchange. Species **52** and **53** did not display any ^{13}C incorporation, but the ion at *m/z* 504 was shifted into a pattern that suggested numerous different levels of ^{13}CO incorporation, up to five carbonyl units. Crucially, however, the peak at *m/z* 246, corresponding to product **58**, did not display any ^{13}C incorporation at all. This observation implied that the carbonyl group in the final product cannot originate from a CO gained through coordination of free CO in the system to an unsaturated cobalt centre. Instead, the CO incorporated in the product must be exclusively gained from a carbonyl group which is present on the original complex. The authors concluded that the most likely mechanism for this to take place is an

internal bridging CO transfer from one metal centre to the other, and use DFT (B3LYP/631LAN) to model potential pathways for this transformation. The calculations showed that it was feasible for a bridging interaction to transfer a carbonyl ligand for incorporation into the final product, and the authors rationalised that this process is more intuitive than a bimolecular pathway, which would likely occur less readily in a dilute solution at high temperatures. The authors concluded that their findings shed light on an important deviation from the accepted Magnus mechanism.

In light of the observations by Gimbert and Greene, Rodriguez and Prieto undertook a theoretical study attempting to rationalise the observed change in endo/exo product ratio when microwave heating is applied to the system.[18] The DFT study (B3LYP/6-311+G(2d,p)/LANDL2DZ on Co), calculated the pathway of the reaction between ethene and norbornadiene using both the Magnus mechanism (with a bimolecular process supplying CO following alkene insertion), and the Gimbert variation (with CO transferred between cobalt centres in a unimolecular process following alkene insertion). The authors found that when norbornadiene is coordinated to the cobalt centre, the *exo* approach (on the less hindered face of the alkene) is more stable than the *endo* approach. The authors find that when considering CO insertion into the cobaltacycle via the Magnus mechanism, the *endo*-pathway is more thermodynamically stable, an observation at odds with the experimentally observed *exo*-selectivity. Conversely, when an intramolecular CO transfer is considered (the Gimbert variation) the *exo* pathway is more feasible than the *endo*, leading the authors to conclude that the Gimbert variation is more likely to be occurring under microwave conditions. The authors noted that the high energy barriers of the Gimbert variation (34.5 and 40.0 kcal mol^{-1}) may explain the change in diastereoselectivity when microwave heating is used. As microwave heating of a sealed vessel is able to raise a reaction to high temperatures and pressures, above the boiling point of the solvent, higher energy pathways which would usually be inaccessible with conventional heating may become feasible.

Non-cobalt analogues have been used to study PK-type intermediates. Hartline and co-workers detailed the use of a dinickel analogue system to simulate dicobalt PKR intermediates, with the expectation that a dinickel centre chelated by a naphthyridine-diimine (NDI) ligand would confer greater stability to the nickel centre.[19] This was seen to be the case, with a dinickel benzene complex **59** readily coordinating to enyne **64** in a manner highly similar to dicobalt species, and undergoing alkene insertion to form a bicyclic five membered nickelcycle , **62**, which was characterised by XRD analysis. Heating of **62** in the presence of CO gave **63**, the expected cyclopentenone product, in good yield (Scheme 20).

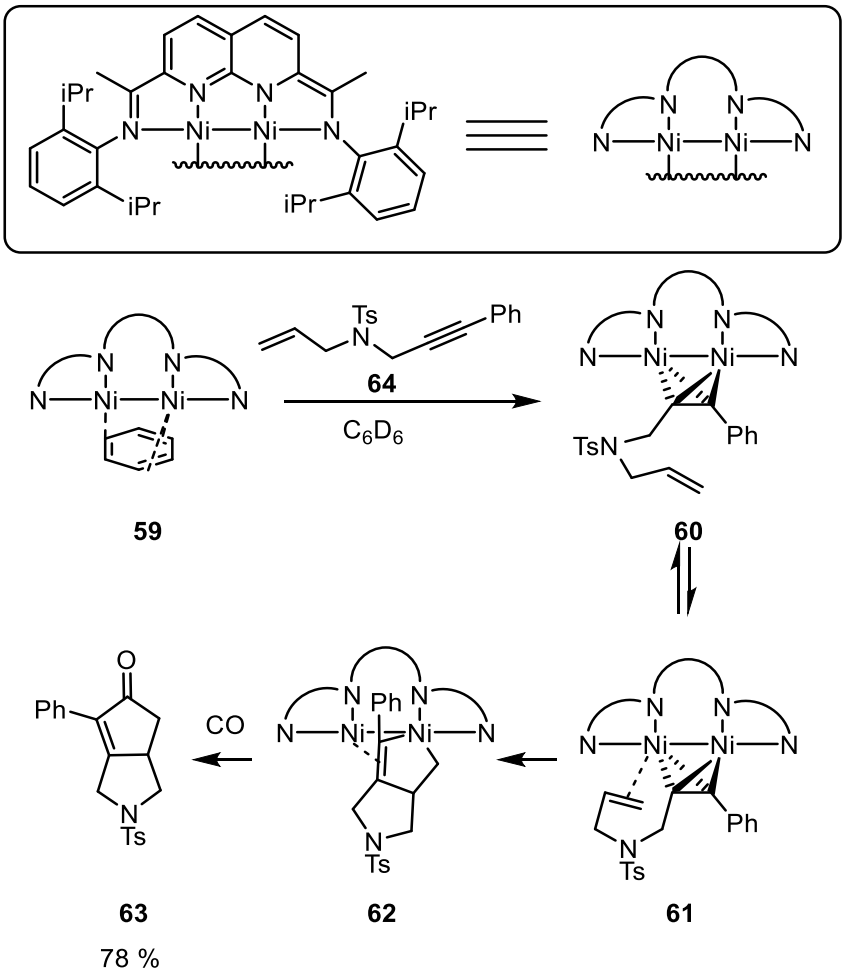

Scheme 20 - The use of a dinuclear Ni_2 center stabilised by a pincer ligand to provide stable analogues of Magnus intermediates.

This study allowed for observation of previously unobserved metallocycle stages of a Magnus-like mechanism. The authors highlighted that in the single-crystal XRD structure of intermediate **61**, there is a clear η^2-Ni-π interaction between the non-cyclised nickel centre and the double bond in the metallocycle, which is thought to act as a stabilising influence to promote metallocycle formation.

To support comparison between the dinickel and dicobalt systems, DFT optimisations (M06/6-31G(d,p)) of the geometries of the corresponding dicobalt analogues of **60** and **62** were calculated, and compared with the single-crystal XRD structures obtained, finding a high level of structural similarity between the two systems.

Following the success in observing dinickel analogues of Magnus intermediates, Hartline and colleagues turned their attention towards a mononickel centre. The authors found that an isopropyl diazadiene nickel cyclooctadiene complex([$^{i\text{-Pr}}$DAD]Ni(COD), **65**), is able to coordinate

enynes with aryl-substituted alkyne terminals. Cyclisation, however, is only possible with an activated alkyne bearing a *para*-trifluromethylphenyl group (**67**), which provides the metallocycle in a low yield (18%). The authors ascribed this lack of activity in the mononickel system to the lack of the η^2-Ni-π interaction observed in the dinickel system.

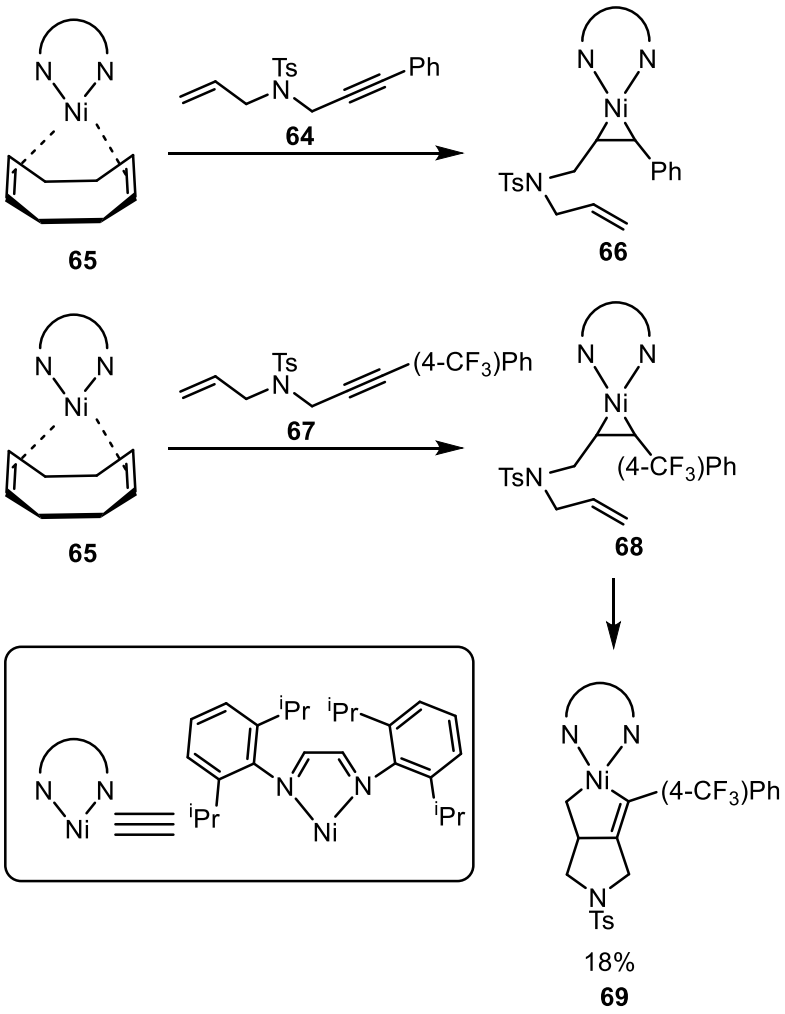

Scheme 21 - Structures and reactivity of a mononickel-enyne complex system.

1.4. Reactivity of alkenes in the PKR

For the PKR to achieve its potential of being a highly attractive synthetic route to functionalised cyclic molecules, the factors behind the reactivity of alkenes required understanding, ideally with a view to optimising the reaction to expand the scope of potential alkene coupling partners. The empirical understanding had generally been that more strained alkenes were more reactive to the PKR than unstrained alkenes, especially in intermolecular processes. Strained bicyclic

species, such as norbornene or norbornadiene, have been seen to be particularly active in the PKR, and used as substrates right from the initial discovery of the reaction. With the better understanding of the Magnus mechanism, research has been undertaken to try and explain and quantify the observed differences in reactivity. Following the demonstration of increased exothermicity in DFT calculations as a result of increased ring strain by Pericas and co-workers in their initial theoretical study into the PKR mechanism,[11] Milet and Gimbert embarked on a more in-depth treatment of the observed behaviour.[20] Considering the reactions of cyclohexene, cyclopentene and norbornene with the cobalt hexacarbonyl propyne complex, the study used DFT (B3LYP/LANL2DZ*) to calculate the geometries and energies of the alkene coordinated state, the initial cobaltacycle state, and the transition state which links the two intermediates. Inspection of the geometries did not reveal any obvious factors which seem to control the reactivity, with all three alkenes coordinating in a similar fashion, with no abnormal alterations in interatomic distances in the calculated optimised geometries. The authors were able to relate the observed interatomic distance differences and reactivities with molecular orbital (MO) characteristics of the alkenes.

The optimised geometries showed a lengthening in the alkene double bond upon coordination, which the authors attributed to changes in the back donation from the cobalt *d*-orbitals to the alkene π*-orbitals. The authors found that increase in back donation from the cobalt should lead to a lengthening of the alkene bond, and a shortening of the alkene-cobalt complexation distance. In practice, this is exactly what was observed, with norbornene (the most reactive alkene studied) receiving the most back donation, and displaying the greatest degree of alkene bond lengthening and the closest Co-(C=C) coordination distance.

The quantified amount of back-bonding can in turn be correlated to the barrier to alkene insertion, with high levels of back donation decreasing the barrier to the cobaltacycle formation step. The authors found that the LUMO (the π*-orbital) of the alkene is the key factor governing activity. Firstly, a lower-lying LUMO is more able to receive back-donation from the metal centre, and secondly the LUMO is involved in the bond formation step to yield the five-membered cobaltacycle. Overall, these factors lead to the LUMO energy providing a good approximation for the activity of the alkene within the PKR.

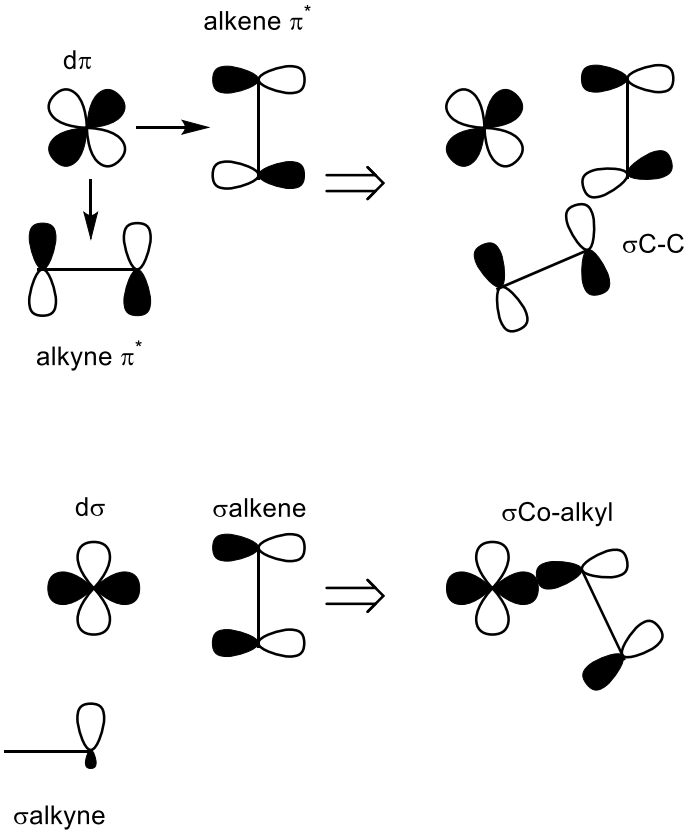

Scheme 22 - HOMO-LUMO interactions governing alkene activity in the PKR.

1.5. Promotion of the PKR

While the methodology discovered by Khand and Pauson allowed for access to novel transformations, there were notable drawbacks inherent in the method. Notably, strongly forcing conditions were required in order to generate the desired products, with long reaction times at high temperatures being required for even intramolecular couplings. Over the course of the reaction's development, various methods of promoting the PKR have been discovered, vastly increasing the versatility of this transformation.

The earliest form of promotion of the PKR was discovered by Smit and co-workers 1986, who unexpectedly observed that the rate and conversion of an intramolecular reaction is greatly increased by adsorption onto silica (SiO_2).[21] The authors demonstrated that by dry-adsorption of the cobalt-enyne complex **70** onto silica, and heating the resulting immobilised complex, the transformation to cyclopentenone **71** was complete within 3 hours (Scheme 23). This activity is remarkable, as when complex **70** is reacted under thermal conditions, very small quantities of product **71** were detected.

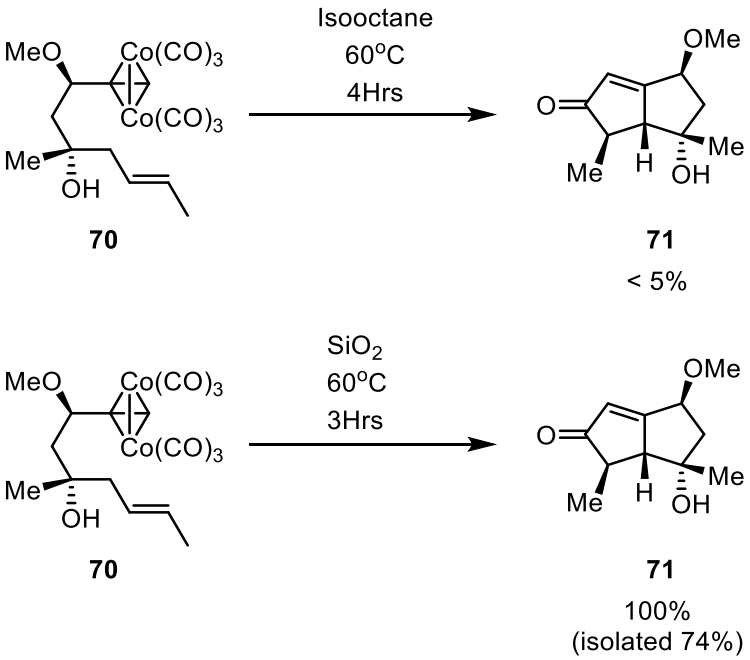

Scheme 23 - The improvement of reactivity gained from immobilisation onto silica of cobalt-enyne complexes as observed by Smit and co-workers.

The authors explored this newfound promotion in a subsequent study,[22] and establish a broad scope of intramolecular reactions which are accelerated by adsorption onto silica gel. The study finds that the water content of the silica plays an important role, and that silica gels containing >30% or <5% water were inactive as promoters for the reaction. While unable to ascertain the exact mechanism of rate enhancement in the reaction (partly as this work was carried out just prior to the publication of the Magnus mechanism) the authors suggested that the enhancement of rate and activity may be due to the effect that adsorption might have on the conformation of the cobalt-enyne complexes. If adsorption, and hydrophobic effects, causes precursors such as **70** to adopt a coiled conformation, the alkene fragment would be situated close to the cobalt-alkyne moiety. In this way, the silica support may act as a form of templating method, decreasing the entropic penalty to the ring formation by restricting the degrees of freedom of the enyne. Notably, the study's substrate scope is restricted to solely intramolecular couplings, with no examples of intermolecular PKRs.

Other early methods of promoting the PKR were examined by Pauson and co-workers in 1988.[23] Their study showed that ultrasound increases the rate of product formation across a range of substrates, but has little effect on yield. Conversely, the use of tributylphosphine-oxide as a reaction additive increased yield, but had little impact on rate. Despite the rate-enhancing effects of the phosphine oxide in the reaction mixture, reactions using starting materials bearing

phosphine ligands did not display any increased reactivity. The study also briefly references the use of trimethylamine-N-oxide as a promoter, citing that “erratic results” were observed when testing this method of promotion.

The use of amine N-oxides as promoters for the PKR has, over time, become the most widely used class of exogenous additives in the field. The first demonstration of the powerful promoting effect of amine *N*-oxides was published in 1990, where Schreiber and co-workers showed the ability of N-methylmorpholine-N-oxide (NMO, **73**) to perform the intramolecular PKR on a wide range of substrates at room temperature, producing cyclopentenone products in good yields (Scheme 24).

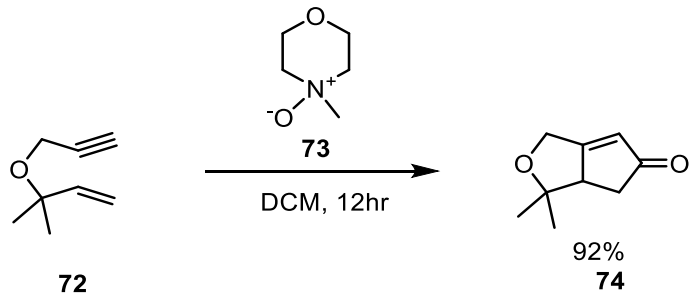

Scheme 24 - Example of NMO promotion of the PKR as demonstrated by Schreiber and colleagues.

This enhancement of rate is also observed with trimethylamine N-oxide (TMANO) as reported by Jeong and co-workers.[24] It is understood to arise from the amine N-oxide oxidising a cobalt-coordinated carbonyl ligand into a CO_2 molecule, which is unable to undergo recomplexation. This in turn converts the equilibrium in the first stage of the Magnus mechanism (carbonyl-alkene exchange) into an irreversible step, lowering the energy demand of the rate-determining step. For further discussion of the mechanism of amine N-oxide promotion of the PKR, see section 3.1.2.

Amine N-oxides are often employed in large excesses (up to six equivalents), which can be disadvantageous. Recently, Kerr and co-workers reported the use of a gel-supported amine N-oxide, which was able to be re-generated and re-used.[25]

In addition to amine N-oxides, primary amines have been demonstrated to act as efficient promoters of the reaction[26]. Sugihara and co-workers detail how hard Lewis bases such as primary amines and alcohols can increase lability of carbonyl ligands on metal centres, by increasing electron density on the metal and disrupting the M-CO σ-bonding. Furthermore, the coordinatively unsaturated species is stabilised by the Lewis base ligand, further increasing the

energetic favourability of the all-important ligand exchange step at the start of the Magnus mechanism.

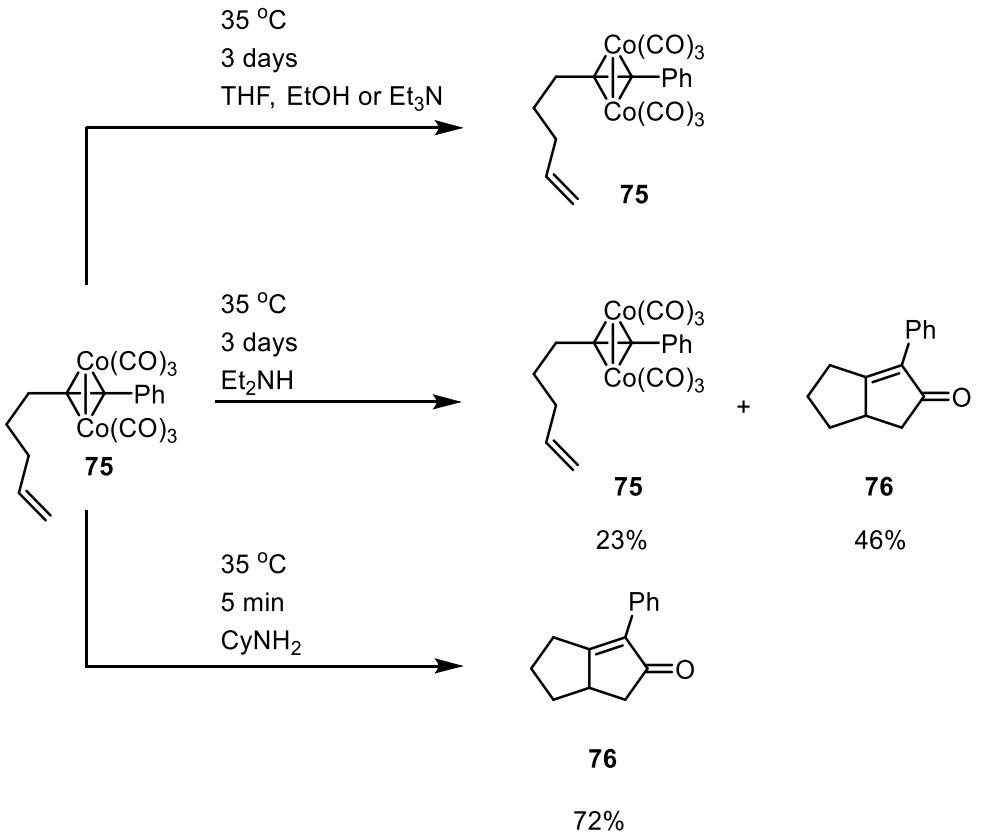

Scheme 25 - Reactivity of an enyne complex under various levels of promotion by amines, as demonstrated by Sugihara and colleagues.

Sugihara and co-workers demonstrated that cobalt-enyne complex **75,** which is inactive to PK cyclisation at room temperature, even in the presence of tertiary amines (Scheme 25 – top), is active to some extent when dissolved in secondary amines (Scheme 25 – middle), and reacts rapidly with good conversion in primary amines (Scheme 25 – bottom). The authors were able to apply this reactivity to an intermolecular PK reaction, and identify two sets of conditions which form the products in excellent yields (Scheme 26). An excess of cyclohexylamine in a chlorinated solvent (dichlorethane, DCE), or a 1:3 mixture of 1,4 dioxane and aqueous ammonium hydroxide can promote the coupling of phenylacetylene and norbornene, achieving near-quantitative conversion.

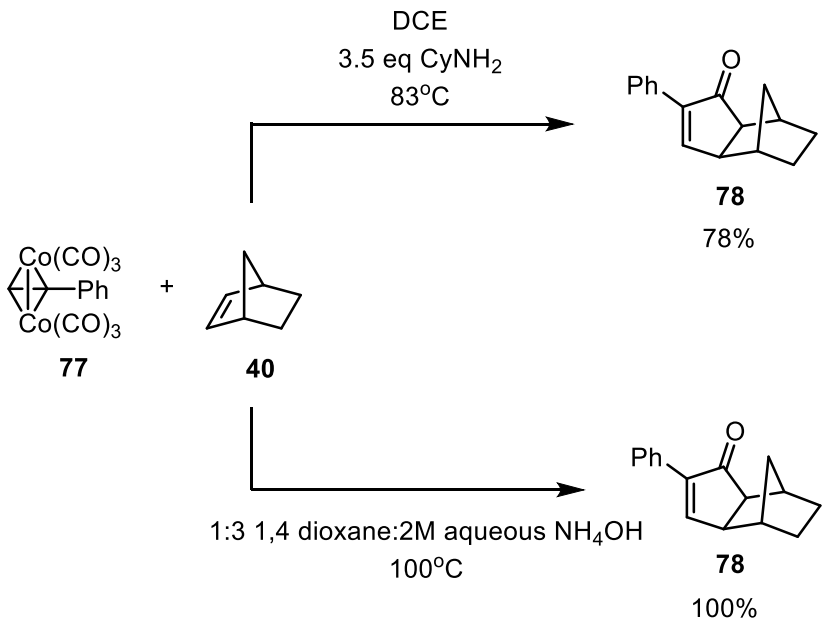

Scheme 26 - Conditions developed by Sugihara and colleagues to perform intermolecular PKRs using amine promotion.

More recently, TEMPO (2,2,6,6-tetramethylpiperidine N-oxide) (Scheme 27 – **80**) has been shown to be highly active in promoting PKRs, allowing for couplings in greatly increased yields at room temperature. Importantly, the mechanism of action of TEMPO is thought to be different from that of other amine N-oxides. Instead of oxidation of a CO ligand to a CO_2 molecule, TEMPO (as a radical species) is thought to promote a radical pathway, which leads to low energy decarboxylation. Pericas and co-workers reported that the promotion effect was particularly marked when sterically bulky alkynes were used. The hexacarbonyl dicobalt complex of tert-butyl acetylene (**79**), for example, saw an increase in conversion from 15% in the absence of TEMPO to 99% with six equivalents of the additive (Scheme 27).

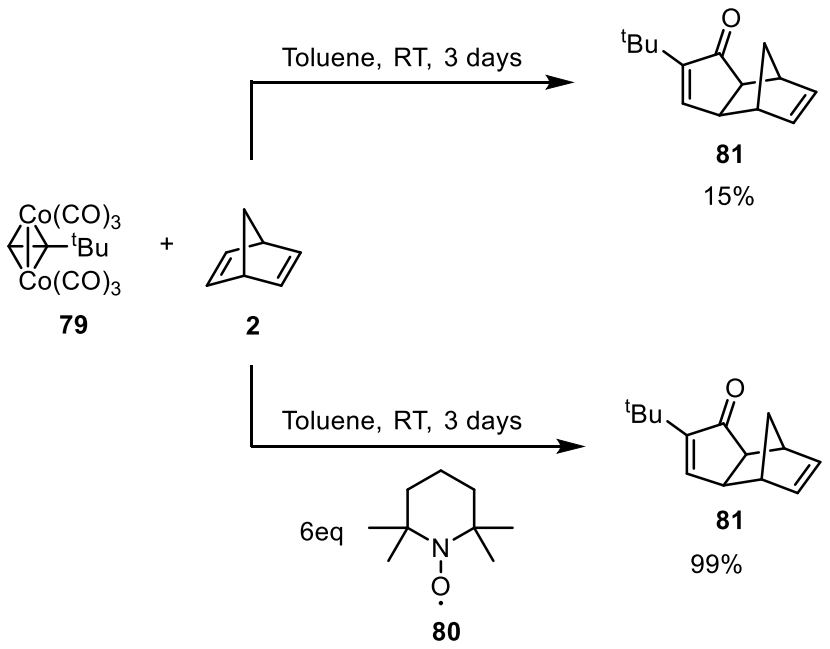

Scheme 27 – Increased conversion in the TEMPO-promoted PKR using mild conditions, as reported by Pericas and colleagues.

Analysis of the headspace gases of the reaction detected no CO_2 present in the effluent, implying that the oxidative decarboxylation characteristic of TMANO and NMO was not occurring when TEMPO was used. The problem was investigated further using DFT methods (B3LYP/LACVP*), on a model system using the cobalt-acetylene complex, and dimethylnitroxide as a truncated equivalent of TEMPO. It became apparent that single-electron reduction or oxidation of the complex carried a prohibitively high energetic penalty. As such, it was dismissed as a possibility. Instead, it was found that coordination of the dimethylnitroxide to the cobalt centre facilitated a radical pathway, which decreased the energy barrier to decarbonylation by an appreciable amount (4.7 kcal mol^{-1}).

Promotion of CO-loss from cobalt complexes can also be performed by photochemical methods. Pagenkopf and Livinghouse demonstrated that the catalytic PKR can be promoted using high-intensity visible light,[27] allowing for previously demonstrated catalytic transformations to be carried out at milder conditions (55 °C and one atmosphere of carbon monoxide). For further discussion of photochemical methods and studies on cobalt-alkyne complexes, see section 4.1.2)

A method of promotion which can increase the accessibility of intermolecular-type PKR products (i.e. monocyclic rings) is the use of “traceless tethers”. This methodology, developed by Pagenkopf and colleagues, uses a silicon-tethered enyne (**82**) in an intramolecular PKR. Concomitant detachment of the silicon tether leads to a monocyclic product (**84**) being formed

without the observation of the bicyclic intermediate (**83**). Use of a terminal alkene allows for the generation of cyclopentenones which would otherwise require reaction with ethene, a substrate which tends to perform poorly due to low activity in the cyclisation step, and represents logistical and safety issues from a practical perspective, generally requiring the heating of a vessel containing a high pressure of flammable gas.

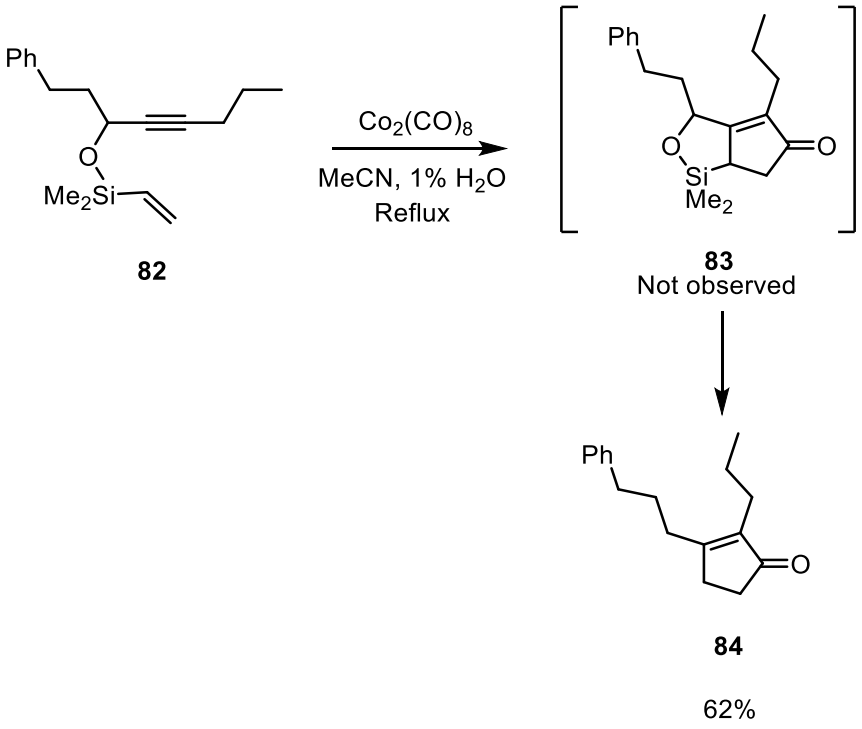

Scheme 28 - The use of traceless silicon tethers to perform pseudo-*intermolecular reactions.*

More recently, this methodology has been applied to synthesise cyclopentenones with a high degree of diastereoselectivity.[28]

Several studies have focused on the results of applying microwave heating to PKRs. Due to the high-energy thermal conditions required to perform additive-free intermolecular PKRs, microwave heating represented an attractive method to supply the required thermal energy to facilitate carbonyl dissociation. Evans and co-workers explored the application of microwave promotion to the PKR in 2002, highlighting the added solvent dependency introduced by this method. Heating of the cobalt complex of trimethylsilylacetylene and norbornaidene in toluene gave a 97% yield of cyclopentenone, but with an impurity of the *endo* norbornadiene product. The proportion of this impurity was lowered when DCE was used as the solvent. This change is thought to arise from the differing microwave cross-section of the two solvents. Microwave cross section (a measure of how much microwave energy interacts with a material) is directly linked

to the dipole moment of the molecule in question. Toluene possesses no dipole moment, and so is heated very inefficiently by microwave irradiation. DCE, conversely, has a larger dipole moment, and a correspondingly large microwave cross section. The significance of this difference is that when toluene is used as a reaction solvent, a greater amount of energy is required to raise the reaction vessel to the required temperature, leading to undesired reactivity from over-irradiation.

Groth and co-workers examine the effect of microwave heating and solvent on the catalytic PKR. Considering a range of solvents, the authors were able to identify a trend between dielectric constant and yield. Strongly polar solvents (with high dielectric constants) produce lower yields of cyclopentenone than microwave transparent solvents. This showed that the reagents themselves are capable of absorbing microwave energy efficiently, and heating of the bulk solvent is not required. Highly microwave transparent solvents, such as heptane, exhibited poor yields as well, which was linked to degradation of the cobalt species within the reaction due to the high level of irradiation required to raise the reaction vessel temperature to the required temperature. As such, Groth and colleagues found that lowering the reaction temperature (especially in highly microwave-transparent solvents) served to increase the yield, by limiting level of irradiation and therefore the catalyst degradation.

1.6. The catalytic PKR

Following the brief mention of a catalytic PKR protocol by Pauson, Khand and co-workers in their initial publication detailing the PKR,[2] there was great interest in the development of a robust catalytic protocol for the formation of cyclopentenones. One of the drawbacks of the original cobalt-mediated PKR is the stoichiometric amount of cobalt carbonyl required to effect the transformation, which is somewhat less sustainable than a catalytic process. This subsection will focus on some of the major advances in the catalytic process of the PKR with cobalt, and with other metals.

1.6.1. Development of catalytic PKR protocols

Several catalytic preparations were published following the discovery of the PKR, driven by the interest in accessing ever-more sustainable and powerful methods for the synthesis of complex molecules, particularly natural products.[29–34] Particularly notable is the catalytic reaction of 1-heptyne with ethene by Rautenstrauch and colleagues,[35] who reported a 49% conversion to product **86** using only a 0.22 mol% catalyst loading of cobalt carbonyl.

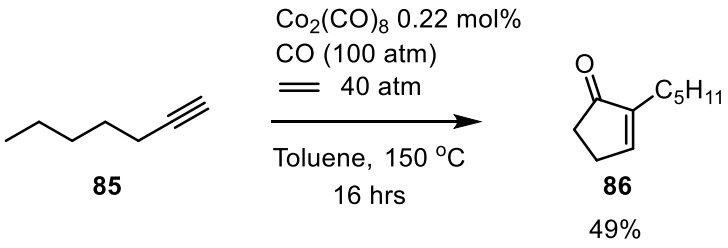

Scheme 29 - The catalytic reaction of 1-heptyne with ethene as reported by Rautenstrauch and co-workers.

This reaction, while able to use impressively low catalyst loadings for cobalt-catalysed systems (which had until this point been generally in the 10-20% range), had the drawback of requiring extremely high pressures and temperatures of carbon monoxide and ethene, both flammable gases. The need for a pressure of CO was one of the main disadvantages of the catalytic PKR, and highlighted the advantage of the stoichiometric PKR, where the cobalt carbonyl is able to act as both a mediator and an in-situ CO source.

However, techniques were soon developed to decrease the necessary pressure of CO. Jeong and co-workers investigated the use of various additives in the catalytic cyclisation of enyne **87**, finding that triphenylphosphite (10 mol%) was able to produce **88** in a 79% yield employing three atmospheres of carbon monoxide, representing a dramatic decrease from Rautenstrauch's conditions.

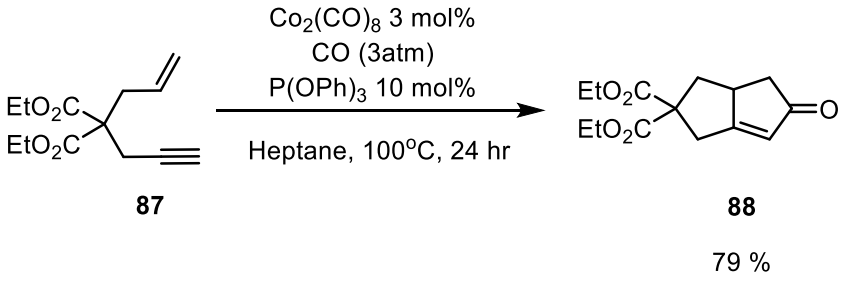

Scheme 30 - Use of triphenylphosphite as an additive to increase activity of catalytic PKRs.

Gibson and co-workers described in two publications how phosphine and phosphite adducts can stabilise catalytic PKR systems, allowing for good conversion using an atmospheric pressure of carbon monoxide.[36,37] Using 5 mol% of cobalt heptacarbonyl triphenylphosphine, the conversion of enyne **87** is shown to proceed in 80% yield with a very slight overpressure (1.05 atmospheres) of CO. Later, it was demonstrated that cobalt hexacarbonyl bis-triphenylphosphine is also suitable as an active catalyst.[38]

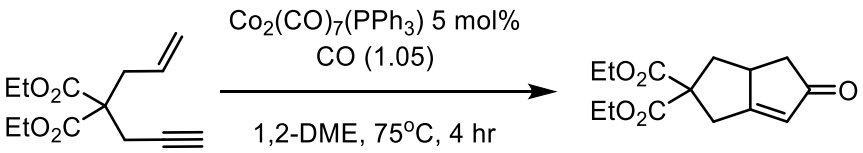

87 **88**

80 %

Scheme 31 - Catalytic PKR behaviour of a triphenylphosphine-coordinated cobalt heptacarbonyl complex.

Gibson and co-workers separately reported the immobilisation of cobalt complexes on a phosphine-functionalised polymer support, and the ability of the polymeric cobalt-phosphine structure to act as heterogeneous catalysts for the PKR.[39] Similarly, immobilisation of cobalt on mesoporous silica was found to be active in the PKR, delivering good yields in intramolecular couplings, but poorer yields in intramolecular transformations.[40] Colloidal cobalt nanoparticles have also been employed as PKR catalysts, with a high degree of reusability. Kim and co-workers found that the nanoparticle system could be used to run four reaction cycles with substrate **87** under CO pressure (5 atm), with yields ranging from 94-94%. TEM imaging following the final reaction cycle showed nanoparticle size to be unchanged, indicating a high nanoparticle stability and resistance to agglomeration.[41] Polyethylene glycol stabilised nanoparticles have also been demonstrated to display high activity and selectivity in intramolecular couplings.[42] Finally, Raney cobalt has also been demonstrated to catalyse the PKR, with a high degree of reusability.[43]

Until this point, catalytic methods of cyclopentenone formation had focused on intramolecular couplings, with intermolecular couplings often suffering from poor conversion. Jeong and co-workers successfully used an indenyl cobalt (I) species to catalyse the coupling of norbornadiene with several terminal and internal alkynes, seeing good conversions.[44]

1.6.2. Asymmetric PKR methodologies

In order to exploit the full power of the PKR in a wide range of synthetic applications, an asymmetric variant was required. The previously demonstrated promotion of the reaction by phosphine substituents meant that the use of chiral phosphines was a highly suitable strategy for development of asymmetric methodology.

Hiroi and colleagues tested a wide range of chiral phosphines in a series of model intramolecular PKRs, to assess the enantiocontrol which could be provided by the chiral phosphine additives.[45] Hiroi found that (*S*)-BINAP is able to confer high degrees of enantioselectivity to the cyclopentenone products. Following this discovery, more research into the mechanism and

intermediates of BINAP-adduct cobalt complexes was performed by Gibson and co-workers.[46–48] Their investigations showed that when pendant alkenes are present in the system, the cleavage of the cobalt-cobalt bond can lead to the production of monometallic cobalt(phosphine)hydride species. Additionally, for activity in the PKR the cobalt-enyne complex required the BINAP to be bound in a chelating manner (with both phosphorus atoms coordinated to the same cobalt centre). Binding in a bridging manner spanning both cobalt centres inhibited the reaction, which is in agreement with observations made by Laschat when considering bidentate phosphines as mechanistic probes for PKR intermediates.[14]

Several chiral phosphine ligands have been applied in catalytic PKRs following the pioneering work reported by Hiroi, Gibson, and respective co-workers.[49,50] Several of these techniques focused on the preparation of a diastereomeric cobalt complex, by complexation of a chiral ligand. The resulting product mixtures can be purified to give diastereomerically pure starting materials. One particularly notable example is the development by Pericas and Riera of a new chiral bidentate ligand designed specifically for Pauson-Khand chemistry.[51] Designed specifically for the intermolecular PKR, the ligand (PuPhos, **91**) contains a 1,3 S-P motif, which allows for bidentate binding in a bridging mode, without the decreased reactivity associated with a bridging diphosphine. The authors show that the BH_3 protected version of **91** can be readily synthesised from (+)-pulegone (**89**), an abundant natural product.

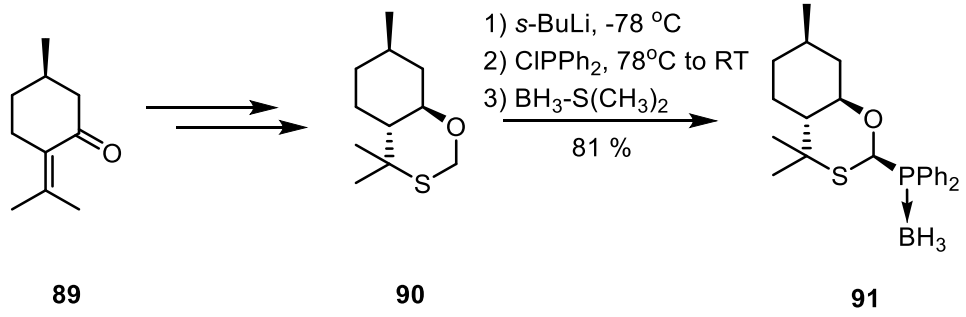

Scheme 32 - The synthesis of PuPhos from (+)-Pulegone, as developed by Pericas and Riera

The bench-stable protected form of PuPhos (**91**) could be readily converted into the active deprotected from by heating in the presence of 1,4-diazabicyclo[2,2,2]octane (DABCO). When **91** was deprotected in the presence of a cobalt-terminal alkyne complex, the expected bridging PuPhos complexes were produced, with two diastereomers produced (**93** and **94**) (Scheme 33).

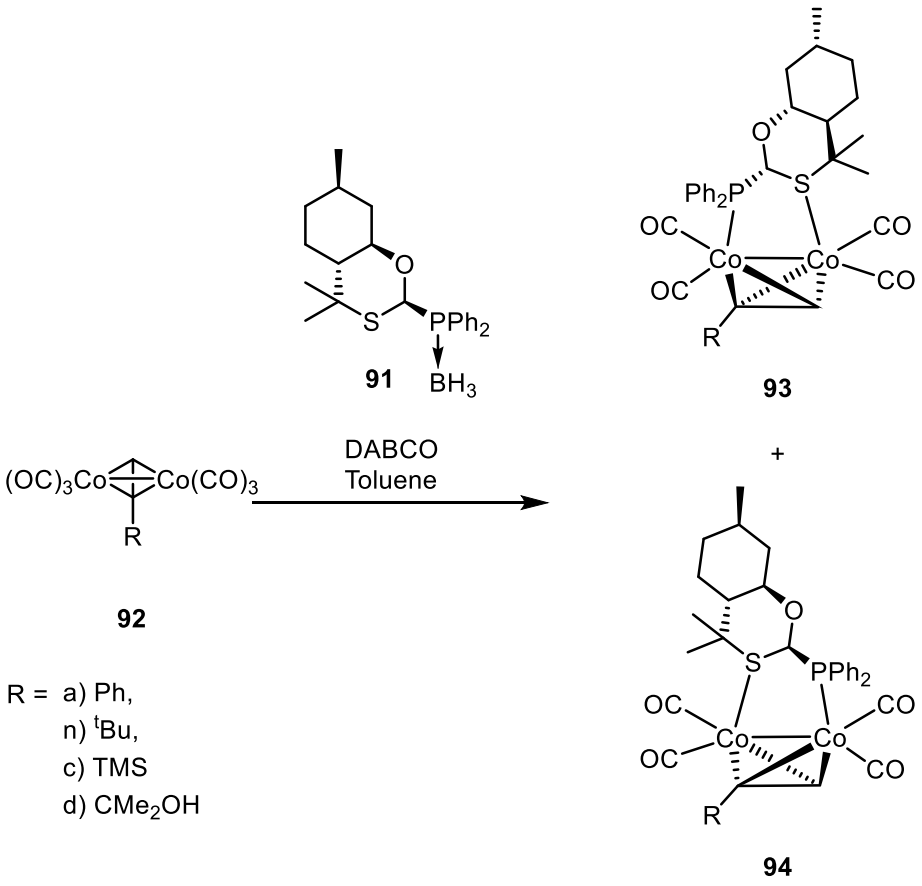

Scheme 33 - The formation of diastereomeric PuPhos-adducts of terminal alkyne cobalt complexes.

The diastereomers **93** and **94** could be separated by column chromatography on silica gel, or in many cases by crystallisation. The unwanted diastereomer could subsequently be treated to re-isomerisation by heating, and further purification to collect more of the desired diastereomer. The cobalt(tetracarbonyl)(alkyne)(PuPhos) complexes were found to be far more reactive than bidentate phosphine complexes, with all surveyed substrates reacting with norbornene under thermal conditions to give excellent yields and generally high enantioselectivity. Reaction at room temperature using NMO promotion was seen to increase the product *ee* of some substrates.

The authors ascribe these impressive results to the binding character of the PuPhos ligand. The cobalt-sulfur interaction is far more labile than that between the phosphorus and cobalt, so will preferentially dissociate, more favourably than the phosphorus or a carbonyl ligand. As such, the position of dissociation will be pre-determined, and the initial energy barrier to the reaction is lowered. The increase in ee observed when using NMO is thought to arise from the promoter's ability to remove free CO in the system. Free CO, the authors explain, is thought to promote epimerisation within the reaction. Overall, the use of PuPhos represents a method of quickly and

easily generating and isolating prochiral cobalt complexes, which can exert stereocontrol within the reaction through preferential dissociation of sulphur, allowing for excellent yields and stereoselectivities. Later, Riera and Verdaguer describe that the proton on the tertiary carbon bridging the O, S and P atoms of PuPhos is capable of forming H-bonding interactions with H-bond acceptors such as carbonyls, biasing diastereomeric ratio and ee in products containing these functional groups.[52]

In addition to chiral ligands, chiral promoters have also been used to provide enantioselectivity in PKR products. Kerr and co-workers use Brucine N-oxide to promote the coupling of norbornene with a range of alkynes, and observe modest enantiomeric excesses.[53] The group find that the stereoselectivity of the product distribution is highly sensitive to temperature and solvent choice. The best enantioselectivities were seen when using coordinating solvents such as THF, either neat or mixed with DCM. The mechanism behind the stereoselectivity is thought to arise from the aforementioned selective decarbonylation of the cobalt-alkyne complex, or from the post reaction product of the amine N-oxide (brucine) coordinating and acting as a chiral ligand. The use of chiral promotion in the context of cobalt-alkyne complexes was further explored by Nicholas and co-workers, in search of methods to provide stereospecificity to the Nicholas reaction.[54] Using Brucine N-oxide, Nicholas and co-workers were able to effect the stereoselective dissociation of a carbonyl, and installation of a phosphine into the newly formed vacant coordination site, thus supporting the hypothesis that enantioselective carbonyl dissociation by the chiral N-oxide is responsible for the observed stereospecificity. Laschat and Verdau carried out further experiments with a range of amine N-oxides derived from naturally occurring alkaloids, including nicotine and quinine, similarly achieving modest regioselectivities (*ee* < 53%).[55] A common factor across all studies involving chiral N-oxides is the observation that the presence of a hydroxy group on the alkyne corresponded to increased stereoselectivities. Laschat and Verdau attributed this behaviour to the presence of a hydrogen-bonding interaction.

Following these observations, Pericas, Maseras and co-workers conducted a thorough theoretical investigation into the use of chiral N-oxides to introduce stereoselectivity from achiral substrates.[56] The authors find that the enantioselectivity does indeed arise from the preferential enantioselective elimination of a CO ligand, forming an enantiomerically pure CO complex. However, a racemisation process driven by CO ligand rearrangement is in competition with the alkene complexation, leading to erosion in stereoselectivity. The authors find that predictions using this model are in good agreement with experimentally-observed values, and highlight that the theoretical limit for attainable *ee* using this method is 90%.

1.6.3. Alternative CO sources

A factor which has been common to almost all catalytic PKRs is the requirement for a CO pressure. While the requisite pressure has been greatly reduced by additives, generally a headspace of CO is required, adding additional logistical complexity to the reaction procedure. Research has been carried out to provide alternate sources of CO, further increasing the versatility of the reaction. Chung and co-workers showed how an α,β-unsaturated aldehyde can be used in a Pauson-Khand type coupling with a cobalt-rhodium nanoparticle catalyst. The aldehyde group acts as a source of CO, circumventing the need for a CO pressure in the reaction. In addition to being a highly atom-economic transformation, this methodology represents a step toward a general protocol for the catalytic intermolecular PKR.

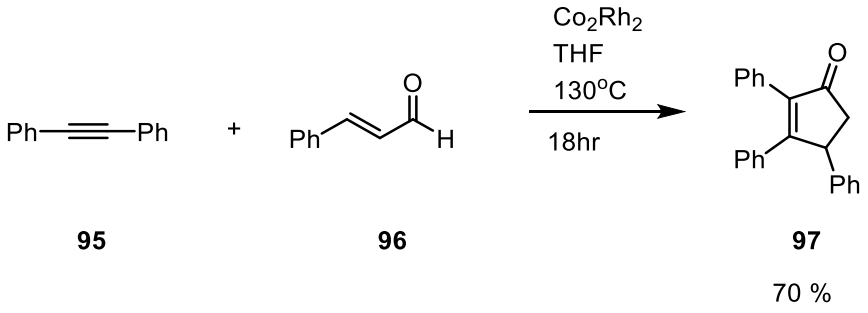

Scheme 34 - Use of unsaturated aldehydes as a pseudo-*CO source, as reported by Chung and colleagues.*

Perez-Castells and co-workers published another method for carrying out catalytic PKRs without supplying a headspace of CO gas to the reaction. By loading molecular sieves with CO gas under pressure before the reaction, the authors were able to carry out catalytic PKRs using solely CO generated by the off-gassing of the loaded molecular sieves. When applied to a model intramolecular system, the use of molecular sieves produced a slightly higher yield than a control experiment with one atmosphere of CO.

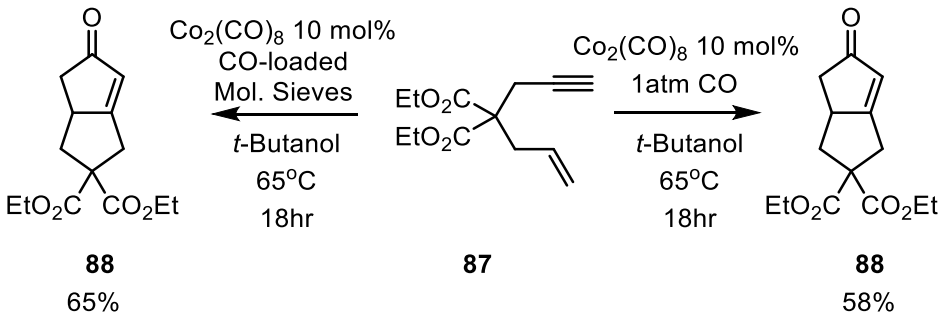

Scheme 35 - The use of CO-loaded molecular sieves as a source of carbon monoxide in the catalytic PKR.

1.7. PKRs with other metals

While a great deal of research has been carried out on cobalt mediated and catalysed PK transformations, there is also a wealth of examples of other metals catalysing this transformation (stoichiometric PK reactions with other metals are not usually carried out). This section describes a selection of other metals known to catalyse PKRs.

In 1996, Buchwald and co-workers reported the first PK cyclisation using a metal other than cobalt, when they showed that titanocene derivatives were able to form cyclopentenones in good yield under relatively mild conditions (~1 atm CO), without the need for additives.[57,58]

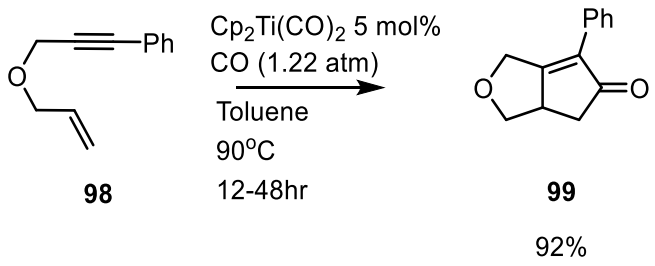

Scheme 36 - Titanocene-catalysed PKR as demonstrated by Buchwald and co-workers.

Once this methodology had been established, Buchwald and colleagues went on to demonstrate the use of a chirally-modified titanocene to perform enantioselective couplings.[59,60]

Following Buchwald's findings, catalytic PKR-like protocols have been established for several other transition metals, including nickel,[61] ruthenium,[62] iridium,[63] rhodium[64] and palladium.[65] Following their initial reporting, there has been a large amount of focus on optimisation of the various methodologies.[49] The versatile toolkit afforded by the optimised range of reaction conditions to form cyclopentenone rings has been used widely in a range of natural product synthesis applications.[66,67]

There have been several mechanistic studies concerning non-cobalt catalysed PK-like reactions, generally with a view to understanding and predicting stereoselectivity of products. Generally, mechanisms of non-cobalt PKRs are assumed to proceed through a Magnus-type pathway around a single metal centre. There have, however, been some notable investigations into these mechanisms for various metals which have highlighted influence of unexpected factors.

The mechanism of the rhodium-catalysed PKR was hypothesized in the initial communication detailing the discovery of the methodology by Jeong and colleagues.[68] The authors observe that the yield and enantioselectivity of the product was variable based on solvent, substrate

substituent and ligand. Furthermore, CO pressure was found to play a pivotal role in determining yield and enantioselectivity. Based on observed results, the authors propose a cationic monometallic mechanism (Scheme 37).

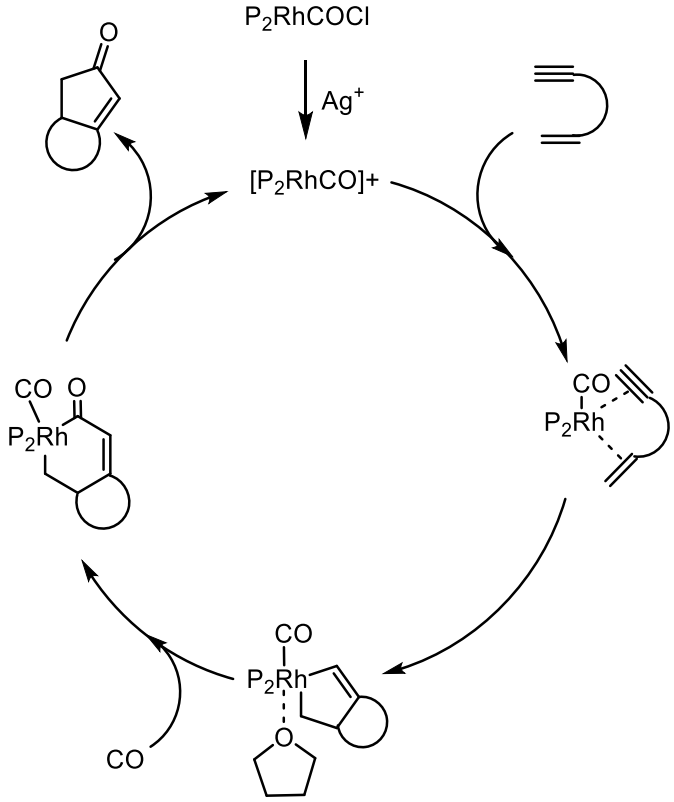

Scheme 37 - A generic mechanism for the rhodium-catalysed PKR, as proposed by Jeong and co-workers.

Baik, Evans and colleagues probed the observed effects of CO concentration on enantioselectivity with a theoretical study.[69] The authors considered a system without phosphine ligand present, and found that the coordination number of the rhodium centre was crucial for the stereoselectivity. The study finds that the changes in coordination geometry caused by the addition of an extra carbonyl ligand to the rhodium coordination sphere (mimicking a high pressure of CO) leads to a notable change in selectivity. Specifically, the trigonal bipyramidal structure assumed by the 5-coordinate [$Rh(CO)_2(\eta^2$-enyne)Cl] intermediate, is highly selective. Experimental validation of these results confirms that in the system surveyed a higher CO pressure is indeed associated with a greater degree of stereoselectivity. The authors conclude that this observation explains the reason that tightly-bound phosphines, which are likely to force the rhodium coordination sphere to adopt a trigonal bipyramidal geometry, are able to attain higher enantioselectivities. Further studies on the mechanism of the rhodium catalysed PKR

were recently carried out by Liu and Brummond, who focus on the origin of enantioselectivity when bidentate phosphine ligands are used.[70]

A theoretical study on the mechanism of the palladium catalysed PKR was conducted by Wu and colleagues.[71] Their investigation focused on the previous observations that a source of chloride was required for reactivity,[72] and the notable increase in yield observed when lithium chloride was used as a reaction additive.[73] To investigate the mechanism behind these observed effects further, the authors undertake a potential energy surface calculation using DFT methods (BP86/6-31+G(d)/SDD on Pd). The authors found a classical Magnus-style mechanism to be less favourable than an alternate pathway in which a chloride attached to the palladium centre is transferred to the terminus of the alkyne. This in turn leads to the generation of a Pd^{IV} centre, which can be stabilised by coordination of lithium.

1.8. Summary and conclusions

The PKR represents an extremely versatile ring- formation methodology, which has found use in a range of natural product syntheses. However, there are still some notable limitations to the methodology currently available, which hinder the reaction's applicability to a wider range of problems. One notable such limitation is the current lack of a versatile intermolecular cobalt-catalysed reaction, which is able form products regio- and stereoselectively. This limitation derives partially from an incomplete understanding of the mechanism of the cobalt-mediated PKR. Despite the in-depth investigations into the mechanism, the exact facts of the pathway are still a matter of some debate, with new studies revealing facts which necessitate amendments to the currently accepted mechanism. A deeper understanding of the mechanism of the cobalt-mediated process is critical to the development of a practical catalytic intermolecular methodology for large-scale synthesis.

1.9. Aims and objectives

Aims:

- Examine the regioselectivity arising from electronic effects in the PKR, with a view to developing methods of improve the efficiency of intermolecular PKR processes.
- Understand the potential for alternate speciation pathways in the PKR which are not currently accounted for in the Magnus mechanism.

- Understand the nature of cobalt-cobalt bonding in cobalt-alkyne PKR precursor complexes, and assess the mechanistic implications of the bonding character.

Objectives:

- Use a descriptor-based modelling approach to build a predictive relationship between electronic parameters and regioselectivity for a set of synthetically relevant internal heterocycle-substituted alkynes, and the use model to infer mechanistic information (Chapter 2).
- Apply *In-situ* IR techniques to cases identified by the model as being of mechanistic interest, to explore factors which may lead to unexpected regioselectivity in these cases (Chapter 3).
- Calculate potential energy surfaces for proposed alternative speciation pathways based on observed *in-situ* IR data, to assess the feasibility of these pathways relative to the Magnus mechanism (Chapter 3)
- Perform ultrafast time-resolved IR experiments (TRIR) on cobalt-alkyne complexes bearing substituents of interest, to examine cobalt-cobalt bonding and potential carbonyl photolysis product pathways (Chapter 4)
- Perform ultrafast TRIR investigations on molybdenum analogues of cobalt-alkyne complexes, for comparative assessment of metal-metal bonding in the two systems, and monitoring post carbonyl-dissociation pathways (Chapter 4).

Chapter 2: Investigation into electronic effects on the regioselectivity of the Pauson-Khand reaction.

2.1. Background

The Pauson-Khand reaction represents a powerful synthetic transformation, but is hindered by a lack of understanding of key features of its mechanism. Specifically, when internal alkynes are used in intermolecular reactions, two regioproducts can be formed. Each alkyne substituent can be oriented in either the α or β position of the ring relative to the carbonyl group (Scheme 38). The regioselectivity displayed in these reactions is not fully understood, leading to inefficiency and uncertainty in the synthesis of cyclopentenones based on these substrates.

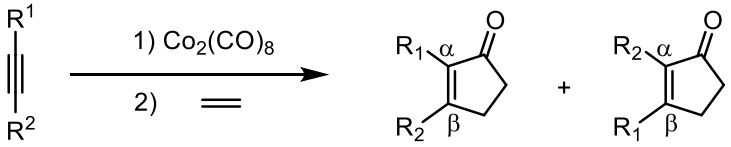

Scheme 38 - The possible regioisomeric products of the PK reaction of an internal alkyne with ethene.

As discussed in Chapter 1, the main obstacle to the understanding of the mechanism is the difficulty in observing or isolating intermediates in the proposed reaction pathway. As such, understanding of the mechanism may need to be derived from other sources than traditional chemical mechanistic investigations.

One such rapidly growing field is that of parameterisation and modelling. By representing the reaction conditions and/or substrates as quantified parameters, these can be related to reaction outcomes using a statistical model, to gain insight into the relationship between these parameters and reactivity. Importantly, this approach can be undertaken without an initial understanding or hypothesis of the mechanistic factors behind this behaviour. Insights gained from the model can in turn be used to optimise conditions to favour a given outcome or (as is desirable in this case) further understand the mechanism of the reaction. This approach is highly suitable for the problem at hand, as it can seek to relate electronic properties (a chemical feature well-suited to parameterisation) of the alkyne substrates with regioselectivity (a quantifiable outcome). This section will detail the current state of the art in novel statistical parameter-based mechanistic study, and detail the historic investigations and current understanding of regioselectivity in the PKR.

2.1.1. Parameterisation of mechanistically-relevant species

A key requirement to the drawing of quantitative conclusions from observed experimental data is quantifiable characteristics of the state of components within the system. For some components, these are already quantified, for instance reaction temperature and time. These characteristics do not require further interpretation in order to build a numerical relationship to describe their effect on the system.

However, many important variables present in a chemical system are not readily quantified. For instance, the steric bulk of a substituent on a molecule, or the charge on an atom, while still numeric quantities, are not readily apparent upon first inspection. It is often highly desirable to be able to construct a relationship between these characteristics and the outcome of the reaction, and to this end, parameterisation is employed.

The parameterisation of a component of a chemical system consists of the determination of these non-quantified characteristics. There are numerous methods which can be employed to carry out these determinations. Historically, characteristics that could not be directly measured could be ascertained by their effect on a model system. A seminal example of this practice is the Tolman electronic parameter (TEP).[74] The electron donating or withdrawing nature of a ligand is challenging to measure directly, but this electronic effect has an impact on the environment at the metal centre, which is itself measurable. In the case of the TEP, it was found that the stretching frequencies of carbonyl ligands on a $Ni(CO)_3L$ centre were sensitive to the electronic qualities of the ligand L (where L was a phosphine ligand). These stretching frequencies (which could be readily measured spectroscopically) could be used as a proxy to describe the electronic effects of ligand L on the metal centre. A metal centre with a strongly electron donating phosphine will display increased backbonding to the carbonyl groups. π-backbonding populates the π* antibonding orbital on the ligand, decreasing the bonding character of the C≡O interaction. The decreased bond strength leads to lower energy vibration, manifesting spectroscopically as a decrease in vibrational frequency. Metals with relatively electron withdrawing ligands will have lower population in their d-orbitals, limiting the amount of backbonding to the carbonyl ligands, causing the ligand stretching frequency to be higher in energy (Figure 2).

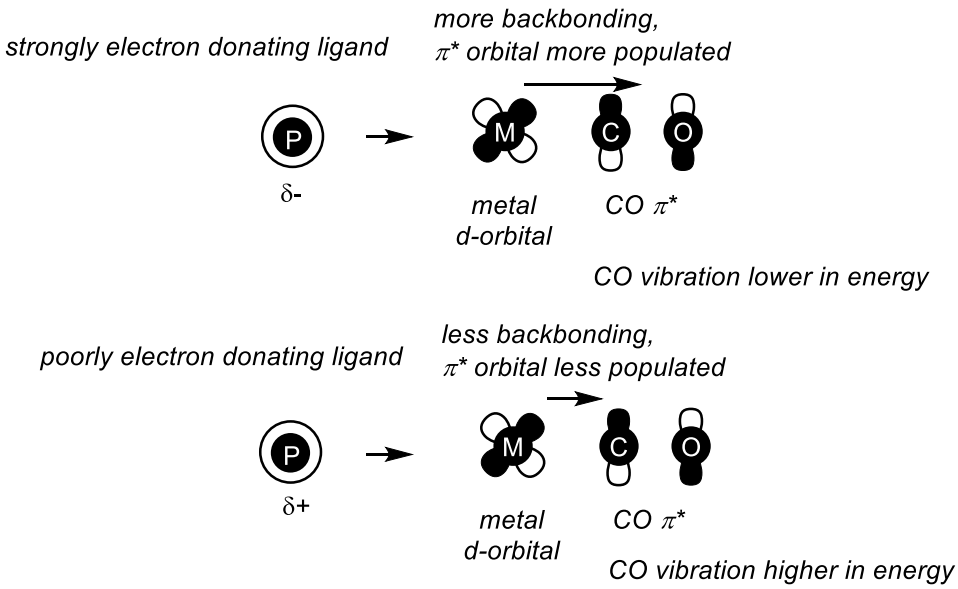

Figure 2 - Orbital diagram representation of the origin of ligand electronics on carbonyl vibrational frequencies, as described by Tolman.

Similarly, the Hammett parameter[75–77] describes the electron withdrawing or donating character of organic groups as substituents on aromatic rings. Rather than the interpretation of spectroscopic observations, however, the parameter instead relies on the equilibrium position of a model system bearing the given substituents. The equilibrium position complex, when compared with the unsubstituted example, is once again used to ascertain the relative donating or withdrawing natures of the substituents (Scheme 39).

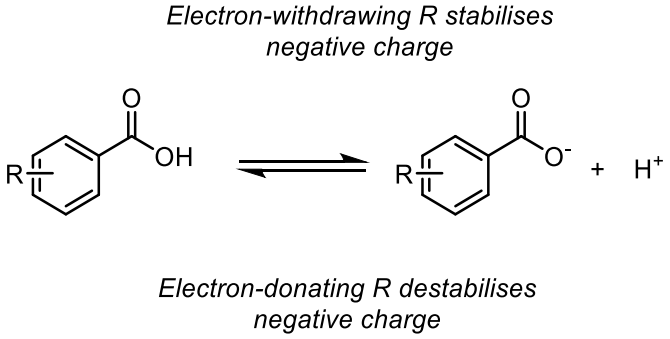

Scheme 39 - The benzoic acid equilibrium used to calculate Hammett constants.

The application of this relationship using known substituent parameters can be used to infer the nature of the charge at the centre of the transition state, based on whether the transition state is stabilised (and therefore facilitated) by electron donating or withdrawing groups. A reaction which is facilitated by electron-withdrawing groups, for example, is likely to build up a negative charge during the rate-determining transition state. This approach allows for the assignment of reaction properties which are not directly measurable, giving key mechanistic information.

These methods of parameter elucidation are highly reliable, as they utilise directly observed experimental results, which can be tied closely with the parameter that they seek to measure. However, this approach displays a significant challenge when applied to larger datasets, as the parameterisation of new examples requires experiments to be performed for each molecule of interest, disadvantaging this class of parameter when large datasets are required.

With the advancement of capabilities for the theoretical computational chemistry, new avenues have become feasible for the generation of parameters for chemical species. Recently, growing access to Density Functional Theory (DFT) methods has allowed for parameterisation of a wide range of chemical systems without limitations from computational resources. By performing theoretical computational calculations, the geometries and electronic structures of small molecules can be estimated. This approach has several advantages over experimental parameter derivation. Firstly, the computational nature of the technique lends itself well to high-throughput parameterisation of a large set of compounds, which would be potentially challenging to carry out experimentally. Secondly, the technique allows for the elucidation of parameters that would be difficult or impossible to measure experimentally.

For example, the partial charge on a particular atom in a molecule can often be linked to the mechanism of a reaction, but partial charges cannot be easily quantified experimentally. Population analysis based on a computationally-derived wavefunction allows for these charges to be estimated numerically. However, there are disadvantages associated with this technique. The quantities calculated by a DFT calculation will always by definition be an estimation of the true state of the 'real' chemical species. The level of theory at which these calculations are performed will dictate how close this estimation is to a true physical description of the state of the molecule. Due to this, the results of DFT calculations can be dependent on the methods used to generate them. This problematic factor can be mitigated to a certain extent by validation of results gained this way with experimental data, where possible.

The power of a computational approach to parameterisation has been demonstrated in one instance by the development of the Ligand Knowledge Base by Nathalie Fey and co-workers.[78–90] In this series of publications, Fey and co-workers set out a range of steric and electronic parameters for ligands of relevance to organometallic chemistry, describing them using a range of metrics. For phosphine ligands, for instance, the parameter set includes molecular orbital energies, proton affinities, and bonding and charges for a range of metal-phosphine adduct structures. Additionally, a novel steric parameter is devised. The helium-8 (He_8) steric parameter

is defined as the interaction energy between the phosphine ligand and a ring of eight evenly spaced helium atoms placed in a standardised position relative to the phosphine (Figure 3).

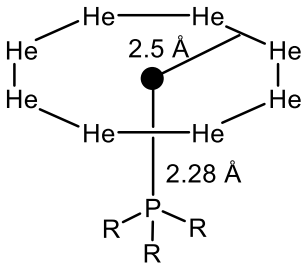

Figure 3 - The He_8 steric parameter, as defined by Fey and co-workers.

Once this range of parameters had been gathered, dimensionality reduction techniques, such as Principal Component Analysis (PCA) were applied to the multiparameter dataset. PCA reduces the number of parameters in a dataset by constructing principal components made up from linear combinations of numerical data to maximise variance along the components. This approach allows a high-dimensionality dataset, with several distinct observations, to be homogenised and reduced into a low-dimensionality reduction, which emphasises variance. In the context of parameterisation, such an approach allows for the grouping of the parameterised molecules by likeness, essentially producing a map of chemical space. Because the PCA method measures variance, observations that are clustered close together in the PCA plot are very alike, and those far from one another are very different. By reducing the dimensionality of the data this way, it is possible to quickly gain a holistic sense of the similarity between two given examples in a dataset.

2.1.2. Statistical model-building to explain and predict reactivity

While parameterisation on its own is useful for gaining a quantifiable sense and hierarchy of a given characteristic for a series of molecules, the true power of the approach arises from the applicability of the parameter set to statistical model building. If an investigator possesses a dataset of compounds and their response variables (i.e. their observed experimental behaviour), these two sets of quantities can be related by a statistical model. This model can be used in a predictive manner to make a speculation as to the chemical behaviour of an unseen example based on its parameters, a useful technique for the pre-screening of potential new substrates or catalysts. Additionally, the coefficients applied to parameters in the model can be used to gain mechanistic insight into the reaction being described. For instance, a model which places a large and significant coefficient on steric parameters, but not electronic parameters, implies that steric

factors are the dominant mechanistic factor in the studied transformation. Finally, outliers from the model can give information about examples in the dataset which may not conform to the same exact mechanistic pathway, meaning the model, which is primarily trained on non-anomalous substrates, fails to accurately model their behaviour.

The main challenge with building models in this way is the relative scarcity of systematic experimental data for training. Ideally, for the training of a descriptive model for a system, the majority of the training data should be consistent in the non-dependent variables, which can be difficult to achieve when varying multiple other parameters. Existing data in the literature may exhibit a large spread of these conditions, introducing new variation which can complicate the analysis. High-throughput screening methods go some way to alleviating this issue, by enabling the generation of large datasets quickly and efficiently, with control over fixed and dependent variables.[91–93]

Furthermore, a challenge more relevant to chemistry in particular is that chemical space is seen as continuous, with a very high number of potential species existing throughout it in a continuous distribution. However, the insight which chemists can gain into chemical space is limited by the feasibility of preparing the chemical species, leading to gaps in the population of this space. Furthermore, there is often a tendency for investigations to focus on a relatively very tightly grouped set of species in chemical space. Models which are trained on these highly clustered datasets would be able to accurately model the behaviour of examples within this small defined region, but would struggle with examples from elsewhere in chemical space.

Multicomponent linear models have proved powerful in predictive and mechanistic analysis across a in the field of catalysis.[94] Perhaps most notably, these models can be used for virtual screening of proposed structures, providing an assessment of activity and selectivity. By estimating the reactivity *in silico*, target catalysts can be identified without the need for the synthesis of a wide scope of potential candidates. The output from regression modelling can be used to inform on the structural features important to catalytic activity, allowing for guided catalyst design.[95] Similarly, the model output can be used to draw mechanistic information from datasets of a wide range of sizes.[96] These approaches can be further empowered when combined with complementary experimental systems, such as Design of Experiments (DoE). Systems such as these seek to provide a dataset which provides the most complete and efficient mapping of chemical space for a given set of variables.[97] This approach represents a notable shift from the

more traditional one variable at a time (OVAT) approach which has been historically the favoured approach to investigating chemical questions.

More recently, there has been a growing interest in the development of machine learning (ML) approaches to provide insights across the chemical sciences.[98–100] Within catalysis, many ML approaches have been employed for automated design of catalytic species.[101] In a particularly notable example[102], SMILES representations of molecular structure could be encoded to a continuous set of values using a neural network, and a gradient-based optimisation approach used for parameter prediction and property optimisation. Following property optimisation, a decoding neural network was used to reconvert the continuous set of values to a discrete SMILES representation. Using this conversion approach, the authors were able to essentially abstract the molecular structure into a purely mathematical representation, and circumvent the need for parameterisation. However, this approach possesses inherent drawbacks. The most notable of these, from a mechanistic perspective, is that the gradient optimisation approach conducted on the continuous representation is a black-box process, delivering little or no insight into the reasoning behind the optimisation approach. While this is powerful for predictive purposes, for mechanistic investigations this will be less informative than a supervised regression approach. This highlights an important consideration when applying machine learning to mechanistic questions, namely that while ML methods are often able to produce strongly predictive models, they often do not give insights into the decision-making process behind the predictions. As such, the mechanistic insight which can be gained from such approaches can be limited.

However, targeted application of ML can be used to great effect to elucidate mechanistic information from a given dataset. Recently, Bures and Larossa demonstrated an exceptionally powerful method of classifying mechanisms of organic reactions.[103] This approach applied the novel tools available through ML methods to kinetic analysis, a method which has historically played an important role in mechanistic investigations. Bures and Larossa demonstrated how these novel tools can streamline and automate the process of using experimental kinetic data to establish reaction mechanisms, turning a multi-step process into a single modelling transformation. Using a deep neural network trained on a large dataset of kinetic data, the finished model is able to accept even comparatively small and inaccurate kinetic datasets and return confident predictions of mechanism. This application of deep neural networks in a classification approach is a powerful tool to assign mechanistic profile estimates. The limitation of this approach is that there is a finite number of potential mechanisms within the model

training dataset. While the scope of mechanisms employed by the authors is exhaustive, models such as this will nevertheless be inherently limited by the breadth of their training dataset.

Additionally, the use of mixed models has been demonstrated to provide excellent quantitative modelling of site selectivity in iridium-catalysed borylation of arenes.[104] Hartwig and co-workers approached the challenge of applying ML methods to estimate energy barriers of mechanistically relevant steps. These energy barriers, usually calculated using QC methods, can be computationally demanding and sensitive to input, leading to inefficiencies when applied on scale. Prediction of these barriers through ML methods, therefore, presents an attractive optimisation of this process. However, the authors noted that the use of a pure machine learning algorithm leads to errors when input structures are not similar to the training set. They detailed, however, that a multicomponent linear model based on steric properties of neighbouring groups to the potential borylation sites is more robust in these cases, and better able to predict cases which are distinct from the training set. As the linear regression model is less accurate when predicting cases closer to the training data, the authors develop a hybrid model, which mixed the two models as a function of the substrate similarity to the training set. Using the Rogers-Tanimoto similarity score[105], the difference between the substrate being estimated and the training set could be quantified. The value of this similarity index then is used to determine which proportion of each model should be used in the estimation. This approach provides a 'best of both worlds' outcome, with each modelling method attempting to mitigate the shortcomings of the other.

2.1.3. The influence of alkyne electronics on PKR regioselectivity

The factor which exerts the most influence on the regiochemistry of the cyclopentenone products in the intermolecular version of the PKR is the steric bulk of the substituents on the alkyne. The regiochemistry is determined by which group the alkene preferentially inserts adjacent to, with the preferred group placed in the β position of the final cyclopentenone ring. A sterically bulky substituent will deter the alkene from insertion adjacent to it, leading to these substituents being found in the α position relative to the carbonyl group. This effect has been

noted from early in the history of the PKR, and is readily observed in the case of terminal alkynes, which will give exclusively α-substituted cyclopentenone products (Scheme 40).[2]

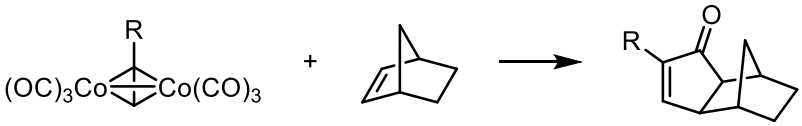

Scheme 40 - Exclusive α-selectivity of terminal alkynes in reactions with norbornene.

However, there have been observations of cases where the observed regiochemistry cannot be solely attributed to steric effects. Krafft and co-workers observed that when conducting reactions with an alkyne bearing an electron-withdrawing group that the electron-withdrawing substituent (although bulkier) is selective for the β position on the ring, defying the expectation that the bulkier substituent should be found in the α position on the final ring due to steric effects.

These electronic effects were investigated further by Gimbert, Greene and co-workers, who applied a DFT-level theoretical study to the problem.[106] The authors investigated on the basis that the regioselectivity from electronic effects of substituents could arise from the preferential dissociation of one carbonyl group on the cobalt over the others. Noting the shifting of resonances of acetylenic carbons upon complexation with cobalt (linked with a change in electron density at the carbon site), the authors proposed that the electronic effects of the substituents manifest as the polarisation of the acetylenic carbons in the cobalt-alkyne complex. The three distinct carbonyl positions on a given cobalt atom can be expressed as *trans-pseudo*equatorial, *cis-pseudo*equatorial, and *pseudo*axial to a given alkyne substituent group (Figure 4).

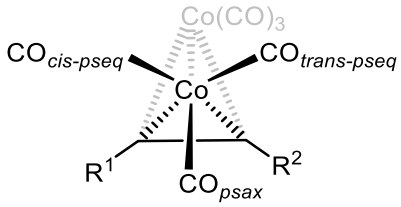

Figure 4- Labelling of carbonyl ligand positions relative the acetylenic carbon adjacent to R^1.

The authors demonstrated that the MO interaction between the $Co_2(CO)_6$ moiety and the alkyne in the cobalt-alkyne complex is largely made up by donation from the cobalt d-orbitals to the acetylene π* antibonding orbital. The authors stated that *"back-donation to the acetylene effectively increases the Co-CO_{pseq} distances"*. This is due to the fact that the same d-orbitals

involved in bonding with the acetylene also perform back-donation to the CO ligands. A difference in charge density on a given carbon would increase or decrease the level of back-bonding capability available from the cobalt centre to the CO ligand in the *trans*-pseudoequatorial position to the carbon in question, exhibiting essentially a *trans*-effect. Carbonyl ligands opposite (*trans*-pseudoequatorial) to an electron rich carbon centre would experience greater back-bonding (Figure 5), and therefore be less labile than a CO ligand situated opposite an electron poor carbon. Loss of these more labile carbonyls, and subsequent coordination and insertion of the alkene at this vacant site, would lead to a selectivity in the product formed (Scheme 41).

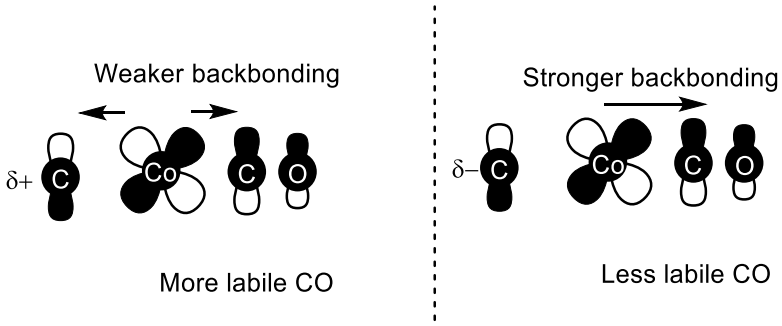

Figure 5 - Backbonding from a cobalt centre to a carbonyl ligand trans-pseudoequatorial to an electron poor (L) and electron rich (R) alkyne carbon.

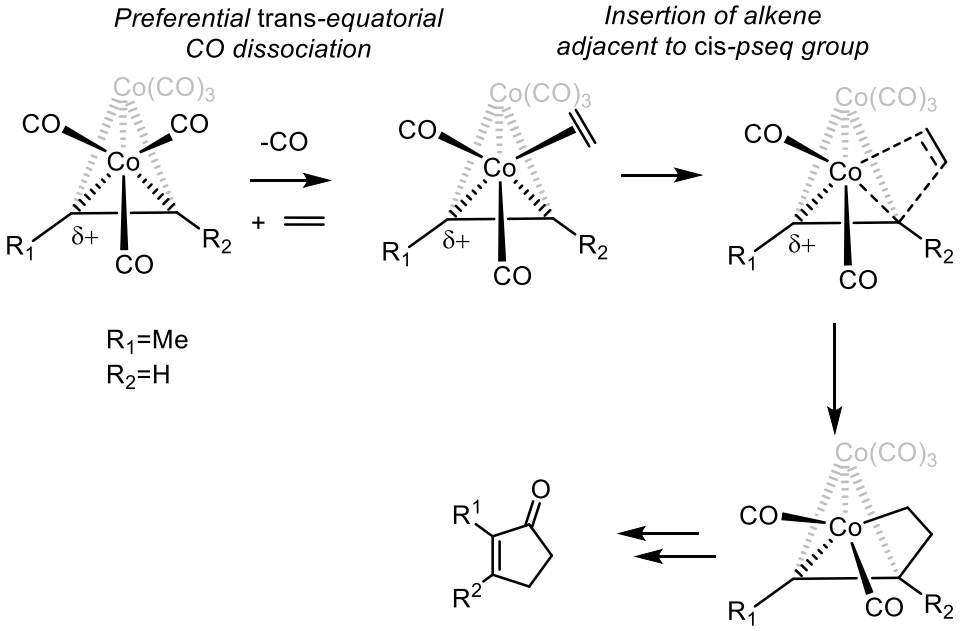

Scheme 41 - The proposed mechanism of site-selective alkene insertion following loss of a labilised carbonyl.

The level of ligand backbonding, and therefore lability, could be roughly correlated to the Co-C(O) bond lengths measured from single-crystal X-ray diffraction. Therefore, the authors proposed, it is possible to draw a qualitative prediction of regioselectivity from either a prediction of the polarisation across the acetylenic carbons (via DFT methods) or by inference from the bond distances in the structure.

Following these findings, this model was explored further by Gleiter and co-workers.[107] Studying a series of five alkynes bearing alkylthioethers, with various substituents, the authors applied the rationale developed by Gimbert and Greene to predict the regiochemical outcomes of their reaction with norbornene. In their analysis, Gleiter and co-workers found that the correlation between DFT-derived polarisation of the carbon atoms in the free alkyne and the cobalt-carbonyl bond lengths was not conserved between all cases. Furthermore, usage of solely the DFT charges or the bond lengths was not able to accurately predict regioselectivity for the entire series. These findings demonstrated that the factors behind the electronic basis of regiochemistry were more complex than first set out by Greene and Gimbert.

Further insight into the observed disconnection between the inconsistent effects of CO ligand lability and regiochemistry can be gained from a study by Milet, Gimbert and co-workers, who applied DFT to examine the energetics of the distinct coordination sites available to a coordinated alkene.[108] The authors observe that the barrier to rotation of the groups in an ethylene-coordinated dicobalt pentacarbonyl propyne complex are very low, and may easily be overcome at room temperature. The authors stated that "*it is apparent that the initial coordination position of ethylene (and other olefins when pseudorotation is relatively facile) does not determine the regiochemistry in the PKR*". This investigation made clear that not only does initial alkene coordination site not dictate final regiochemistry, but that furthermore (due to the axially coordinated alkene being the minimum energy state of the system) pseudorotation would likely always take place to result in the alkene being coordinated in the axial position (Scheme 42).

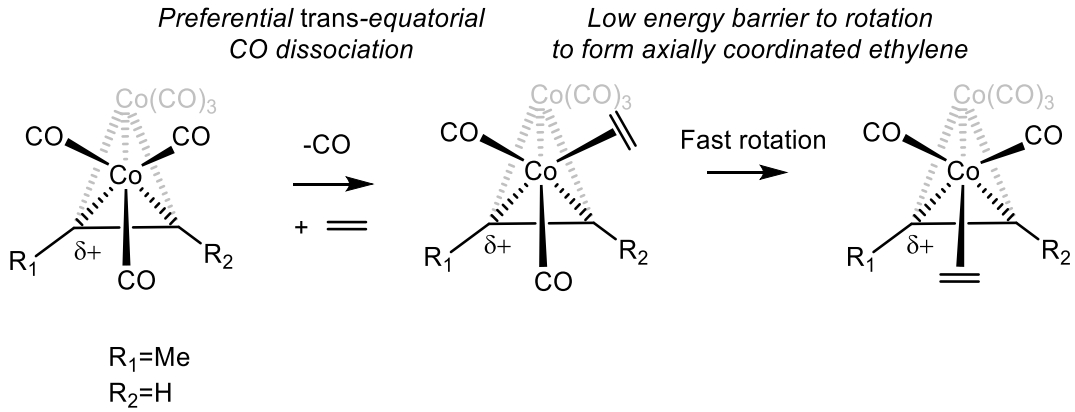

Scheme 42 - The states involved in the fast interconversion of equatorially and axially coordinated alkenes in the early stages of the PKR.

The observation that alkene insertion occurs favourably from the axial position, although previously considered based on experimental data,[109] had not previously been investigated theoretically. Taking into consideration this mode of insertion, it was now more likely that the electronic environment of the alkyne influenced regioselectivity *via* the initial C-C bond formation step, as opposed to the previously hypothesised CO dissociation step.

To further explore the ramifications of this effect, Greene and Gimbert carried out further theoretical study, focusing on the cobaltacycle formation step of the mechanism.[110] Considering a propyne-ethylene PKR, the authors calculated the various possible insertion transition states from axial and equatorial positions on the cobalt centre. The authors confirmed that in addition to the transition state for axial insertion occupying the lowest energy, it is the more likely mode of insertion from a kinetic perspective. Utilising kinetic simulations based on the calculated energies, the authors found that following the proposed pseudoequatorial CO dissociation and subsequent alkene coordination, the low barrier to rotation leads to an equilibrium between axially and equatorially coordinated alkene on the nanosecond timescale. Furthermore, it was found that the insertion *via* the axial position occurs approximately eight times faster than insertion at the initial equatorial site. Given that insertion from the axial position can access either acetylenic carbon, the authors compared the energetics of the transition states for each insertion across a range of alkynes differing in polarisation. The authors found that the transition states for coupling at the carbon with greater electron density were generally more favourable, leading them to conclude that the electronic selectivity observed arises from this stabilisation of the insertion transition state by excess electron density on the acetylenic carbon. Thus, electron withdrawing substituents, which polarise the density on the alkyne bond towards themselves and their adjacent acetylenic carbon atom, are selective for the β position.

This general rule, however, has been found in some cases to be inconsistent. For example, Verdaguer, Riera and co-workers investigated the regioselectivity of PKRs with fluorinated alkynes and norbornadiene.[111] They found that in these cases, the strongly electron-withdrawing difluoroalkyl group was in fact selective for the α position on the cyclopentenone, in defiance of the generally accepted rule. This was true even when the opposing group on the alkyne was a phenyl group, which would be expected to be selective for the α position due to its increased steric bulk.

Some recent investigations have explored this effect in greater detail. The Fairlamb[112] and Helaja[113] groups have both carried out investigations into the reaction of norbornene with internal alkynes bearing aromatic and heteroaromatic substituents. The Helaja group related their observed regioselectivities to Natural Bond Orbital (NBO)-derived charges across the alkyne bond, giving good correlations between charges across the alkyne bond and regioisomer distribution. This correlation was encouraging, as it represented a quantitative connection between alkyne polarity and regioselectivity for PKR transformations which were not completely selective for one isomer.

The Fairlamb group's investigation, however, details some unexpected regioselectivity. Electron-withdrawing substituents such as pyrones and pyridyl groups tended to favour the β position, but furans and thiophenes (despite being electron rich) also tended to favour this position, despite the expectation based on the current understanding that they would favour the α position.

These unexpected regioselectivities are a sign that upon widening the chemical space surveyed, the currently accepted understanding of electronic regioselectivity effects may not continue to be as reliable, and further study is warranted.

2.1.4. Summary

The understanding of the electronic effects governing regioselectivity in the PKR have been the subject of much study. Following experimental observations that the regiochemical outcome of these reactions could not always be explained by steric effects alone, various theories have been proposed as to the identity of the mechanistic influence played by electronic characteristics of alkyne substituents. Initial hypotheses regarding the favouring or disfavouring of CO dissociation sites were later shown not to be able to account for all cases of regioselectivity in some systems studied. Later study revealed that while CO dissociation is very likely to be affected by

substituents, low barriers to rotation of the groups on the cobalt centre equilibrate the post-coordination environment towards a neutral position too fast for the preferential coordination site to have any affect. Instead, the energetics of the ring-forming transition state have been found to play a crucial role in the selectivity. However, even with this knowledge in hand, it is still challenging to predict regioselectivity of sterically balanced alkynes, with exceptions to the rule appearing often. This implies that there are still elements and factors influencing the delicate balance of regioisomers which remain unexplored, and that these unanswered questions currently present a barrier to fully reliable prediction of the regiochemical outcome of any given PKR.

Many of the studies which sought to gain more insight into this effect have been rigorous, in-depth investigations into the behaviour of a small set of species. While these investigations have been able to provide highly precise knowledge of the energetics of these particular species, this approach has led to a concentration in chemical space of the current knowledge on the subject. As many of the unexpected observations are made regarding species which are outside of these specific regions of chemical space, an expansion of the understanding of these effects into new regions of chemical space is highly desirable.

Current capabilities in parameterisation and statistical modelling allow for a larger-scale holistic approach to this challenge, allowing for the consideration of large datasets and the drawing of inferences across broader regions of chemical space. As demonstrated by the Helaja group, a parameter-based approach has been able to provide a good description of electronic regioselectivity. This approach can be expanded to assess its suitability for applications farther afield in chemical space.

2.2. Aims and objectives.

The aim of the work presented in this chapter is to further develop the understanding of electronic contributions to regioselectivity in the PKR. Following encouraging results in the literature which suggest that computationally derived parameters can be used to model and predict regioselectivity, this investigation seeks to expand the scope of this approach by applying it to new areas of chemical space, with the goal of producing a more versatile model to link the electronic structure of internal alkynes to the distribution of their cyclopentenone products.

2.3. Selection of literature data for further investigations.

The Helaja group investigation used biaryl alkynes with electron donating or withdrawing substituents attached to the phenyl rings.[113] As no heteroaromatic groups were considered, this investigation was somewhat limited in its coverage of chemical space. Due to the fact that synthetic methodology employed to collect regioselectivity data was consistent between the investigations of the Helaja and Fairlamb[112] groups, a combined set of observations from both reported studies, and previously unpublished data from the Fairlamb group, represented an attractive opportunity to assess to what extent this relationship was conserved in wider regions of chemical space. The two datasets were combined to form a starting set. To aid systematic analysis, the set was restricted to internal alkynes with cyclic groups on both sides of the alkyne bond. Terminal alkynes were excluded, as were alkynes which contained charged groups such as ammonium cations.

Furthermore, in the Fairlamb group's discussion of their results, they remark on the unusual regioselectivity displayed by the 2-pyridyl substituent in certain cases. Data from the PhD thesis of Nasiru Yahaya, a former member of the Fairlamb group, was also included in the combined dataset.[114] These additional investigations, which once again utilise the same methodology, focus on alkynes containing the 2-pyridyl group, expanding the chemical space surveyed by this study into this area.

The final dataset, as detailed in Figure 6 and Figure 7, consisted of 32 internal alkynes, bearing aromatic and heteroaromatic substituents. From the literature data, it was possible to extract the regiochemical product distribution from the reported reactions with norbornene. The reported literature regiochemical outcomes were used as the response variable in all models built with the dataset in this investigation.

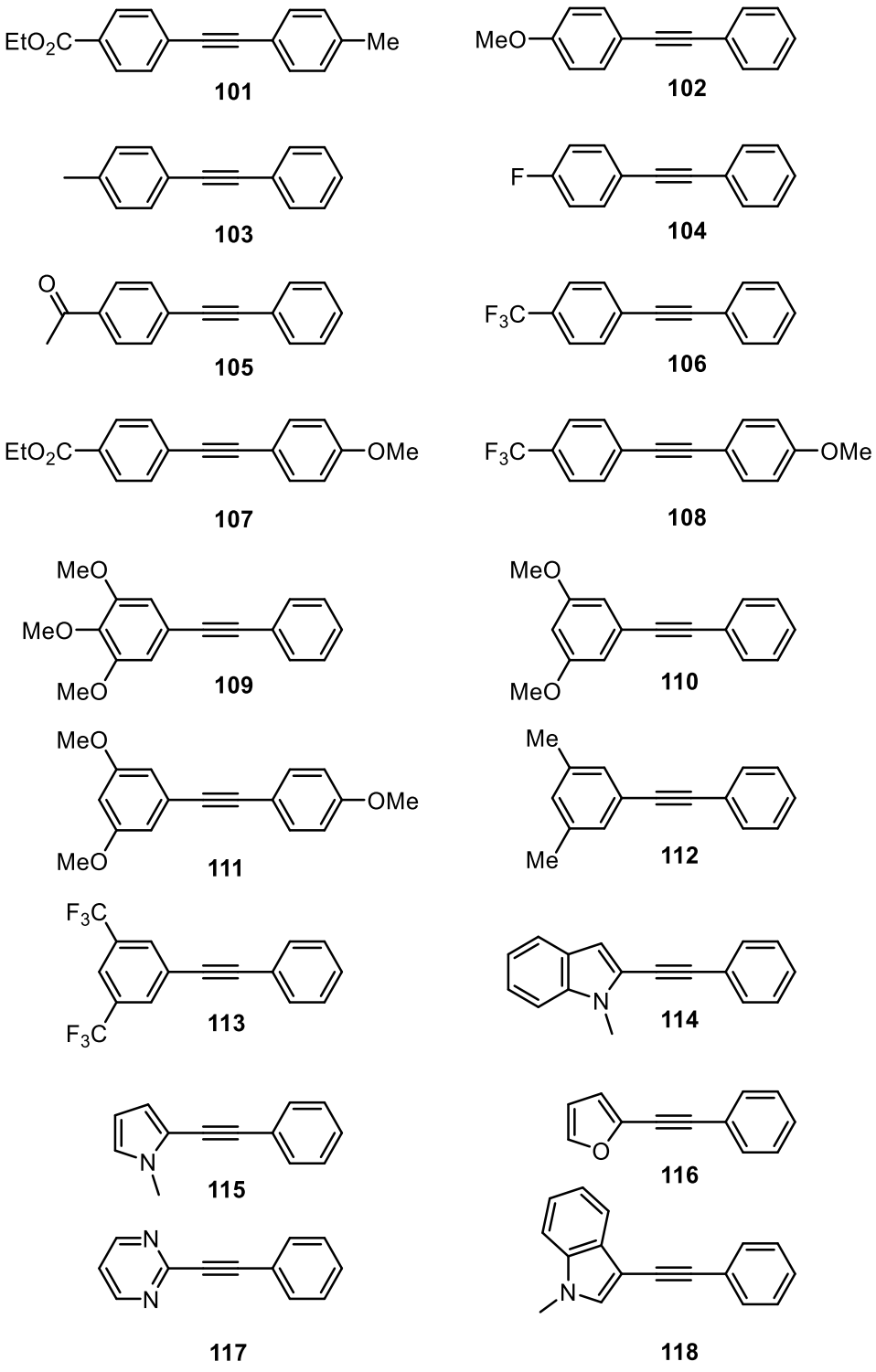

Figure 6 - The alkynes used in the full dataset.

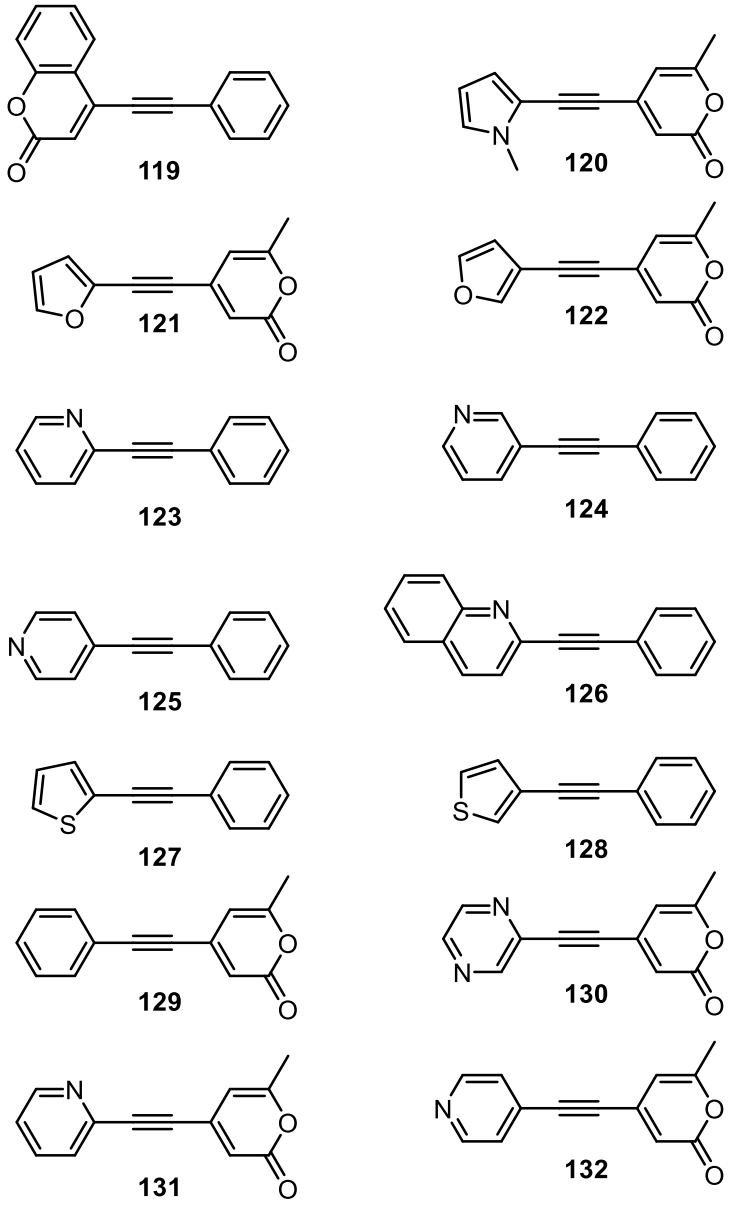

Figure 7 - The alkynes used in the full dataset (continued).

2.4. Parameterisation of alkyne substrates

Previous theoretical studies into this area have focused on the transition states of the relevant mechanistic steps, but the optimisation towards transitional stationary points is a non-trivial task, which is highly sensitive to geometry. Transition state following algorithms optimise towards first-order saddle points on the reaction potential energy surface, which may not necessarily be the lowest energy points along the desired reaction coordinate. As such, the input geometry supplied to the calculation has a high degree of influence over the final stationary

point identified. This necessitates the careful construction of input geometries for transition state optimisations, a process which is challenging to reliably automate. For a wider approach, a more efficient and robust method of computing parameters was desirable. The more attractive route was the parameterisation of the free alkyne ligands themselves. With the expectation that the effect of the groups on their adjacent acetylenic carbon would not change appreciably upon complexation (as found by NMR studies[115]), it was taken that the free alkyne is a good model for the electronic and steric effects of the substituents within the complex.

2.4.1. Point charges on carbon atoms

Following the success of the Helaja group in linking the difference in point charges to regioselectivity,[113] the first parameter to be calculated was the difference in partial charge between the two distal carbons on the alkyne. The geometries of all the alkynes in the dataset were optimised at the BP86/SV(P) level of theory using the Turbomole software suite, and a single-point energy calculation undertaken at the B3LYP/DGTZVP level using Gaussian 09. Following the single point energy calculation, NBO population analysis run was using NBO7. NBO population analysis is one of several methods of representing the continuous calculated wavefunction from a DFT calculation as a chemically intuitive picture of discrete electrons and bonding interactions.[116–118] For each alkyne, carbon atoms 1,2,3 and 4 were designated across the alkyne moiety. These numbers were related to the final product distribution, where the product with carbon atom 1 bound in the α position was assigned as the α product, and the alternative isomer with carbon atom 1 in the β position assigned as the β product.

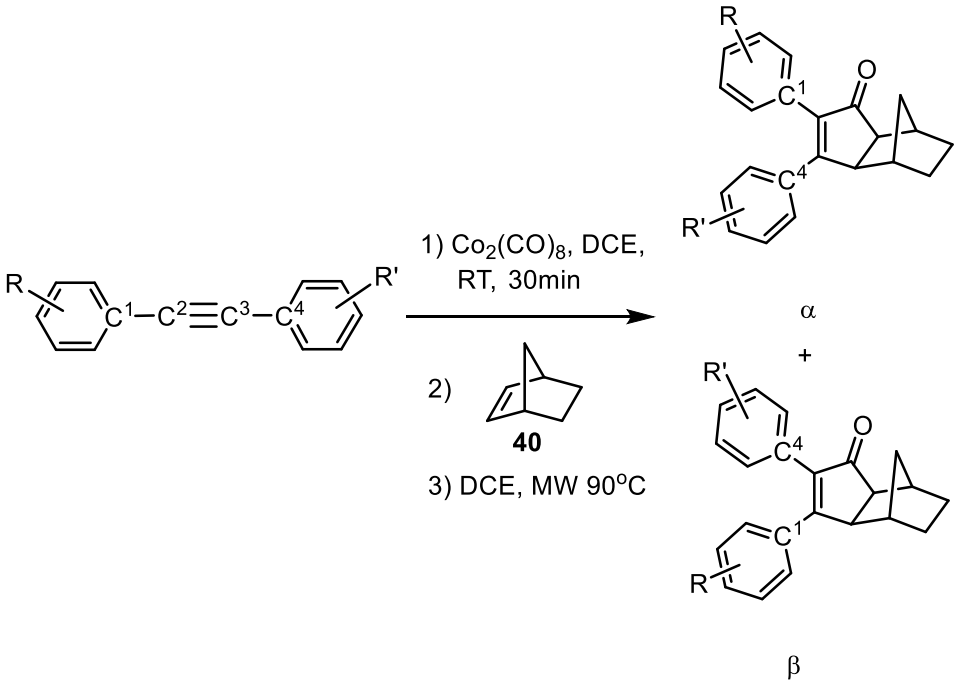

Scheme 43 - Sample reaction scheme for the coupling of an alkyne with norbornene, and assignment of the α and β products with regards to C¹

Regioselectivity was represented as the proportion of α product in the product mix, as shown in Equation 1:

$$alphaprop = \frac{\alpha}{\alpha + \beta}$$

Equation 1 - Method of expressing proportion of α product, where α = percentage conversion of α product, β = percentage conversion of β product.

The resulting partial charges from this method were plotted against the observed proportion of α product. Qualitatively, the general trend of electron-donating groups being selective for the α-position was observed. For instance, in the aromatic examples, the most negative value of Δ(C1-C4) was -0.034, which corresponded to the highest alpha product proportion (0.62). This example, compound **102**, contained a *para*-methoxy substituent, an electron-donating group. Similarly, electron withdrawing groups on the C1 ring were seen to lead to high positive values of Δ(C1-C4) such as **111**, which has two *meta*-substituted methoxy groups attached to the C1 ring. Overall, these results indicate that in the aromatic examples the Δ(C1-C4) parameter is a good method for representing the electron donating or withdrawing nature of the substituents.

As could be clearly seen, the correlation was closer when considering the examples in the original Helaja group dataset, while the data associated with heteroaromatic species did not show such an obvious correlation. This lack of correlation was not unsurprising. It is well known that the

electronic influences which govern regioselectivity are delicate, and can be easily overridden by other effects.

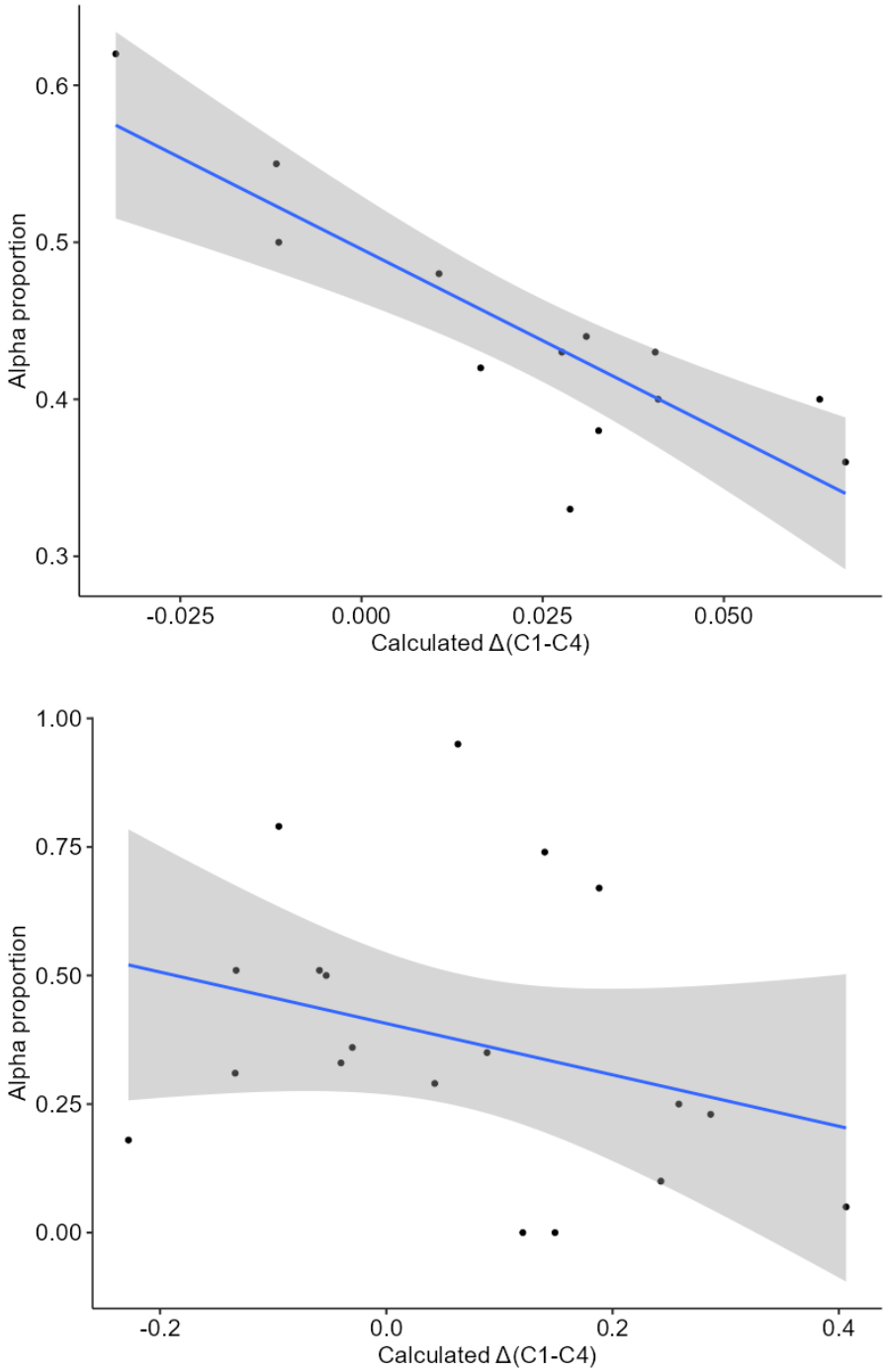

Figure 8 - Correlations between charge difference between substituent carbons and regioselectivity for the previously-examined aromatic dataset (top) and newly-introduced heteroaromatic data (bottom). Grey shading on fit line denotes 95% confidence interval.

In order to further understand the differences between the two datasets, the calculated NBO atomic charges were compared. The comparison of the distribution of charges for each position

across the dataset showed that while the C2 and C3 charges were generally comparable between the previously studied aromatic examples and the newly parameterised heteroaromatic subset. However, pronounced differences could be seen especially for the C1 position (the position located on the heterocyclic substituent for examples containing a heterocycle and a phenyl group). The range of values in the heteroaromatic subset for the C1 position is substantially wider. Similarly, the C4 position displays a wider range of values, raised in particular by the electron-deficient pyrone group.

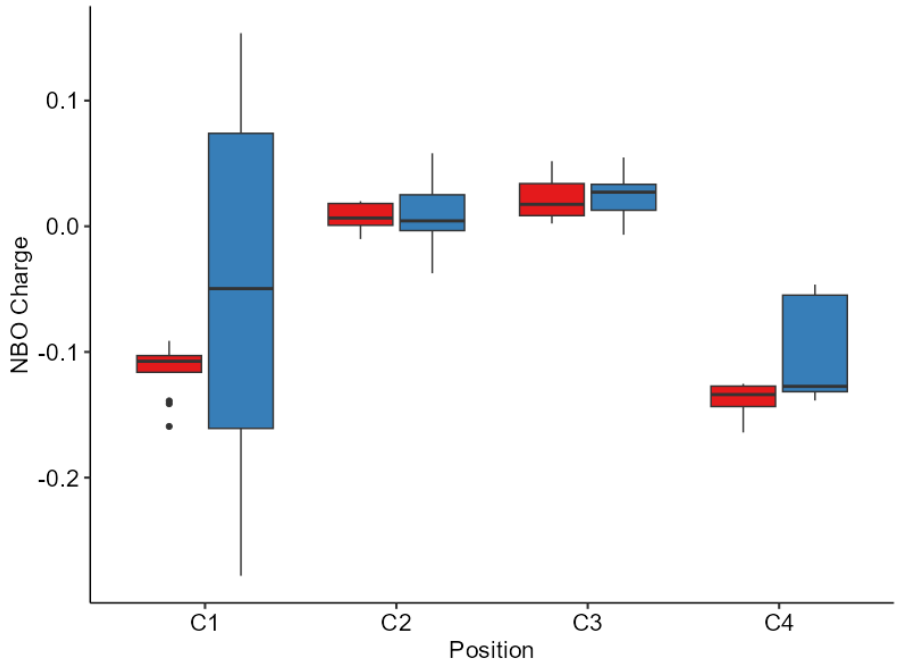

Figure 9 - Comparison of the distribution of calculated charges for non-heteroaromatic (red) examples and heteroaromatic (blue) examples for each position.

The broadening of the distribution of charges in the heteroalkyne subset demonstrates the comparatively wider area of chemical space which the newly introduced subset explores. These observations imply that while the direct correlation of this charge difference is able to describe the regioselectivity in the narrower region of chemical space occupied by non-heterocyclic dataset, this metric alone is inadequate to build a predictive model for the wider heterocyclic dataset. To provide more accurate and reliable predictive power, a model which accounts for other relevant metrics must be built.

2.4.2. Lewis structure perturbation analysis

While the individual charges on the carbon atoms are clearly able to model inductive effects into the alkyne bond, the resonance effects of orbital contributions from the ring may not be so well

described by this metric. To attempt to model this effect, another metric calculated by the NBO analysis was investigated. Second order perturbation theory examines the deviation from the ideal Lewis structure of the molecule displayed by the natural bond orbitals calculated. In essence, this is a measure of the stabilisation gained from the delocalisation of electron density from one orbital to another. This stabilisation in turn is a description of how much delocalisation is occurring, and can be used as a method of representing charge transfer between the natural bond orbitals.

By modelling the delocalisation from the pi system of the aromatic rings into the alkyne triple bond, a metric of pi-delocalisation into the bond could be determined. This was used as a proxy measurement for the resonance contribution of the rings into the alkyne bond polarisation (Figure 10).

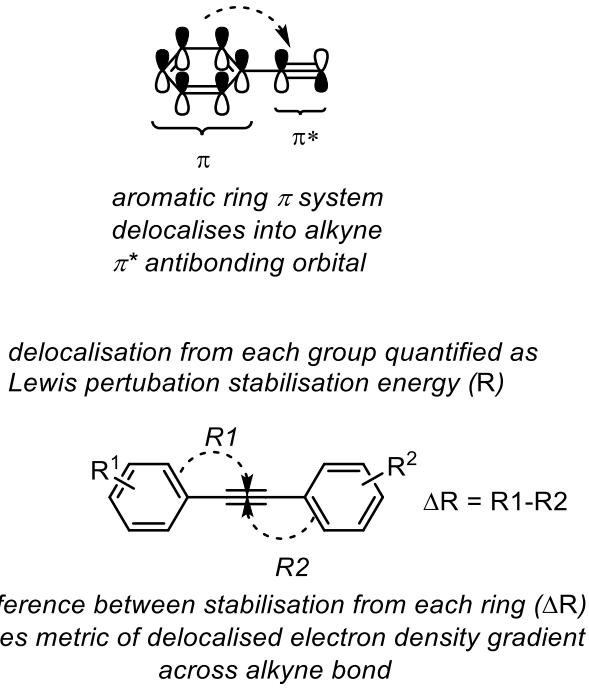

Figure 10 - The orbital delocalisation used to quantify conjugation effects from aromatic rings adjacent to the alkyne in Lewis structure perturbation analysis.

The final parameter for modelling was expressed as the difference between the contributions from the two ring systems. In this parameter, a positive value denotes that the ring centred upon carbon 1 is more strongly donating, with a negative value denoting the opposite. A value of or close to zero implies that the alkyne bond experiences no significant polarisation as a result of resonance contributions from the substituent pi systems.

2.4.3. Steric description of alkyne substituents

Although the substituents on the alkynes surveyed were initially chosen to be as sterically similar to one another as possible, there will intrinsically always be a certain level of steric imbalance between the two groups. Given the well-observed sensitivity of the system to steric effects, it was desirable to include a parameter in the model which could represent these contributions.

Producing an accurate steric description of the groups attached to the alkyne was required a considered approach. At first, a standard cone-angle metric was trialled. However, the shape of the alkyne substituents often meant that the groups attached to the ring, especially in the para position, are essentially masked by the ortho-carbons in the ring. This effect leads to groups with para-substituents having the same cone angle from the alkyne perspective as the unsubstituted ring. This method of steric parameterisation may lead to inaccuracies, and as such required refinement.

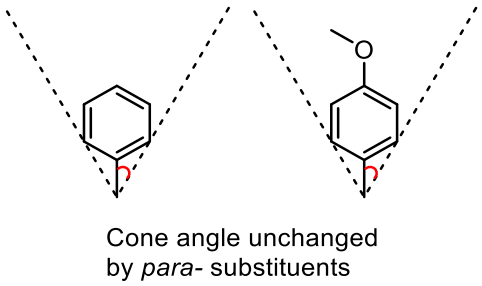

Figure 11 - Schematic demonstrating the inability of a cone-angle metric to differentiate between a phenyl and para-*methoxy phenyl substituent.*

To adjust the cone angle metric for better description of remote alkyne substituents, the parameter was redesigned as the volume of the smallest cone which could be drawn to encompass the entire group. This approach retained the cone angle concept, while additionally accounting for substituents that would otherwise be overshadowed.

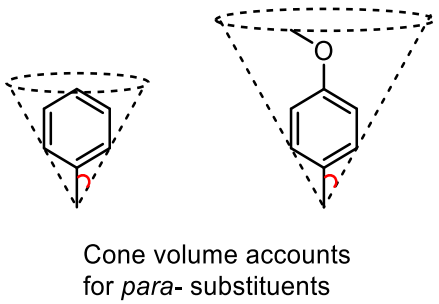

Figure 12 - Schematic demonstrating the different cone volumes of a phenyl and para-*methoxy phenyl substituent.*

The modelling of proximal vs remote steric effects can be a delicate balance in describing the relevant steric environment to the mechanism in question. Wu and Doyle[119] have successfully

explored this question in the context of phosphine ligands, demonstrating how different methods of parameterising the steric character of these ligands can have a strong influence on model accuracy. The authors note here that by taking into account remote steric effects, they are better able to model the activity of a range of nickel-based catalyst systems.

While the alkynes considered here are generally isosteric in the immediate environment of the alkyne bond, the substituents on the rings can lead to potential differences in remote steric character. Given the sensitivity of the insertion step of the PKR to these steric differences, it is important that even remote steric character is considered in the analysis.

2.5. Statistical model building

Once the parameters had been generated for the alkynes in the dataset, a statistical model could be constructed linking these parameters to the distribution of regioisomers in the products. A multicomponent linear regression model was used, as this was capable of clearly presenting the combination of parameters in an easily interpreted format. Similarly, with the relatively small number of observations in the dataset, the use of more complex statistical relationships such as polynomial fits could lead to overfitting of the data. Similarly the number of fitting parameters was not increased past the three described above. With the dataset at hand, increasing the number of parameters might similarly lead to overfitting. The full dataset used for model building can be found in Appendix 2.

2.6. Insights from statistical models

The building of a multicomponent linear model correlating the product α proportion to the computed parameters gave the following formula:

$$alphaprop = 0.0022DiffSec - 0.0297deltaC1C4 + 0.0440deltaR + 0.379$$

Equation 2 – Formula with coefficients of parameters for a linear model of the full dataset.

In the above formula, the parameter *DiffSec* refers to the calculated steric difference between the substituents using the smallest encompassing cone model. The second parameter, *DeltaC1C4*, describes the difference in NBO-calculated point charge between carbon atoms 1 and 4 across the alkyne bond. The third parameter, *deltaR*, describes the stabilisation energy arising from donations from ring π systems into the antibonding orbital of the alkyne. In addition to the formula, tables of metrics could be generated for the model, providing

information on the model errors and significance scores assigned to the fitted values (Table 1 and Table 2). These tables were used to ascertain the quality of the model fit.

Table 1 - Estimates and statistical metrics for parameters in a linear model of the full dataset.

Coefficient	Value	Error	T value[b]	Pr(|t|)[c]
DiffSec	0.00221	0.00108	2.042	0.0506
deltaC1C4	-0.0297	0.329	-0.09	0.9287
deltaR	0.044	0.0162	2.719	0.0111
Intercept	0.389	0.0412	9.189	5.89×10^{-10}

Table 2 - Statistical metrics for the multicomponent linear model of the full dataset.

Model Parameter	Value
Residual standard error	0.187
Multiple R-squared	0.250
Adjusted R-squared	0.250
p-value	0.0113

The adjusted R-squared of the overall model was 0.250. Similarly, the overall model p value of 0.011, despite being below the commonly used significance threshold of 0.05, was very high, essentially making it difficult to reject the null hypothesis (i.e. no meaningful connection between the parameters and outcome). Similarly, the p values for two of the parameters (diffsec and deltaC1C4) are very high, essentially indicating that the coefficients are functionally zero, and that these parameters have no bearing on regioselectivity. Finally, the intercept of the model was found to be 0.398. Given that the intercept is the value which the model should return if the values of all parameters are zero (in this case meaning that the alkyne is perfectly balanced in every relevant aspect), this intercept should be as close to 0.5 as possible. A value far away from

[b] T value: Value of coefficient divided by standard error.
[c] Significance p-value: Percentage chance of being unable to reject the null hypothesis (in which the coefficient in question is equal to zero).

0.5 implies a skew in the model. Overall, this model is not able to adequately describe the dataset.

Given the expected connection of the chosen parameters to regiochemistry, this lack of fit was unexpected, so the density distribution plot of the residuals was examined (Figure 13). In a relatively homoscedastic case, where all data points in the model display similar variance, this density would be expected to be a single normal distribution about the origin. However, in this case there are distinct peaks formed separately from the main normal distribution, implying that there are datapoints where the variance from the model is not consistent with the majority of the dataset.

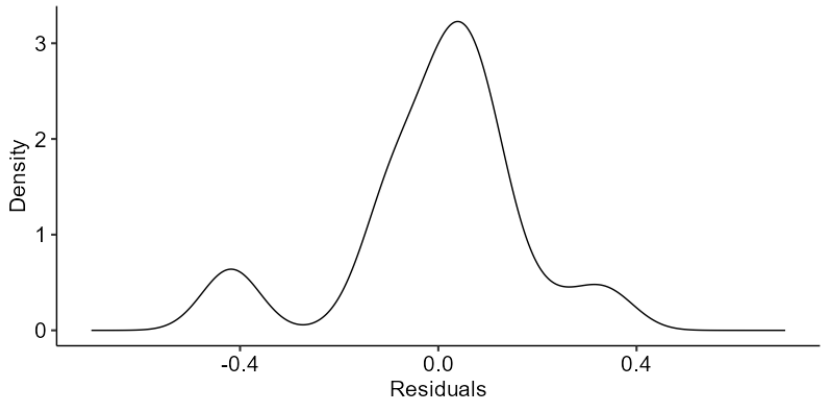

Figure 13 - Density profile of residuals for the fitted model of the full dataset.

To interrogate these cases further, the normal Q-Q plot can be generated (Figure 14). This technique compares the position of each residual to the expected theoretical normal distribution. Points that lie far from the diagonal line have non-standard variance. As can be seen from this plot, the cause of the non-normally distributed negative residuals is three data points, alkynes displaying the 2-pyridyl or 2-thiophenyl group, which Fairlamb and co-workers remarked to display unpredictable selectivity when first investigated.

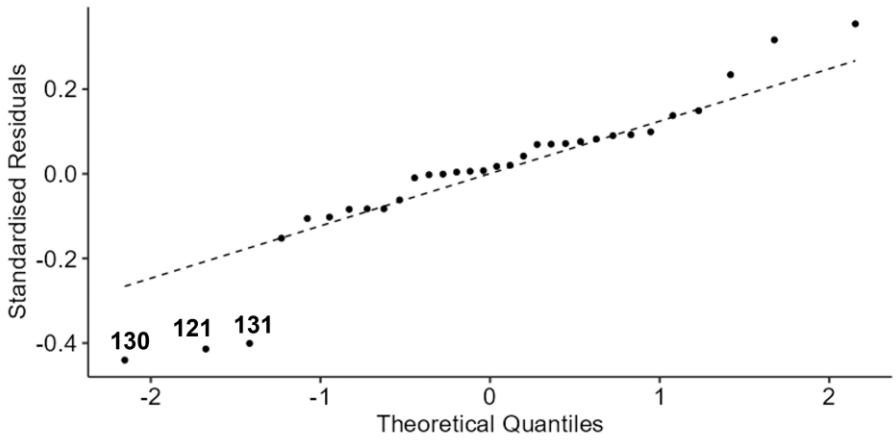

Figure 14 - Normal Q-Q plot of residuals for the fitted model of the full dataset.

When comparing the predicted and measured α-substituted proportions, it can be seen that the total selectivity for the β position displayed by **131** is strongly deviating from the model prediction. Residuals for alkynes bearing 3- and 4- pyridyl groups do not display similar anomalous behaviour, implying that this specific selectivity may derive from the presence of a Lewis basic group in the 2-position of the ring.

Eight entries containing a group with a single non-protonated heteroatom in the 2-position were identified (Figure 15). Exclusion of these cases from the model building provides a better fit, raising the adjusted R-squared of the new truncated model to 0.91. This change signifies that the species removed were severely disrupting model fitting. Thus, we can infer that the regioselectivity of these examples arises from factors not modelled in the current approach, and not accounted for in the working understanding of electronic regioselectivity.

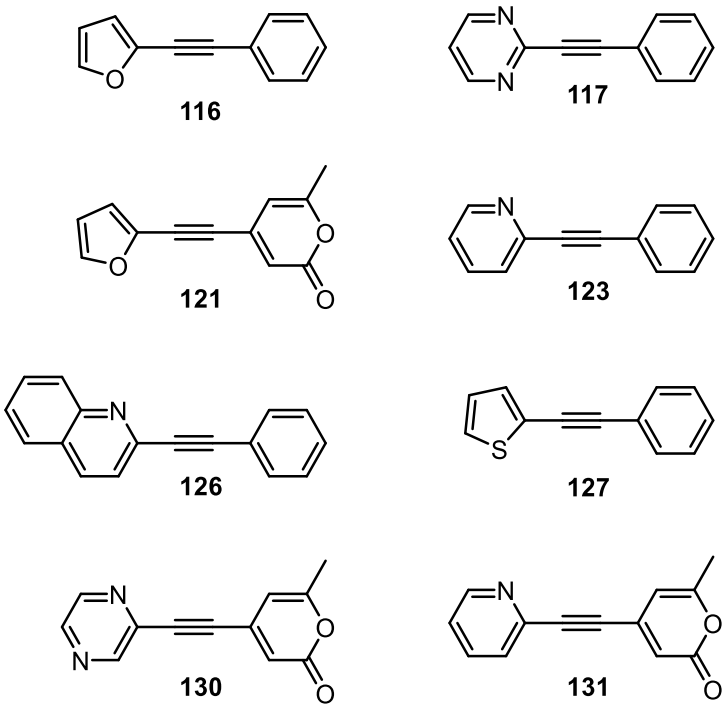

Figure 15 - The 2-donor containing alkynes excluded for the building of the truncated model.

$$alphaprop = 0.00321DiffSec + 0.992deltaC1C4 + 0.0751deltaR + 0.477$$

Equation 2 - Coefficients for the parameters from modelling the truncated dataset.

Table 3 - Estimates and statistical metrics for parameters in a linear model of the truncated dataset.

Coefficient	Value	Error	T value	Pr(|t|)
DiffSec	0.000311	0.000335	0.926	0.366
deltaC1C4	0.900	0.161	5.58	1.85×10^{-5}
deltaR	0.0746	0.00522	5.58	5.92×10^{-12}
Intercept	0.481	0.0130	37.1	$< 2 \times 10^{-16}$

Table 4 - Statistical metrics for the multicomponent linear model of the truncated dataset

Model Parameter	Value
Residual standard error	0.0498
Multiple R-squared	0.918
Adjusted R-squared	0.906
p-value	4.78×10^{-11}

Alongside the drastic increase in the value of the R-squared parameter, the p-value of the overall model is seen to decrease to 4.78×10^{-11}, a value low enough to confidently discard the null hypothesis. The significance values of the individual parameters are now able to give some insight into the impact of these parameters on the model. The two electronic parameters used in the model are both assigned a very high degree of significance, with low p-values. The steric parameter, however, is assigned a very low degree of significance, with a high p-value. Additionally, the coefficient estimate is very low, and within error of zero. The implication of these statistical metrics is that in this case the steric parameter is not highly significant to the model, and can be viewed as a poor metric for prediction. This finding is not surprising, given that the rationale for the selection of the cases examined in the original literature from which these data were gathered was for relatively sterically balanced examples of unsymmetrical internal alkynes, so as to isolate the electronic element of selectivity. This rationale can be validated here, where the model would suggest that this is indeed the case, and that the steric imbalances displayed by the alkynes in this dataset play a minor role in the regioselectivity

compared to the electronic effects. In order to train a larger model which could reasonably make predictions based on steric characteristics, a more sterically diverse dataset would be required.

This drastic alteration in model quality highlights the sensitivity of this class of approach to unexpected deviations from expected mechanistic behaviour. A small number of outliers can seriously compromise the predictive ability of a model, especially when the sample size is not large. However, the disruptive influence of these cases can also be a source of information, providing a qualitative statistical connection between similar species which are poorly described by the model. Essentially, this approach allows for the precise identification of areas of chemical space for which the current modelling parameters are not a good description of the behaviour (i.e. there is mechanistic behaviour present that is currently unidentified).

2.7. Comparison of linear model fit with machine-learning methods.

To compare the multicomponent linear regression model to machine-learning methods, a machine learning approach was also employed to relate the same calculated parameters to regioselectivity. As mentioned previously, smaller datasets are not necessarily suitable for machine learning approaches, as these methods can be susceptible to overfitting, or biased by outliers. In an attempt to control for these effects, a Random Forest algorithm was used. Random Forest algorithms are capable of producing predictive models to analyse either classification or regression tasks. The algorithm produces multiple decision trees using an out-of-bag (OOB) approach. This approach assigns multiple randomly selected subsets of the training dataset, sampling with replacement (i.e. the same datapoint can be selected for use in multiple decision trees). The algorithm then builds the decision trees, using each tree to build its own predictive model. The finished trees are then averaged to build a final overall predictive model. This approach seeks to minimise overfitting by using different subsets of the training data in the different decision trees. Trees which are overfitted are then averaged out in the combination stage, allowing for the final model to be less prone to this issue. Similarly, outlier contributions are lessened as strongly outlying values will likely be spread across multiple decision trees, and any undue biasing they bring to the model will be controlled for by the unbiased trees.

For assessment of the models' relative abilities to provide accurate predictions of regioselectivity, leave-one-out cross-validation (LOOCV) was applied. This validation method involves building as many models as there are datapoints. For each model, one datapoint is excluded as a test case and the remaining data is used as the training set. The built models are then tested using the excluded datapoint, and the prediction error recorded. The root of the

mean of the squares of these errors is calculated, giving a final root mean squared error (RMSE) value. Such an approach is advantageous when working with smaller datasets, as each iteration of the model is built with the maximum amount of data possible while still retaining an unseen case for validation. Furthermore, each case is individually validated, removing the random element of a standard test/train partition approach. This approach is also more favourable than using the Residual Standard Error metrics as seen in the model metrics. Residual Standard Error is derived from the errors in the residuals of data in the training set, and not from unseen validation data.

Cross validation of models built using both the full and truncated datasets using each method yielded the following RMSE metrics:

Table 5 - Root Mean Squared errors derived from leave-one-out cross validation of the range of models surveyed.

Dataset	Method	Root Mean Squared Error
Full	Random Forest	0.218
Full	Multicomponent Linear Model	0.210
Truncated	Random Forest	0.110
Truncated	Multicomponent Linear Model	0.055

As would be expected from the fit parameters from the model output, modelling with the full dataset produces a high RMSE. Both methods of model construction give a similar level of error, indicating that in this case both approaches are similarly affected by the outliers, despite the aforementioned robustness to outliers inherent to the Random Forest approach.

Truncation of the dataset *via* the exclusion of the alkynes bearing 2-donor substituents leads to a decrease in the RMSEs. In this case, the multicomponent linear model performs significantly better than the Random Forest, demonstrating an over 50% reduction in RMSE. It is likely that this is due to the dataset being less of a valid case for the application of ML methods at this size. As mentioned previously, the OOB approach to decision tree building in the Random Forest algorithm leads to smaller subsets of the data being used for each tree, which can be problematic when applying this method to a smaller dataset.

The best model from those surveyed, the multicomponent linear model of the truncated dataset, displayed a LOOCV RMSE of 0.055, essentially meaning that the error implied on any new predictions of α product percentage made using this model would be 5.5%. This relatively low error is consistent across the majority of the chemical space surveyed, with the highly notable exception of the 2-donor containing examples, which essentially cannot be predicted accurately using this approach. However, with this otherwise descriptive model built using the truncated dataset, it can now be applied to the 2-donor containing examples to assess the differences between the model's predicted regioselectivity and the experimentally observed outcome.

Table 6 - Measured and predicted α product proportions of the alkynes bearing 2-donor groups

Entry	Measured Alphaprop	Predicted Alphaprop	Prediction Error
116	0.230	0.665	0.435
117	0.050	0.317	0.267
121	0.180	0.658	0.478
123	0.100	0.500	0.400
126	0.250	0.228	-0.022
127	0.310	0.386	0.076
130	0.000	0.743	0.743
131	0.000	0.725	0.725

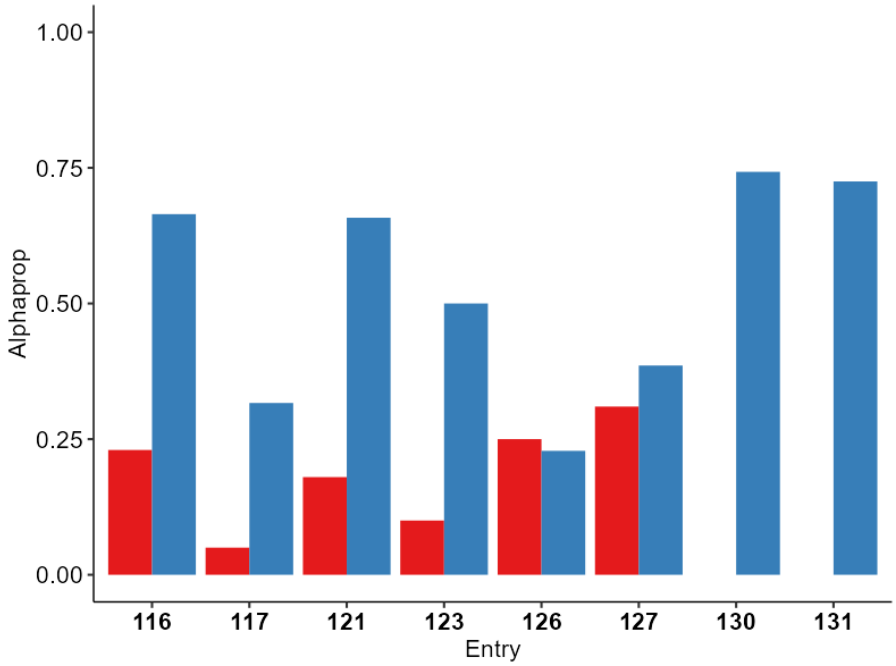

Figure 16 - Predicted (blue) vs measured (red) α product proportions of the alkynes bearing 2-donor groups.

As can be seen in Table 6 and Figure 16, as well as in agreement with the abnormally negative residuals observed during the initial exploratory model building process, this model tends to vastly overestimate the α selectivity of groups containing a donor atom in the 2-position. Essentially, many of these groups display more selectivity for the β position than the truncated linear model would assign them. Two examples from this subset (**126** and **127**) are still predicted relatively well by this model. From their structures, it can be seen that alkyne **126** represents the only bicyclic substituent in the 2-donor subset, and **127** the only S-heterocycle within the subset.

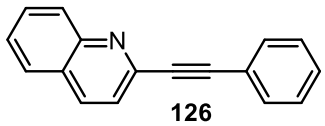

126

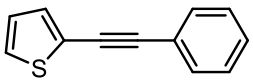

127

*Figure 17 - The structures of dataset entries **26** and **27.***

Following these observations, a theory can be put forward as to why groups with a heteroatom in the 2-position display a strong and unexpected selectivity towards the β position of the

cyclopentenone ring. As previously established, selectivity for the β position implies preferential C-C bond formation at the adjacent acetylenic carbon in the first ring-forming transition state. Therefore, the inclusion of a heteroatom at the 2-position of the ring must have an additional means of stabilising the insertion transition state at this site. The use of co-ordinating groups on alkenes has been explored by Krafft and co-workers in several studies.[6,7,9] It was found that the presence of an S or N-alkyl group on the alkene fragment in an intermolecular PKR imparted strong regioselectivity, and increased the activity of unstrained alkenes. This behaviour was attributed to the heteroatomic moiety acting as a chelating ligand coordinating to the cobalt, and applying a directing effect to the cyclisation step. Later, Itami and co-workers found that a 2-pyridylsilyl group on the alkene was capable of increasing conversion and regioselectivity in the ruthenium-catalysed PKR variant.[120,121]

These studies clearly show the regiocontrol which directing groups can exert on the intermolecular PKR, but all are focused on directing groups situated on the alkene fragment. There have been no reported cases of the alkyne fragment bearing directing groups which can influence the regiochemical outcome of the PKR. Given the deflected geometry generally adopted by the alkyne when complexed to the dicobalt hexacarbonyl framework, it is likely that the heteroatom in a pyridyl or furanyl group would be geometrically unable to coordinate to either cobalt centre. Instead, it is more likely that an alkene-alkyne interaction is present which plays a stabilising role in the key regiochemistry-determining transition state.

Based on the geometry of the transition step, a hydrogen-heteroatom interaction from the heterocycle to the alkene hydrogen situated at the carbon-carbon bond formation site is more feasible. The five-membered ring formed may serve to further stabilise the transition state for the insertion adjacent to the pyridyl group. Stabilisation of the alkene insertion adjacent to the heteroaromatic group would bias the product distribution to favour the regioisomer featuring the heteoaromatic group in the β position (see Scheme 44). The lack of anomalous selectivity observed in the cases of bicyclic and S-heterocyclic examples above may arise from a steric interference (in the case of **126**) or poor coordination from the sulfur atom (in the case of **127**).

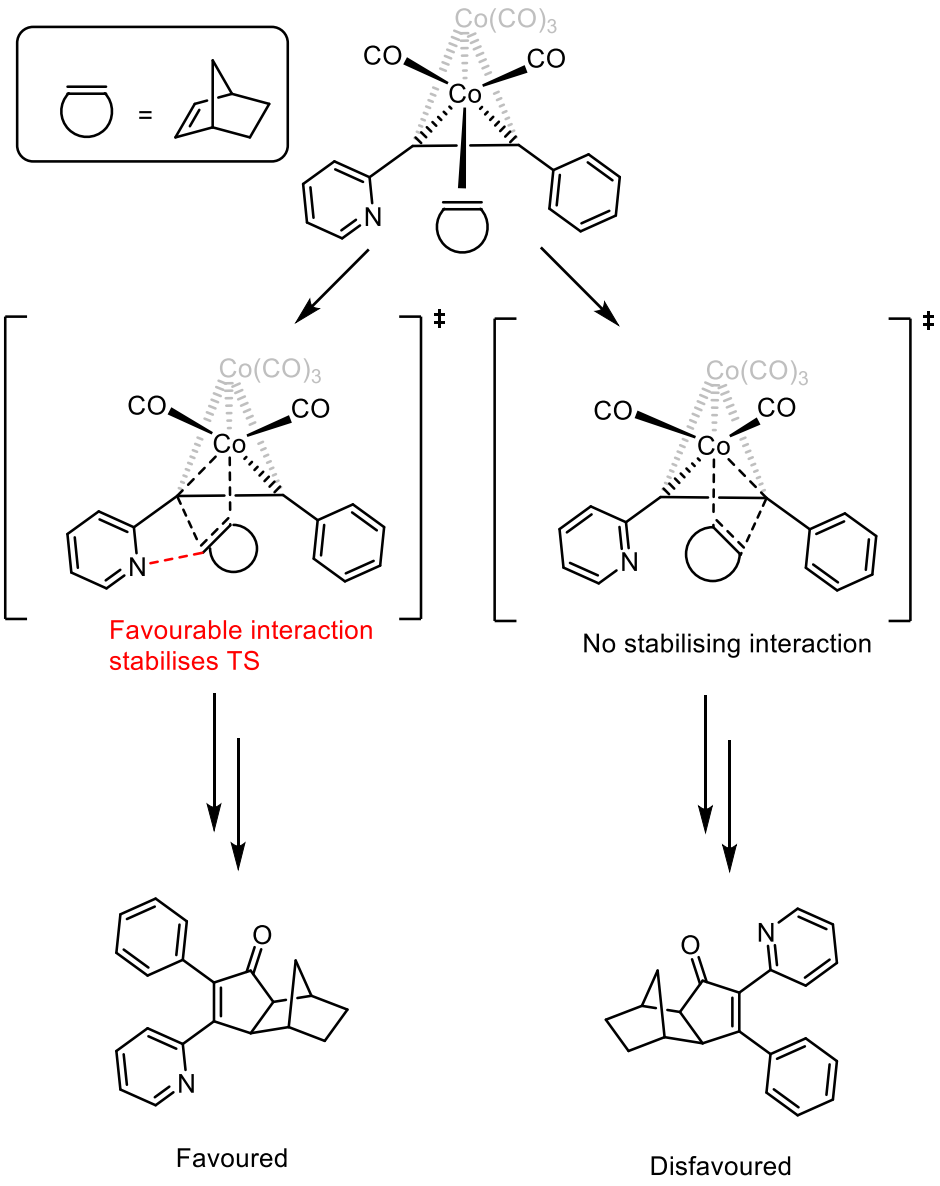

Scheme 44 - Proposed origin of regiocontrol exerted by 2-donor alkyne substituents.

2.8. Summary and Conclusions

A parametric approach has been used to build a multicomponent linear model to further investigate electronic contributions to regioselectivity of internal alkynes with norbornene in the cobalt-mediated stoichiometric PKR. The multicomponent linear model was able to describe the majority of the data well, giving good predictive ability. A defined subset of the data was not well described by the model, causing non-standard variances and a severe drop in model fit. This subset of the data, which contained 2-heterocyclic groups, was then proposed to display non-standard regioselectivity, and alternate regiochemical influences from these groups were

proposed. This investigation highlights the ability of complex parameterised linear model building and *post-hoc* exploratory data analysis of the fitted data to qualitatively determine non-standard behaviour, allowing for identification of regions of chemical space which may exhibit behaviour of interest. Importantly, these findings also show that the same approach can be used for aliphatically and heteraromatically-substituted internal alkynes in the absence of further complicating factors, implying that for the majority of the dataset, this is a suitable and robust model.

The presence of a heteroatom in the 2-position of a substituent evidently causes unexpected regioselectivity, which warrants further study to identify the exact nature of the coordination effect which gives rise to this behaviour. This will be explored in more detail in Chapter 3. Full characterisation of this effect may allow for the design of alkyne substrates which can increase activity and selectivity in the intermolecular PKR.

Chapter 3: Pauson-Khand reactions with internal alkynes

3.1. Background

3.1.1. Electronic contributions to regioselectivity in the PKR

The regioselectivity of internal alkynes in the Pauson-Khand reaction (PKR) is influenced by steric and electronic parameters of the alkyne. Sterically, the bulkier of the groups on the alkyne will preferentially occupy the α position of the cyclopentenone ring formed. The reasoning behind this observation is linked to the origin of regioselectivity. As noted previously, the regiochemistry-defining step in the Magnus mechanism is the formation of the 5-membered cobaltacycle. Whichever substituent on the alkyne which the alkene inserts adjacent to will be found in the β position of the final product. The steric repulsion interactions around larger substituents will deter the alkyne from adjacent insertion, leading to the more sterically hindering group being in the α position relative to the carbonyl.

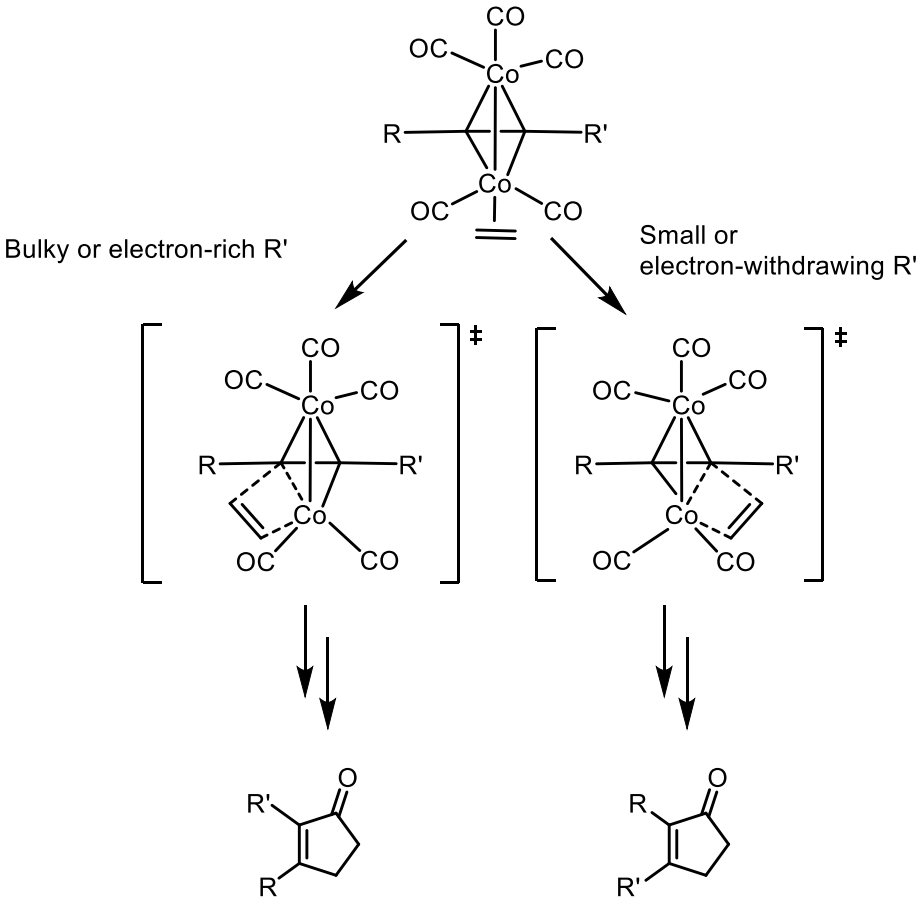

While influence of steric parameters is well understood, the electronic parameters are not as clearly defined. The commonly observed trend is that more electron-withdrawing substituents are generally selective for the β position of the cyclopentenone. This selectivity arises from the polarisation across the alkyne bond, directed by the electronic character of the substituents. This selectivity is more challenging to predict, and further study is warranted.

3.1.2. Promotion of the PKR with amine N-oxides

The use of tertiary amine N-oxides is well established in the PKR. Since 1990, when the first use of NMO as a promoter was reported, it has gained a status as an established promoter of the PKR[122–124]. While additives of this type are often employed alongside thermal activation methods, this method of promotion when employed alone allows for the reaction to run at room temperature, albeit generally at reduced yield. This practice is particularly attractive in some systems as by obviating the need for thermal activation entirely, the coupling of thermally-sensitive substrates can be performed without side-reactions of those substrates taking place. A key example of this is in stereoselective synthesis, where elevated temperatures could lead to equilibration of substrates or products occurring over time, eroding enantioselectivity in the reaction.

Amine N-oxides are capable of chemically promoting CO loss by the at-site oxidation of a carbonyl ligand into carbon dioxide. This method of CO abstraction is differentiated from most by the irreversible nature of the transformation. In most CO-loss methods, the abstracted CO can remain free in solution, and act as a competitive ligand during the alkene coordination step, resulting in an equilibrium of early states. The oxidation to CO_2, however, leads to the CO being converted into a non-competitive species in the reaction, favouring the onward reaction.

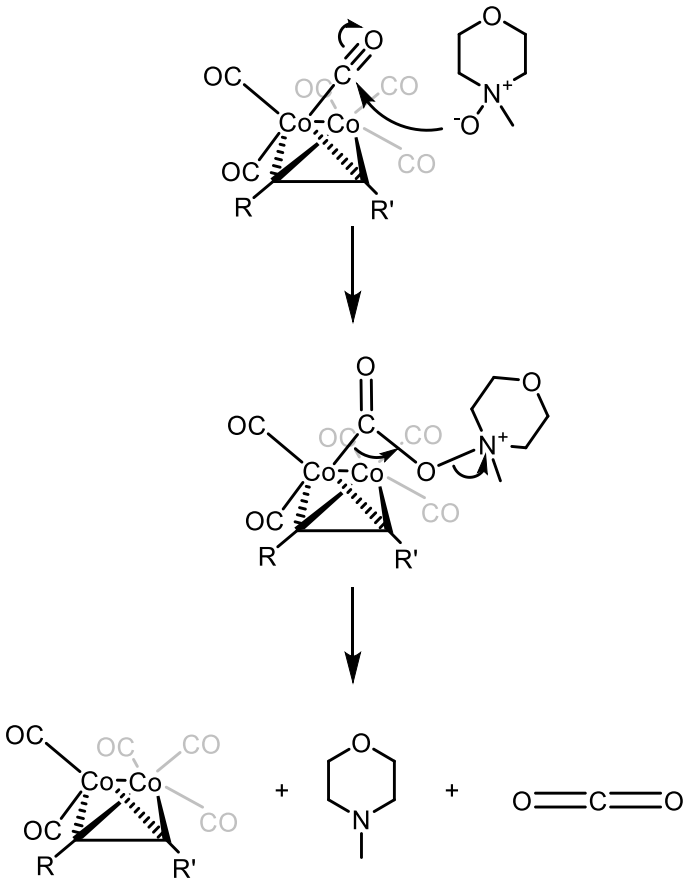

Scheme 45 - The oxidation of a CO ligand to CO_2 by NMO to form a pentacarbonyl cobalt alkyne complex.

3.1.3. *In-situ* FTIR as an analytical technique for the PKR

In-*situ* FTIR spectroscopy is a technique well suited to the PKR, with the carbonyl groups on the cobalt centre acting as reporting groups. Unfortunately, there are few examples of its employment in this field in the literature. Previously, Verdaguer and co-workers have used this method to study the kinetics of cobalt-catalysed intermolecular systems.[125] The authors noted that despite the great interest in the cobalt-catalysed intermolecular PKR, there had been at the time surprisingly little investigation into the kinetics of the system. *In-situ* FTIR is showcased as a versatile method for recording events in the reaction and collecting both kinetic and characterisation data. Dicobalt octacarbonyl catalysed coupling of trimethylsilylacetylene and norbornadiene was investigated, and in-situ IR used to track product formation and the formation of mechanistically relevant intermediates, such as η^2(NBD) dicobalt species **134.**

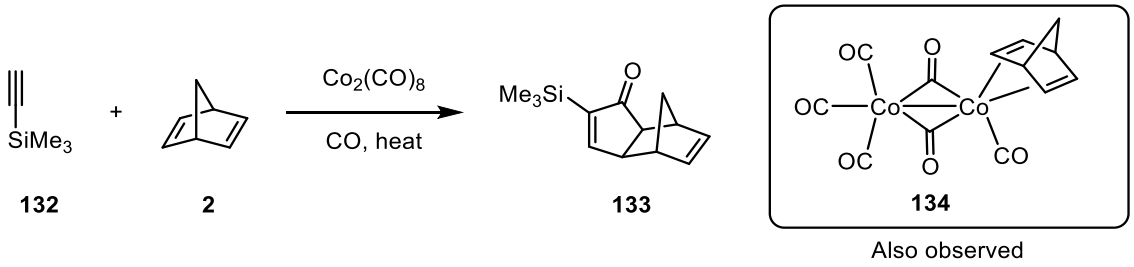

Scheme 46 - The catalytic PKR system studied by Verdaguer and co-workers. Inset: A cobalt carbonyl norbornenyl species identified by in-situ IR.

The same group make use of this technique again in the study of cobalt-catalysed intermolecular PKRs utilising the bidentate PuPHOS ligand (**90**) discussed in section 1.6.2.[126] The metal carbonyl region of the FTIR spectrum gave mechanistic insight into the status of the cobalt-alkyne-phosphine carbonyl complexes during the reaction, allowing for the identification of two ligand binding modes (bridging and pendant) of the bidentate ligand. This insight was in turn related to a decrease in product stereoselectivity. The use of *in-situ* monitoring methods in the course of this experiment allowed for quick identification of mechanistic behaviour that would have been difficult to glean otherwise.

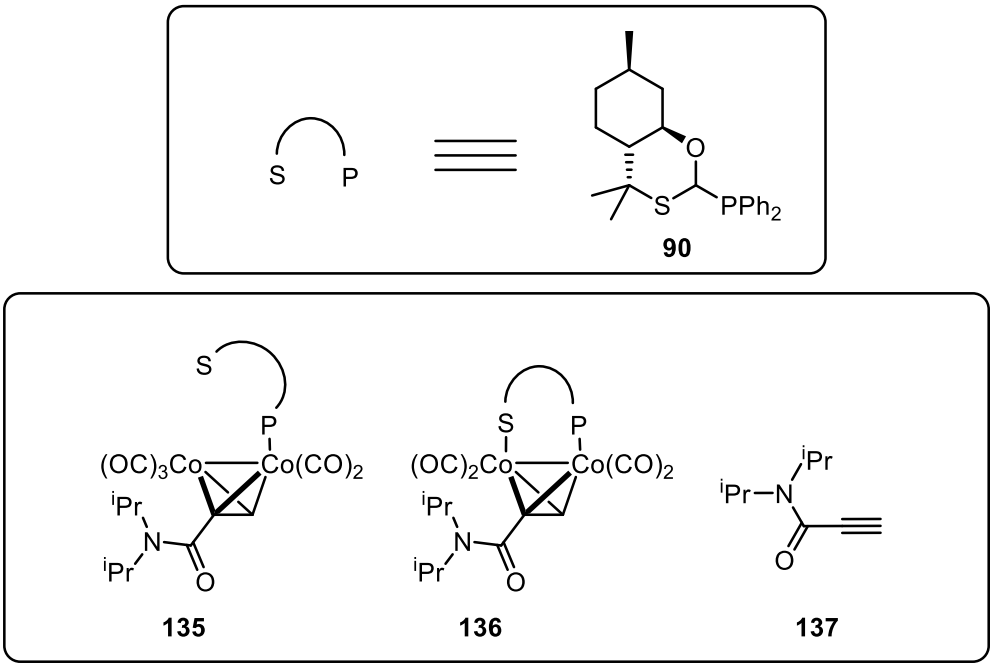

Scheme 47 - The identified binding modes of PuPhos by Verdaguer and co-workers, identified by in-situ *IR.*

More recently, Geary and co-workers made use of this method to study the effect of nitrous oxide as a promoter for the reaction.[127] Nitrous oxide promoted the coupling of phenylacetylene and norbornene in good yields (86% at 40°C), surpassing the performance of six equivalents of

NMO, a commonly used promotion regime (75% with this system). Conveniently, N_2O is reduced to N_2 gas once it has facilitated CO loss, leaving no by-products in the reaction mixture.

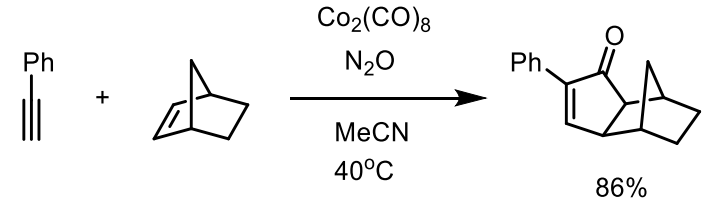

Scheme 48 - The system studied by Geary and co-workers, demonstrating the use of in-situ methods to observe oxidation-promoted PKRs.

In their study, *in-situ* FTIR is able to detect the evolution of CO_2 gas in the reaction mixture, confirming the activity of N_2O as a CO-loss promoter analogous to NMO. In addition to demonstrating an intriguing new method for the byproduct-free promotion of CO-loss in PKRs, this study once again demonstrates the unique insights which can be gathered using this technique.

3.1.4. Conclusions

An in-depth understanding of the factors determining the regiochemical outcome of the intermolecular PKR is critical to improving the applicability of the technique to a wider range of synthetic opportunities. The largest barrier to this understanding at the moment is the incomplete understanding of the electronic effects underlying the alkene insertion step. Gaining deeper insights into this stage of the mechanism will allow for more accurate prediction of product distribution in these reactions.

In-situ methods allow for the observation of sensitive or short-lived intermediates which may be easily observable or isolable outside of the reaction medium, and are well-suited for gaining insight into events occurring during the PKR. It is clear that this is an underutilised technique, which has been able to produce unique insights when it has been applied in the literature. It is hoped, therefore, that application of this technique to this problem will bring forth new observations which can provide a new perspective on this system.

3.1.5. Aims and objectives

The aim of the work described in this chapter was to further explore the unusual regioselectivity of alkynes containing 2-pyridyl groups and other heteroaromatic groups featuring heteroatoms

in the 2-position which was made apparent in Chapter 2. Additionally, this work sought to apply *in-situ* IR reaction monitoring methodology to the PKR in new applications. *In-situ* monitoring of this type is highly suited to the PKR, and while it has been utilised in some studies, this work seeks to demonstrate its applicability to mechanistic investigations of the PKR. Additionally, this work aims to take advantage of the modern availability of computational power to extend the full potential energy surface knowledge of the PKR, modelling the Magnus mechanism with bulky and functionalised substituents to present a more realistic description of intermediates in the reaction.

3.2. Development of a model PKR system

Based on insights from Chapter 2, regarding the unusual regioselectivity of alkynes containing 2-heterocycles, alkyne **131** was chosen as a target of study. A reaction replicating conditions from the dataset in Chapter 2 was carried out with norbornene under microwave conditions, leading to only one cyclopentenone isomer being observed. The cyclopentenone product was isolated and confirmed to contain the β-pyridyl group by single crystal X-ray diffraction (scXRD). The XRD results were consistent with those collected for the same compound by Nasiru Yahaya in his PhD thesis, but with a marginally higher level of data quality (R_1 = 3.57% as compared to 5.43%).[114]

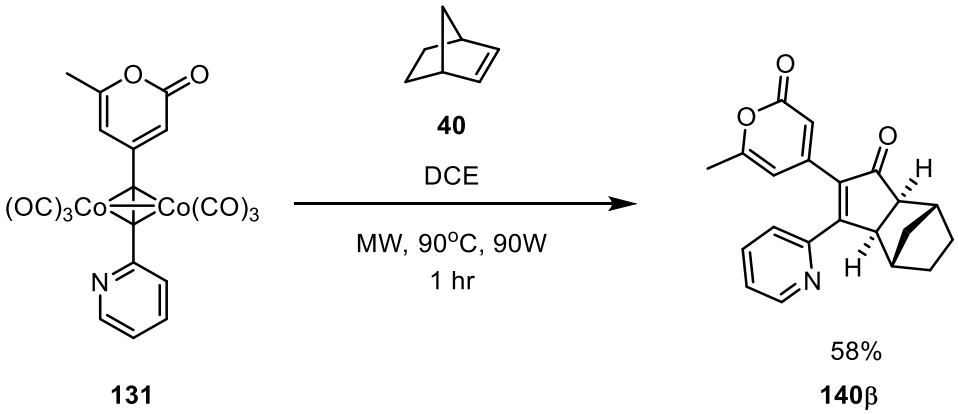

*Scheme 49 – Microwave reaction to form **140** with 100% β-pyridyl selectivity.*

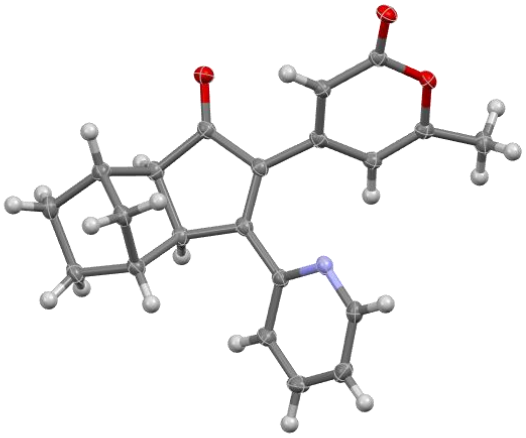

*Figure 18 – Single-crystal XRD structure of **1408.***

The PKR is a system which is highly suited to the use of *in-situ* FTIR reaction monitoring. The metal carbonyl groups on the cobalt centres in the starting complex and in the proposed intermediates have high-intensity bands at diagnostic positions in the IR spectrum. However, the use of microwave promotion is incompatible with the employment of *in-situ* monitoring equipment, so an altered experimental system was required. The reaction was promoted using *N*-methylmorpholine N-oxide (NMO, **73**), a well-known abstractor of CO ligands from metal complexes. NMO was selected as it represented a well-characterised method of promoting PKRs, and had a clearly defined mechanism of action. A new system was prepared as shown in Scheme 50, with the quantities of norbornene and NMO (X and Y respectively) adjusted.

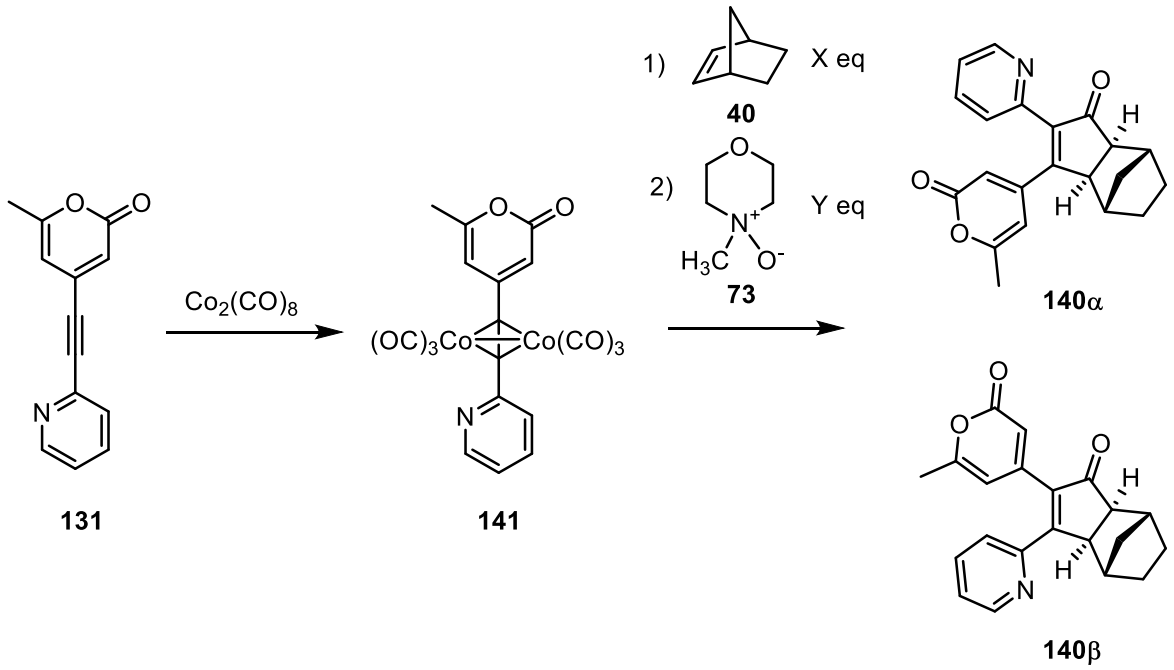

*Scheme 50 - General scheme of NMO-promoted PK reactions with alkyne **131.***

3.3. *In-situ* FTIR measurements of NMO-promoted PK reactions

The synthesis of the cobalt-alkyne complex **141** was carried out in the reaction vessel, by stirring an equimolar amount of alkyne and cobalt carbonyl at room temperature. By observation of the metal carbonyl IR bands in the reaction mixture, the conversion of $Co_2(CO)_8$ to complex **141** could be monitored (Figure 19). After a period of 30 minutes, no further increase in intensity of the metal carbonyl IR bands was observed, and complex formation was determined to be complete.

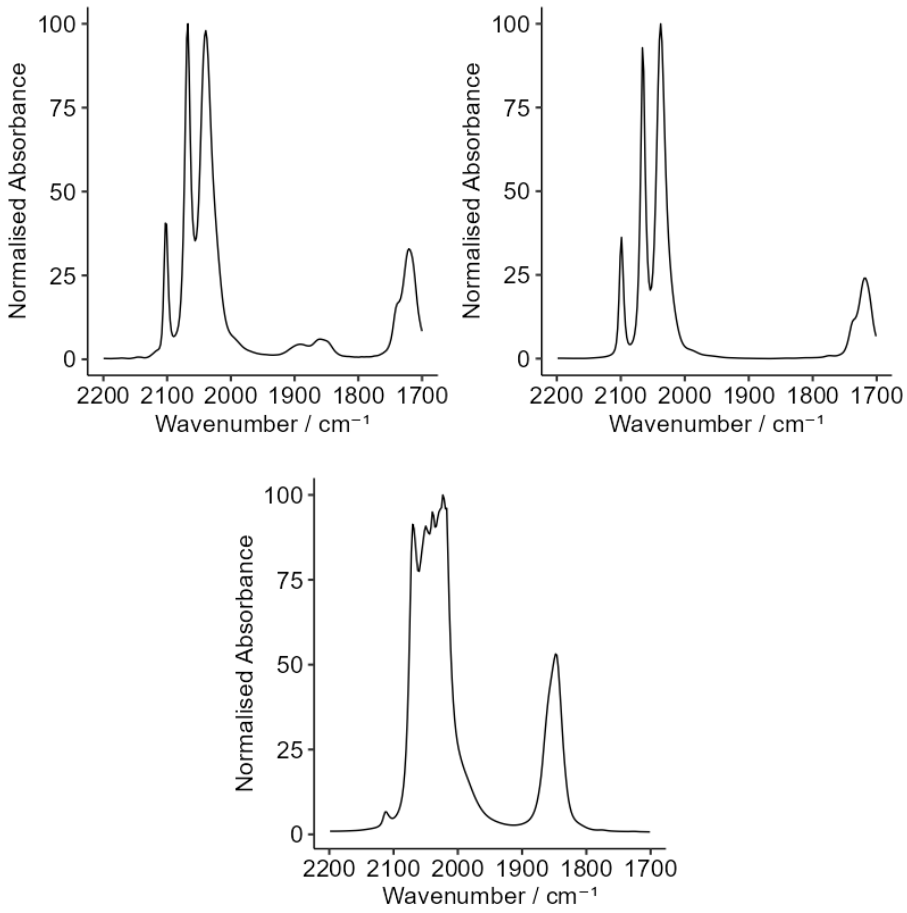

*Figure 19 – Top left: FTIR bands of the reaction 30 minutes after addition of cobalt carbonyl and alkyne **131** Top right: Reference sample of complex **141.** Bottom: Reference IR spectrum of cobalt carbonyl.*

Once complexation was completed, norbornene was added to the solution, followed by two stoichiometric equivalents of NMO. Upon NMO addition, the signals for the complex band decreased in intensity, and new bands were observed in the metal carbonyl region at 2030 and 2000 cm^{-1}. Additionally, a lower-energy band at 1892 cm^{-1} was also observed, which was assigned as formation of the $[Co(CO)_4]^-$ anion, based on its characteristic peak position and intensity.[128,129]

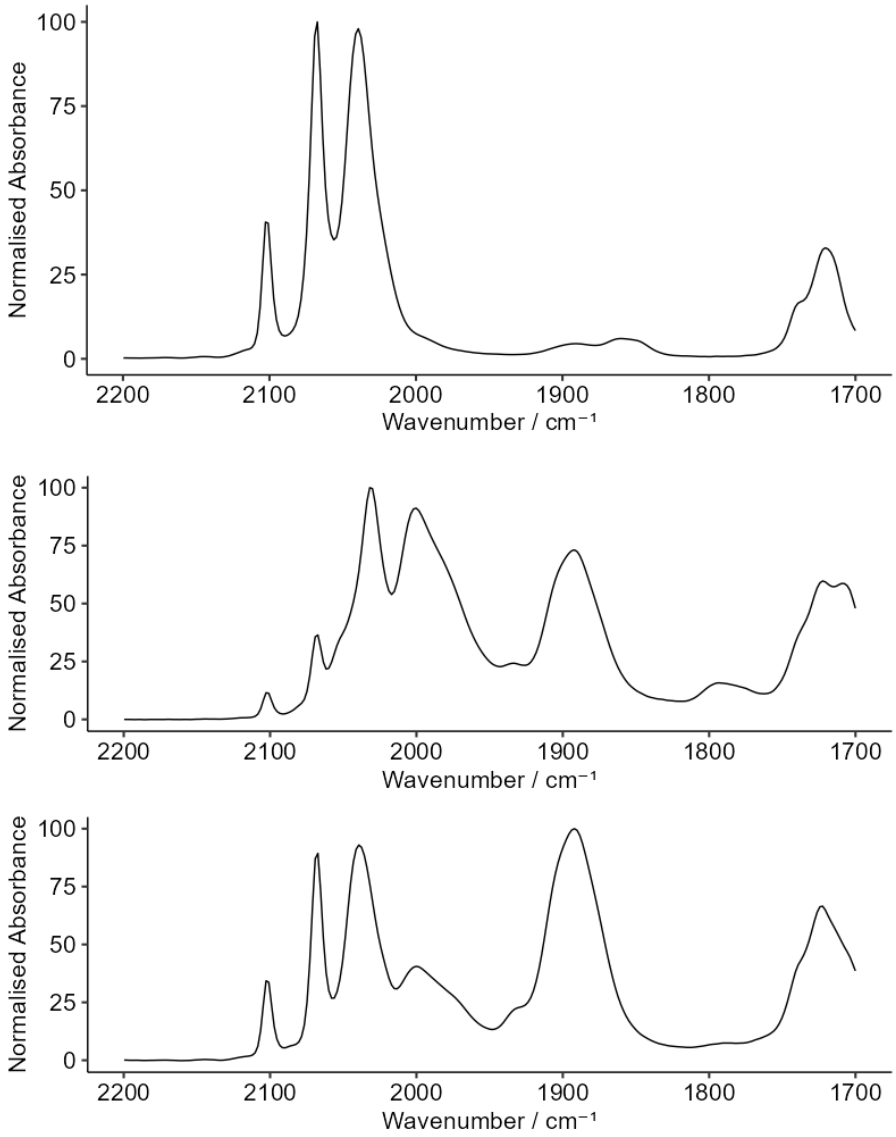

Figure 20 - The metal carbonyl region of the reaction prior to NMO addition (top), immediately following NMO addition (middle) and after eight hours (bottom).

Over time, the newly formed metal carbonyl peaks decreased in intensity, and the peaks for complex **141** begin to recover in intensity. The profiles of bands for the new metal complex species (2000 cm^{-1}) and complex **141** (2068 cm^{-1}) following NMO addition suggest that the two species slowly interconvert over the course of the reaction (Figure 21).

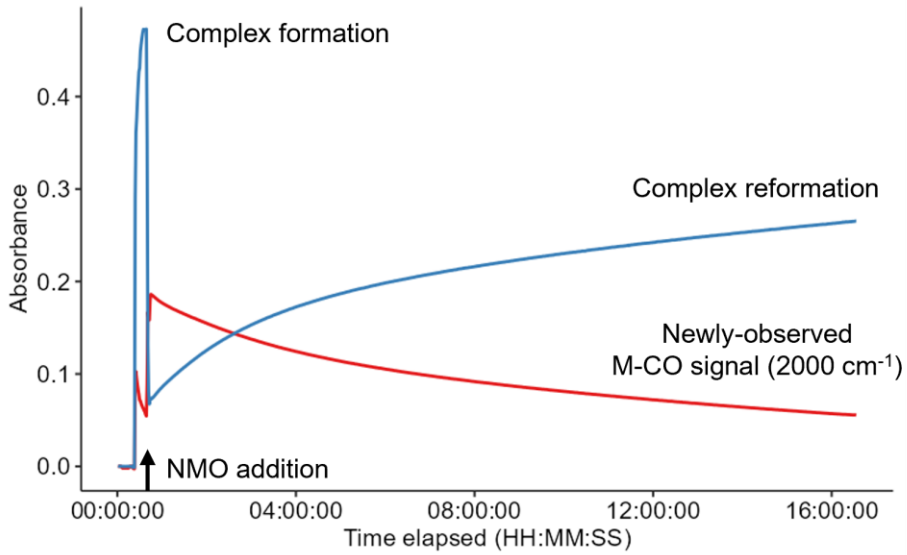

*Figure 21 - Profiles of peaks for **141** (blue) and the unidentified signal at 2000 cm^{-1} (red) following activation of **141** with two equivalents of NMO.*

Unlike the microwave-promoted reaction, the NMO promotion did not yield exclusively the β-pyridyl regioisomer **140β**. The purified cyclopentenone-containing fractions from silica chromatography contained two sets of pyridyl and pyrone proton environments. The identities of the species could be confirmed by NMR comparison to the sample previously generated by microwave methods, showing that **140β** was the major component of the regiosiomeric mixture. The deviation from total regioselectivity was unexpected, as the α-pyridyl regioisomer is not usually detected when **131** is reacted with norbornene. One possible implication of the presence of the α-pyridyl product is that the NMO-promoted conditions are leading to a mechanistic influence on the system, skewing the regiochemical outcome. The overall yield of isolated complex (15%) was low, but this was not unexpected considering the gentle activation conditions employed. As suggested by the *in-situ* IR, the reaction mixture contained unreacted cobalt-alkyne complex.

Repeating the reaction using six equivalents of NMO led to the suppression of complex re-formation, with the newly observed bands at 2000 and 2030 cm^{-1} observed until the end of the reaction. However, yield of the isolated product was not increased, as would generally be expected from this alteration to the experimental procedure.

3.3.1. Effect of alkyne on conversion with NMO

Using the NMO-promoted system, the identity of the alkyne was found to play a role in the ability of the complex to react to yield cyclopentenone products. Unexpectedly, when

diphenylacetylene (**95**) was used as the alkyne, no conversion to cyclopentenone product **144** was observed. The *in-situ* complexation process was seen to occur as expected, with IR bands assigned to the diphenylacetylene complex **142** identified to form over the course of 30 minutes. Addition of NMO, however, led to an initial decrease in intensity of these bands, before a nearly full recovery to their starting intensity followed. Once the reaction had been stirred for 24 hours, the resulting crude material was worked up as per the general procedure, and separated by column chromatography. Unreacted cobalt-alkynyl complex **142** was recovered, alongside a trace amount of diphenylacetylene cyclotrimerisation product **143**.

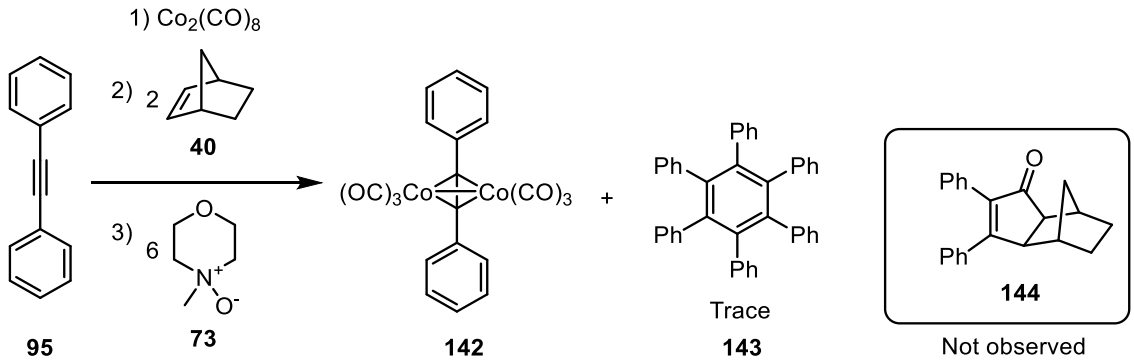

While not observed spectroscopically, this trace amount was isolated via crystallisation and characterised by single-crystal X-ray diffraction. This alkyne cyclotrimerization pathway, while known for other cobalt-based systems,[130] cobalt carbonyl[131] and dicobalt-alkyne hexacarbonyl complexes[132] is not commonly observed when carrying out the PKR. It is notable that diphenylacetylene, an alkyne which is not generally known to display issues with activity in the intermolecular PKR, displays such unusual reactivity in this system.

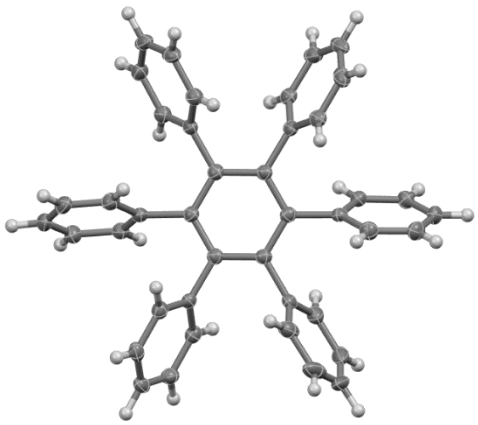

*Figure 22 - Hexaphenyl benzene (**143**), the cyclotrimer product of diphenylacetylene.*

A *bona fide* sample of the diphenyl acetylene complex was synthesised (see 3.3.4.1) for comparison, and the IR bands found to match the complex observed *in-situ* and isolated post reaction. These observations imply that that **142**, despite being activated by the dissociation of CO (as evidenced by fast decrease in intensity of the complex IR bands upon NMO addition), does not undergo the alkene insertion and subsequent steps which lead to the expected PK product, instead complex re-formation occurs to re-generate the cobalt-alkyne complex, and only trace side-products are recovered.

3.3.2. Observation of metal carbonyl signals during reaction

The peak at 1889 cm^{-1} is assigned to the formation of the cobalt tetracarbonyl anion, and the higher energy signals are within the commonly cited range for metal carbonyl species (1950-2150 cm^{-1}). These peaks were not observed in the applications of *in-situ* IR on PKRs in the literature, implying that this is new reactivity specific to this system. Presence of a monocobalt anionic species requires the breakdown of the cobalt-cobalt bond. As no free alkyne is observed in the IR spectra collected due to the reaction, it is possible that this breakdown process takes the form of a disproportionation of the cobalt-cobalt bond to generate a cationic cobalt(I)-alkyne species as the counterion to the observed $[Co(CO)_4]^-$.

Similar behaviour of dicobalt alkynyl complexes has previously been observed in work by Lynam, Fairlamb and co-workers.[133] In their study, they probed the potential uses of μ^2-alkyne dicobalt complexes analogous to **141** as carbon monoxide releasing molecules, in a DMSO solution. During this process, they observed the formation of a similarly strong band at 1890 cm^{-1}. Observing no free alkyne in the system, the hypothesis was proposed that the counter ion for the cobalt tetracarbonyl anion may be a cationic monometallic alkyne-bound species, formed from the disproportionate breakdown of a dinuclear μ^2-alkyne cobalt starting material (Scheme 51).

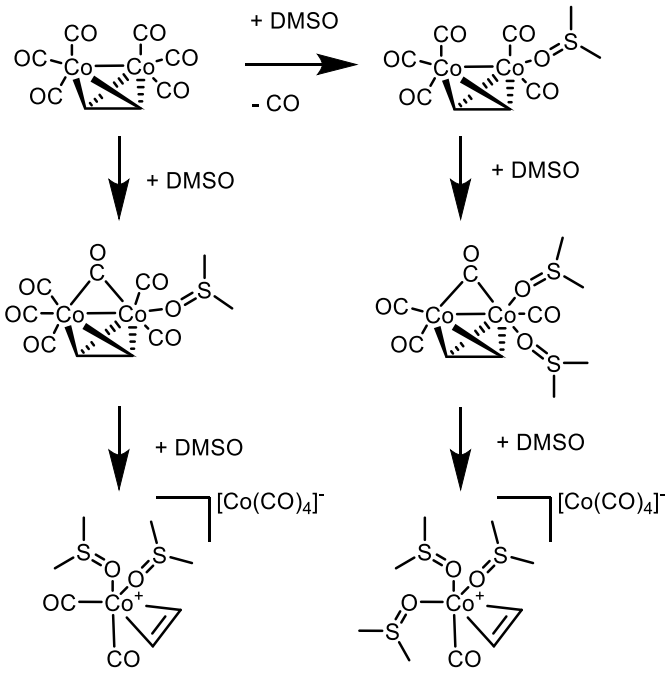

Scheme 51 - The proposed mechanism of the DMSO-facilitated activation of a μ² alkynyl dicobalt species to form a cobalt tetracarbonyl anion and a monocobalt alkynyl cation by Fairlamb and Lynam.

Lynam and Fairlamb noted that the formation of the anion was not observed when the complex was dissolved in neat ethanol, implying that this speciation is solvent dependent, relying on a co-ordinating group in the system to stabilise the vacant co-ordination sites on the cationic cobalt.

Cobalt is well established to act as a monometallic species to play a role in important catalytic processes such as hydroformylation and hydrogenation. Similarly, other metals, such as rhodium (Scheme 52) which are able to perform Pauson-Khand type reactions are often described to proceed through monometallic cationic cycles.[69,70]

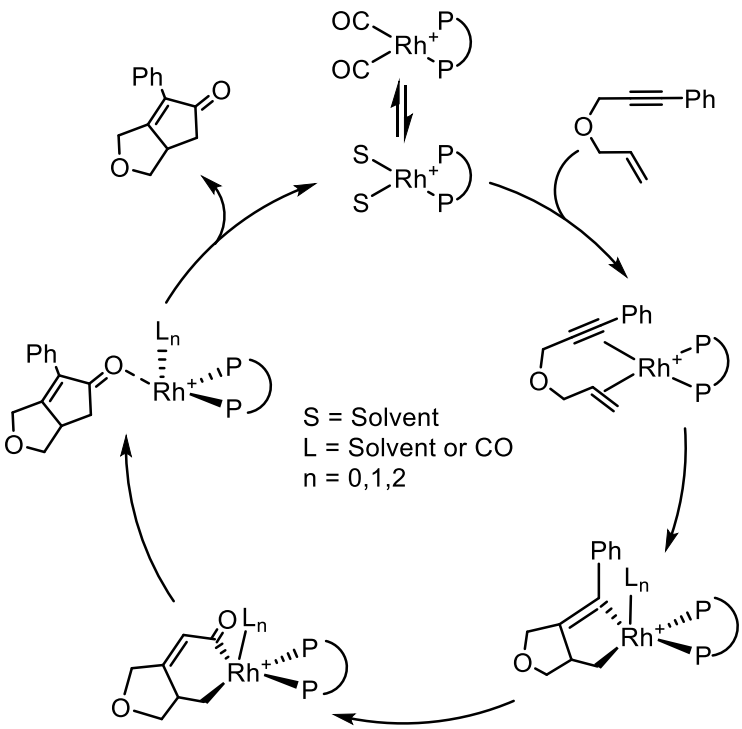

Scheme 52 - The proposed mechanism of a rhodium-catalysed intramolecular PKR, catalysed by a rhodium-BINAP (abbreviated for clarity) centre.

It is, therefore, possible that the observed breakdown of the Co-Co bond to form monometallic species could play a mechanistically relevant role in the cobalt-mediated PKR. It has been observed by Gibson and co-workers that the use of a pendant alkene attached to a BINAP-ligated cobalt-alkyne complex leads to readily accessible cobalt-cobalt bond breaking to form the ionic pairing of the (BINAP) dicarbonyl dihydride cobalt cationic complex and the cobalt tetracarbonyl anion.[48] The implication of this finding is that the presence of a donor ligand in the system can lead to accessible cobalt-cobalt bond breaking. The authors conclude that this demonstration of the ease of cleaving the cobalt-cobalt bond to yield ionic products is relevant to potential alternative pathways in the PKR. Mechanistically, the Magnus mechanism proposes that all of the transformations in the mechanism proceed about a single cobalt centre, with the other bound $Co(CO)_3$ moiety anchored away from the site of the chemistry, and not directly participating. The spectating nature of the anchored moiety implies that its presence may not be required for the reaction to proceed, allowing for reactivity about a single metal centre to be possible with cobalt.

3.3.3. Re-formation of μ^2-alkynyl dicobalt hexacarbonyl complex during reaction

When two equivalents of NMO promoter were used, a re-appearance of the bands associated with complex **141** was observed. Due to the fact that the mechanism of CO abstraction by amine N-oxides leads to the CO moiety being converted to CO_2 and lost irreversibly from the system, the re-formation of complex **141** does not have any obvious source of CO. To further probe re-formation of the complex, the reaction was carried out with the NMO being added in three separate doses, each of two equivalents and spaced one hour apart.

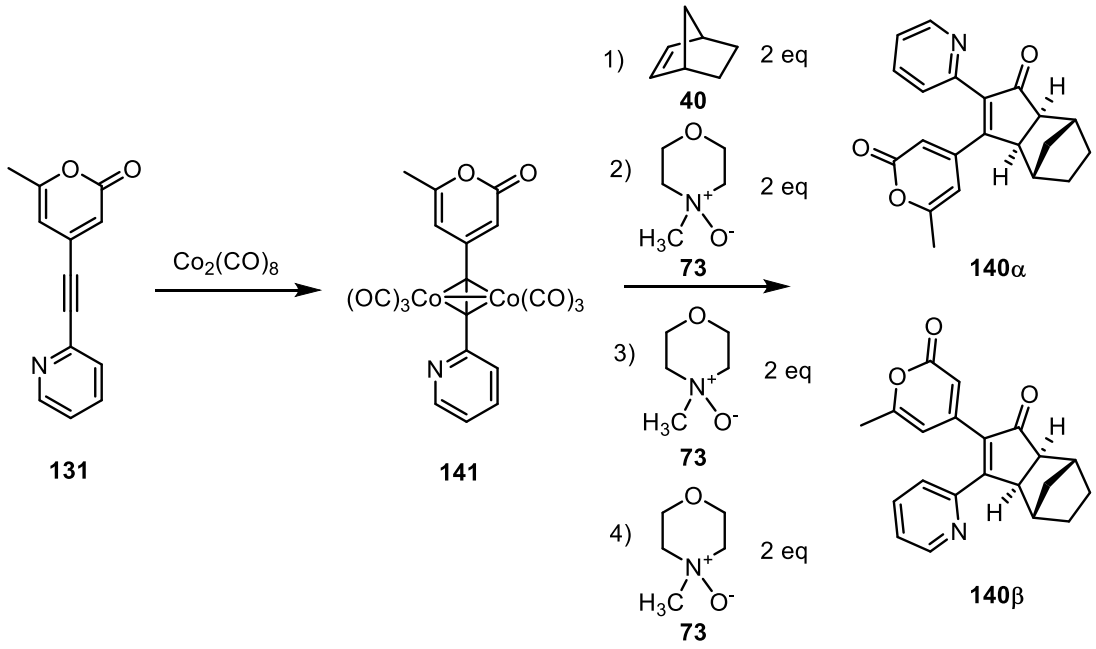

As before, complex re-formation was observed following the first two equivalent addition, with the bands associated with complex **141** re-forming before each of the next two additions, each time to a lesser intensity than before (Figure 23). Each addition caused the intensity of complex bands to drop sharply, showing that the re-formed complex was similarly sensitive to CO-loss by NMO promotion.

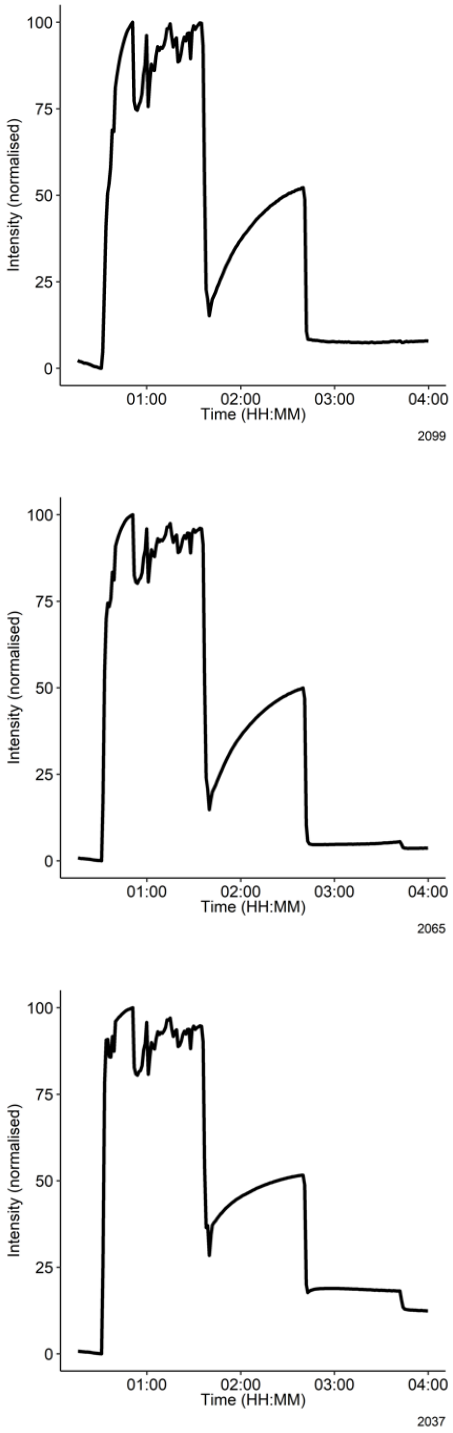

Figure 23 – Normalised intensity traces of IR peaks at 2099, 2065 and 2037 cm^{-1}, showing the re-formation of complex following NMO addition

The observed re-formation implied a source of labile or free CO in the system. This may arise from free CO in the reaction mixture following the loss of two CO ligands in the in situ formation of **141** from **131** and $Co_2(CO)_8$ (Scheme 53).

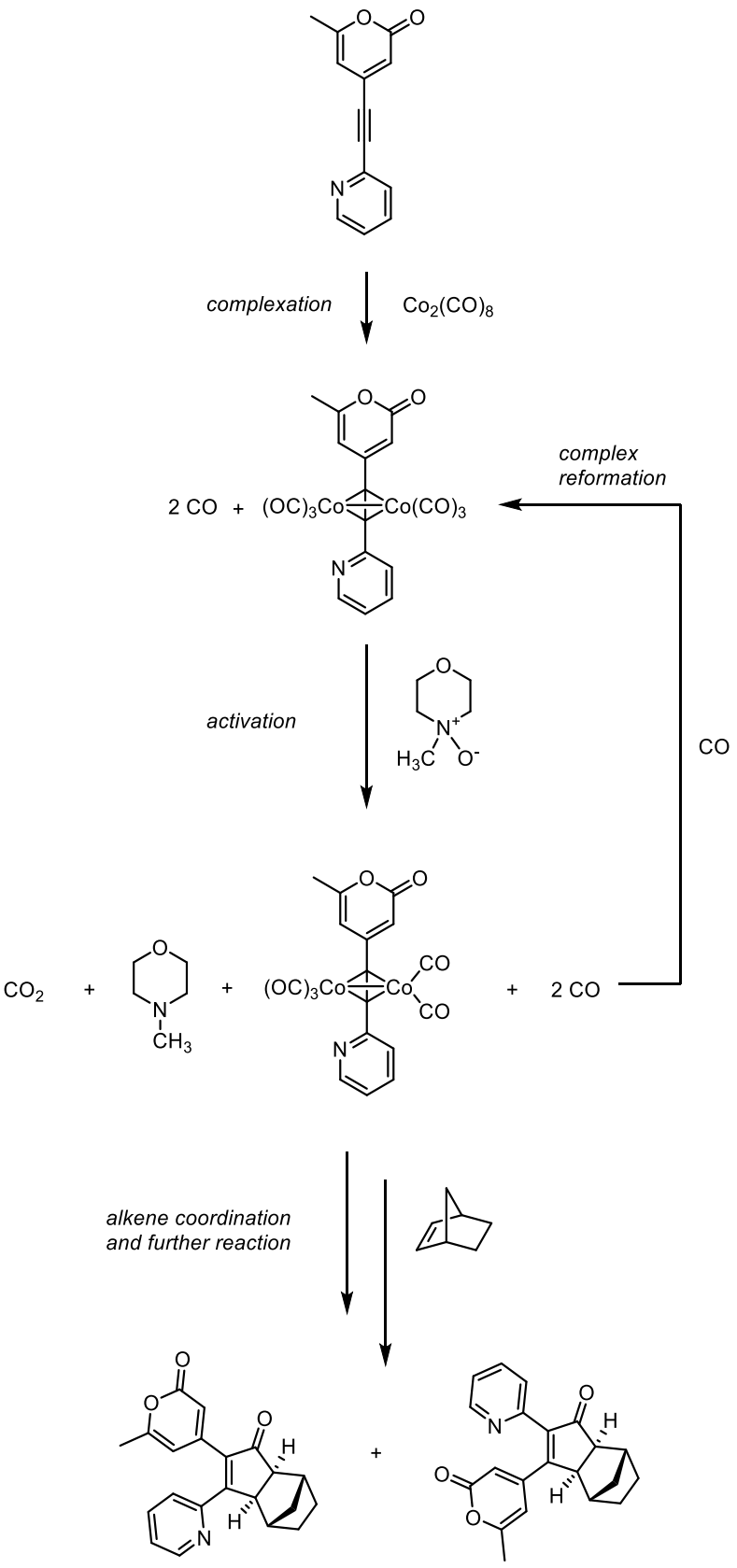

Scheme 53 - The proposed mechanism of re-formation from competition between free CO from the complexation step and norbornene.

3.3.4. PKR with *ex-situ* generated μ^2-alkynyl hexacarbonyl dicobalt complexes

To further investigate the proposed speciation behaviour, the reaction was altered to use pre-generated and isolated dicobalt-alkyne complex **141**. By precluding the *in-situ* complexation step, there would be no opportunity for free CO to develop in the system. Additionally, the characterisation of cobalt-alkyne complexes would allow for investigation into the presence any effect the 2-pyridyl group may have on the initial cobalt hexacarbonyl complex, which may contribute to the unusual regioselectivities observed for 2-pyridyl substituted alkynes in Chapter 2. To fully explore this effect, a set of alkynes bearing various combinations of phenyl, pyrone and pyridyl groups were synthesised and characterised.

3.3.4.1. Synthesis and characterisation of μ^2-alkynyl hexacarbonyl dicobalt species

The complexes were synthesised by stirring equimolar amounts of internal alkynes with dicobalt octacarbonyl ($Co_2(CO)_8$) under nitrogen in dry THF (Scheme 54). These conditions proved capable of removing two CO ligands to form the alkyne-bound species, forming the complexes in relatively good yields without the need for forcing conditions.

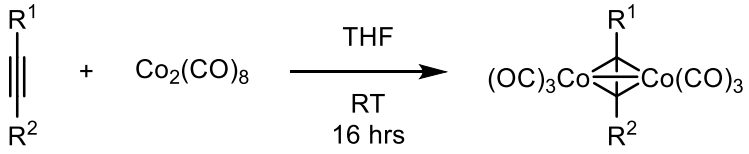

Compound	R^1	R^2	Yield / %
141	2-pyridine	4-(6-methyl-2-pyrone)	72
142	Ph	Ph	56
145	2-pyridine	Ph	50
146	Ph	4-(6-methyl-2-pyrone)	62

*Scheme 54 – Synthesis of μ^2-alkyne dicobalt hexacarbonyl complexes **141, 142, 143** and **145.***

Purification was achieved through filtration through a silica plug followed by recrystallisation, yielding the complexes as crystalline solids. Characterisation was performed with NMR, solution

phase IR and X-ray diffraction. The metal carbonyl ligands on these complexes demonstrated diagnostic IR shifts, as shown in Table 7:

*Table 7 - Metal carbonyl IR peaks for compounds **141, 142, 143** and **145.***

Compound	ν_{max} (M-CO)
141	2098, 2066, 2037
142	2090, 2055, 2026
145	2092, 2057, 2029
146	2096, 2062, 2035

3.3.4.2. X-ray crystallographic characterisation

The structures from these crystals showed that upon complexation, the alkyne adopts a bent geometry, with the alkyne ring groups deflected away from the metal-alkyne trapezoidal centre.

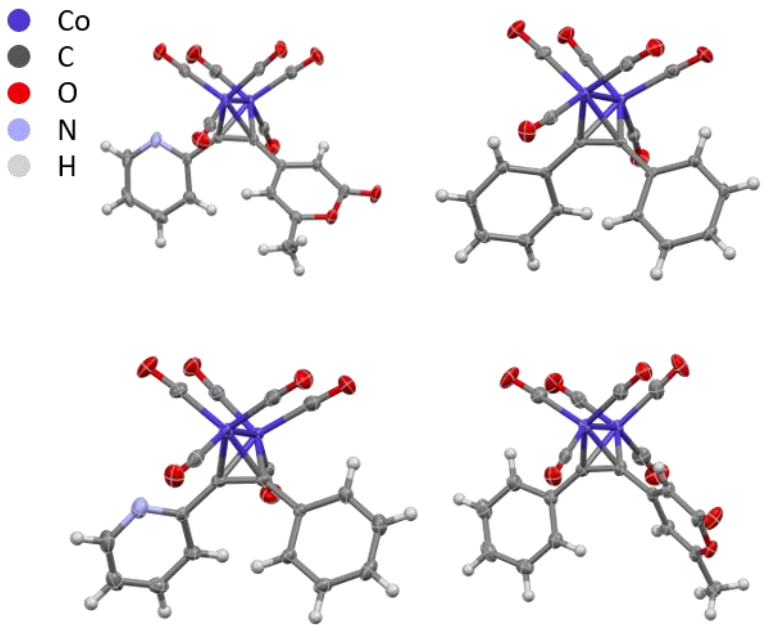

*Figure 24 - X-ray diffraction structures of complexes **141** (top left), **142**, (top right), **145** (bottom left) and **146** (bottom right)*

To assess any impact from the 2-pyridyl group on the geometry of the complexes, bond metrics were compared between the structures (labelling based on the generic structure shown in Figure 25.

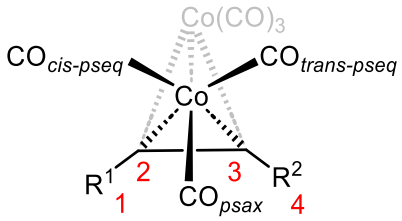

Figure 25 - Definitions of carbonyl positions, with carbon numbering in red and R groups as defined in Scheme 54 (cis and trans positions are labelled relative to R¹).

*Table 8 - Bond metrics measured from SCXRD structures of **141, 142, 143** and **145.***

Bond	**141**	**142**	**145**	**146**
Co - Co	2.4658(8)	2.4684(8)	2.4715(8)	2.4727(9)
C1-C2	1.462(4)	1.465(6)	1.462(5)	1.455(4)
C2-C3	1.353(3)	1.352(2)	1.344(5)	1.360(4)
C3-C4	1.450(4)	1.449(6)	1.460(4)	1.454(4)
Co-$CO_{trans\text{-}pseq}$	1.817(3)	1.836(5)	1.827(4)	1.841(4)
Co-$CO_{cis\text{-}pseq}$	1.830(3)	1.808(4)	1.815(3)	1.820(3)
Co-CO_{psax}	1.808(3)	1.807(5)	1.806(4)	1.812(4)

Inspection of the structures in Figure 24 and the measured metrics in Table 8 does not reveal any effect on complex geometry arising from the presence of the pyridyl group. Therefore the abnormal regiochemistry observed using 2-pyridyl substituents is unlikely to arise from any structural feature in the initial starting complex.

3.3.4.3. Effect of *ex-situ* generation of 141 on complex re-combination

When pre-generated complex was used, no increase in intensity of bands for complex **141** was observed following NMO addition. From this observation, it can be taken that this alteration to experimental protocol had the effect of halting the re-generation pathway. This behaviour implies that the presence of free CO in the system from the complexation step had been the cause of the re-generation behaviour, rather than disproportionation of two pentacarbonyl species. The reversible nature of CO-loss from cobalt-alkyne complexes is well-known, and indeed goes some way to explain the need for strongly CO loss promoting conditions to activate PKR substrates (be they thermal, chemical, or photochemical), particularly when carrying out intermolecular transformations. However, this finding highlights the previously underacknowledged competition between CO lost from *in-situ* complexation methods and re-coordination with Co complexes that are important for later steps in these reactions, a consideration not often made when designing PKR systems. This is of particular importance

when considering a sealed system, as is routinely employed in microwave-promoted thermal activation methods of the PKR. In such a system, CO evolved during the complexation step is unable to escape the headspace and can remain competitive with the alkene during the alkene coordination step.

Additionally, these observations may go some way to explaining the higher-than-expected stoichiometry of amine N-oxide promoter required to activate PKR substrates. It is well established in the literature that the optimal stoichiometric loading of an amine N-oxide is in the range of four to six equivalents. This amount seems anomalously high, as due to the irreversible nature of CO loss which is characteristic of this promotion method, and the requirement for only a single CO ligand to be abstracted to allow for alkene co-ordination, theoretically only one equivalent of N-oxide should be required to achieve full activation of the cobalt-alkyne complex. However, if these competition effects arising from free CO in solution and in the headspace of the reaction vessel are considered, there is in fact an excess of CO relative to the cobalt-alkyne complex, which require a greater amount of promoter to fully abstract from the system as CO_2.

To investigate whether the species observed in the *in-situ* FTIR spectra were capable of carrying out transformation to cyclopentenone products, and not simply an off-cycle side product, the reaction was carried out with the NMO-activation of the starting cobalt alkyne product prior to norbornene addition. Pre-isolated and purified **141** was added to the reaction vessel, and activated by three sequential two equivalent doses of NMO, to ensure full consumption of the starting complex. After these three sequential additions, no peaks associated with the starting complex were observed, and it was taken that full conversion to an alternate cobalt speciation system had taken place.

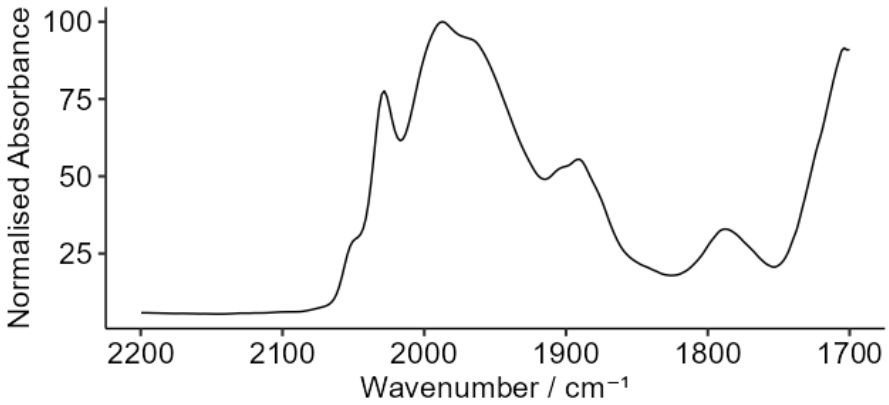

*Figure 26 – Observed bands in the metal carbonyl region following activation of complex **141** in the absence of alkene (See page 114 for the spectrum of **141**).*

Following this observation, the standard two equivalents of norbornene were added to the reaction mixture and the reaction allowed to proceed as usual. Purification of the reaction mixture gave the expected 20:80 **140α**:**140β** ratio, in a 16% yield.

This comparable spectroscopic observations and product conversion regardless of order of addition suggests that the species associated with the observed metal carbonyl bands following NMO activation are mechanistically relevant, and do not have alkene coordinated.

3.4. Proposed non-Magnus monometallic reactive pathways

3.4.1. Theoretical investigations into the energy profiles of the proposed monometallic pathways

Following the spectroscopic observations of the model system, focus was turned to using theoretical methods to understand the mechanistic relevance of metal carbonyl species which arise from the Co-Co bond cleavage. Potential energy surfaces were constructed using Density Functional Theory (DFT) for various potential pathways at the BP68-SV(P) level of theory using the alkene and alkyne from the model system. Geometries were calculated in gas-phase without dispersion or solvation correction. Single-point calculations were then carried out at the optimised geometries to give DFT-D3 dispersion-corrected values with COSMO implicit solvation, using DCM as the modelled implicit solvent, to provide corrected electronic energies. Finally, thermodynamic parameters calculated at 298K were used to generate dispersion and solvation corrected Gibbs energies, which are reported below. A wide isomer space was surveyed in order to find the most feasible pathways for the proposed mechanism, and only some examples are discussed in depth in this section.

The proposed pathways rely on a donating ligand in the system to fill vacant co-ordination sites on the Co^{+} centre (Scheme 51). For the purposes of this study, the solvent THF was was included explicitly and modelled as the donating ligand(s) where the metal complex was coordinatively unsaturated, thus completing the first solvation shell of the metal. While the experimental system does contain other species that can coordinate to Co (notably the N-methylmorpholine formed following complex activation), THF is present in very large quantities relative to these, and is likely to play a key role in the solvation of intermediate states. While other ligand coordination cannot be ruled out, THF as the sole coordinating group within the model was judged to be a reasonable assumption for the investigation at hand, and allowed isomer space for the complexes to be kept to a feasible size. Two main pathways were investigated, which

differ by the number of CO ligands attached to the cationic cobalt centre (either one or two CO ligands). Each pathway begins with the proposed structures that would arise from a disproportionate dissociation pathway similar to that which has previously been proposed to occur in DMSO-promoted Co-Co bond breakdown (Scheme 51). Monocarbonyl and dicarbonyl starting complexes are both thought to be able to arise given the formation method proposed above in Scheme 51. The onward reaction pathways put forward were based on understanding of mechanisms which are thought to proceed around single-metal centres, as shown in Scheme 52 and discussed in section 1.7. Within each pathway there is a divergence point upon alkene insertion to form the five-membered cobaltacycle, with each resulting sub-pathway arising from a different alkene insertion position, and thus leading to a different regioisomer. The pathways and nomenclature for the monocarbonyl and dicarbonyl intermediates are shown in Scheme 55 and Scheme 56 respectively. Intermediates are labelled with an identifier for their pathway (**MC** or **DC** respectively) and a number for the position in the pathway. The number of carbonyl groups and coordinated THF ligands are specified for each state, with the isomer number stated at the end for example the first isomer of the intermediate in the monocarbonyl pathway would be designated **MC1 CO THF2 iso1.** A full reference table of isomer structures can be found in Appendix 5.

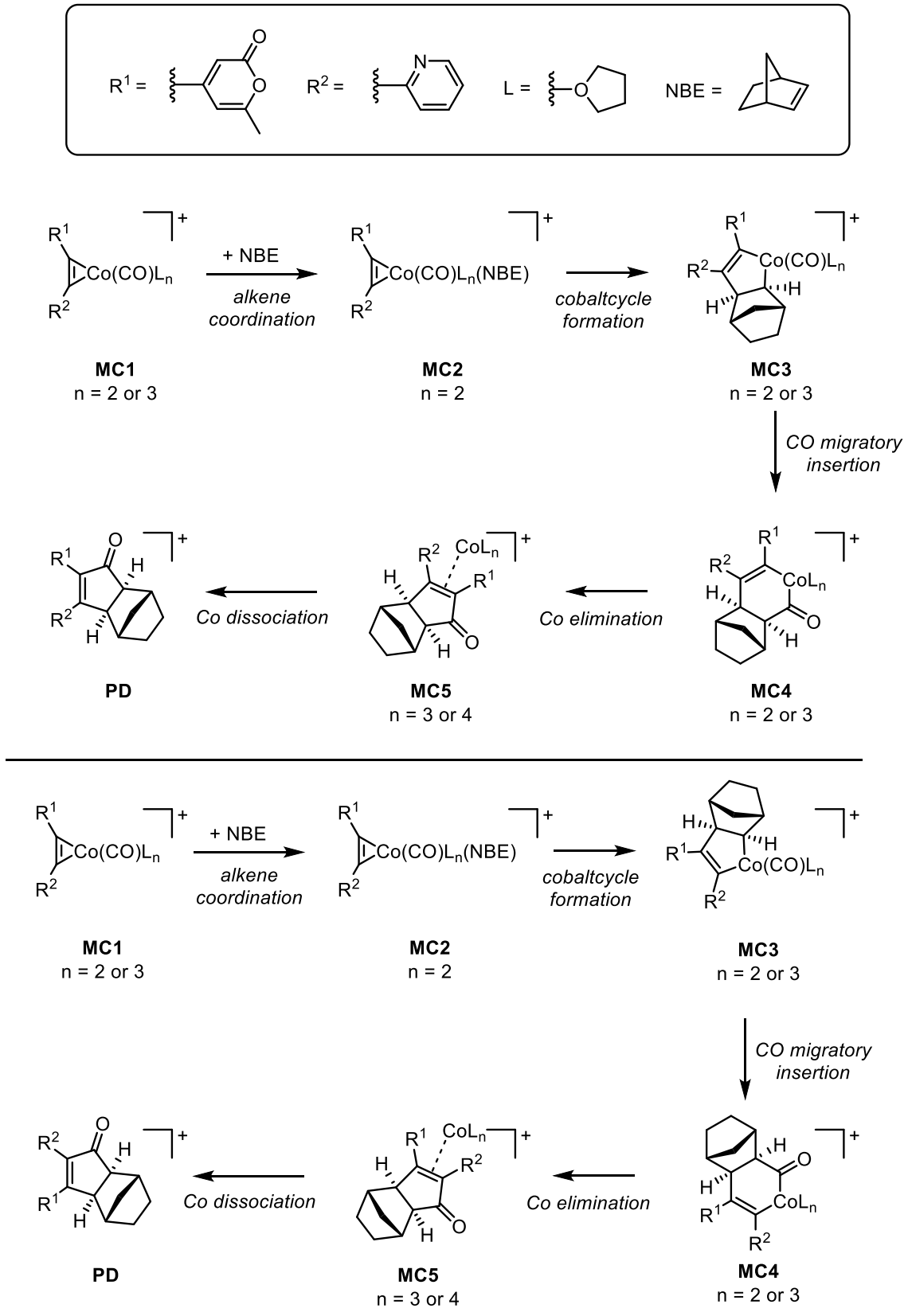

*Scheme 55 - General scheme of proposed monocarbonyl monocobalt-based pathways leading to **140β** (top) and **140α** (bottom).*

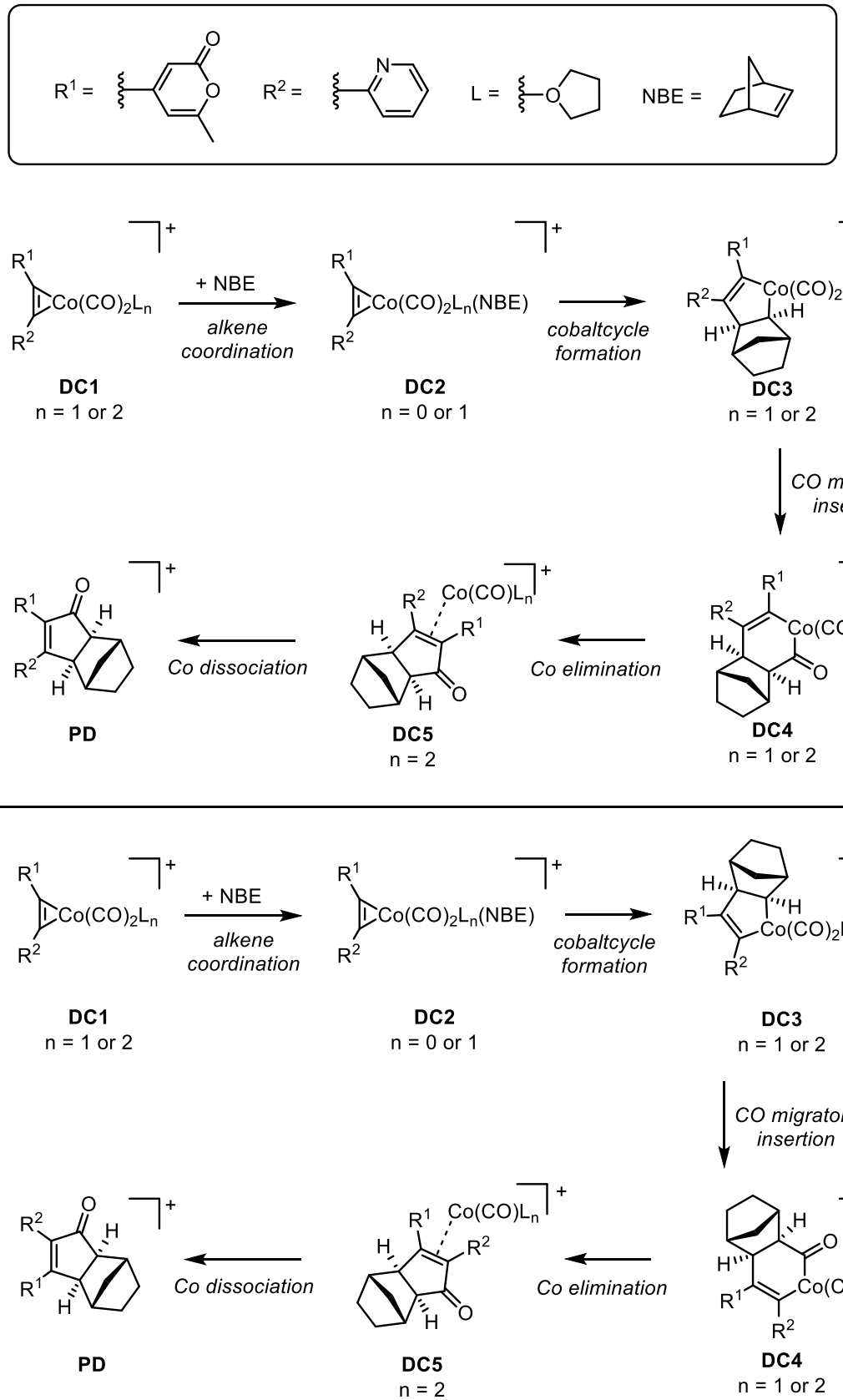

*Scheme 56 - General scheme of proposed dicarbonyl monocobalt-based pathways leading to **140β** (top) and **140α** (bottom).*

This section will examine the potential energy surface of each pathway, to ascertain their relative feasibilities. Intermediates along the pathway are labelled as shown in bold in Scheme 55 and Scheme 56. For each intermediate, several isomers are possible. These isomers are labelled as **iso1**, **iso2**, etc. For a full list of the structures of all isomers, see Appendix 5.

3.4.2. Monocarbonyl monocobalt cationic pathways

The starting point for the monocarbonyl pathways is a five-coordinate cobalt centre **MC1 CO THF_3**, complexed to the alkyne, a carbonyl ligand and three THF fragments. Across the isomer space, it was found that the lowest energy conformation was a trigonal bipyramidal structure, with the carbonyl group axial to the alkyne (Figure 28). For norbornene coordination to occur, dissociation of a THF is required. Steric crowding of the cobalt coordination sphere by alkene substituent groups and other ligands makes an associative mechanism via an octahedral complex unfeasible. Loss of a THF ligand gives the square planar complex **MC1 CO THF_3 iso2** (Figure 28).

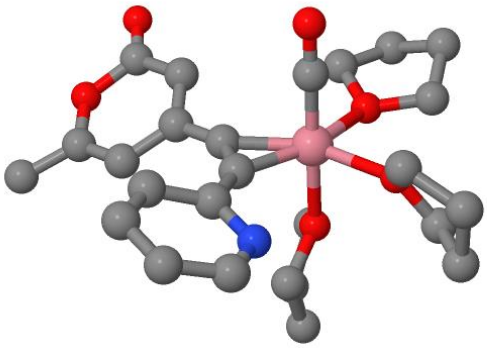

*Figure 27 – Optimised geometry of **MC1 CO THF_3 iso1.** H atoms omitted for clarity.*

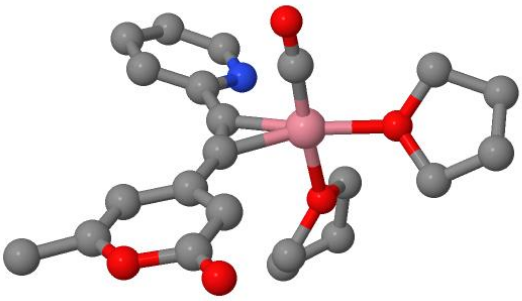

*Figure 28 - Optimised geometry of the square planar complex **MC1 CO THF$_2$ iso2.** H atoms omitted for clarity.*

Norbornene may now co-ordinate to this unsaturated cobalt centre, re-forming a trigonal bipyramidal complex, **MC2 CO THF$_2$**. There are two principal directions from which the norbornene can approach to coordinate, on each face of the square planar geometry at the cobalt (Figure 29).

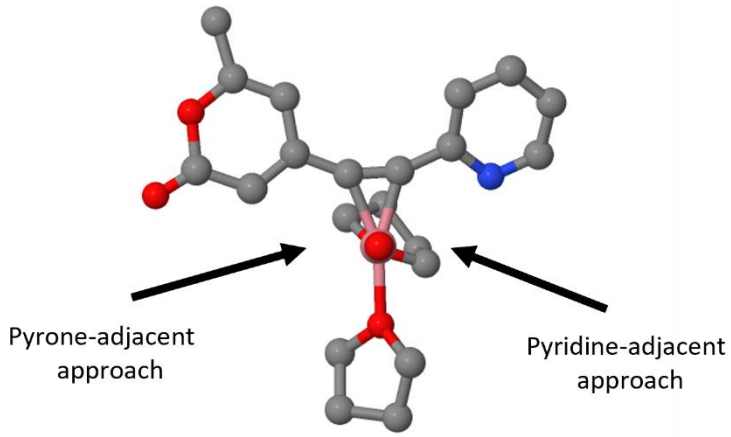

*Figure 29 - **MC1 CO THF$_2$ iso2** viewed along the (CO)-Co-THF axis, showing the two possible norbornene approach sites. H atoms omitted for clarity.*

Each approach pathway will leave the norbornene situated adjacent to one of the alkyne substituents. Substituents which facilitate the approach pathway to the face adjacent to themselves will be selective for the β position of the final cyclopentenone ring.

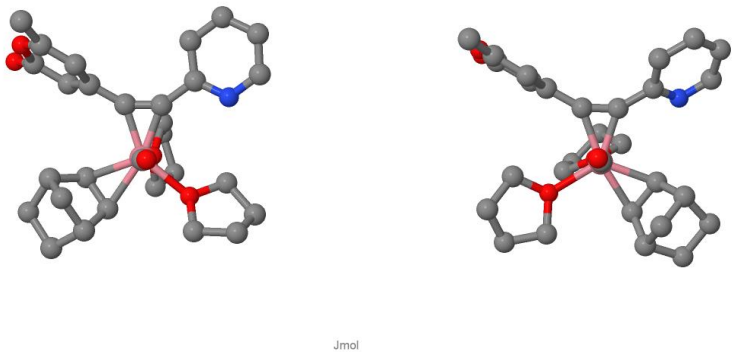

*Figure 30 -Optimised geometries of **MC2 CO THF$_2$ iso1** (L) and **iso2** (R), viewed along the CO-Co-THF axis. H atoms omitted for clarity.*

There is, however, no appreciable difference between the energies of the optimised geometries of the two states (Scheme 57), implying that there is no energetic favourability for either configuration over the other.

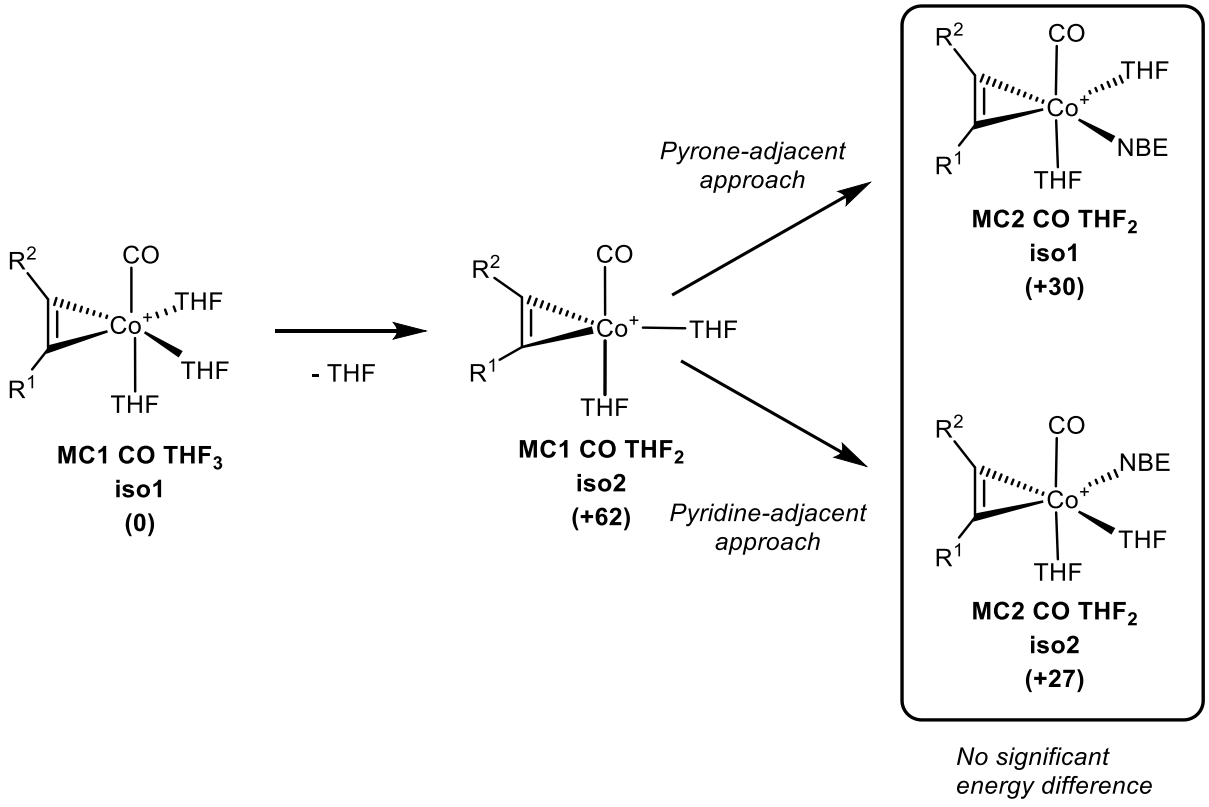

*Scheme 57 - The energetics of norbornene coordination to **MC1 CO THF$_2$ iso2.***

The next step of the process is the formation of the initial five-membered cobaltacycle ring. This is achieved by the formation of a new carbon-carbon bond between one of the central sp-hybridised alkyne carbons and one of the sp2-hybridised norbornene carbons. Generally, in the

Magnus mechanism, cobaltacycle formation is thought to occur from a geometry where the alkene occupies a pseudo-axial position. Analogously in this system, insertion was found to be facilitated more easily from an equatorial-equatorial arrangement of alkyne and alkene in the trigonal bipyramidal starting complex. The transition states isolated from this insertion show a ”slippage” of the two ligands away from the cobalt centre and towards the formation of the ring, which now acts like a bidentate ligand. The smaller bite angle of this ring leads to the resulting species displaying a square pyramidal geometry (Scheme 58).

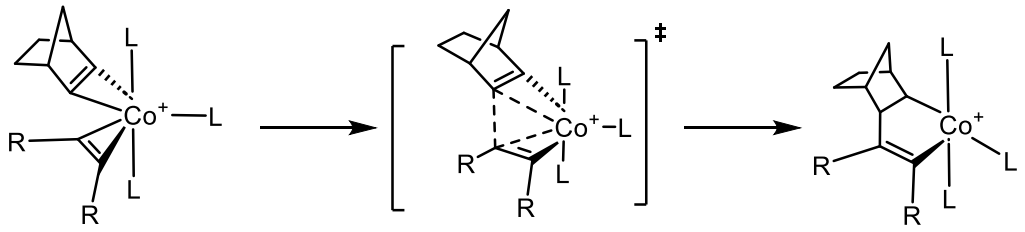

Scheme 58 - General scheme of cobaltacycle formation from a trigonal bipyramidal starting complex.

The insertion of the alkene denotes the establishment of the final product regiochemistry. At this point, two separate sub pathways were considered, each relating to a distinct alkene insertion site, and therefore final regiochemistry. Each sub-pathway was considered independently, with a full isomer space for the pathways following each insertion site modelled. This allowed for comparison of configurational effects from the position of the alkyne substituents on the cobaltacycles in the subsequent intermediates.

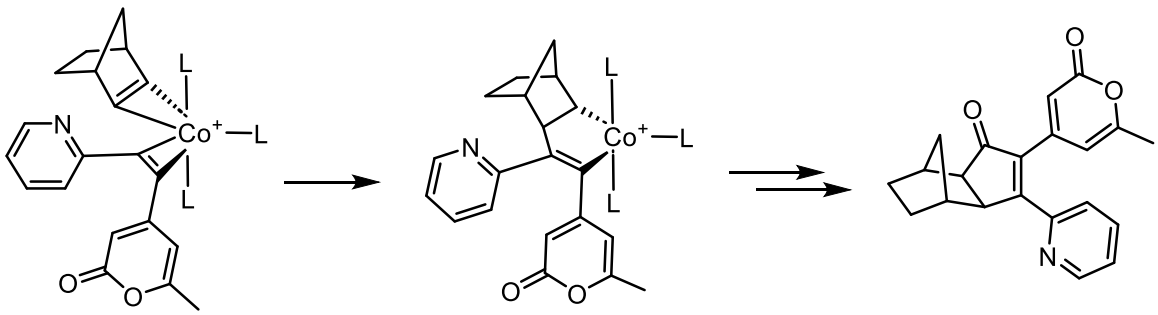

Scheme 59 - Insertion of the norbornene adjacent to the pyridyl group leading to the β-pyridyl product.

For the sub-pathway leading to the β-pyridyl product, alkene insertion occurs adjacent to the pyridyl group (Scheme 59). During the isomer space search for the resulting **MC3 CO THF$_2$** complex, a range of coordination geometries were considered. It was apparent that square pyramidal structures with an equatorial ring were not energetically favourable, and would rapidly rearrange during geometry optimisation to yield axial ring structures (Scheme 60). Of the resulting square pyramidal complexes, **iso1** was found to be the most energetically favourable,

with a relative pathway Gibbs energy of -83 kJ mol^{-1}. This energetic stabilisation is notable as in the analogous step of the Magnus mechanism, the initial formation of the 5-membered cobaltacycle has been found to be thermoneutral, with the energetic stabilisation arising from the subsequent co-ordination of a further carbonyl group.

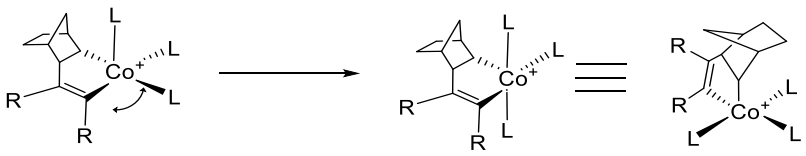

Scheme 60 - The rearrangement of equatorial ring structures to the axial counterpart.

In **MC3 CO THF$_2$ iso1**, the metal carbonyl is situated *cis* to the ring, and the norbornene-containing portion of the five-membered cobaltacycle in the axial position of the square pyramid (Figure 32). This isomer was found to be slightly more stable (-7 KJ mol^{-1}) than the equivalent isomer with the alkynyl moiety occupying an equatorial position, but it is likely that interconversion between these two ring orientations is accessible.

The transition state for the cobaltacycle formation is high in energy, with a Gibbs energy of 124 kJ mol^{-1} relative to **MC1 CO THF2**.

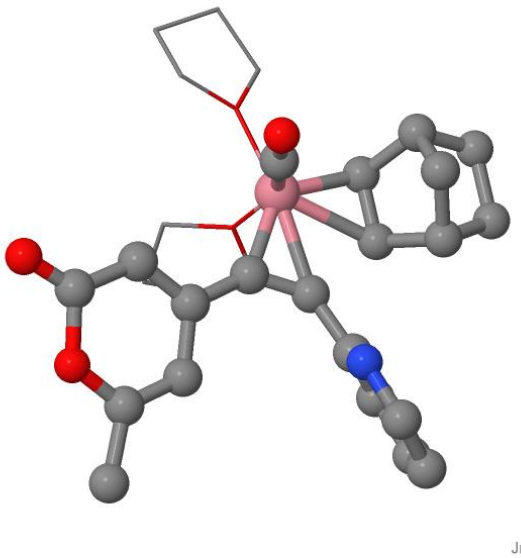

*Figure 31 - The transition state **MCTS23 iso1** for the β-pyridyl pathway. H atoms omitted and THF groups modelled as wireframes for clarity.*

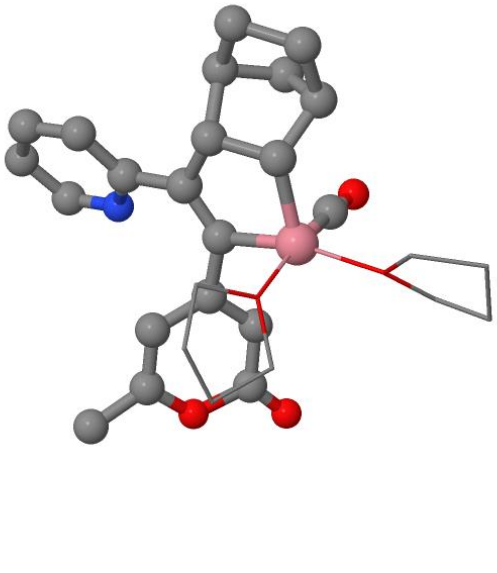

*Figure 32 - The optimised geometry of **MC3 CO THF$_2$ iso1.** H atoms omitted and THF groups modelled as wireframes for clarity.*

The cis orientation of the metal carbonyl ligand to the ring in the cobaltacycle product confers some stability, with the analogous trans-CO structure lying 69 kJ mol^{-1} higher in energy. This may be due to a trans-effect of the ring destabilising the CO ligand's bonding with the metal centre. In the optimised geometries of the two intermediates, the Co-C(O) bond distance is 0.15 Å greater in the trans configuration than in the cis, suggesting a weakening of the carbonyl ligand-metal bonding when opposite the ring (Scheme 61).

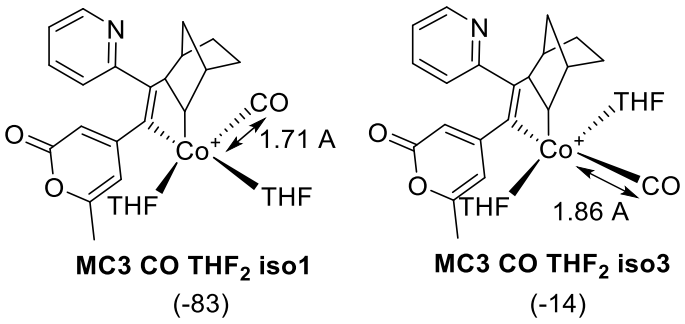

*Scheme 61 - The difference in energy (in kJ mol^{-1} relative to **1 CO THF3**) and geometry due to altering carbonyl position.*

The vacant coordination site afforded by the rearrangement of the complex geometry from a trigonal bipyrimidal to square pyramidal arrangement is filled by an additional THF molecule, forming the first coordinatively-saturated octahedral complex of the pathway, **MC3 CO THF$_3$**. The THF co-ordination represents another significantly energetically favourable step. The lowest

energy isomer, representing a further stabilisation of 58 kJ mol^{-1} relative to **MC2 CO THF_2**, features the metal carbonyl ligand in an axial position relative to the ring. This stabilisation upon coordination of a new group following alkene insertion is in agreement with the previously discussed observations of the energetics of the initial cobaltacycle formation in the Magnus mechanism.

Here, it is possible for the carbonyl ligand to insert into either Co-C bond present in the complex. The site of insertion in this case has no bearing on the identity of the final product, as following subsequent steps and the reductive elimination of cobalt, the carbonyl group will always occupy the same position in the ring.

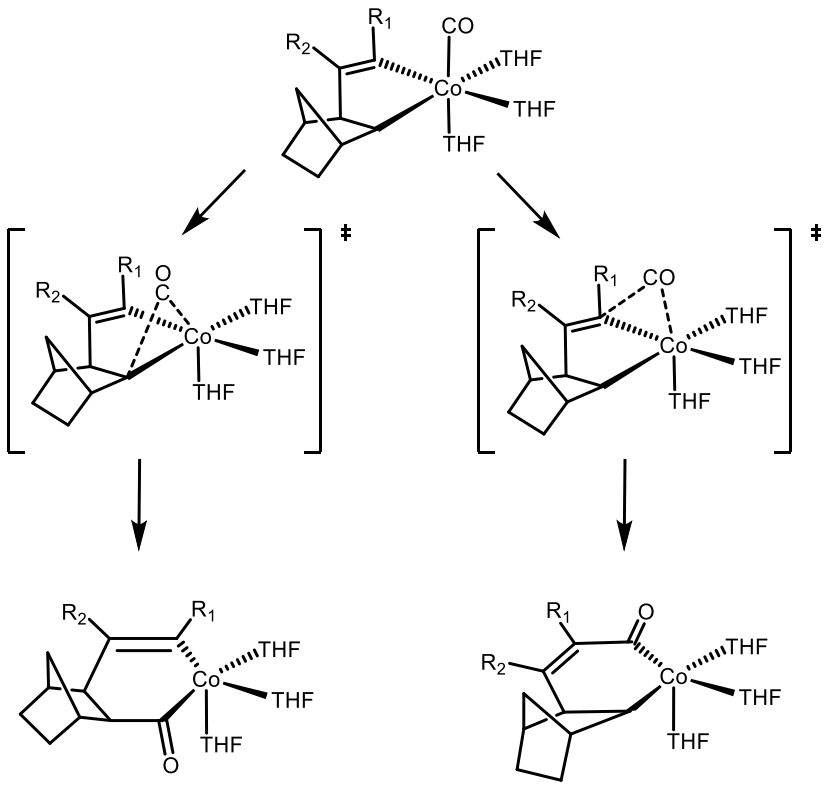

*Scheme 62 - The two possible migratory insertion pathways to form **MC4 THF3**, their transition states, and their resulting products.*

As noted previously, particularly by Yamanaka and Nakamura, the conventional understanding regarding the Magnus mechanism is that the carbonyl will preferentially insert adjacent to the olefin moiety in the ring, in this case the norbornene. This can also be seen to be the case here, as the lowest energy isomer of the resulting complex, **MC4 THF_3**, features the carbonyl group adjacent to the norbornene.

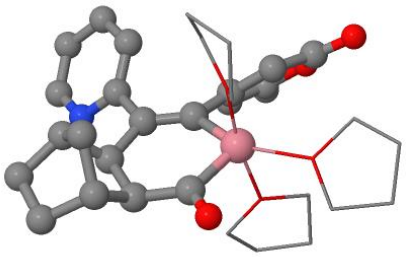

*Figure 33 - The optimised geometry of **MC4 THF$_3$ iso6.** Hydrogens and THF groups modelled as wireframes for clarity.*

As seen previously with **MC3 CO THF$_2$**, structures containing equatorially-oriented rings often undergo ligand re-arrangement during optimisation to yield axial ring arrangements, in either square pyramidal or trigonal bipyramidal geometries. This is likely due to steric concerns. When there are two relatively large substituents on the alkyne, an equatorial ring can lead to a steric clash between the substituent proximal to the cobalt centre, and nearby ligands. An axial ring, on the other hand, minimises this interaction by placing the proximal substituent below the plane of the base of the square pyramidal structure.

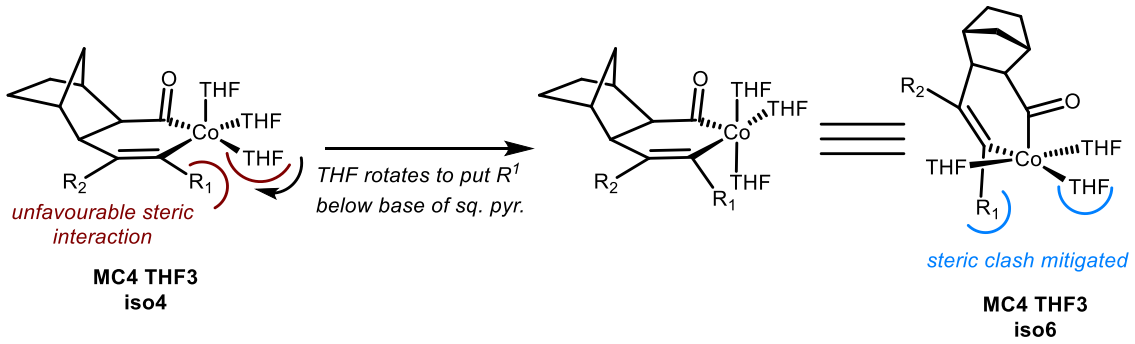

Scheme 63 - Minimisation of steric interactions by ligand rearrangement.

The transition state for carbonyl migratory insertion is modelled as the insertion of the carbonyl group axial to the ring in **MC3 CO THF$_3$** into the bond between the proximal norbornene carbon

and the cobalt centre. The transition state found in this case, **MC TS34 iso1**, presents an activation barrier of 71 kJ mol^{-1} for this transformation.

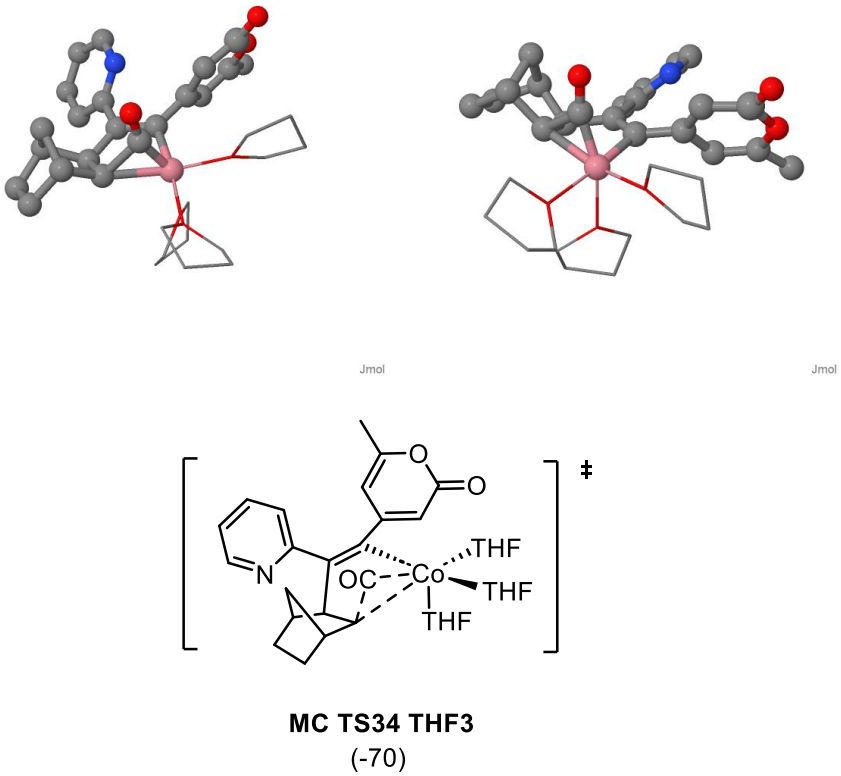

*Figure 34 - The geometry, structure, and energy (relative to **MC1 CO THF3)** of **MC TS34 THF3.** Hydrogens omitted and THF ligands represented as wireframes for clarity.*

The resulting complex is square pyramidal with an equatorial cobaltacycle, which undergoes fast rearrangement of THF ligands to form the axial cobaltacycle, with the carbonyl group in the axial position.

MC4 THF3 then undergoes elimination of the cobalt to give the final five-membered cyclopentenone product, which coordinates to the cobalt centre through the alkene.

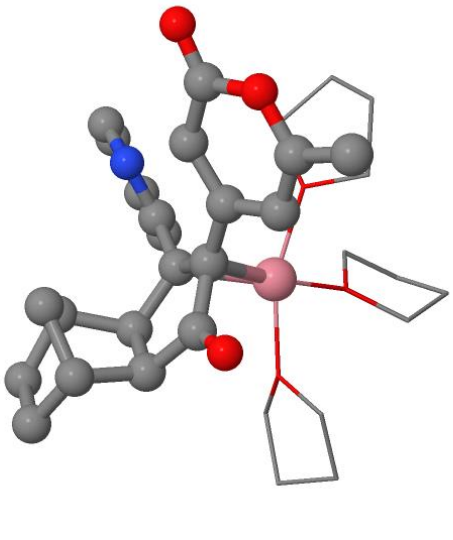

*Figure 35 - Geometry of **MC5 THF$_3$.** H atoms omitted and THF groups modelled as wireframes for clarity.*

This state, **MC5 THF$_3$**, adopts a square-planar geometry, and is approximately equal in energy to the cobaltacycle. De-coordination from the cobalt follows, to yield the cyclopentenone product. Overall, the energy of the pathway is analogous to the Magnus mechanism, with the first transition state representing a sizeable energy barrier, and the subsequent steps proving more energetically favourable (Figure 36).

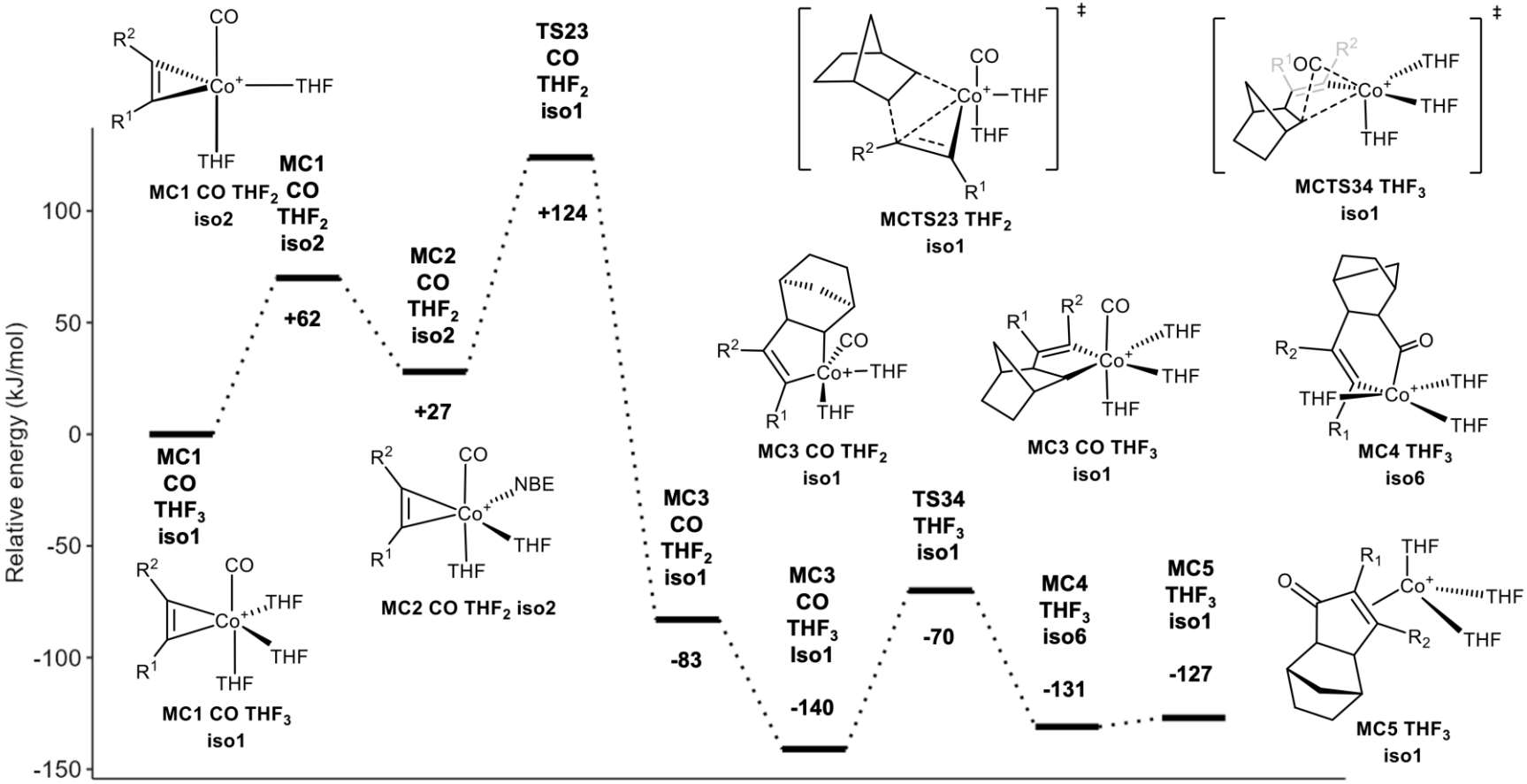

*Figure 36 - BP86/SV(P) Gibbs energies with DCM solvent and DFT-D3 dispersion correction of intermediates on the monocarbonyl pathway (**MC**) to give 140ß.*

Conversely, the alkene may also insert adjacent to the pyrone substituent of the alkyne, leading to the pyridyl group being situated in the α position of the final product. The transition state proceeding from **MC2 CO THF_2 iso1**, **MCTS23 iso4**¸ is structurally and energetically similar to **MCTS23 iso1**.

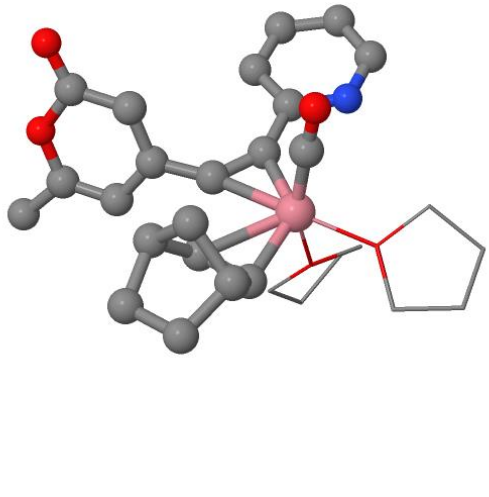

*Figure 37 – Optimised geometry of **MCTS23 CO THF2 iso4**. H atoms omitted and THF groups modelled as wireframes for clarity.*

The lowest energy resulting structure of this insertion, **MC3 CO THF_2 iso4** is structurally analogous to that of the β pathway, with the exception of an interaction from the pyridyl nitrogen (Figure 38). From the position adjacent to the cobalt, the 2-pyridyl nitrogen is able to interact with the vacant coordination site on the cobalt, at the base of the square pyramidal structure. This interaction renders the complex geometry *pseudo*-octahedral.

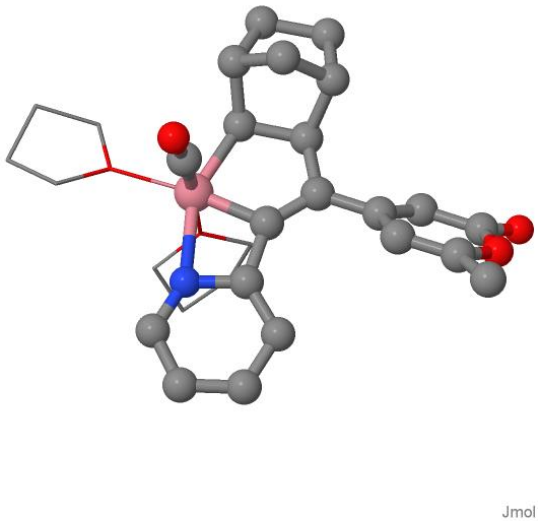

*Figure 38 - Optimised geometry of **MC3 CO THF$_2$ iso4.** H atoms omitted and THF groups modelled as wireframes for clarity.*

Displacement of this interaction by THF, however, is energetically favourable (representing a stabilisation of 15 kJ mol^{-1}) and yields the octahedral complex **MC3 CO THF$_3$ iso5** (Figure 39).

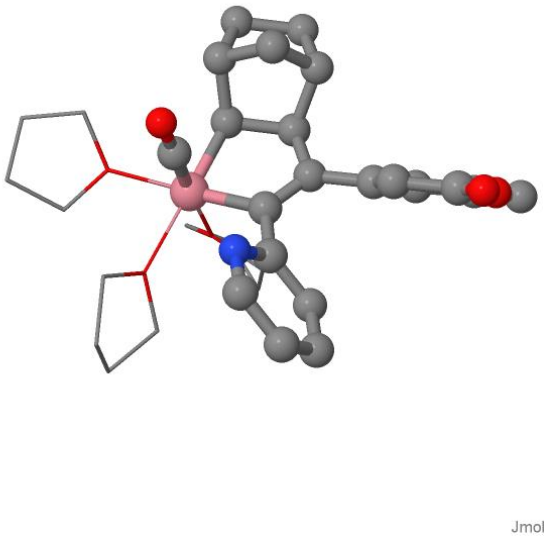

*Figure 39 - Optimised geometry of **MC3 CO2 THF$_3$ iso5.** H atoms omitted and THF groups modelled as wireframes for clarity.*

The insertion of the carbonyl into the 5-membered cobaltacycle occurs analogously as well, with the carbonyl highly energetically favoured to insert adjacent to the norbornene via transition state **TS34 THF3 iso4** (Figure 40), and be situated in the axial position of the resulting square pyramidal complex **MC4 THF3 iso12** (Figure 41).

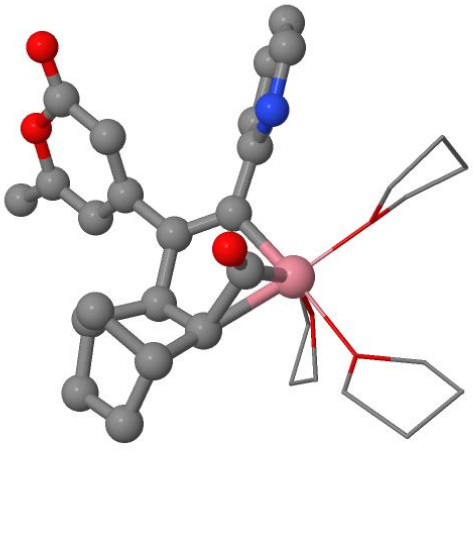

*Figure 40 – The optimised geometry of **MC TS34 iso4.** H atoms omitted and THF groups modelled as wireframes for clarity.*

In this complex a further interaction from the nitrogen in the pyridyl ring can be identified, filling the vacant co-ordination site at the base of the pyramid to give a pseudo-octahedral structure. This coordination lowers the energy of the α pyridyl intermediate by 24 kJ mol^{-1} compared to the β pyridyl analogue, which is unable to display similar coordination due to the altered position of the pyridyl group in the ring (Scheme 64).

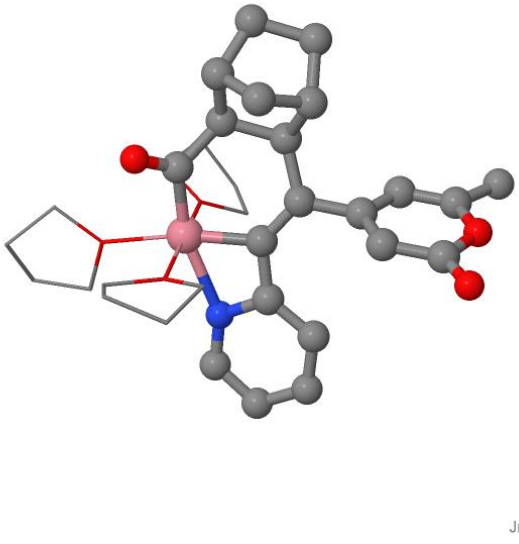

*Figure 41 - The optimised geometry of **MC4 THF3 iso12.** H atoms omitted and THF groups modelled as wireframes for clarity.*

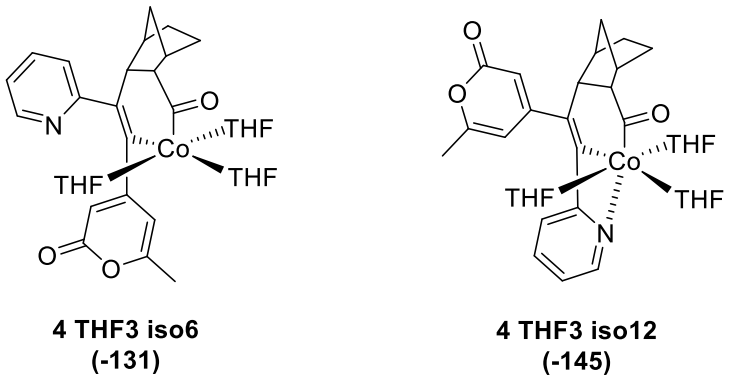

*Scheme 64 - Comparison of the lowest energy isomer structures for **MC4 THF3** on the α and β pathways, demonstrating the ability the pyridyl nitrogen to coordinate to the cobalt in **iso12** and the associated energetic stabilisation.*

The final step of the pathway is the elimination of cobalt to form the coordinated cyclopentenone, **MC5 THF3**. As with the β pyridyl pathway, this state has a square planar geometry (Figure 42). These pathways, and the energies of other pathways, will be summarised in Section 3.6.

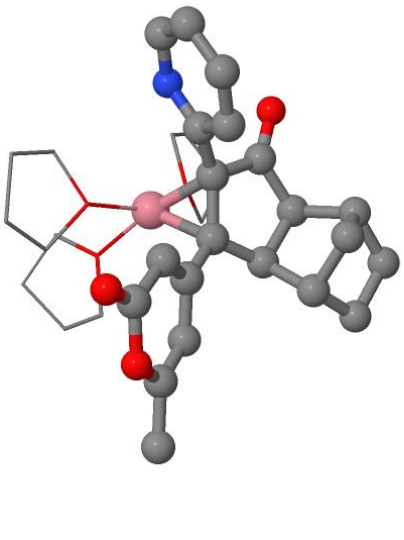

*Figure 42 - The geometry of **MC5 THF3 iso4.** H atoms omitted and THF groups modelled as wireframes for clarity.*

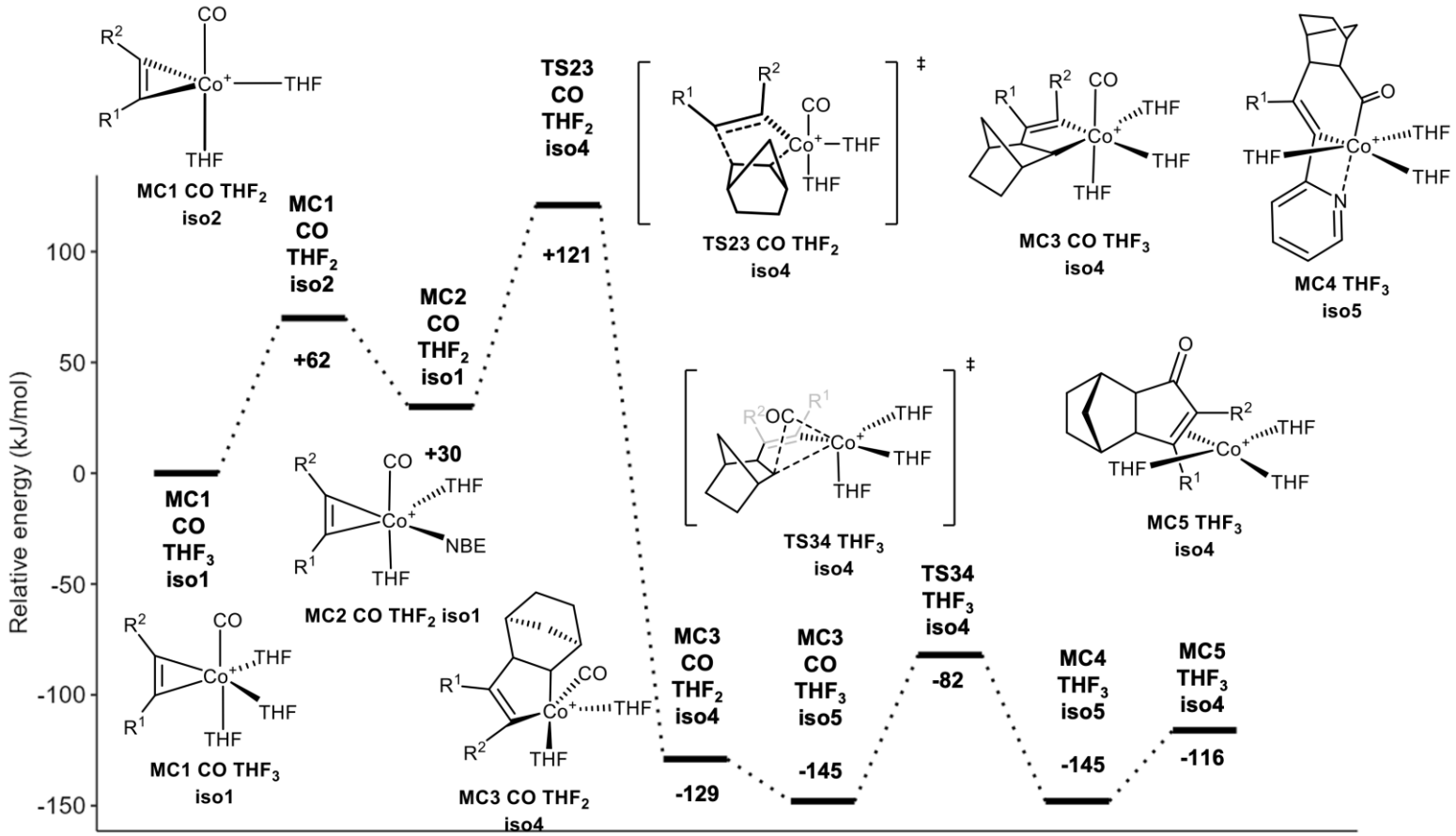

*Figure 43 - BP86/SV(P) Gibbs energies with DCM solvent and DFT-D3 dispersion correction of the monocarbonyl pathway (**MC**) to give **140α.***

3.4.3. Dicarbonyl monocobalt cationic pathways

As demonstrated in Scheme 51, the proposed disproportionation process which is thought to give rise to monometallic cobalt fragment species can lead to cationic cobalt complexes with two carbonyl ligands. Potential energy surfaces of the subsequent reaction to give cyclopentenone products were modelled. As seen in the monocarbonyl pathway, the pathways diverge based on the alkene insertion site, and sub pathways leading to both regiochemical products are considered.

The starting point for these pathways is the five-coordinate cobalt species **DC1 CO2 THF2**, which adopts a trigonal bipyramidal geometry.

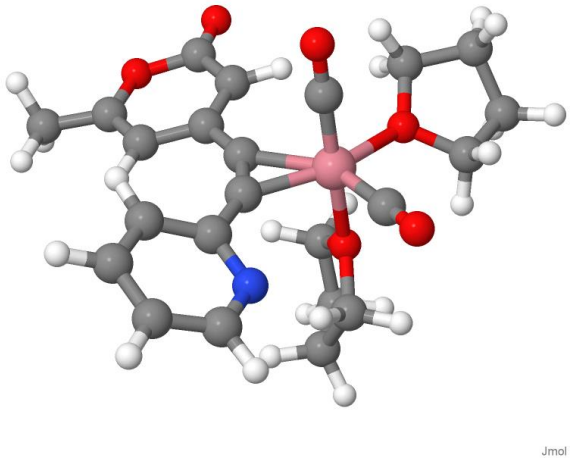

*Figure 44 - Optimised geometry of **DC1 CO2 THF2.** .*

Norbornene co-ordinates in a dissociative process, where the de-coordination of a THF leads to the unstable coordinatively unsaturated species **DC1 CO2 THF**. The minimum energy configuration of **DC1 CO_2 THF** adopts a tetrahedral geometry, and lies 84 kJ mol^{-1} above **DC1 CO_2 THF_2**. Norbornene may now coordinate, forming the trigonal bipyramidal structure **DC2 CO_2 THF**. The lowest energy isomers of this state feature the norbornene an equatorial position, with the THF occupying an axial position. As observed in the monocarbonyl pathway, there is no energetic preference for which of the alkyne groups the norbornene co-ordinates adjacent to, with both isomers being equivalent in energy.

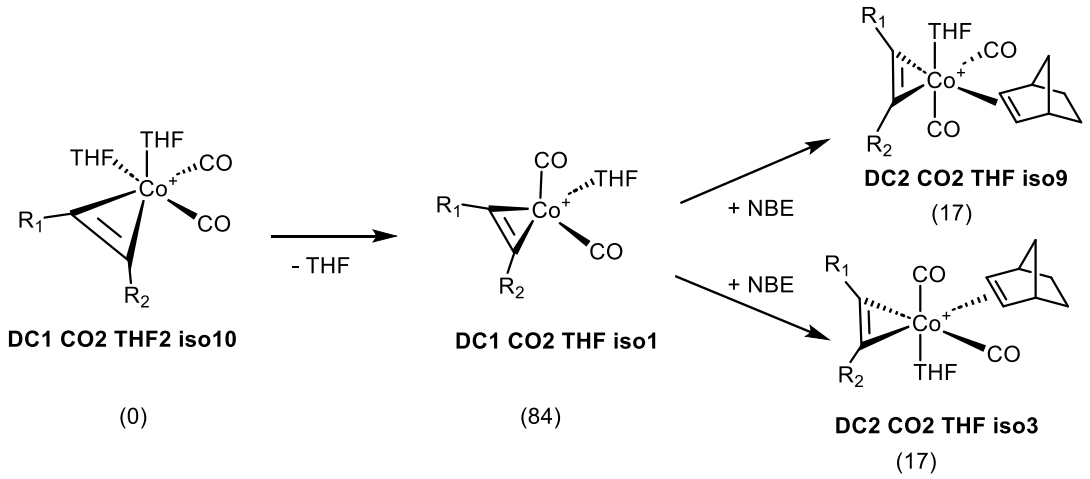

*Scheme 65 - The dissociative substitution of THF for norbornene, with energies relative to **DC1 CO2 THF2** in kJ mol^{-1}.*

The transition state for the ring formation to begin the β-pyridyl pathway lies 85 kJ mol^{-1} above **DC1 CO2 THF2 iso10.**

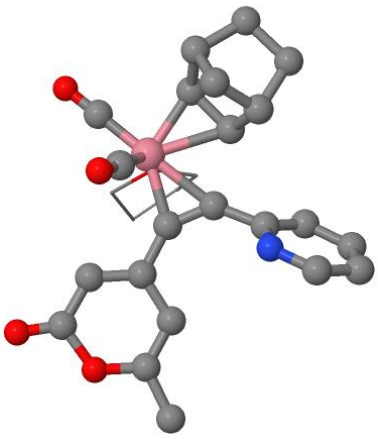

*Figure 45 - The geometry of **DCTS23 CO2 THF2** with norbornene inserting adjacent to the pyridine. H atoms omitted and THF groups modelled as wireframes for clarity.*

The resulting cobaltacycle species, **DC3 CO_2 THF**, occupies the expected square pyramidal geometry, with the norbornene-containing side of the ring occupying the axial position. The ring structure **DC3 CO_2 THF** lies 64 kJ mol^{-1} lower in energy than **DC2 CO2 THF iso9**. Coordination of a THF to the vacant site provides further stabilisation.

This energetic profile is similar to that found in calculations of the Magnus mechanism, where little to no stabilisation is gained from the formation of the ring, and it is the subsequent

coordination of another group (in the Magnus mechanism, another CO moiety) which provides the energetic stabilisation. In this case, the ring formation already represents a significant energetic stabilisation, and solvation is able to further stabilise the coordinatively unsaturated species.

From this octahedral complex, CO migratory insertion can take place to give the six membered cobaltacycle. The most energetically favourable configuration of **DC3 CO_2 THF_2** features a CO *cis* to the ring. Isomers with CO coordinated *trans* to both ring coordination sites carried a heavy energetic penalty. Due to this, CO insertion was modelled as taking place from an axial position.

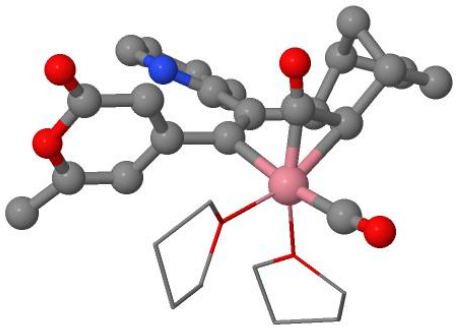

*Figure 46 – The optimised geometry of **DCTS34 CO THF_2 iso1.** H atoms omitted and THF groups modelled as wireframes for clarity.*

As expected, the lowest energy isomer of the six-membered cobaltacycle ring has the carbonyl adjacent to the norbornene, in the axial position of a square pyramidal geometry. Reductive elimination can take place directly from **DC4 CO THF_2**, yielding the tetrahedral cyclopentenone-coordinated intermediate **DC5 CO THF_2**, which results in an energetic stabilisation of 48 kJ mol^{-1}.

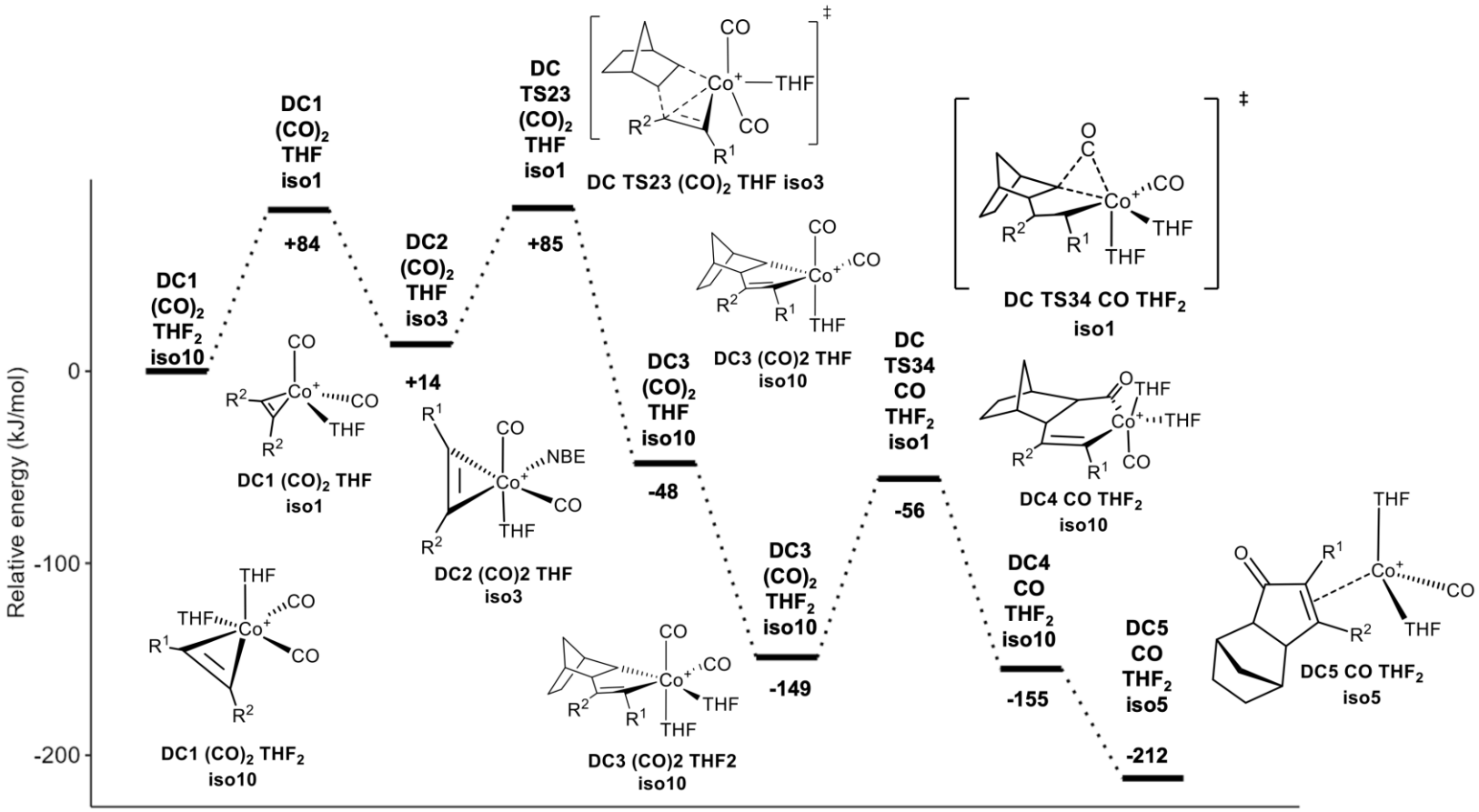

*Figure 47 BP86/SV(P) Gibbs energies with DCM solvent and DFT-D3 dispersion correction of the dicarbonyl (**DC**) pathway to give the β pyridyl product.*

As with the monocarbonyl mechanism, the alternative insertion product in the transformation from **DC2 CO_2 THF** to **DC3 CO_2 THF** can also be considered, modelling the norbornene inserting adjacent to the pyrone group, placing the pyridyl group in the α position of the final reaction product. The lowest energy isomer of **DC3 CO_2 THF** in this case is **iso 7**¸which lies significantly lower in energy (40 kJ mol^{-1}) than its counterpart in the β pyridyl mechanism (**iso 10**). This stabilisation arises from the coordination of the pyridyl nitrogen atom onto the cobalt centre, filling the vacant coordination site at the base of the pyramidal structure (Figure 48).

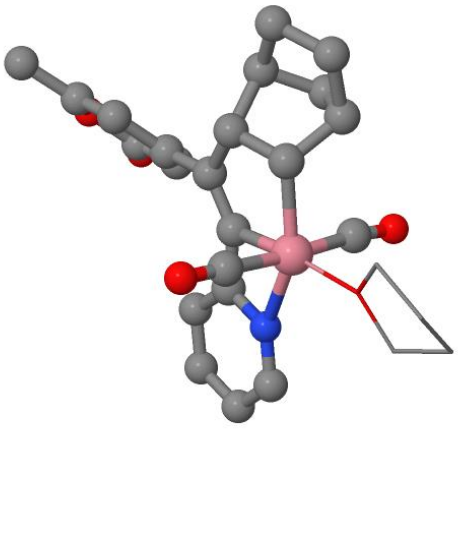

Figure 48 – The structure of ***DC3 CO_2 THF iso7****¸showing coordination from the pyridyl group in the α position of the ring. H atoms omitted and THF groups modelled as wireframes for clarity.*

As seen in the monocarbonyl pathway, THF outcompetes the pyridyl group binding to the metal centre, with THF coordination to form **DC3 CO_2 THF iso7** representing a 40 kJ mol^{-1} stabilisation. Migratory CO insertion occurs from this coordinatively saturated state, yielding **DC4 CO THF_2**, which similarly features a pyridyl group interaction to render the cobalt complex geometry *pseudo*-octahedral. Finally, the cobalt atom is ejected from the ring, forming **DC5 CO THF_2.** For a summary and comparison of these pathways with other related pathways, see Section 3.6.

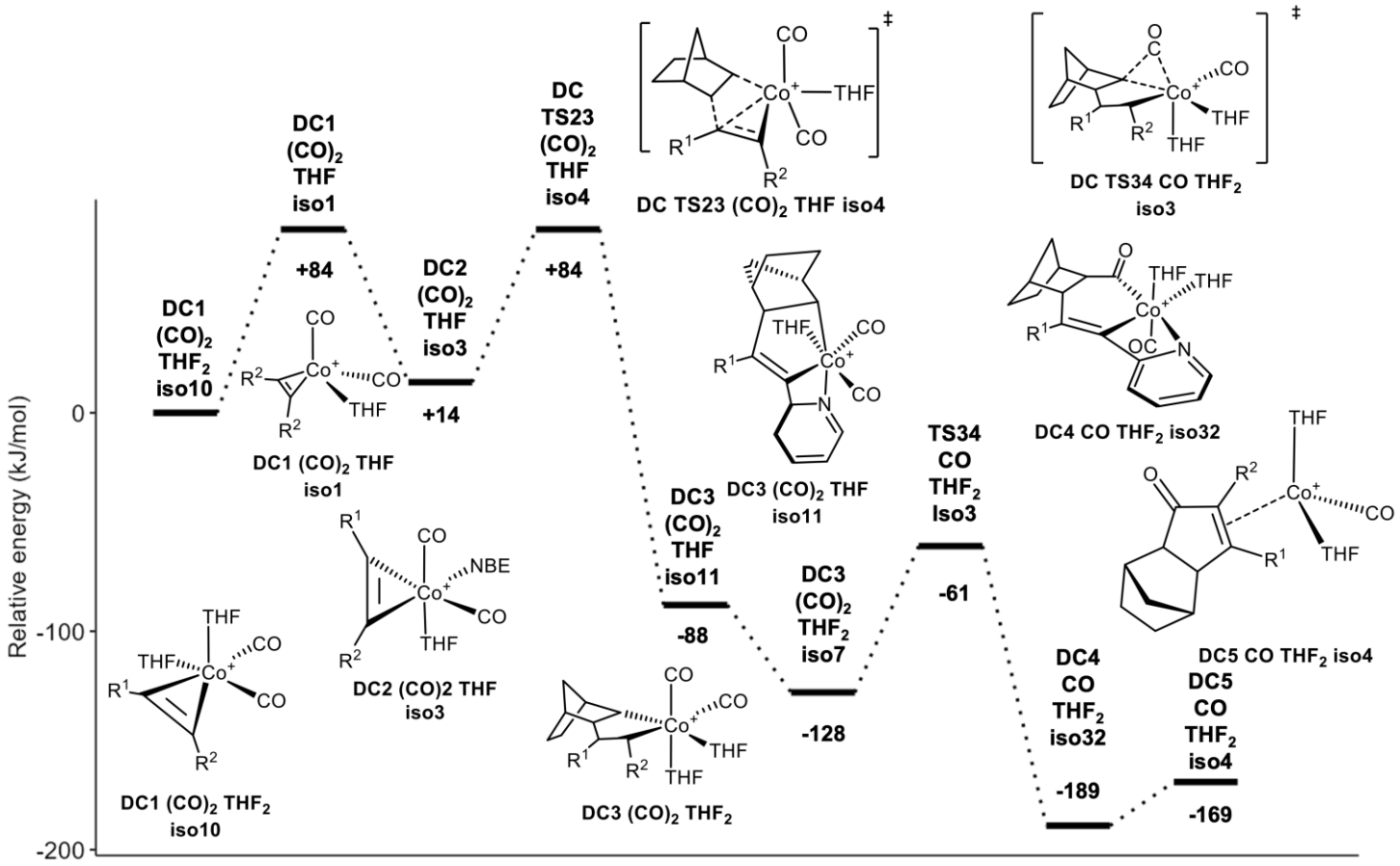

Figure 49 - BP86/SV(P) Gibbs energies with DCM solvent and DFT-D3 dispersion correction of the dicarbonyl pathway to give the α-pyridyl product.

3.5. Modelling of the Magnus pathway with relevant substituents

During the course of the investigation, it became apparent that to date there is little in the way of full energy-surface modelling of intermolecular Magnus-type reactivity with bulkier, more realistic, substituents in the literature. Yamanaka and Nakamura's seminal initial investigation of the mechanism used acetylene and ethene as substituents. While expedient with regard to computational resources, these reagents do not very accurately represent the substrates seen in the majority of PKRs performed. Especially the alkene, ethene, is not similar to the strained cyclic alkenes often employed in these transformations. As discussed previously, strained alkenes are more active than their unstrained counterparts due to the effects of ring strain on frontier molecular orbital characteristics.[20] Similarly, a sterically minimal and symmetrical alkyne is not particularly analogous to the complex heterocyclic substrates which the PKR is often employed to react with in total synthesis applications. While individual steps have been subjected to in-depth theoretical analysis, full potential energy surfaces for more chemically diverse intermolecular systems remain underexplored.

To address this, the Magnus mechanism was modelled using the reactants from the model system, to facilitate an accurate comparison of the bimetallic and monometallic pathways. To facilitate comparison, the mechanism was surveyed with the CO-loss product **CP2** as the starting point.

In this case, CO loss can occur from either an equatorial or axial position. With an unsymmetrical alkyne, the two *pseudo*-equatorial sites are distinct, and can be described as *cis* and *trans* to an alkyne substituent (Scheme 66).

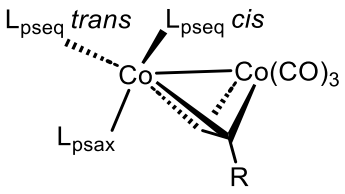

Scheme 66 - Designation of the cis and trans coordination sites with respect to group R.

In this case, loss of the pseudoequatorial CO *trans* to the pyridyl group was found to be marginally more favourable than the loss of the CO *trans* to the pyrone. Loss of the pseudoaxial CO was the least favourable, lying around 45 kJ mol^{-1} higher in energy than the other states (Scheme 67).

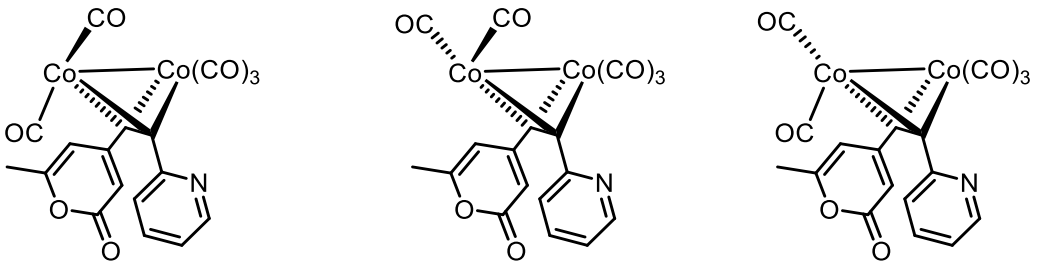

iso1 (0) **iso2** (+44) **iso3** (+8)

*Scheme 67 - The surveyed isomers of CO-loss product **CP2**, with relative energies given in kJ mol^{-1}.*

Following the findings of Gimbert and Greene[13], it is clear that that regardless of alkene co-ordination site, the barrier to rotation in alkene-coordinated complexes is easily surpassed at room temperature, leading to the insertion site being dictated by the energetics of the bound alkyne state **CP3**, and the transition state to form the initial cobaltacycle (**TS45**), instead of the initial coordination location of the alkene. In this case, the most energetically favourable coordination site of the norbornene was found to be in the pseudoaxial position on the cobalt (Scheme 68) implying that coordination takes place at the vacant site at the *trans*-pseudoequatorial site to the pyridyl ring, followed by a pseudorotation to give the axially coordinated isomer of **CP3**.

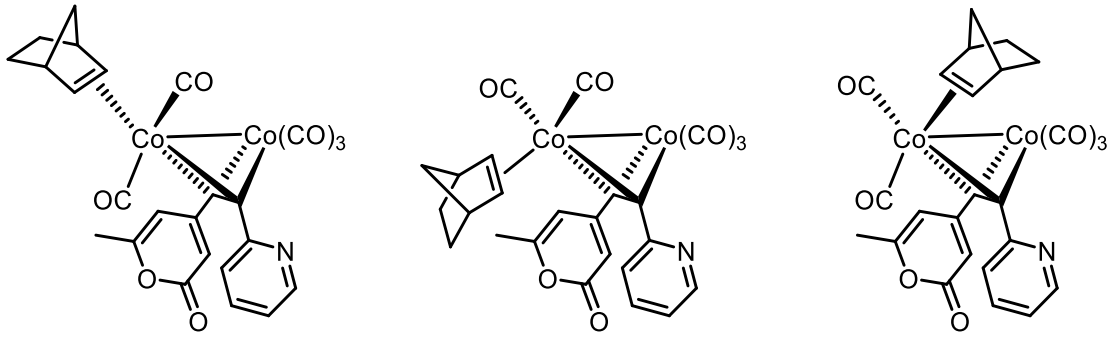

iso1 (-66) **iso2** (-80) **iso3** (-36)

*Scheme 68 - The isomers of norbornene-coordinated intermediate **CP3**, with relative energies to **CP2 iso1** given in kJ mol^{-1}.*

The axially-coordinated isomer of **CP3** features a slight deviation from the eclipsed carbonyl geometry that would be expected from a symmetric coordination. The dihedral angle between the pseudoequatorial carbonyl groups in the pentacarbonyl alkene-coordinated complex is on average 20.9°, compared to 14.3° in the hexacarbonyl complex. The driving force for this break from planarity is the interaction between the pyridyl nitrogen and the alkene carbon on the

norbornene, 'dragging' the group away from the centered pseudoaxial position and towards the pyridyl substituent.

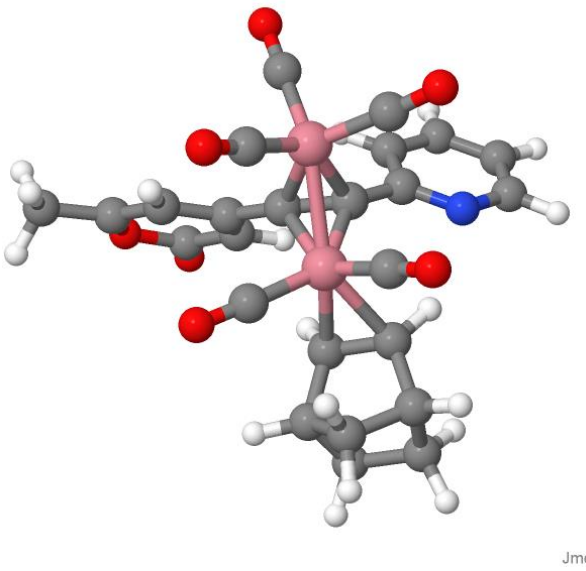

*Figure 50 - Optimised geometry of **CP3** featuring norbornene in the pseudoaxial position, displaying bending away from centre towards the pyridyl ring.*

This interaction may contribute to the selectivity for the β-position exhibited by the pyridyl group, as stabilisation of the norbornene inserting adjacent to the pyridyl group would favour the mechanism leading to the β-pyridyl isomer of the final cyclopentenone ring. However, we can also consider the isomer of **CP3** which features norbornene coordinated in the *cis*-pseudoequatorial position relative to the pyridyl, a geometry which maximises the potential for this interaction. The optimised geometry for this interaction does indeed show alignment of the pyridyl nitrogen towards the norbornene alkene proton, and a relatively favourable N-H distance for interaction (2.25 Å). However, the energy of this isomer lies significantly (45 kJ mol^{-1}) above that of the axially-coordinated isomer, and somewhat (28 kJ mol^{-1}) above coordination in the *trans*-pseudoequatorial site. While these interactions are capable of perturbing geometry, they do not confer sufficient energetic stabilisation to render the *cis*-pseudoequatorial position favourable for alkene coordination. As such, it is not clear how the presence of this interaction would contribute to the experimentally observed selectivity.

The initial cobaltacycle formation to form **CP4** was modelled as the insertion of norbornene from the axial position on the cobalt. There are two possible locations for insertion in this case, one adjacent to each alkyne R group, which will lead to different regioisomers. Insertion of norbornene adjacent to the pyridyl group will lead to the β-pyridyl isomer. In this case, the axial-insertion transition state lies 90 kJ mol^{-1} higher in energy than **CP3**, with the formation of a bond

between the alkyne carbon adjacent to the pyridyl ring and an alkene carbon on the norbornene. Geometrically, the transition state features a rotation of all three groups on the cobalt centre, replacing the eclipsed arrangement of groups seen in **CP3** with a staggered arrangement. This allows for the norbornene alkynyl bond to align with the Co-C-C plane formed by the cobalt atom and the acetylenic carbons on the alkyne, facilitating insertion. Due to the concerted movement of all three groups, this transition state can proceed directly from the axially coordinated (and energetically favourable) isomer of **CP3 (iso2)**.

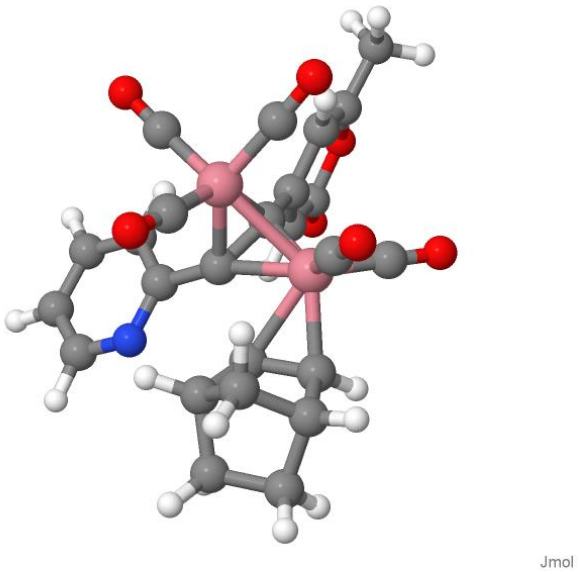

*Figure 51 - The optimised geometry of **TS34 iso1**, with insertion adjacent to the pyridyl group.*

The resulting state of this ring formation is the five membered cobaltacycle **CP4** which lies 10 kJ mol^{-1} higher in energy than **CP3**. This finding was unusual, as generally the **CP3** → **CP4** transformation is considered to be thermoneutral. Insertion from the energetically unfavourable *cis-pseudo*equatorial position adjacent to the pyrone was found to be thermoneutral, Insertion from a *pseudo*equatorial position, is the same as that modelled by Yamanaka and Nakamura, who did not consider alkene rotation to give coordination at an axial position in their potential energy surface. When this rotation is taken into account, the energetics of the initial ring formation step can differ from those observed by Yamanaka and Nakamura.

Similarly to the findings of Yamanaka and Nakamura, the co-ordination of a further CO ligand to give **CP5** represents a large energetic stabilisation, with **CP5** lying 92 kJ mol^{-1} lower in energy than **CP4.** This step of the mechanism represents the first major energetic gain of the reaction, and is proposed to be the step which leads to the mechanism being fast and irreversible.

From **CP5** carbonyl insertion may now take place. While insertion can happen adjacent to the alkene or alkyne side of the ring from the cobalt centre, is has been assumed since the proposal of the Magnus mechanism that this insertion occurs adjacent to the alkene.

The calculated energies of the intermediates support this assumption, with the resulting alkene adjacent insertion product isomer 64 kJ mol^{-1} lower in energy than the alkyne adjacent counterpart. The transition state, **TS56** consists of the migratory insertion of a pseudoaxial carbonyl into the Co-C bond with an activation barrier 66 kJ mol^{-1} above **CP5**.

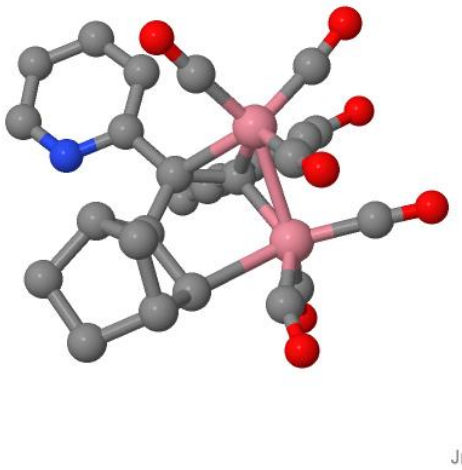

*Figure 52 - Optimised geometry of **TS56 iso1.** H atoms omitted for clarity.*

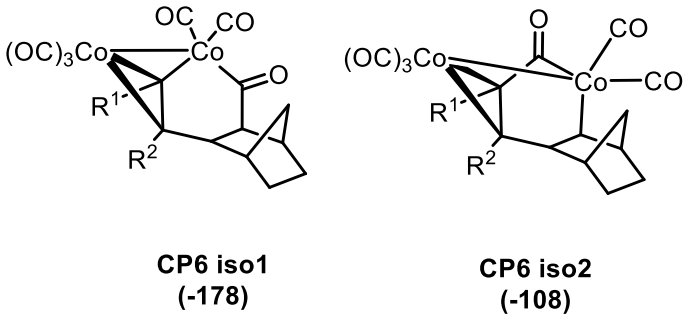

*Figure 53 - Structures and energies of **CP6 iso1** and **CP6 iso2**, highlighting the energetic preference for carbonyl insertion adjacent to the alkene.*

The resulting complex **CP6** features an unsaturated ligand sphere at the mechanistically active cobalt centre, and undergoes coordination of a carbonyl ligand to form **CP7**. In this intermediate, the pyridyl nitrogen begins to interact with the carbonyl ligands on the spectator cobalt, pulling one away from the metal centre into a bridging position.

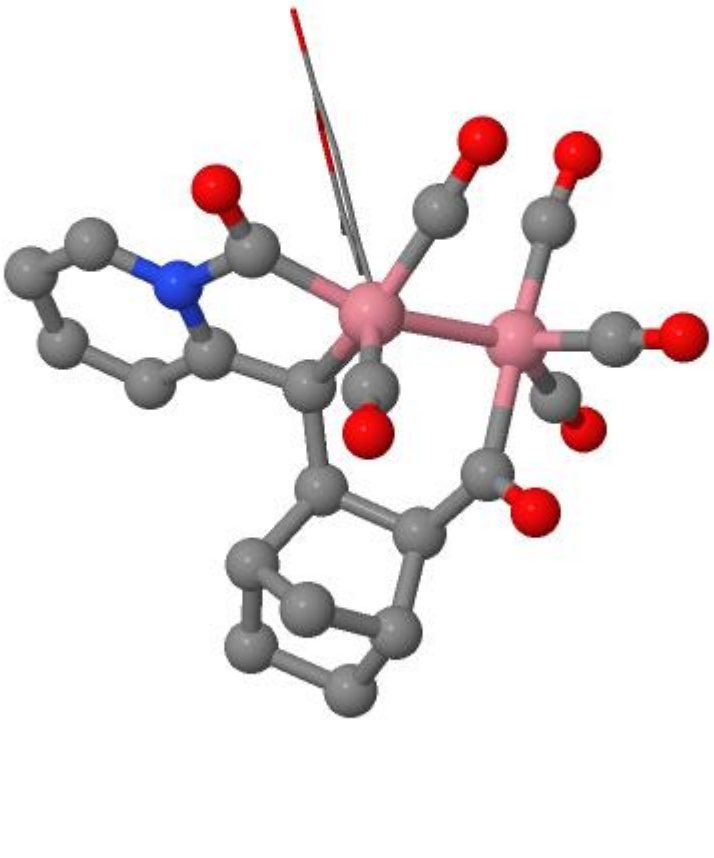

*Figure 54 - The optimised geometry of **CP7** with the pyridyl group in the β position, showing the interaction between the pyridyl nitrogen and a carbonyl ligand. Pyrone group represented as wireframe for clarity.*

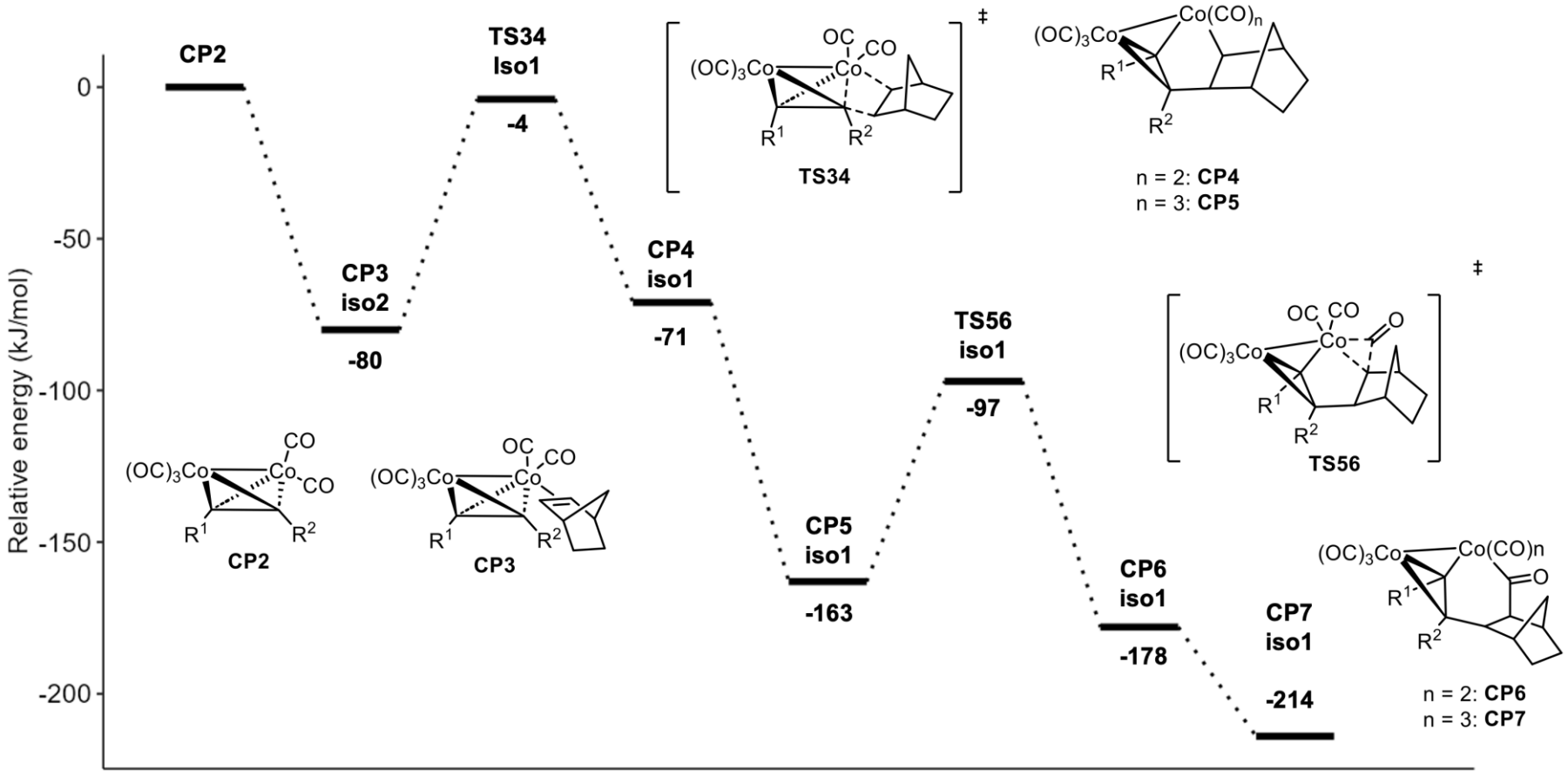

Figure 55 - BP86/SV(P) Gibbs energies with DCM solvent and DFT-D3 dispersion correction of Magnus pathway to give the β pyridyl product.

Alternatively, insertion to **CP4** can proceed adjacent to the pyrone group, leading down the pathway towards the α-pyridyl product. The transition state for this insertion, **TS34**, was found to be essentially isoenergetic with the insertion transition state for the β-pyridyl pathway, implying that while pyridine-alkene interactions are present in the complexation steps of the Magnus mechanism, they do not seem to confer any stability to the transition states, and thus do not influence regioselectivity in this mechanistic pathway.

Similarly, the resulting cobaltacycle product **CP4 iso2**, is slightly more unfavourable, lying 14 kJ mol^{-1} higher in energy than the β-pyridyl pathway analogue **CP4 iso1**. The subsequent coordination of a CO ligand to form **CP5** provides stabilisation of 95 kJ mol^{-1}. The migratory insertion transition state of a carbonyl adjacent to the norbornene is similar in energy relative to the equivalent transition state in the α pyridyl pathway, but due higher energy α pyridyl isomer of **CP5** the activation energy for this step is actually lower than in the β pyridyl pathway. The subsequent steps are essentially equal in energy to the β pyridyl pathway.

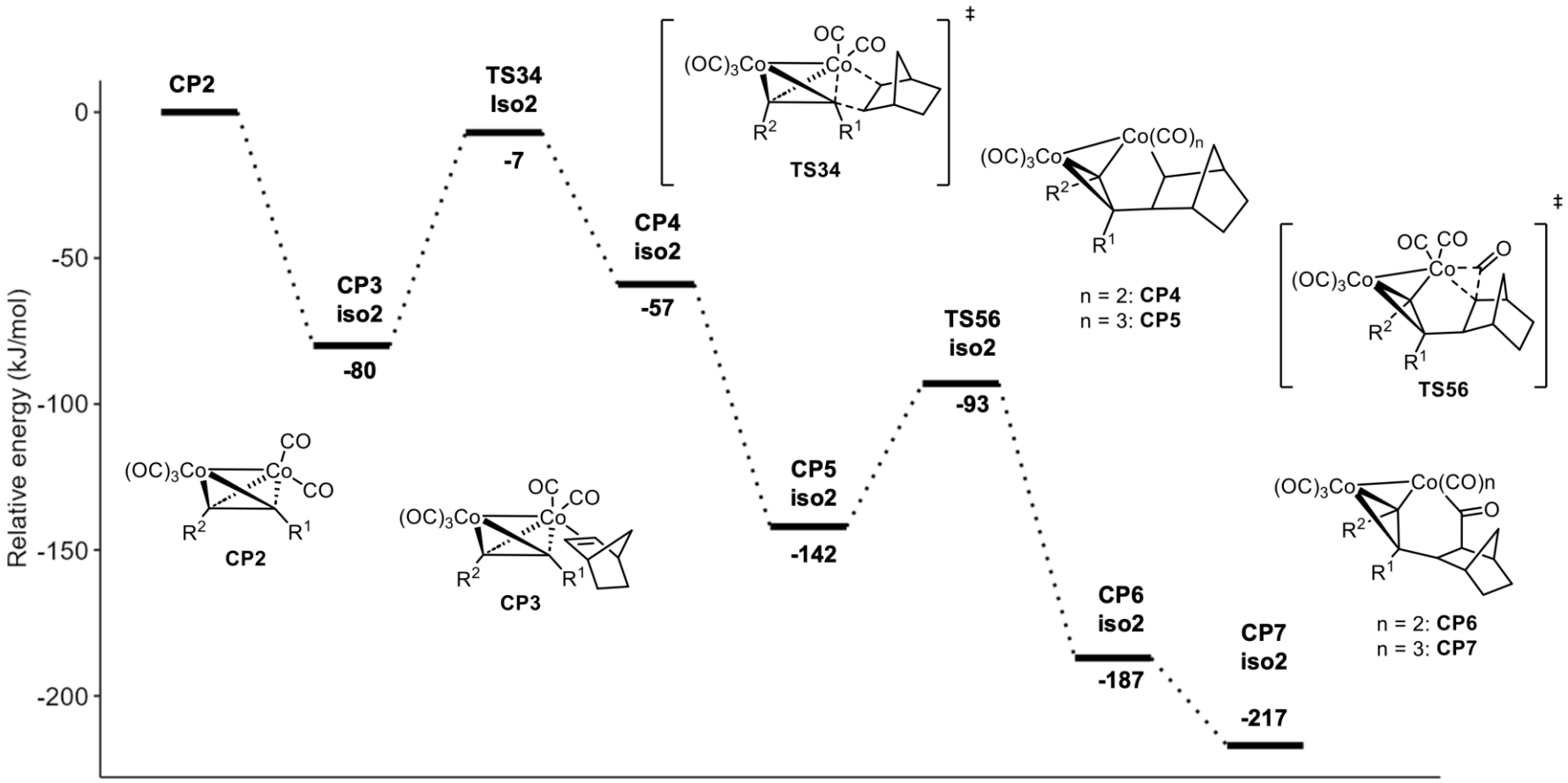

Figure 56 - BP86/SV(P) Gibbs energies with DCM solvent and DFT-D3 dispersion correction of Magnus pathway to give the α pyridyl product.

3.6. Comparison of the calculated pathways

With the energy surfaces of the predicted pathways calculated, the different energy pathways could be compared. Overall, the pathways all contain the same essential sequence of steps, conserving features of norbornene coordination, formation of a five-membered cobaltacycle, insertion of a carbonyl to give a six-membered cobaltacycle, and ejection of the cobalt to give the separated product. By comparing the energetic spans of these pathways, their relative feasibilities could be determined (Table 9).

Table 9 - Energy spans for transition states across all pathways. Spans measured as energy difference between transition state energy and lowest preceding state.

Pathway	Intermediate	Transition state	Energy span (kJ/mol^{-1})
Monocarbonyl β	**MC1 CO THF_3**	**TS23**	**124**
Monocarbonyl α	**MC1 CO THF_3**	**TS23**	**121**
Dicarbonyl β	**DC3 CO_2 THF_2**	**TS34**	**93**
Dicarbonyl α	**DC1 CO_2 THF**	**TS23**	**84**
Magnus β	**CP2**	**TS34**	**76**
Magnus α	**CP2**	**TS34**	**73**

In all pathways, initial ring formation to give the five-membered cobaltacycle represents a significant energetic barrier, and generally proves the differentiating factor between the feasibility of the pathways. The exception to this trend is the dicarbonyl β-pyridyl pathway, where the insertion of the carbonyl into the ring (**TS34**) is the rate-determining state. Cobaltacycle formation had the smallest activation energy in the Magnus pathways, and the highest in the monocarbonyl pathways, all within the region of 70-125 kJ mol^{-1}. Based on these activation parameters, the dicarbonyl mechanism appears to be the more favourable of the two monometallic pathways put forward. Overall, the energetic span of the Magnus mechanism is the most favourable, with a span of 73 or 76 kJ mol^{-1} between **CP3** and **TS34** for the β and α pathways respectively (compared to 84 and 93 for the dicarbonyl monocobalt pathways). The observed trend in reactivity (dimetallic being more favoured than monometallic) is in agreement with the findings of Hartline and co-workers, who characterised and compared reactivity around a di- and mono-nickel centres constructed as analogues of dicobalt PKR catalytic centres (discussed in detail in section 1.7).[19] The investigation found that substrates which readily reacted with a di-nickel system were

inactive when applied to a mono-nickel system, and even activated substrates reacted slowly and in low yield. The results presented here suggest that a similar reactivity trend may be present in a cobalt system, and that reaction around a monocobalt center is feasible, but disfavoured relative to a dicobalt-centred process.

Following the formation of the first cobaltacycle, all reactions proceed with a general downwards trajectory energetically. As has been noted often in reference to the Magnus mechanism, this downward trend in energies signifies rapid formation of the product once the slow initial step has been accomplished. It is likely, therefore, that the metal carbonyl vibrational bands observed in the *in-situ* IR experiments result from a pre-coordination and -cyclisation species, as intermediates following this step will be too short-lived to be observed on the IR timescale. This is supported by the observation that the newly-observed metal-carbonyl IR bands can form following NMO promotion in the absence of alkene. This theory goes some way to explain the observation that increasing the stoichiometry of NMO in this case does not affect conversion. As CO loss is thought to be facile and rapid with amine N-oxide promotion, in this system it is unlikely to be the rate-limiting step as it often is found to be in the PKR. Instead, as demonstrated by the potential energy surfaces in this chapter, the slow rate-limiting step for these reactions, in both Magnus and non-Magnus pathways, is the formation of the initial cobaltacycle. This step is unaffected by NMO stoichiometry, and the activation energies calculated for the Magnus and monometallic monocarbonyl mechanisms estimate that it would proceed slowly at room temperature, explaining the experimentally observed low amounts of product formation. Thus, on the timescales that these reactions are being observed, the amount of CO-loss product following NMO addition is not exhausted by the end of the experiment. Application of heating, as is often applied, should increase the energy available to the system to overcome the energy barrier to proceed from the CO-loss product to the cobaltacycle product, increasing conversion.

3.7. The effect of the 2-pyridyl group in calculated pathways

Following observations in Chapter 2, it was hypothesised that an attractive interaction between the pyridyl nitrogen and the alkene may lead to the observed regioselectivity. This investigation has revealed that the pyridyl group does not confer any influence on geometry to the cobalt-alkyne complexes, but can form interactions which can influence the geometry of the calculated intermediate structures. The relative approach complexes of norbornene adjacent to each alkyne substituent are found to be essentially energetically equal in all

calculated pathways, indicating that there is no energetic bias to favour norbornene coordination adjacent to either group.

Notable interactions originating from the pyridyl nitrogen are present in the simulated monometallic pathways, where the pyridine nitrogen is in a position to coordinate to the cobalt centre following cobaltacycle formation, with a significant stabilising effect. However, these interactions are only present in the α-pyridyl pathways, which would imply that these effects would lead to a selectivity for the α-pyridyl product, the inverse of what is observed experimentally. Crucially, though, the states which benefit from these pyridine-cobalt interactions are after the regioselectivity has been determined in the **TS23** cobaltacycle formation step, meaning that the observed coordination will not influence regioisomer distribution. In the Magnus mechanism, interactions can be seen prior to the first cobaltacycle formation step, with the alkene coordination position in the pseudoaxial site offset toward the pyridyl group, similar to the interaction proposed in Scheme 44. However, this interaction is not present in the transition state for cobaltacycle formation, leading to the two transition states being isoenergetic (Scheme 69). These observations suggest that while an interaction is certainly possible between the pyridine and the alkyne, there is no suggestion from these calculations that the interaction is regiochemistry-defining. Thus, the impact of pyridyl substitution on the regiochemistry is still undetermined.

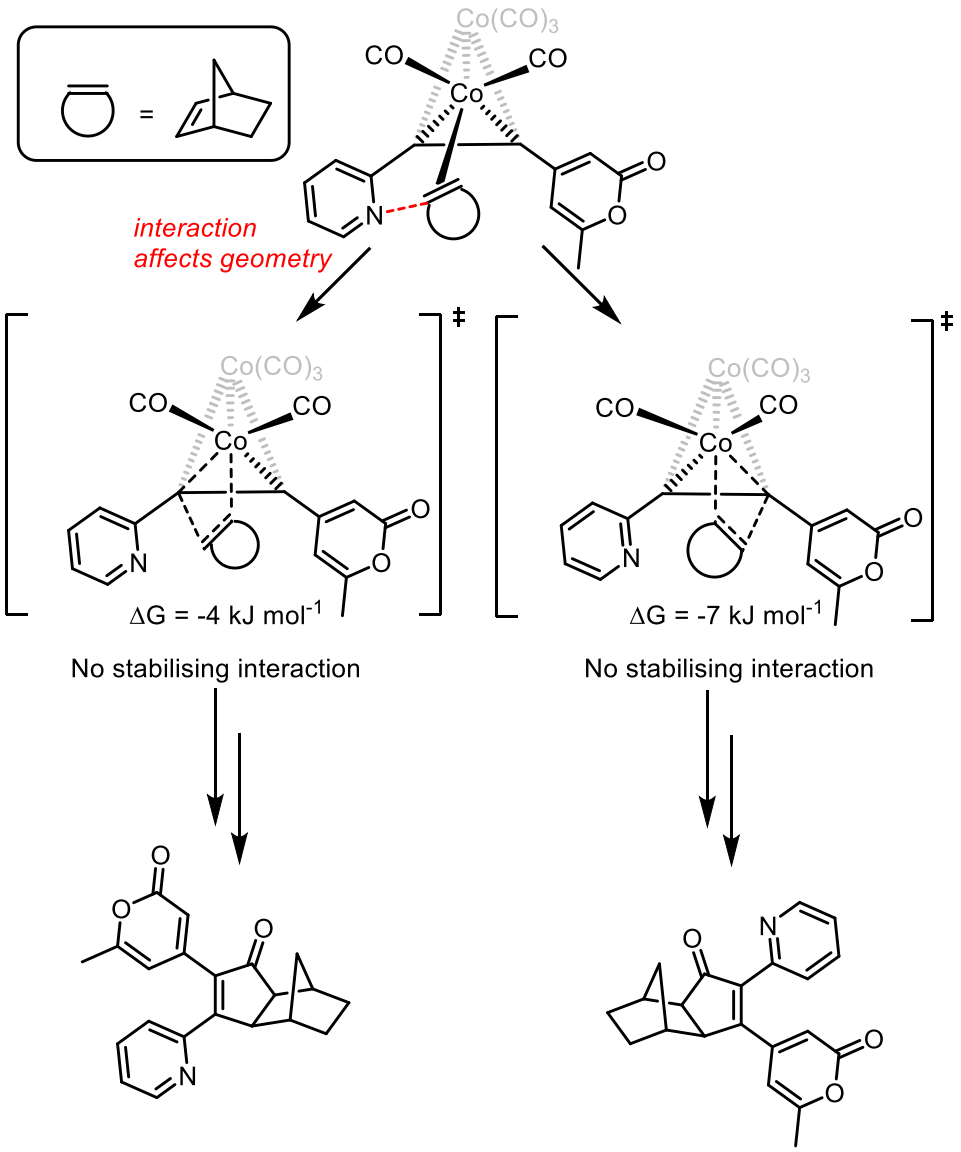

Scheme 69 – Effect on geometry and energetics of observed interaction between pyridyl nitrogen and alkene found in this investigation.

3.8. Summary and Conclusions

Investigations with a model system have demonstrated that *in-situ* FTIR monitoring is a powerful technique for the monitoring of the PKR, suitable for the detection of unstable and non-isolable species within the reaction mixture, which would be challenging or impossible to analyse by other methods. DFT investigations were then able to provide insight to the experimental observations and construct PESs for alternative reaction pathways. The PES of the Magnus mechanism was calculated using the substituents from the model system, and the energy pathways compared. It was found that pathways proceeding via monometallic cationic cobalt complexes had higher activation barriers than the Magnus mechanism,

showing that reactivity via a monocobalt pathway is not likely to outcompete dicobalt-based pathways. The immediate disappearance of bands associated with complex **141** following NMO addition implies that the activation of **141** by NMO is an immediate, and not a gradual process. As product evolution is slow, this implies that there must be a state which exists between carbonyl dissociation and the alkene coordination which leads to further reaction. In the Magnus mechanism, this state is **CP2**, the pentacarbonyl cobalt alkyne complex. The work presented here suggests that there is a breakdown process which follows NMO activation to form the ionic system, which may represent a more stable configuration than **CP2**.

The onward reactivity of the system may then proceed through multiple different pathways, which can currently only be hypothesised. The mechanism of the onward reaction is dependent on the speciation of cobalt within the reaction system. Comparison of the PESs of the monocobalt pathways with the Magnus pathway show that the monocobalt pathways are less energetically favourable, and that if the speciation of the system included both monocobalt and dicobalt complexes, the Magnus reactivity would dominate. Experimentally, it has been shown that the formation of product **140** is still observed when the alkene is added following NMO addition and the exclusion of all signals for **141** in the reaction mixture, implying that no dicobalt species are present in solution at this time. The availability of the Magnus pathways in this case, therefore, is dependent on the ability of the ionic system to recombine into **CP2** (Scheme 70). A recombination of this type is implicit in the reformation of complex **141** when free CO is present in the system, but the ability of the ionic system to recombine in the absence of CO is currently unknown. If CO coordination was required prior to cobalt-cobalt bond formation, the recombination pathway would only be accessible with free CO present in the system, and **CP2** is not likely to be formed, essentially rendering the cobalt-cobalt separation irreversible. If this were the case, the only onward reactivity with norbornene available to the system would be the monocobalt-centred pathways. Conversely, however, if cobalt-cobalt bond formation to form **CP2** occurs prior to CO coordination, this would mean that the ionic species and **CP2** would be in equilibrium, enabling access to Magnus reactivity.

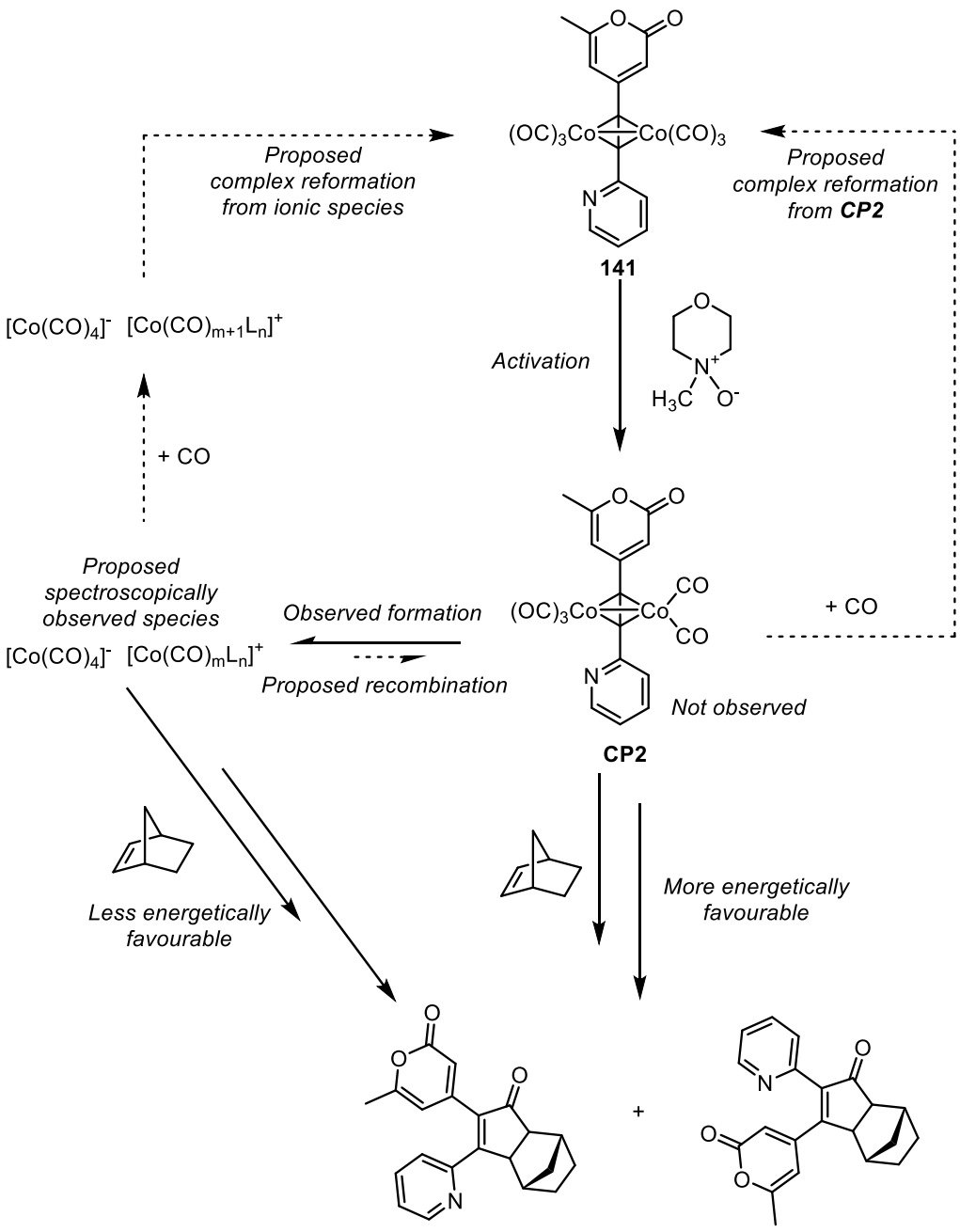

*Scheme 70 - The proposed mechanism onward reaction pathways following activation of complex **141**.*

Questions about the exact nature of electronic effects on the regioselectivity of the intermolecular PKR still remain unanswered, but observations of the interaction of the 2-pyridyl group with ligands and metal centres in calculated theoretical intermediate geometries highlights that pyridyl coordination to incoming substrates or the metal is possible. While sterically bulky or coordinating groups on the alkene coupling partner are well-documented to exert regiocontrol over the system,[6,8] the result of similar coordination behaviour from the alkyne remains unexplored. It is clear from this work, however, that the

alkyne coordinating groups are able to participate in interactions with both the alkene and the metal centre during the mechanistic pathway.

Chapter 4: Ultrafast time-resolved infrared spectroscopy with cobalt and molybdenum alkynyl complexes

4.1. Background

4.1.1. Time resolved IR spectroscopy.

Time-resolved ultrafast IR spectroscopy is a spectroscopic technique that can offer unique mechanistic insights, directly observing events on a timescale ranging from picoseconds to microseconds. Time-resolved multiple probe spectroscopy (TR^MPS) uses a synchronised pump-probe method to collect time-resolved data; one laser pulse (the pump) causes a photochemical activation in the sample, and a second pulse (the probe) is used to spectroscopically interrogate the nature of the resulting photoproducts.[134] By sequentially carrying out multiple pulses, and varying the time between the pump and probe pulses, a series of spectra can be obtained across multiple time points.

Collected time-resolved difference spectra can be used to monitor the species in the sample at the time of reaction, and construct "real time" timelines of mechanistic events. The wavelength of the pump irradiation can be adjusted to allow for excitation of different electronic transitions within the sample. Changing the probe allows for monitoring of different spectroscopic features (such as absorption in the IR or UV-Vis regions of the spectrum). TR^MPS is often carried out using a UV-pump/IR-probe setup. Excitation of the target molecules takes place in the UV-visible region, and IR transmission spectra are recorded at multiple time points.

The data recorded from such experiments is often presented in the form of difference spectra. The IR spectrum recorded is based on the change in absorption at each measured position in the spectrum relative to the final resting state of the experiment. Therefore, IR absorption bands of species which are lost following the pulse will manifest as negative peaks on the spectrum, referred to as bleaches. Similarly, new products formed in the ensuing reaction, which were not present pre-experiment, will appear as positive peaks on the difference spectrum, referred to as transients. These bleaches and transients can be used to gain insight into events occurring in the mechanism.

Metal carbonyl complexes are particularly attractive targets for TR^{M}PS methods, as the carbonyl groups can act as reporting groups in the resulting time-resolved IR spectra. Metal carbonyl (M-CO) peaks have very intense, high energy absorption bands compared to organic carbonyls. The high intensity is due to the strong dipole across the group, and the characteristic high energy absorption arises from back-donation from the metal centre, strengthening the C≡O oscillator. Therefore, these peaks can be easily observed by IR methods, providing a strong signal-to-noise ratio even at the short path lengths and concentrations often found in time-resolved spectroscopic setups. Secondly, photoactivation of metal carbonyls is a highly accessible and widely used initiation method for metal-catalysed reactions.[135] Generally, the photochemical dissociation of a CO ligand from a metal centre proceeds via metal-ligand charge transfer (MLCT). This process occurs when a metal complex is photoexcited, promoting an electron from a filled metal-carbonyl orbital into a vacant nonbonding orbital on the carbonyl. This carbonyl ligand, having had its bonding orbital depleted, is now able to photodissociate, leaving a vacant coordination site on the metal centre. This method of CO loss is also implicated in steady-state photochemistry, meaning that TRIR methods are an accurate way of determining the mechanism of catalytic photochemical processes.

4.1.2. The photochemical PKR.

As well as thermally or chemically promoted PKR variants, the reaction can also be carried out photochemically. Early studies showed that treatment of cobalt-alkyne complexes with light in the UV-Visible spectrum could lead to CO loss, as well as Co-Co bond homolysis.[136,137] It was found that steady-state excitation of a cobalt-alkyne complex at 532nm would lead to CO-loss, the products being identified by trapping ligands such as triphenylphosphine. Similarly, irradiation of thermally or chemically-promoted PKRs around this wavelength would enhance conversion in these cases.

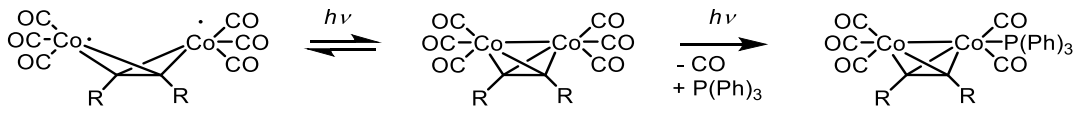

Scheme 71 - Observed steady-state photochemical behaviour of cobalt-alkyne complexes. Left: metal-metal bond homolysis. Right: CO loss with product isolated via *trapping reagent ($P(Ph)_3$)*

Later, Pryce and co-workers reported a room-temperature photochemical variant of the PKR.[138] Irradiation with broad spectrum visible light yielded moderate conversion to PKR product at room temperature.

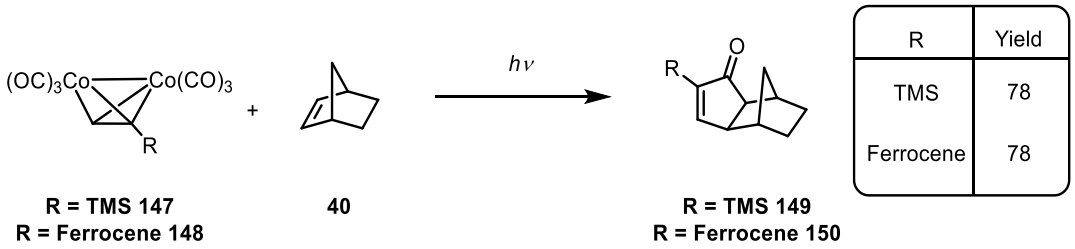

R	Yield
TMS	78
Ferrocene	78

While there has not been as much focus on photochemical promotion methods as there has been with other promotion methods such as amine N-oxides,[123] the technique has been used in certain cases. For instance, a photochemical flow reactor was demonstrated to be efficient for the synthesis of a range of cyclopentenones, with the authors remarking that such a system precluded the wastage that often arises when using stoichiometric additives, and was suitable for the production of heat-sensitive cyclopentenone products.[139]

4.1.3. Ultrafast photochemical studies on cobalt-alkyne complexes.

Time-resolved spectroscopic methods have been previously applied to cobalt-alkyne complexes by Pryce and co-workers. Following excitation at 400 nm, short lived transient peaks were observed, with lifetimes around 50-70 ps for the cobalt complexes of a series of alkynes (Figure 57).[140]

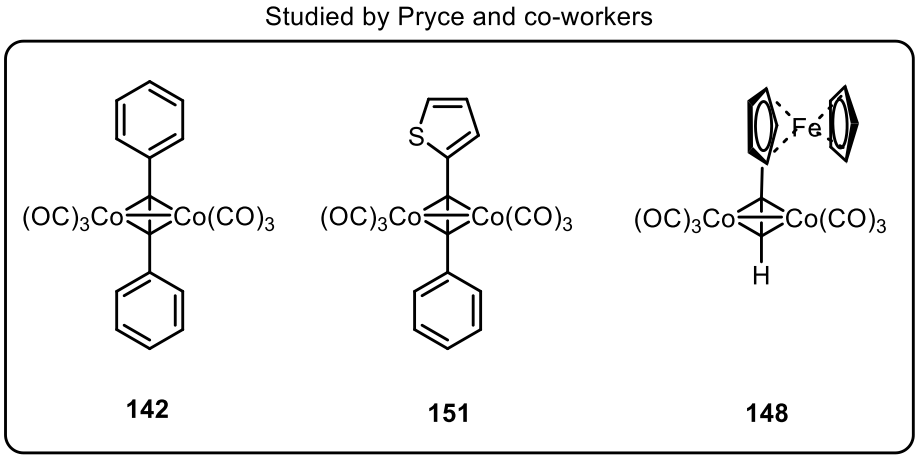

Figure 57 – Cobalt complexes surveyed by Pryce and Co-workers.

These transient peaks were assigned to a species exhibiting the lengthening of the Co-Co bond, in a short-lived breathing mode. No CO ligand dissociation was observed in these cases. These findings were unexpected, as Co complexes readily undergo photodissociation at these wavelengths in steady-state photochemical systems.[141] The lack of observed CO-loss products was assigned to the low quantum yields of this process.

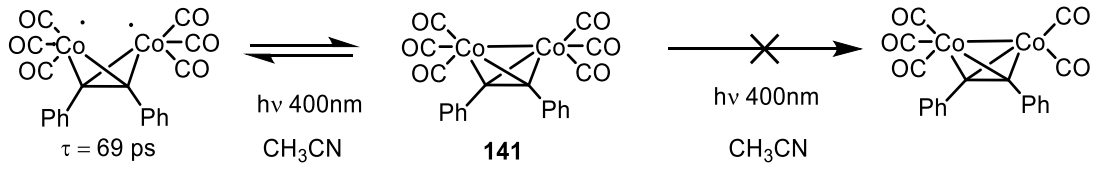

Scheme 72 – Ultrafast photochemical behaviour of cobalt-alkyne complexes as observed by Pryce and co-workers.

Insight into the accessibility of the breathing mode of the cobalt-cobalt bond is given by theoretical investigations by Platts and co-workers into the bonding character between the two cobalt centres in bimetallic dicobalt alkynyl systems.[142,143] Platts made the case that while these systems are often considered to be formally bonded metal-metal interactions, the actual bond index between the two centres is considerably less than one. The value varies based on the method employed, but was found to be 0.26 using CAS-SCF. Therefore, Platts argued, a singlet diradical characteristic might be a more suitable way to consider the electronic state of the metal centres in this case.

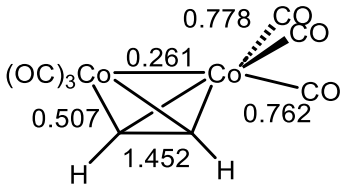

Scheme 73 - Bond orders calculated by Platts and co-workers using CAS-SCF.

More recently, Pryce and co-workers investigated the TRIR behaviour of cobalt-alkyne complexes further,[144] observing a small amount of photochemical CO loss on a picosecond timescale. The process, described as being ultrafast but highly inefficient, is measured using UV-Vis pump and IR probe methodology. The authors commented on the very low efficiency of the CO loss, and pointed out that even substrates which are very unsusceptible to ultrafast

CO photolysis are still competent mediators of light-promoted PKRs. Following this, it was suggested that perhaps the increase in length of the cobalt-cobalt bond (the most accessible excited state), and the subsequent movement into a high spin singlet diradical state, may be mechanistically relevant. The authors presented a proposed mechanism which does not proceed from CO-loss, but instead from the lengthening of the cobalt-cobalt bond causing the excited cobalt-alkyne species to be capable of undergoing alkene coordination and insertion. The high-spin nature of the proposed photoproduct is shown to stabilise the alkyne insertion step.

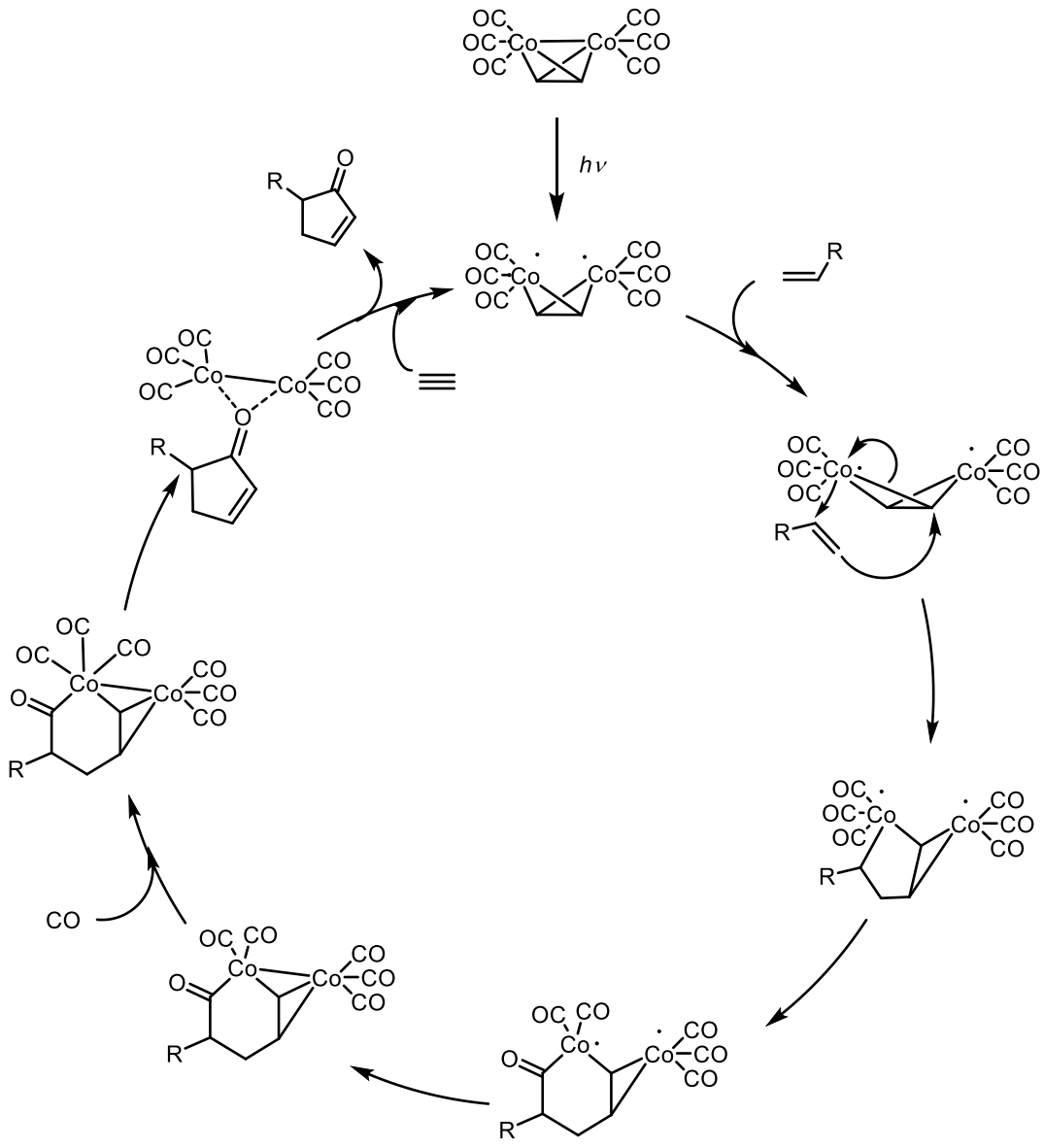

Scheme 74 - The proposed photochemical PKR mechanism by Pryce and co-workers, initiated by bond homolysis in place of carbonyl dissociation.

4.1.4. Molybdenum-mediated PKRs.

Among the many metals applied in the PKR, molybdenum has been used in several applications to form cyclopentenone products. Hanoaka and co-workers demonstrated how a molybdenum dicyclopentadienyl alkyne complex (structurally analogous to a cobalt-alkyne complex as the $CpMo(CO)_2$ and $Co(CO)_3$ groups are isolobal) is capable of reacting with norbornene to give cyclopentenones.[145] Interestingly, they note, when terminal alkynes are used in this system, the usual exclusive selectivity of the bulky group for the cyclopentenone 2-position is not apparent, and a mix of regioisomers is obtained.

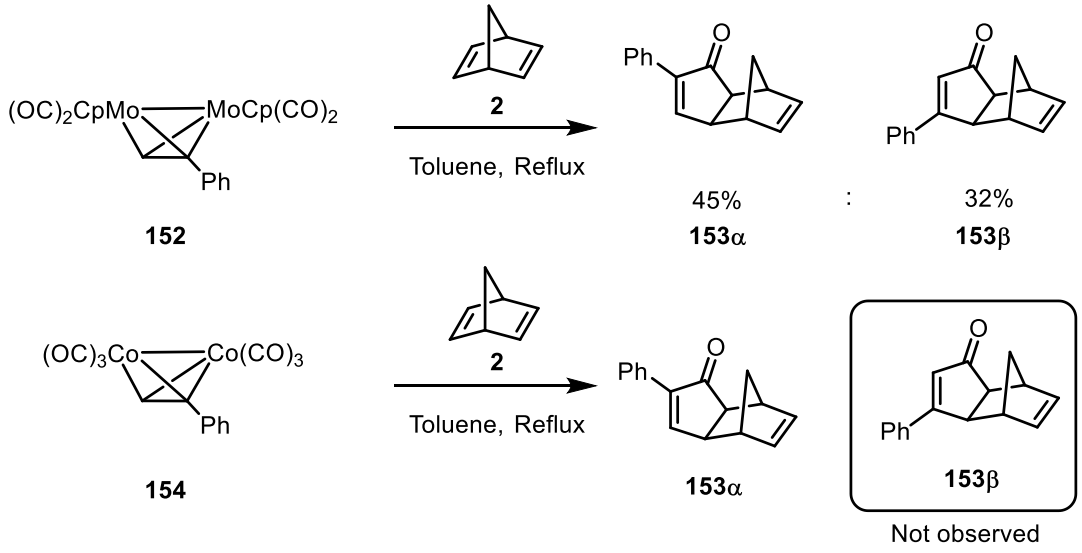

Scheme 75 - Altered regiochemical outcomes arising from molybdenum tetracarbonyl dicyclopentaidenyl phenylacetylene complexes compared to cobalt analogues, as observed by Hanoaka and co-workers.

Additionally, heterobimetallic molybdenum-cobalt alkynyl complexes have been demonstrated to perform PKR chemistry.[146] The mixed-metal centre introduces an inherent asymmetry to the process, providing avenues to enantioselective formation of PK products.

While these compounds have been demonstrated their competency in thermally and chemically promoted PK reactions, there has been little study of them in a photochemical light. Molybdenum carbonyls have provided ultrafast insight into other systems,[147–150] and the structurally analogous molybdenum cyclopentadienyl alkynyl species offer a method of gaining valuable ultrafast insight into the mechanism of the PKR.

4.1.5. Conclusions.

It is clear that the electronic structure and nature of bonding in cobalt-alkyne complexes is a highly complex system. Investigations by steady state photochemical methods, using ligand trapping, have shown that CO loss can be promoted at certain UV-Visible wavelengths, and that this can lead to the formation of cyclopentenone products. Similarly, ultrafast TRIR methods have provided spectroscopic insight into the nature of cobalt-cobalt bonding in PKR starting materials, reinforcing theoretical findings. The application of these TRIR methods to molybdenum analogues of these PKR starting materials represents an opportunity to gather new insights into the nature of metal-metal and metal-carbonyl bonding in these species.

4.1.6. Aims and objectives.

The aim of the work presented in this chapter was to explore the nature of metal-metal and metal-carbonyl bonding in PKR-relevant precursor complexes. The nature of metal-metal bonding in cobalt complexes represents an important factor when considering theoretical and mechanistic properties of this system. To gain further insight and context into these properties, similar molybdenum species were prepared to use as a comparison. A set of cobalt and molybdenum based bimetallic molecules were synthesised and investigated through $TR^{M}PS$. The photoproducts observed during these investigations will be characterised and their reactivity assessed. To rationalise the electronic impacts of irradiation at different pump wavelengths, Time-Dependent DFT (TD-DFT) was applied to simulate excited state transitions in the molecules. Simulated spectroscopic properties of potential photoproducts were used in the assignment of the identity of photoproducts formed in the reaction.

4.2. TRIR investigations of cobalt-alkynyl complexes.

4.2.1. Synthesis and characterisation of cobalt-alkynyl complexes.

As reported in section 3.3.4.1, cobalt-alkyne complexes were prepared by combination of an equimolar mixture of the relevant alkyne and dicobalt octacarbonyl in THF at room temperature. Purification by silica column chromatography yielded the complexes as pure crystalline solids, suitable for characterisation by single-crystal X-ray diffraction.

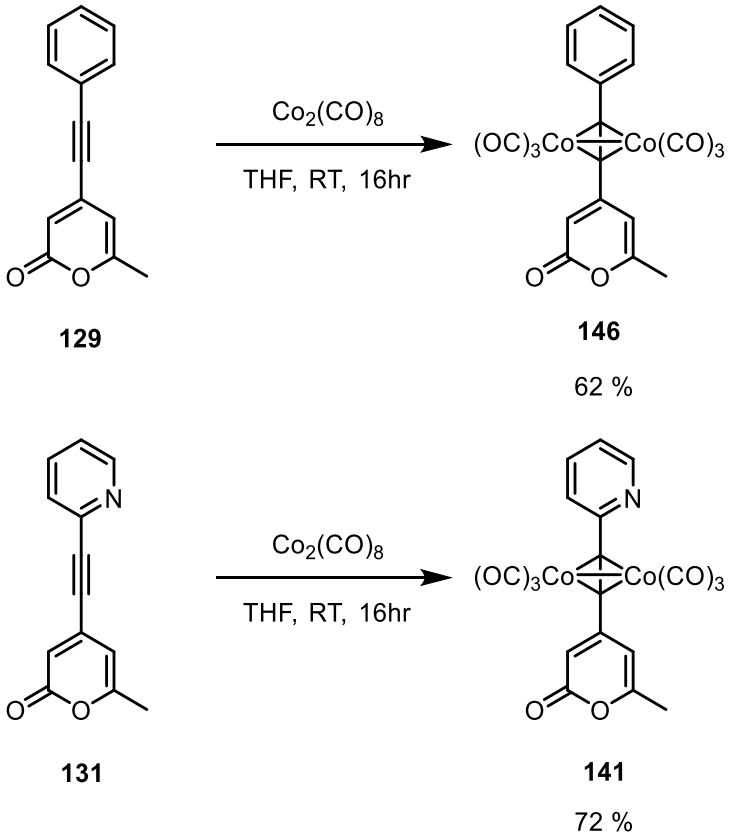

*Scheme 76 - Synthesis of cobalt-alkyne complexes **141** and **146.***

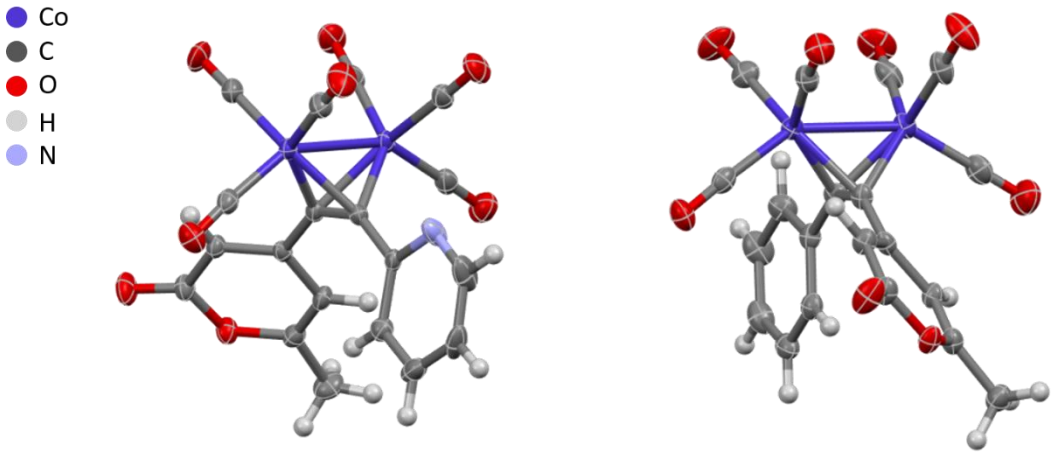

*Figure 58 - Single crystal x-ray structures of **141** (left) and **146** (right). Thermal ellipsoids at 50% probability.*

The carbonyl environments in the solid state consist of two pseudoequatorial and one pseudoaxial environment per metal centre. For each alkyne substituent R group, one pesudoequatorial carbonyl can be considered in a *cis*-position and the other in a *trans*-arrangement.

The ground-state IR of the complexes showed three unique bands, indicating C_s symmetry of the overall complex. While this would be expected from a symmetrical alkyne, unsymmetrical alkynes such a **129** and **131** should theoretically exert non-symmetric electronic effects on the metal carbonyls, disrupting the C_s symmetry. However, this can be rationalised by taking into account the low barrier to rotation of the metal carbonyl groups, leading to an "averaging" of the alkyne R group effects across each of the carbonyl ligands.

Furthermore, pyrone-containing compounds also display a relatively strong IR band in the organic carbonyl region (1700-1750 cm^{-1}), which can be followed by time-resolved IR spectroscopy. The presence of this IR signal allows for observation of conditions at the alkynyl fragment of the complex, in addition to the metal-carbonyl environment.

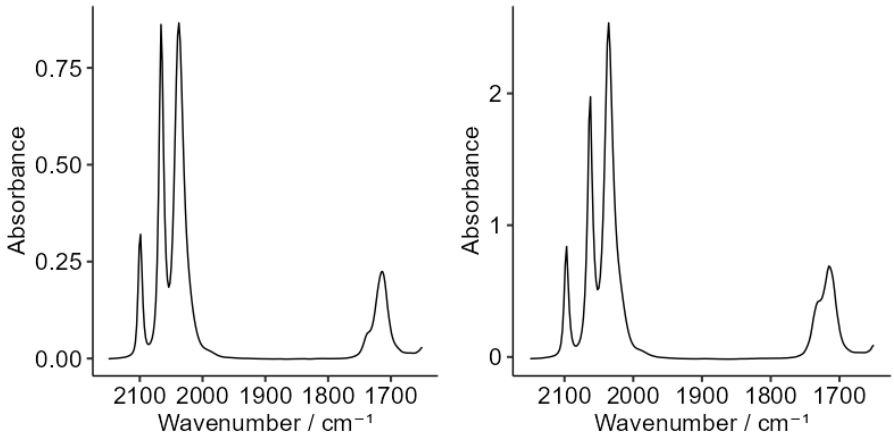

*Figure 59 - Ground state FTIR spectra of **141** (L) and **146** {R}*

4.2.2. TDDFT excited-state modelling of cobalt-alkynyl complexes.

Geometries of complexes **141** and **146** were optimised at the BP-86 SV(P) level of theory, followed by an electronic single point calculation at the PBE0 DEF2-TZVPP level, using the Turbomole software package. ESCF TD-DFT calculations then performed on the single point electronic structures to produce excitation transmission simulations. The calculated transitions are ordered in energy, from the highest energy detected transition first and decreasing in energy. Twenty transitions were calculated in all cases, which proved to be sufficient to model the accessible excitations in the regions of the spectrum at which the complexes were irradiated.

From the calculated transmissions, simulated UV-Vis spectra could be constructed, allowing for the relation of excitation wavelength to specific electronic transitions

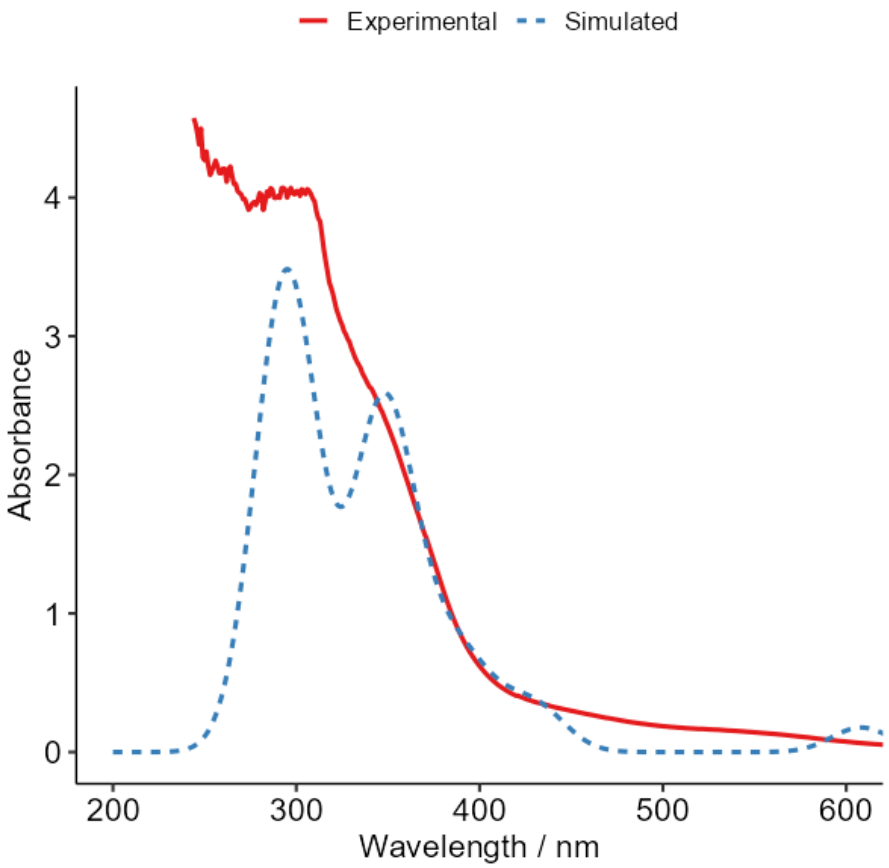

*Figure 60 - Simulated and experimental UV-Visible spectra of **141.***

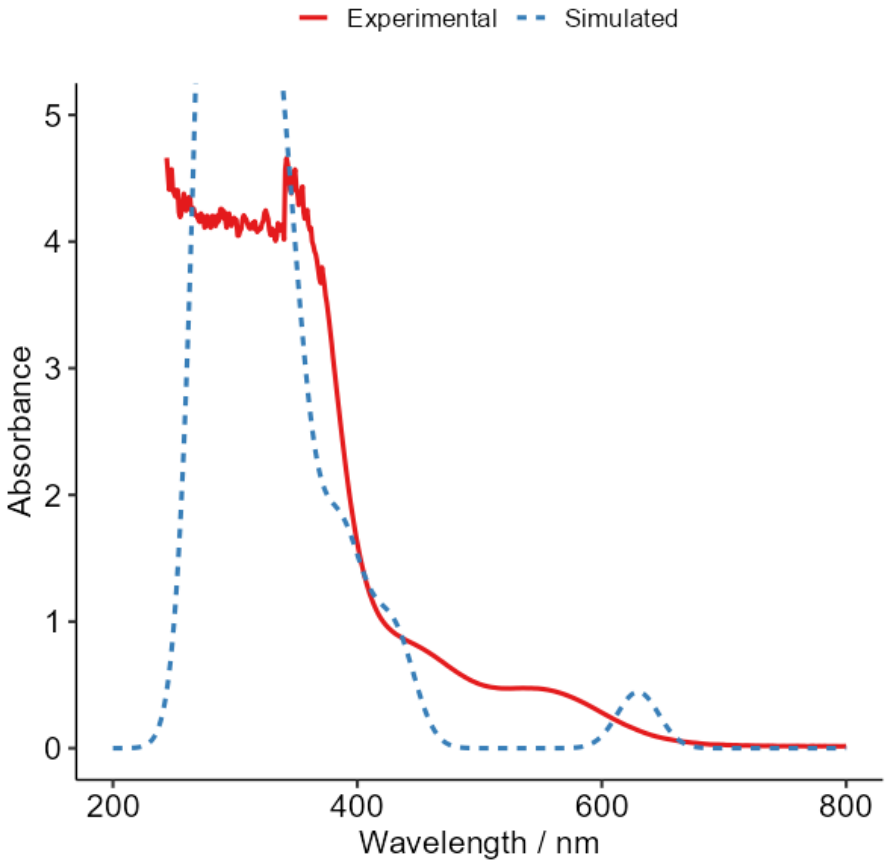

*Figure 61 - Simulated and experimental UV-Visible spectra of **146.***

For each complex, the simulated electronic transitions identified three major transitions (possessing a high oscillator strength) accessible at 400nm (Figure 62 and Figure 63). The transitions represent the excitation from a range of occupied orbitals into the complex LUMO (Table 10 and Table 11). Importantly, a strong contribution from a HOMO ➔ LUMO excitation appears in each case. Pryce and co-workers assign the origin of the Co-Co breathing mode to this transition, as the LUMO of dicobalt hexacarbonyl alkyne complexes has been found through various investigations to be antibonding with respect to the Co-Co bond.[151–153]

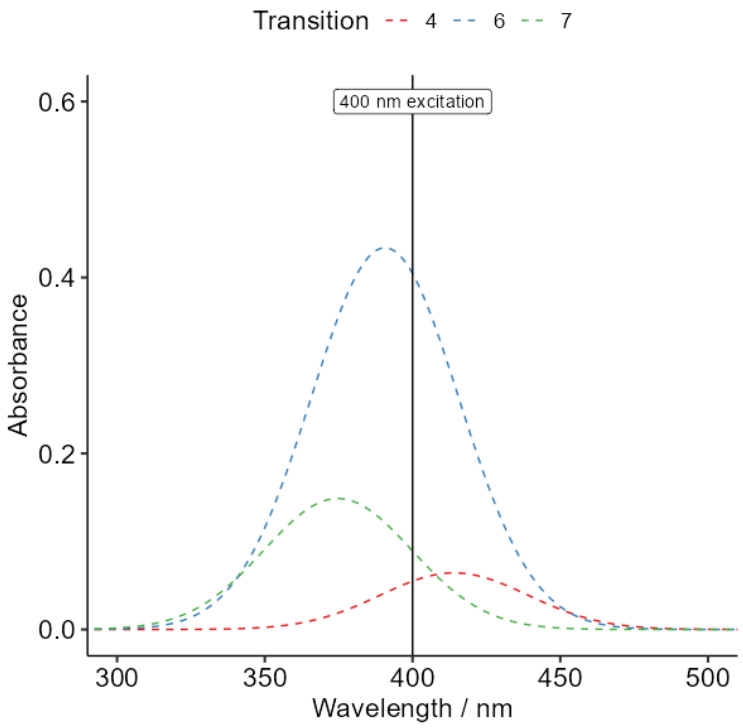

*Figure 62 - Transitions accessible at 400nm in **141.***

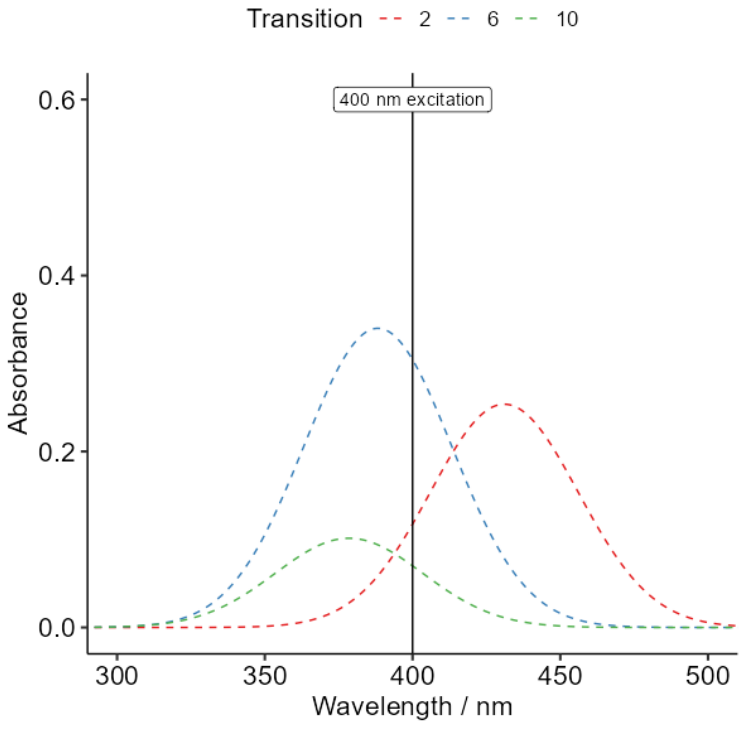

*Figure 63 – Transitions accessible at 400nm in **146.***

*Table 10 – Table of major transitions accessible at 400nm in **141***

Excitation number	Occupied orbital	Energy / eV	Virtual orbital	Energy / ev	Contribution coefficient
4	HOMO -4 (120a)	-7.92	LUMO (125a)	-2.9	24.5
	HOMO -7 (117a)	-8.32	LUMO (125a)	-2.9	14.9
6	HOMO -4 (120a)	-7.92	LUMO (125a)	-2.90	18.7
	HOMO -2 (122a)	-7.23	LUMO (125a)	-2.90	17.6
	HOMO -6 (118a)	-8.09	LUMO (125a)	-2.90	13.0
	HOMO -5 (119a)	-7.95	LUMO (125a)	-2.90	12.8
7	HOMO-1 (123a)	-6.95	LUMO (125a)	-2.90	26.9
	HOMO (124a)	-6.77	LUMO (125a)	-2.90	26.9
	HOMO -3 (121a)	-7.65	LUMO (125a)	-2.90	26.9

*Table 11 - Table of major transitions accessible at 400nm in **146***

Excitation number	Occupied orbital	Energy / eV	Virtual orbital	Energy / ev	Contribution coefficient
2	HOMO -4 (122a)	-7.27	LUMO (125a)	-2.9	38.7
	HOMO -5 (119a)	-8.02	LUMO (125a)	-2.9	29.2
6	HOMO -5 (119a)	-8.02	LUMO (125a)	-2.9	38.9
	HOMO -4 (122a)	-7.27	LUMO (125a)	-2.9	17.9
10	HOMO (124a)	-6.73	LUMO (125a)	-2.9	41.2
	HOMO-1 (123a)	-6.93	LUMO (125a)	-2.9	12.9
	HOMO -11 (113a)	-8.88	LUMO (125a)	-2.9	11.5

4.2.3. Ultrafast time-resolved IR measurements of cobalt alkynyl complexes.

Cobalt alkyne complexes **141** and **146** were analysed by UV-pump IR-probe TR^{M}PS. In each case, bleach bands for the ground state metal carbonyl signals were observed following excitation. Transient bands for a short-lived state were observed (Figure 64). The three transient bands implied that the number of carbonyl groups on the molecule was unchanged, as all three signals were conserved from the ground state. The positions of the transient bands (2010, 2054 and 2085 cm^{-1} for **141**) were highly similar to the positions of those observed by Pryce and co-workers (2019, 2048 and 2082 cm^{-1} in CH_3CN for **142**). Due to these similarities, and the results of the excited-state modelling, the observed transients were assigned to similar Co-Co breathing modes as previously observed by Pryce and co-workers.

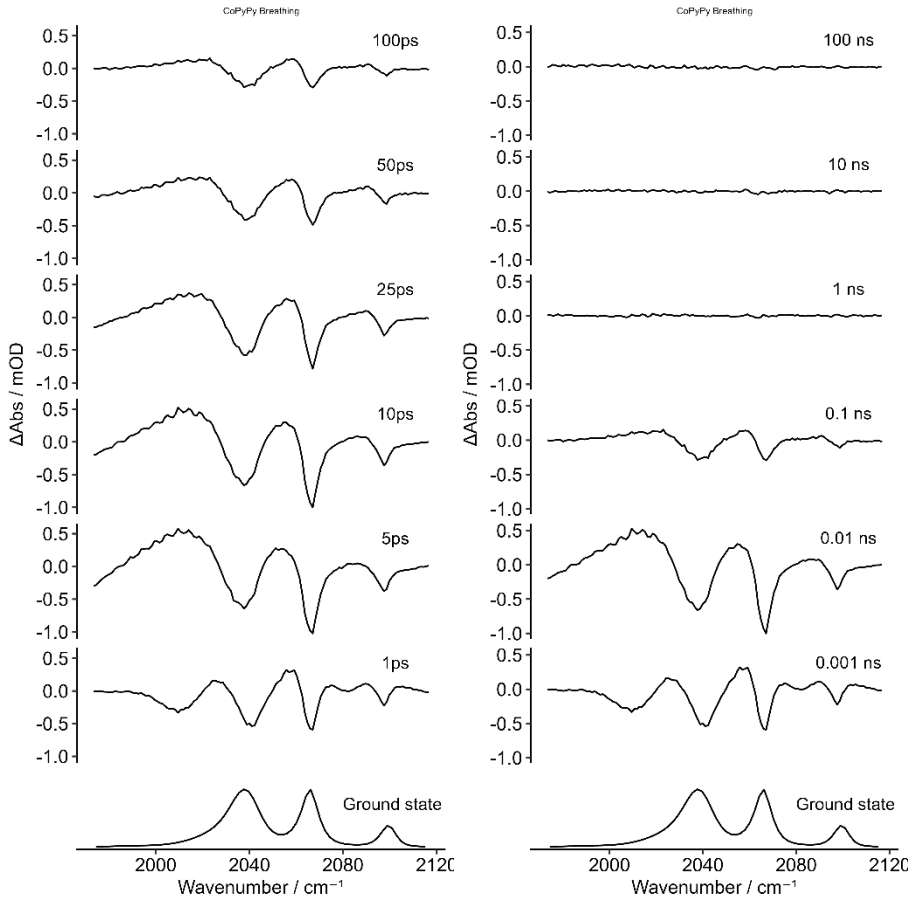

*Figure 64 – TRIR difference spectra of **141** following excitation at 400nm.*

One nanosecond after excitation, no peaks were observed in the difference spectra, indicating a return to the ground state. Similarly, short-lived bleach peaks for the organic carbonyl groups could be observed, showing that the bond homolysis affected the organic carbonyl environment. Full equilibration of the organic carbonyl difference peaks by the end of the experiment showed that the final alkyne organic carbonyl environment was conserved. This observation confirms that homolysis was fully reversible.

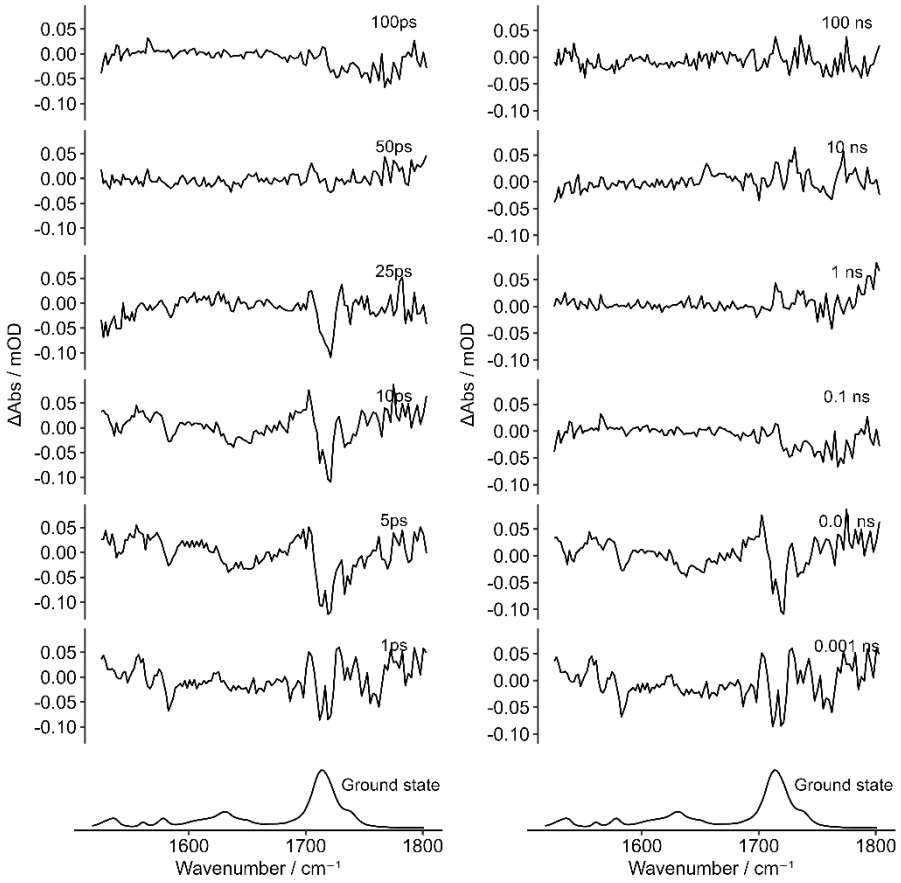

*Figure 65 – TRIR difference spectra observed in the organic carbonyl region of **141** following excitation at 400nm.*

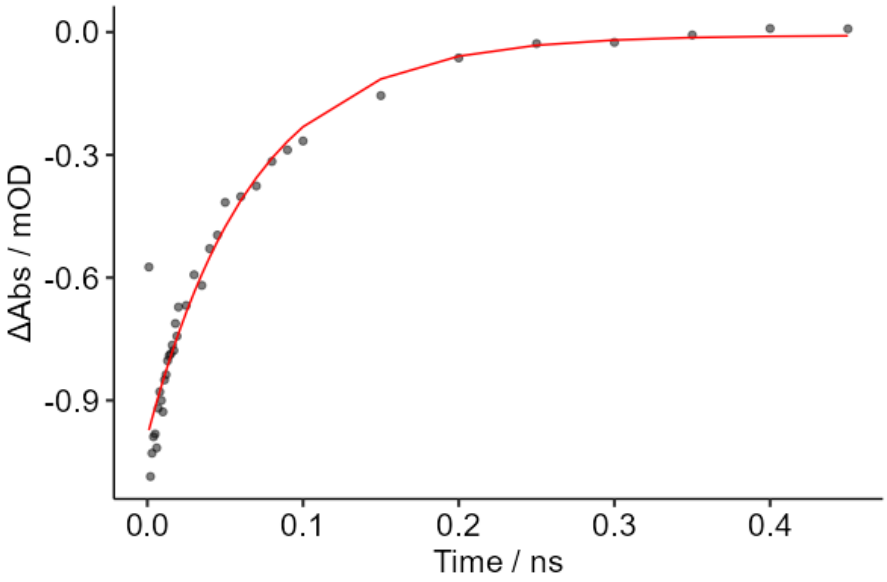

*Figure 66 - Kinetic plot of bleach recovery at 2066 cm^{-1} following excitation of **141** at 530nm*

By applying Equation 3, the rate constant for the recovery of the starting complex bleach band can be determined, assuming first order kinetics. Non-linear fitting to this first order rate law gives a rate of 1.47 ±0.17 x10^{10} s^{-1} for the bleach recovery (Figure 66), and by applying $\tau = \frac{1}{K}$, the lifetime of the state can be calculated to be 68 ± 7 ps

$$Abs_t = a + be^{-kt}$$

Equation 3 - First-order exponential fitting equation

These lifetimes were in the same range as values for similar compounds in the literature. Pryce and co-workers had previously reported the lifetime of the same cobalt-cobalt bond homolysis behaviour using **142**.[140] When the complex was excited at 400nm, the Co-Co breathing mode was found to be 69 ± 5 ps (See Table 12 for a full comparison of breathing mode lifetimes between measured and literature species).

4.3. TRIR investigations of molybdenum cyclopentadienyl alkyne complexes.

Following the observations of breathing modes with the cobalt system, an analogous system was developed using molybdenum cyclopentadienyl centres. Molybdenum tetracarbonyl dicyclopentadienyl complexes are structurally similar to cobalt-alkyne complexes, and are capable of reacting in similar ways (see section 4.1.4). Crucially, the molybdenum tetracarbonyl dicyclopentadienyl complexes exhibit a similar metal-metal-alkyne core to the

PKR precursor complexes,[154] a key feature of interest in studies of cobalt-alkyne complexes to date.

4.3.1. Synthesis and characterisation of molybdenum cyclopentadienyl alkyne complexes.

The synthesis of molybdenum cyclopentadienyl alkyne complexes was not as facile as that of their cobalt analogues. Generally the synthesis of dimolybdenum cyclopentadienyl tetracarbonyl alkyne complexes proceeds from the molybdenum tricarbonyl cyclopentadienyl dimer **155**, via the CO-loss product, molybdenum dicarbonyl cyclopentadienyl dimer **156**.[155,156,154] This CO loss requires heating at reflux for prolonged periods to complete. These forcing conditions led to some notable complications compared to the cobalt system.

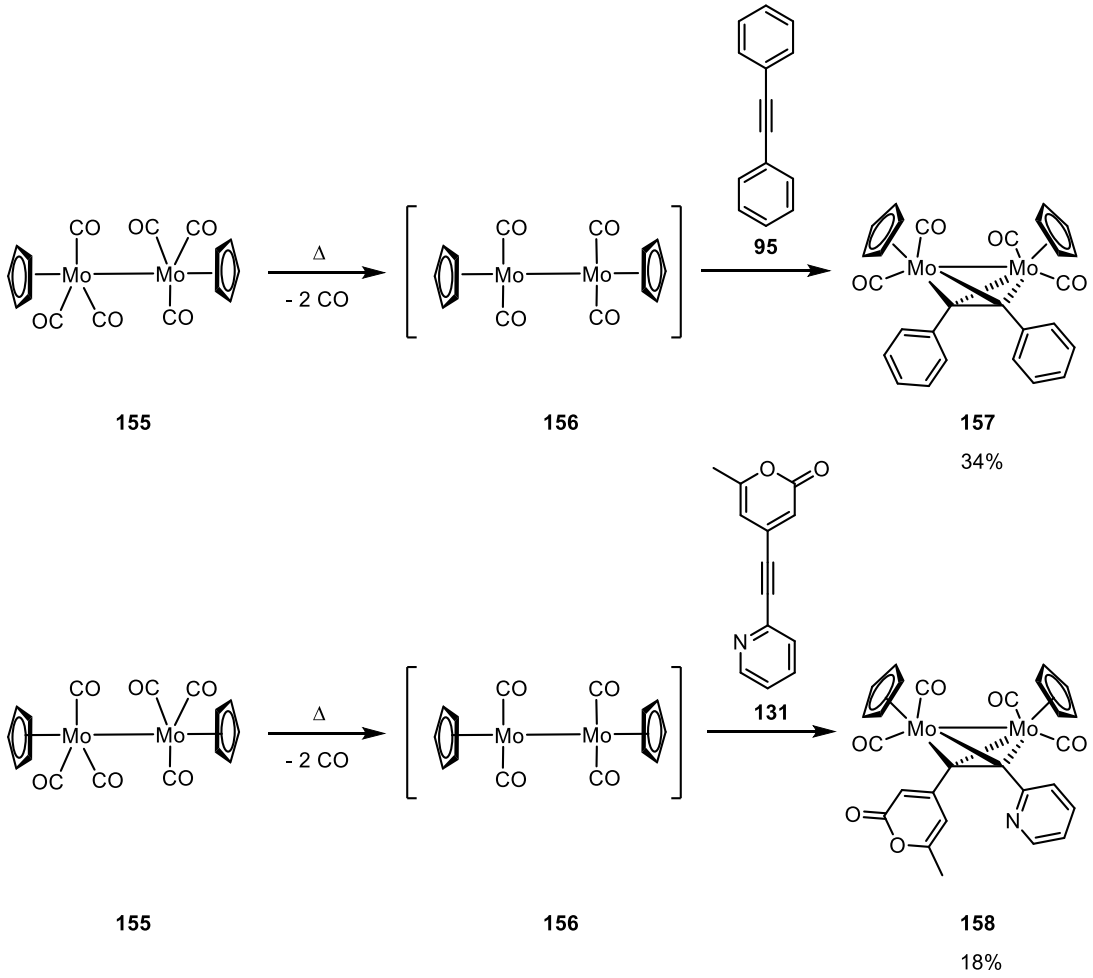

*Scheme 77 - General scheme for formation of molybdenum tetracarbonyl dicyclopentadienyl alkyne complexes **157** and **158** from a molybdenum tricarbonyl cyclopentadienyl dimer **155**, via a molybdenum tetracarbonyl cyclopentadienyl dimer **156** (not isolated in this work).*

Complexation with diphenylacetylene (**95**) progressed as expected, with IR reaction monitoring showing conversion of starting material **155** to product **157** after 16 hours. The product could be isolated in moderate yield (34%) via silica column chromatography.

Complex formation with alkyne **131**, however, required altered conditions. Reaction with identical conditions to the formation of **157** led to very low conversion to product **158** after 24 hours (<5%). Addition of the alkyne **131** in the form of doses of stock solution every 8 hours increased conversion, but at extended reaction times degradation of the metal complex became more likely, with complete loss of all metal carbonyl peaks in the IR spectrum after 36 hours.

Ultimately, synthesis of complex **158** was achieved via the dosed addition of a stock solution of alkyne **131** into a toluene solution of molybdenum tricarbonyl cyclopentadienyl dimer at reflux, over the course of 24 hours. IR analysis of the reaction mixture showed presence of residual molybdenum starting material. Column chromatography was used to obtain the pure product at a low, but acceptable yield (18%).

Crystals suitable for X-ray diffraction were obtained for both samples by cooling from hot toluene. The crystal structures showed similar geometry to the cobalt-alkyne complexes, with a trapezoidal geometry about the metal and alkyne centres. The cyclopentadienyl ligands adopt a staggered conformation across the Mo-Mo bond. As previously observed in structural studies of this group of compounds,[157] one of the carbonyl ligands is in a semi-bridging position, with the M-C-O angle deflected by 10^{o} in both **157** and **158**.

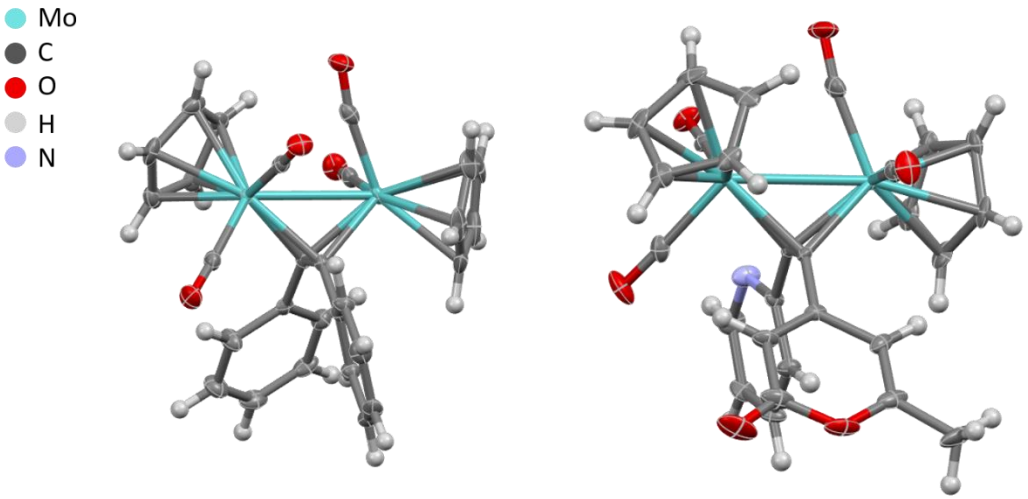

*Figure 67 - Single-crystal X-ray structures of **157** and **158**. Ellipsoids at 50% probability*

The IR spectra of the molybdenum complexes exhibit three bands in the 1800-2000 cm^{-1} region, but in this case the pseudo C_s symmetry present at the cobalt centres is lost following the replacement of one CO ligand with a cyclopentadienyl group. Furthermore, the two metal centres themselves are rendered inequivalent by the presence of the semibridging carbonyl. The simulated IR spectrum can be represented as its constituent modes to aid assignment of the bands. For instance, in the simulated IR spectrum of **157**, there are four bands arising from the metal carbonyls in the simulated vibrational frequency. Bands are numbered in ascending energy referring to the vibrational mode numbering identified during the frequency analysis calculation.

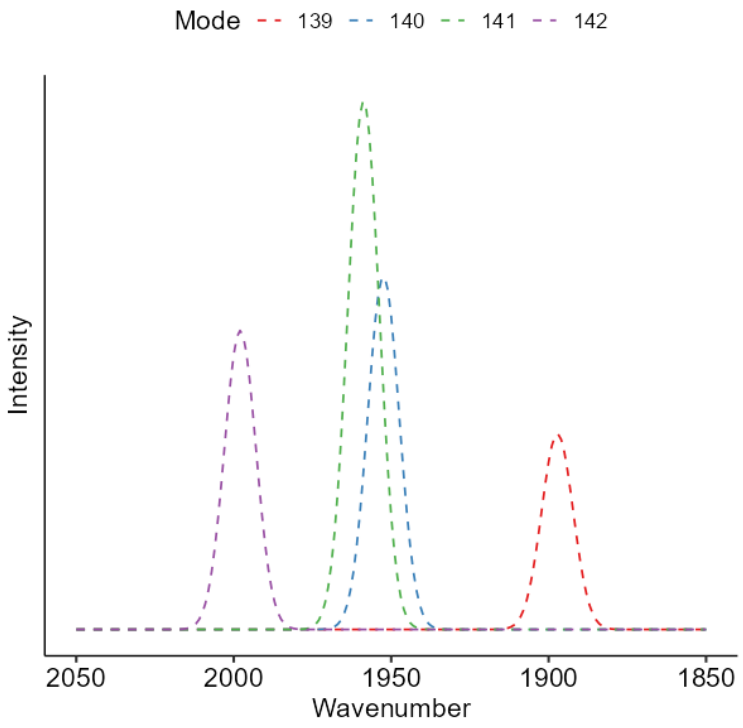

*Figure 68 - The simulated metal-carbonyl IR bands arising from **157.***

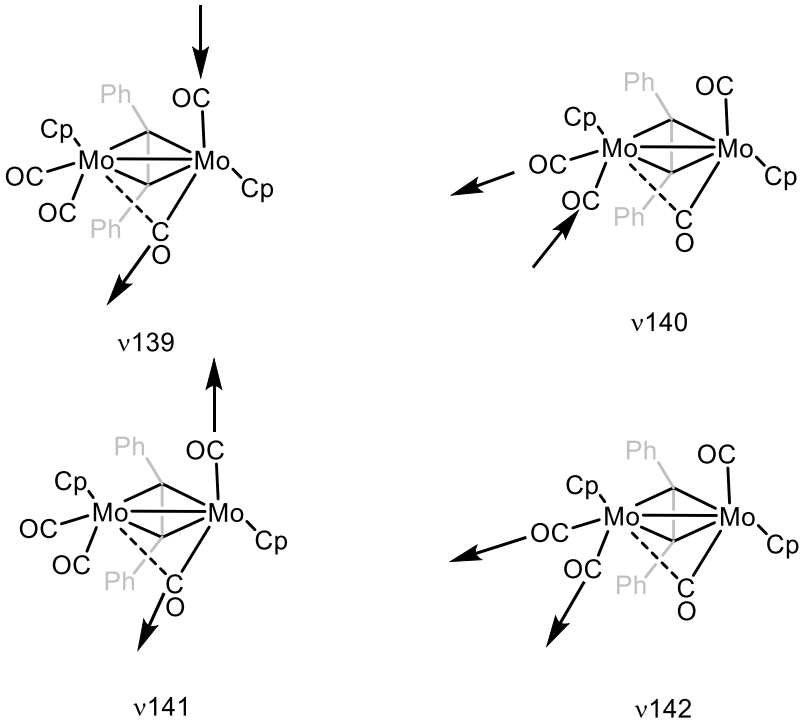

*Figure 69 - The simulated metal carbonyl vibrational modes of **157.***

The three distinct peaks observed in the spectrum arise from an overlap of the symmetric stretching mode carbonyl pair containing the semi-bridging carbonyl (v141) with the asymmetric stretching mode of the two terminal carbonyls on the opposite molybdenum centre (v140).

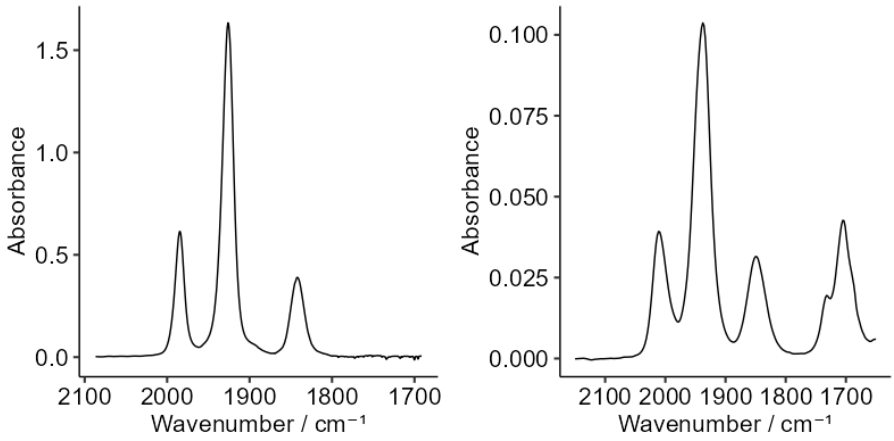

*Figure 70 - Ground state FTIR spectra of **157** (L) and **158** (R). Displaying three resolved metal carbonyl peaks in the 2050-1800 cm^{-1} region, and a lower-energy organic carbonyl peak for **158**.*

4.3.2. TDDFT excited-state modelling of molybdenum-cyclopentadienyl-alkynyl complexes.

Excited state transition modelling was performed in the same manner as described in section 4.2.2. The calculated transitions were used to build simulated UV-Visible spectra for the compounds, which were compared to experimental data. These simulated spectra will be discussed further in section 4.3.5.

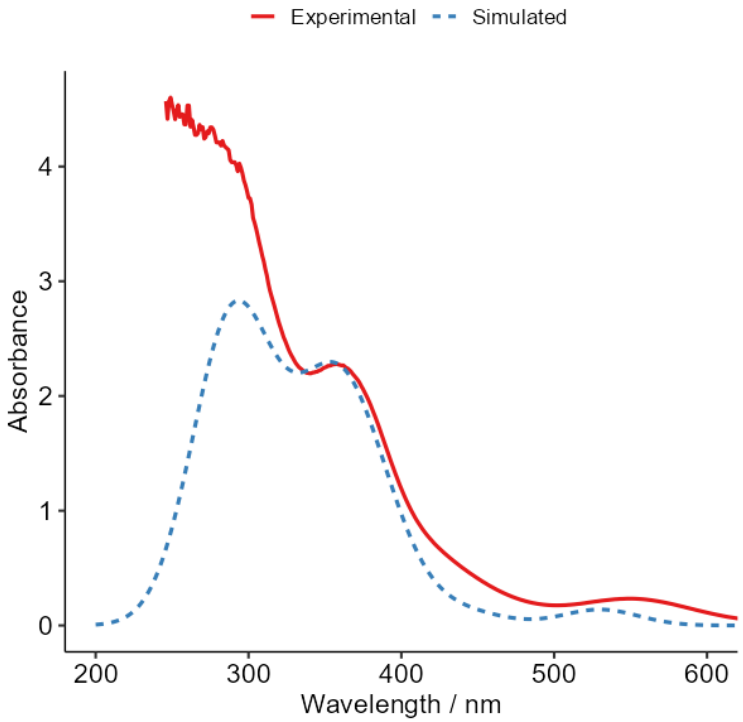

*Figure 71 - Measured and simulated UV-Visible spectra of **157.***

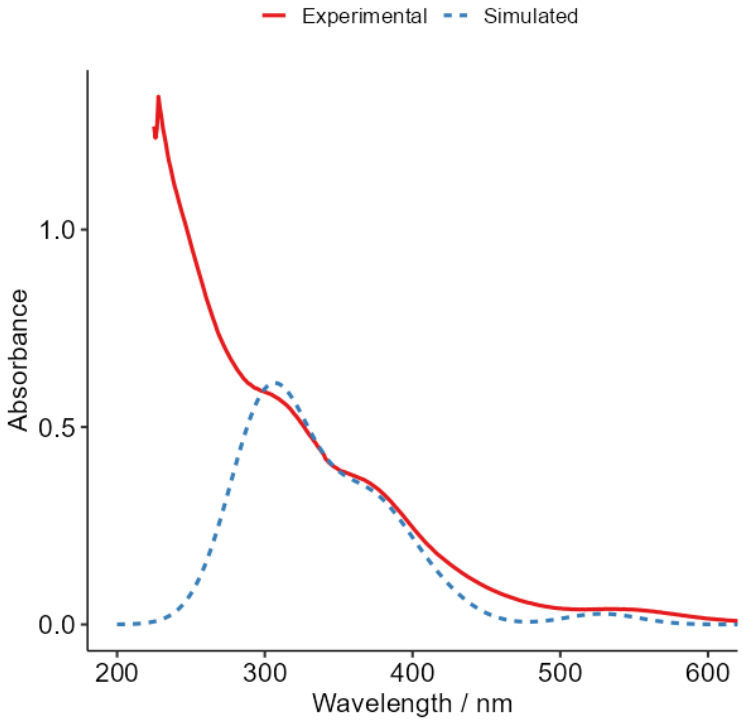

*Figure 72 - Measured and simulated UV-Visible spectra of **158.***

4.3.3. Ultrafast time-resolved IR measurements of molybdenum cyclopentadienyl alkynyl complexes.

When the molybdenum complexes were excited at 530nm, negative (bleach) peaks were observed for bands corresponding to the ground state complex, implying that a photolytic process was decreasing the concentration of the complex in solution. Simultaneously, positive (transient) peaks were observed, indicating the formation of new photoproducts. The magnitude of all observed peaks decreased throughout the course of the experiment, and by 1 ns post-excitation no peaks were detectable (Figure 73). This behaviour, very similar to that observed in the cobalt system, implied a similar molybdenum-molybdenum bond homolysis process was active as had been previously exhibited by the cobalt-alkyne complexes.

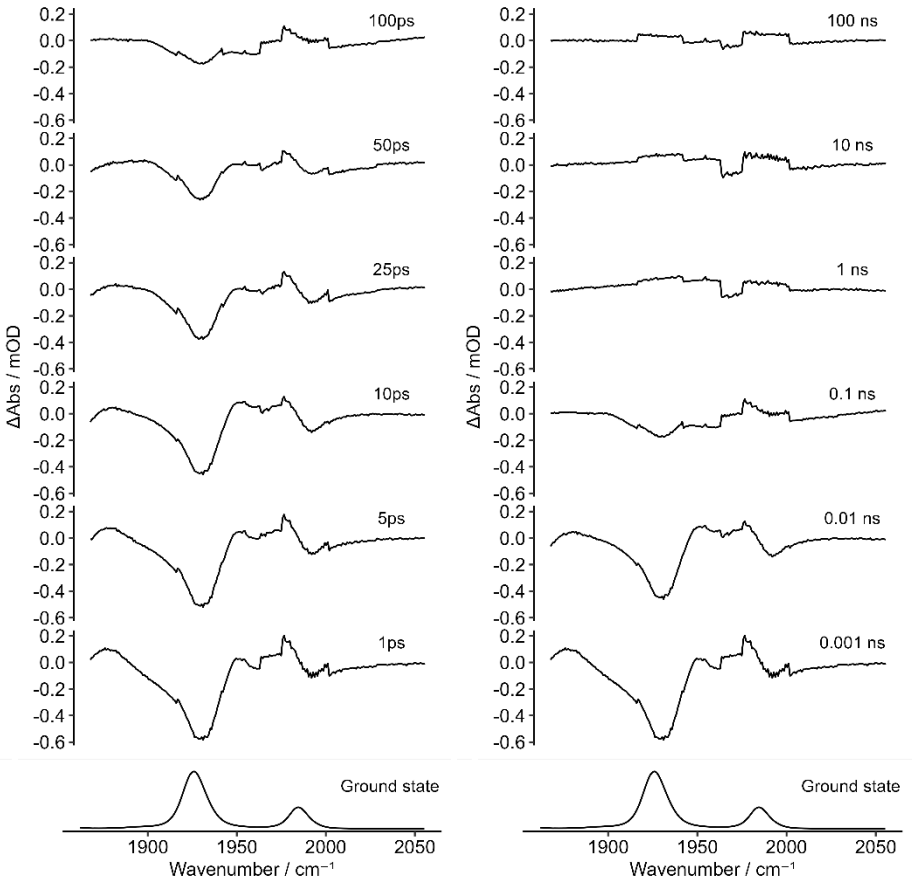

*Figure 73 - TRIR spectra following the excitation of **157** at 530nm.*

Non-linear fitting to an exponential first order rate law gives a rate of 1.29 ±0.15 x10^{10} s^{-1} for the bleach recovery (Figure 74), and by applying $\tau = \frac{1}{K}$, the lifetime of the state can be calculated to be 78 ± 1 ps. This lifetime is slightly longer (by ~10ps), than that exhibited by the cobalt analogue of **157**, **141**, implying that while the metal-metal interaction in the molybdenum system may be slightly weaker, overall it is a good model for the cobalt compounds.

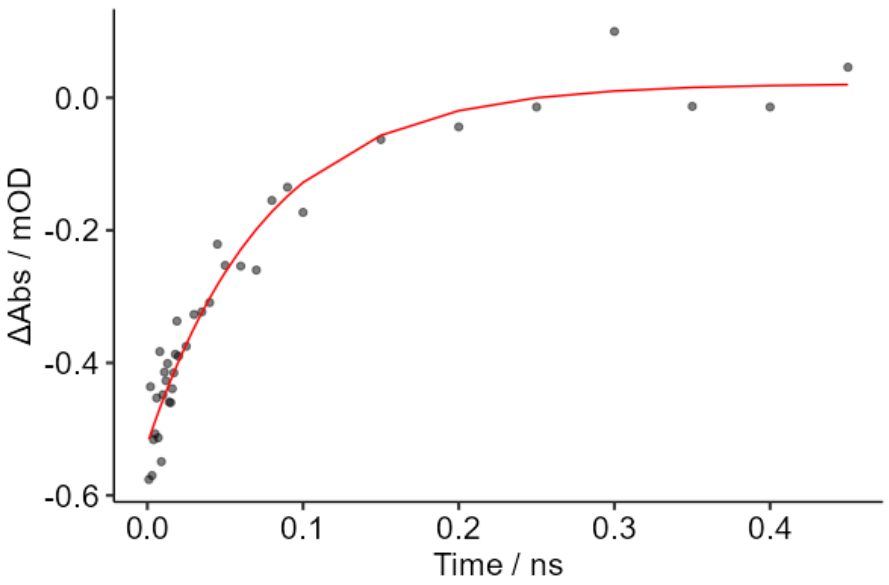

*Figure 74 - First-order exponential fitting of bleach recovery at 1925cm^{-1} following the excitation of **157** at 530 nm.*

Analysis of the excited state transitions predicted for compound **157** shows that the UV-Vis spectrum absorption around 530nm is associated with the **132** → **133** (HOMO → LUMO) transition (Figure 75). The molecular orbital numbering scheme used numbers the molecular orbitals in ascending order of energy. As identified by TD-DFT, the energetic span of an excitation from MO 132 (the highest energy occupied molecular orbital, or HOMO) to the MO 133 (the lowest energy unoccupied molecular orbital, or LUMO) matches the energy of a photon with wavelength 350nm. Excitation at this wavelength, therefore, will promote the excitation of an electron from the HOMO to the LUMO of the molecule.

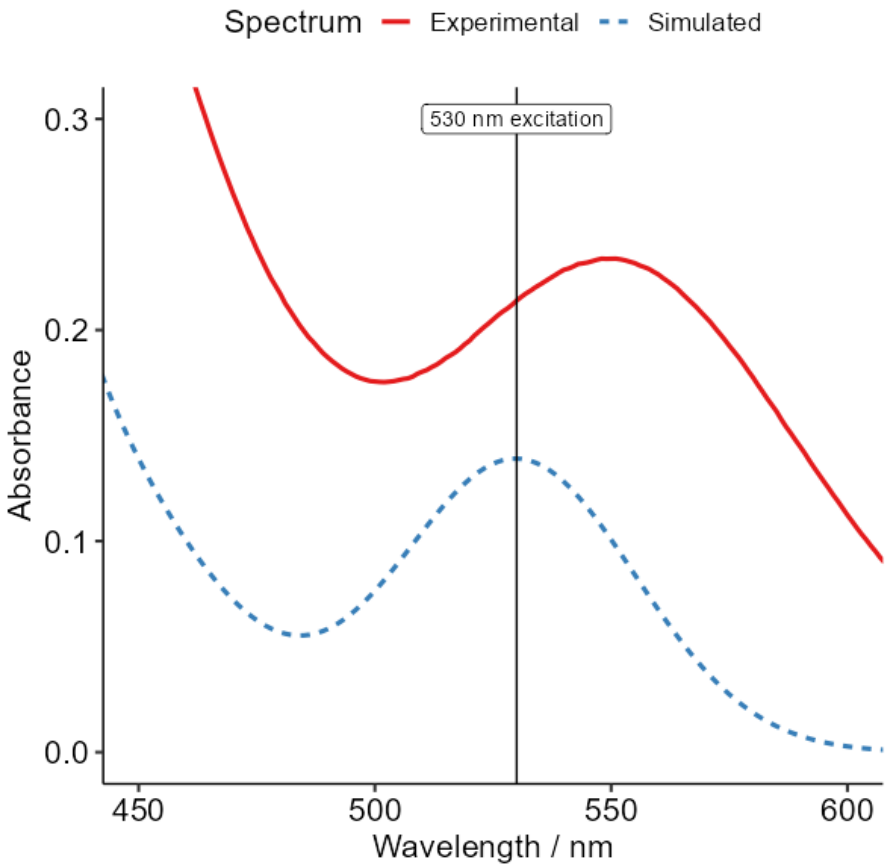

*Figure 75 – The position of the excitation wavelength in comparison to the simulated and measured UV-Vis peaks in **157.***

The metal-metal bonding in the metal complexes can be compared using solid-state, theoretical and kinetic measurements. For comparison, the breathing mode lifetimes of cobalt-alkyne complexes included in Pryce and co-workers' study are also listed.

Table 12 - Comparison of measured and calculated characteristics regarding metal-metal bonding.

Complex	SCXRD bond length / Å	BP86-SV(P) bond length / Å	Breathing mode lifetime / ps	Wiberg bond index
141	2.4658(8)	2.47	68 ± 7	0.4529
146	2.4728(7)	2.47	65 ± 25	0.4452
157	2.9734(3)	3.01	77 ± 9	0.4239
158	2.9679(3)	3.01	44 ± 3[4]	0.4245
142[140]			69 ± 5	
151[140]			63 ± 5	
148[140]			50 ± 5	

Electron density maps of the HOMOs of complexes **157** and **158** show that in both cases electron density is concentrated in the molybdenum-alkyne bonds. In the LUMOs of these complexes, the majority of the electron density is shifted to the metal-carbonyl bonds and the alkyne.

[4] Excitation at 355nm

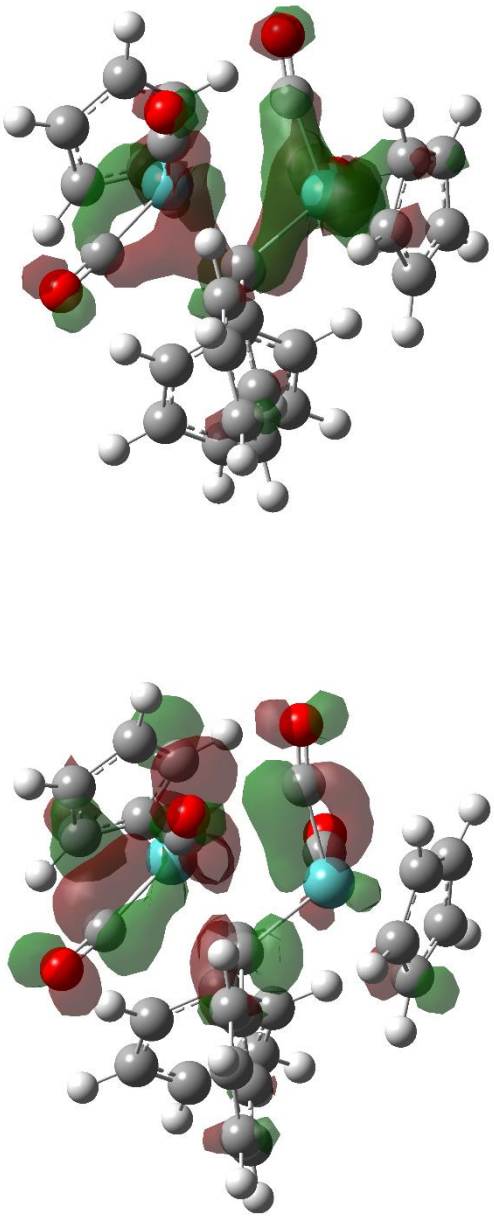

*Figure 76 - The HOMO (top) and LUMO (bottom) of **157**. Isosurface value at 0.04, atom colours as in Figure 67.*

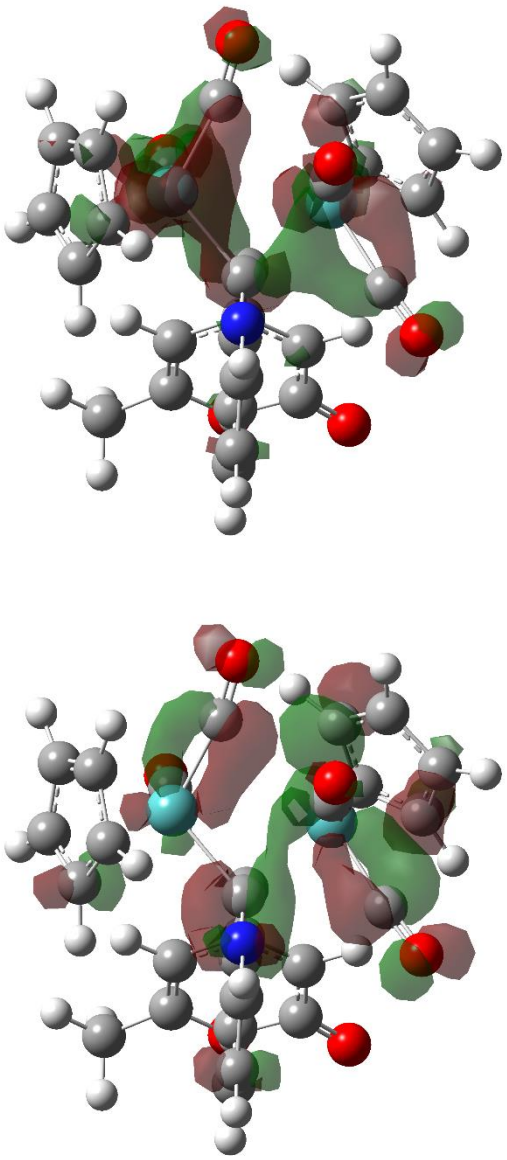

*Figure 77 - The HOMO (top) and LUMO (bottom) of **158**. Isosurface value at 0.04, atom colours as in Figure 67.*

It is unclear immediately why this shift in orbital occupancy would contribute to the lengthening of the molybdenum-molybdenum distance. To rationalise these observations, one must consider the character of the molybdenum-molybdenum bonding. Similarly to the cobalt complexes, the interaction between the metal centres is weak, with calculated Wiberg bond indexes of ~0.42, lower than those calculated for the cobalt complexes. Similarly, both calculated and experimental Mo-Mo bond lengths are around 0.5 Å greater. Together, this suggests that the Mo-Mo interaction in these complexes is relatively weak. Therefore, the metal-alkyne bonds can be seen as the main attractive interaction between the two metal

centres. Weakening of these metal-carbon bonds causes in increase in metal-metal distance, and leading to the observed breathing mode.

Excitation of the molybdenum complexes at higher energy (355 nm) produced the same initial bleaches and transitions that were observed at lower energy excitations (530 nm) (Figure 78, left). These observed spectral features were assigned to the breathing mode. However, at later time points in the experiment (> 1ns) spectral features are still observed in the difference spectrum. Bleach peaks are still observed for the ground state complex, and transient peaks are present (Figure 78, right). These newly introduced features persist until late in the experiment (50 µs). The longevity of these spectral features implies that they do not arise from dynamic processes like the breathing mode, but instead are associated with the formation of long-lived stable photoproducts, which persist until the end of the experiment.

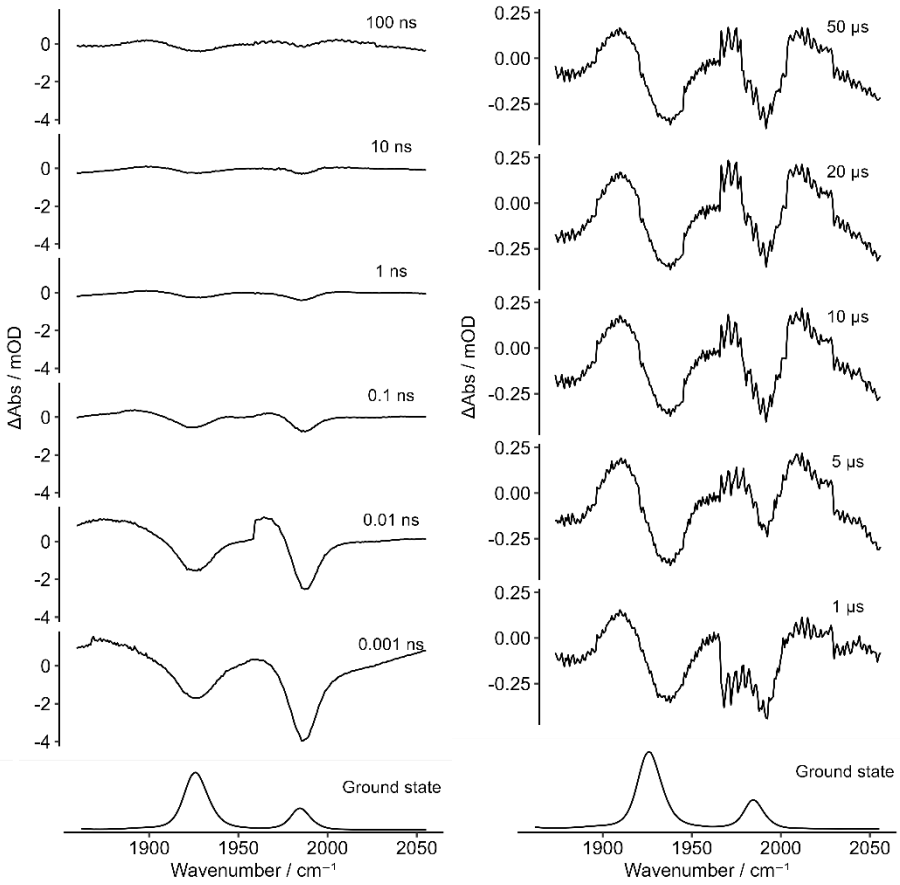

*Figure 78 - Longer-timescale difference peaks observed following excitation of **157** at 355nm.*

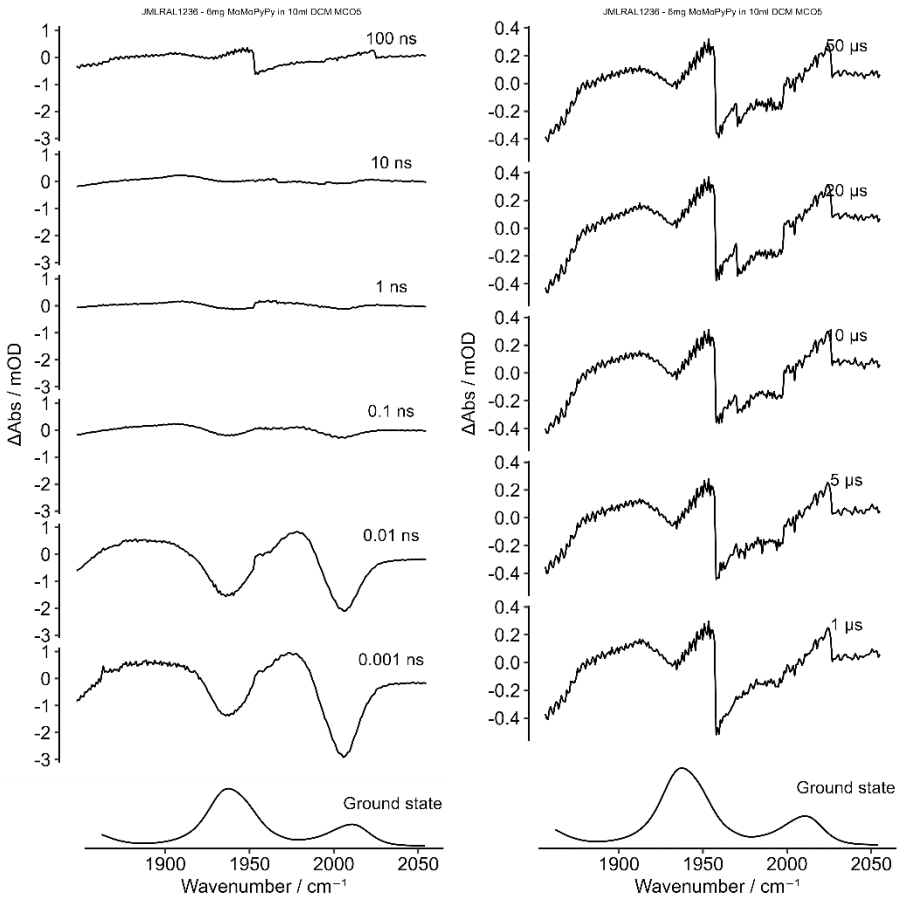

*Figure 79 - Longer-timescale difference peaks observed following excitation of **158** at 355nm.*

The photoproducts associated with the long-lived transient peaks are hypothesised to be associated with CO-loss photolysis products. Only two transient peaks are observed in the long time-scale spectra, implying that the number of carbonyl groups on the metal centres has changed as a result of photolysis. The lowered intensity of the long-lived transients compared to the dynamic breathing mode spectral features is consistent with the low quantum yield for CO-loss associated with metal-carbonyl-alkyne compounds. The intensity of the transients and bleaches for **157** is greater than that of **158**, demonstrating a higher degree of long-lived photoproduct formation in the case of **157**.

4.3.4. Development of a scaling factor to compare simulated and measured vibrational spectra.

One method of further investigating the identity of the long-lived photoproducts seen when high-energy excitation is used is the calculation of proposed post-photolysis structures by DFT methods. The calculated structures can be used to build an energetic profile of the proposed post-photolysis events, giving an indication as to their feasibility. Additionally, the simulated

vibrational spectra of the proposed photoproducts can be compared to the transient peaks in the spectrum to aid assignment. However, calculated vibrational modes of this type are usually not completely equivalent to their real-world counterparts, and are usually shifted or offset in energy, as was found to be the case in this instance (Figure 80). This is due to a number of factors, including the fact that most vibrational calculations use a harmonic, rather than anharmonic, oscillator approximation. Due to these prediction inaccuracies, post-calculation adjustment is often required to bring the calculated quantities in line with those which would be observed experimentally. To this end, there are scaling factors which can be employed for each functional/basis set combination to adjust these values to be more in-line with experimental observations.[158,159] Alternatively, a bespoke scaling factor can be obtained by the comparison of simulated and measured band energies.[160] A linear regression relationship can be drawn between the two datasets to allow for an approximate conversion from one to the other, allowing for the adjustment of the simulated spectra of compounds which cannot be easily isolated and measured.

*Table 13 -Simulated and experimental CO band positions for compounds **141**, **146**, **157** and **158**.*

Complex	Calculated (BP86/SVP) / cm^{-1}	Experimental / cm^{-1}
141	2104	2098
	2076	2066
	2056	2037
146	2102	2097
	2073	2063
	2050	2036
157	1998	1985
	1957	1926
	1897	1841
158	2021	2011
	1966	1937
	1899	1850

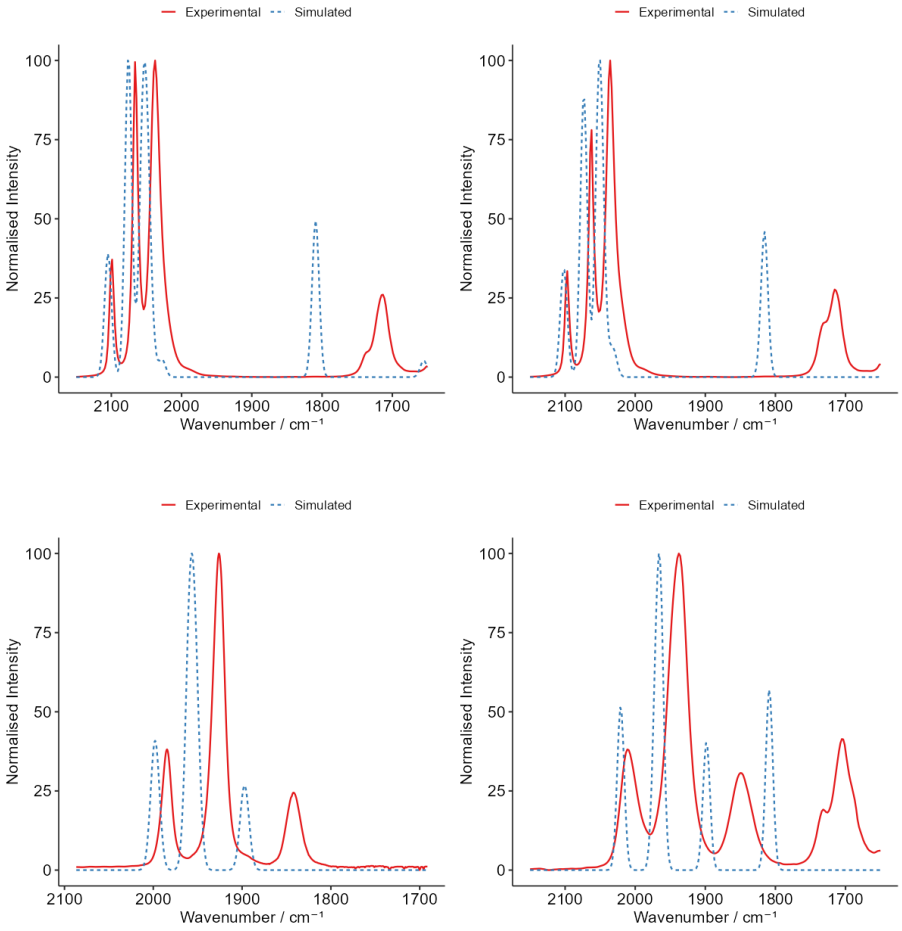

*Figure 80 - Experimental and unscaled simulated spectra of compounds **141** (top left), **146** (top right), **157** (bottom left) and **158** (bottom right)*

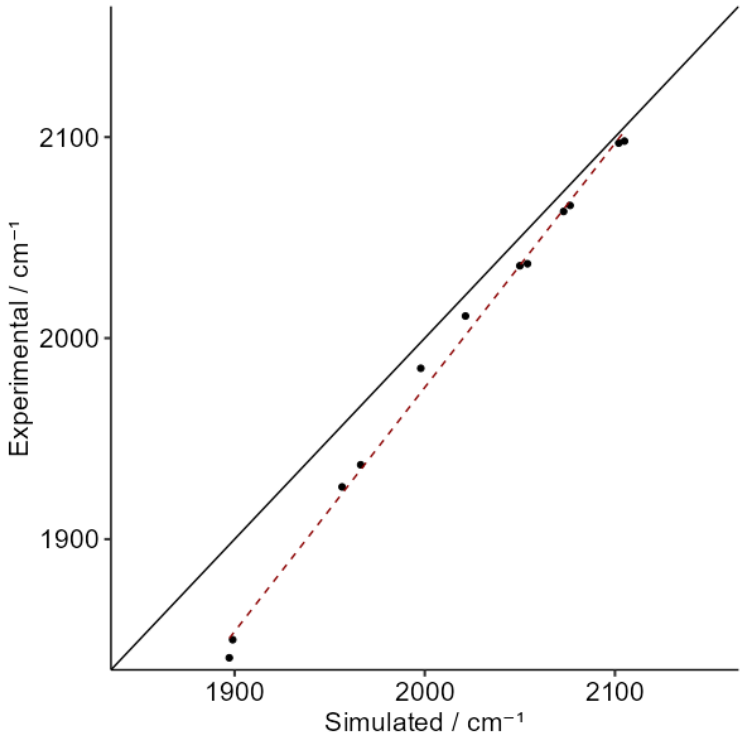

Figure 81 - Peak positions in simulated and experimental IR spectra. Solid diagonal line shows Simulated=Experimental. Red dashed line shows best-fit line used for calibration.

As can be seen in Figure 81, there is a general overprediction of peak position in the simulated spectra, with the effect being particularly pronounced for the lower energy semi-bridging peaks in the molybdenum compounds. A linear relationship was derived between the simulated and measured peaks, providing a fitting equation:

$$Exp = \ 1.21 \times Sim - 452.7$$

Equation 4 - The derived scaling factor for metal carbonyl IR bands

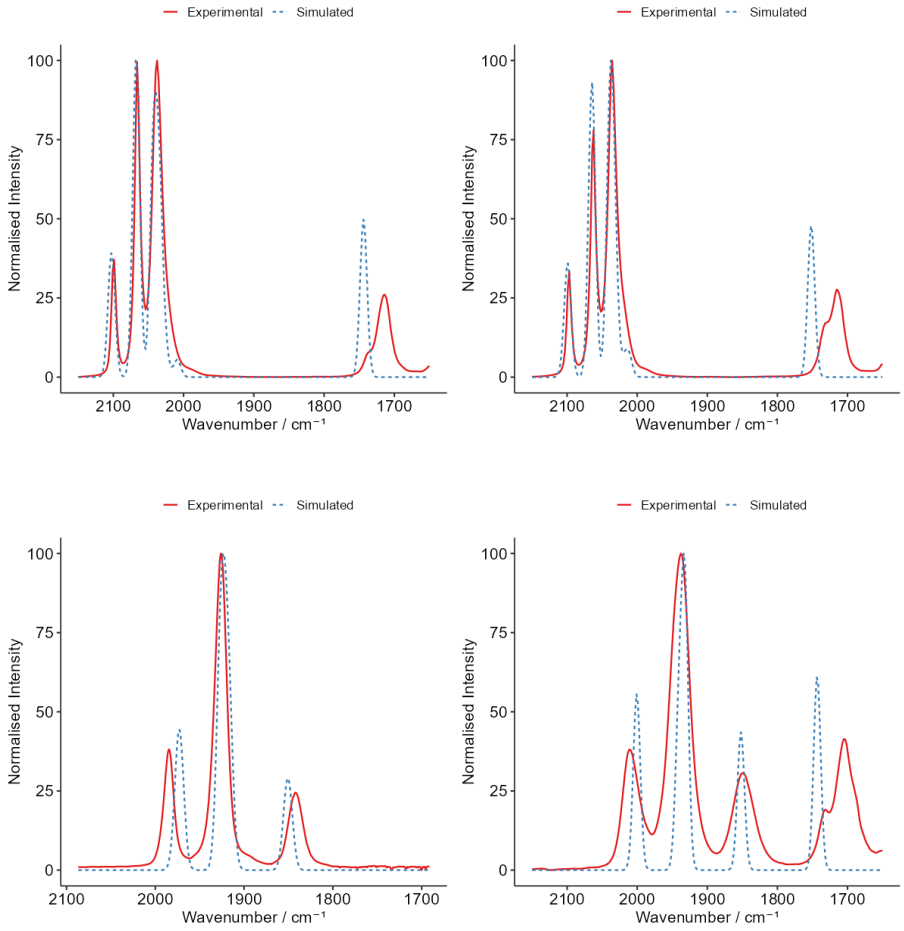

*Figure 82 – Experimental and scaled simulated spectra of compounds **141** (top left), **146** (top right), **157** (bottom left) and **158** (bottom right)*

As can be seen in Figure 82, application of the scaling factor causes the simulated spectrum (blue dotted line) to have a closer overlap with the experimentally measured data (red solid line). This derived scaling factor can now be applied to simulated IR spectra of proposed photoproducts to make the spectra more representative of real-world observed data for these species, facilitating photoproduct identification *via* comparison between scaled simulated spectra and transients observed in the TRIR data.

4.3.5. Investigation of electronic transitions leading to CO photodissociation

Excitation at 355 nm was capable of facilitating CO dissociation in compounds **157** and **158** where excitation a 530 nm was not. To rationalise this difference, the electronic transitions activated by 355 nm excitation can be examined. To do so, the simulated additive UV-Visible

spectra shown in Figure 72 and Figure 71 can be de-constructed into their constituent transitions. The major transitions (i.e. with high oscillator strength) which are centred around 355nm are shown in Figure 83 and Figure 84.

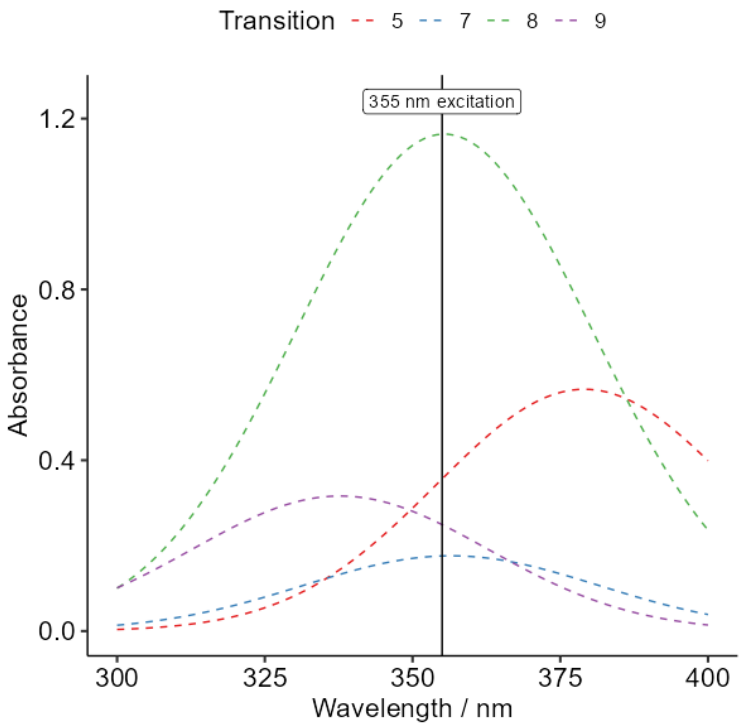

*Figure 83 – Transitions activated by excitation at 355 nm in **157.***

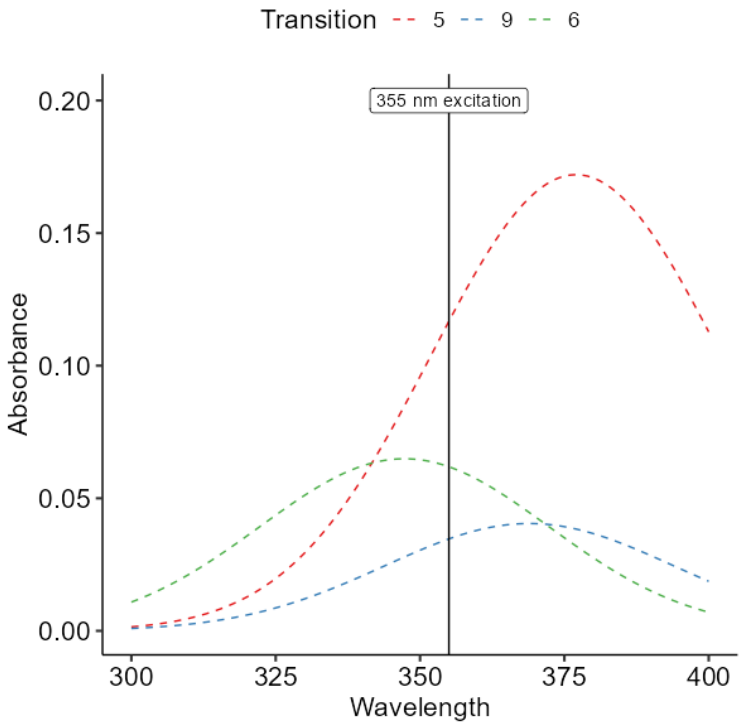

*Figure 84 – Transitions activated by excitation at 355 nm in **158.***

In complex **157**, there are 4 excitation bands which intersect with the 355nm excitation. As can be seen in Table 14, these bands primarily consist of excitations involving the frontier orbitals. As expected, none of these are a direct HOMO-LUMO transition, as this is situated at lower energy as discussed previously.

*Table 14 - Table of transitions accessible by 355nm excitation in **157**.*

Excitation number	Occupied orbital	Energy / eV	Virtual orbital	Energy / ev	Contribution coefficient
5	HOMO -1 (123a)	-5.78	LUMO +1 (126a)	-1.37	53.3
	HOMO -2 (122a)	-6.34	LUMO (125a)	-1.85	17
	HOMO (124a)	-5.46	LUMO +2 (127a)	-1.19	10.4
7	HOMO -1 (123a)	-5.78	LUMO +2 (127a)	-1.19	82.7
8	HOMO -1 (123a)	-5.78	LUMO +1 (126a)	-1.37	30.8
	HOMO -2 (122a)	-6.34	LUMO (125a)	-1.85	21.2
	HOMO -1 (123a)	-5.78	LUMO (125a)	-1.85	13.1
9	HOMO -2 (122a)	-6.34	LUMO +1 (126a)	-1.37	72.7

The strongest excitation (5) is situated almost directly at 355nm. This peak is made up by contributions from three different orbital pairings. The primary contribution is made by the HOMO -1 to LUMO +1 transition, which is also the main contributor to excitation 8.

The electronic structure of **157** was optimised at the PBE0-def2TZVPP level of theory, and the electron density plots for the molecular orbitals examined. In the HOMO -1 (123a) orbital, density is primarily centred around the metal-metal bond and alkyne bond, as well as on the semi-bridging carbonyl ligand. In the LUMO +1, the electron density is shifted away from the

metal-alkyne centre, onto the carbonyl opposite the semi-bridging carbonyl. This transition represents metal-ligand charge transfer (MLCT) and promotes the dissociation of the carbonyl group.

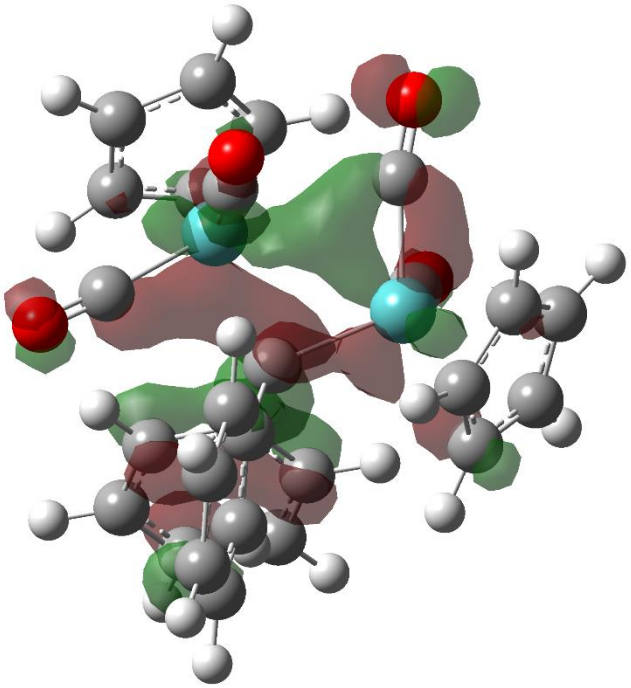

*Figure 85 - Electron density of the HOMO-1 (123a) of **157**. Isosurface value at 0.04, atom colours as in Figure 67.*

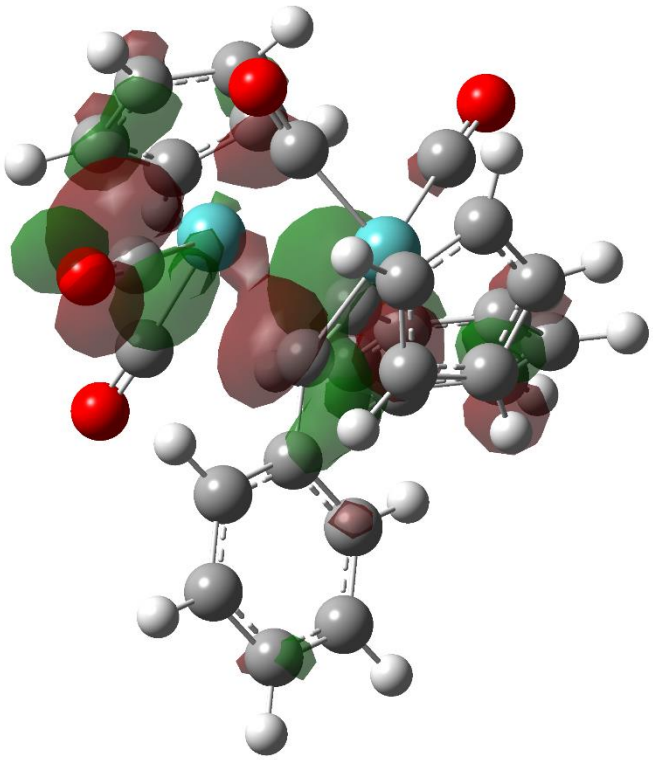

*Figure 86 - Electron density of the LUMO+1 (126a) of **157**. Isosurface value at 0.04, atom colours as in Figure 67.*

In **158**, there are three bands associated with the 355 nm excitation wavelength.

*Table 15 - Table of transitions accessible by 355nm excitation in **158.***

Excitation number	Occupied orbital	Energy /eV	Virtual orbital	Energy / eV	Contribution coefficient
5	HOMO-2 (130a)	-6.53	LUMO (133a)	-2.05	32.3
	HOMO-1 (131a)	-6.09	LUMO (133a)	-2.05	24.9
6	HOMO-1 (131a)	-6.09	LUMO+1 (134a)	-1.79	71.9
	HOMO (132a)	-5.65	LUMO+3 (136a)	-1.08	11.5
9	HOMO-1 (131a)	-6.09	LUMO+2 (135a)	-1.57	39.7
	HOMO (132a)	-5.65	LUMO+3 (136a)	-1.08	20
	HOMO-2 (130a)	-6.53	LUMO+2 (135a)	-1.57	10.3

However, in this case the LUMO and LUMO+1 orbitals do not receive contributions from orbitals situated on a carbonyl, so are not capable of performing MLCT. Instead, the LUMO+3 orbital shows large amounts of contribution arising from orbitals on a carbonyl ligand, making it a likely source of photodissociation (Figure 89). The HOMO → LUMO+3 transition is accessed by excitations 6 and 7, but with low contribution coefficients. This, coupled with the low oscillator strengths (overall peak intensities) of excitations 6 and 7 means that it is likely that the quantum yield for photodissociation in **158** will be lower than that of **157**. The likely reason for this is the presence of the pyrone group on the alkyne. As can be seen in Figure 87, the majority of the orbital contribution in the LUMO is made up of the π-system of the pyrone ring. Pyrone, an electron-withdrawing ligand, is in this case acting as an electron density sink, preventing photoexcited electrons from populating the normally accessible orbitals on the carbonyl ligands.

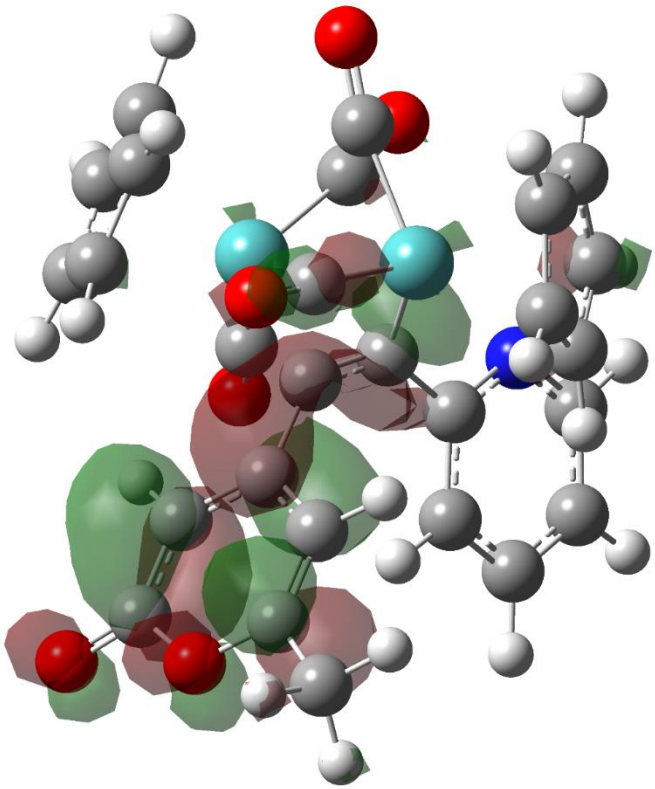

*Figure 87 - Electron density of the LUMO+1 in **158**. Isosurface value at 0.04, atom colours as in Figure 67.*

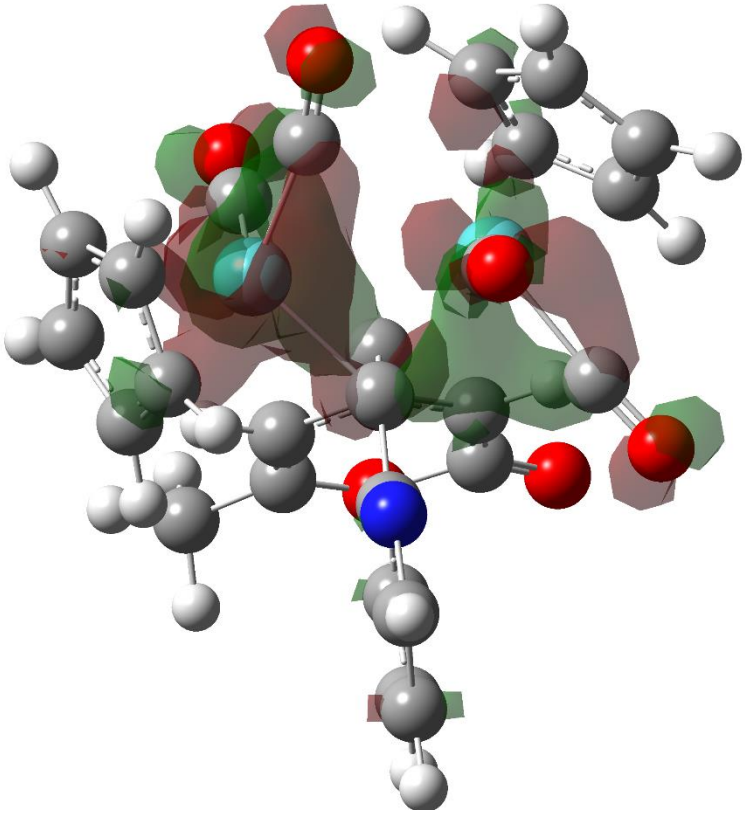

*Figure 88 – Electron density of the HOMO (123a) of **158**. Isosurface value at 0.04, atom colours as in Figure 67.*

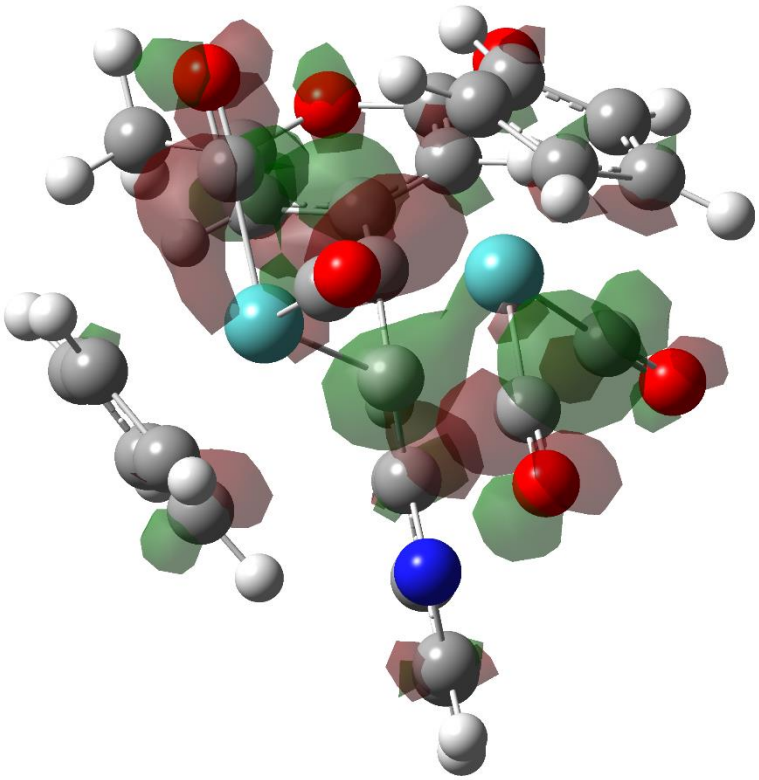

*Figure 89 - Electron density of the LUMO+3 (126a) of **158**. Isosurface value at 0.04, atom colours as in Figure 67.*

4.3.1. Investigation of post-photolysis ultrafast coordination behaviour

The coordinatively unsaturated tricarbonyl species resulting from CO loss are likely to be highly unstable in solution, and quickly bind any ligand available. The most abundant potential ligand in the system is the DCM solvent, which is able to coordinate to fill the resulting coordination vacancy and form a DCM solvation complex. Although dry solvent is used for the experiment, trace water may still be present. Therefore, the coordinated DCM may over time be displaced by water. The geometries of the four possible isomers of the resulting tricarbonyl complex **PP1** (one for each possible CO loss) were optimised at the BP68-SV(P) level of theory for each compound. These geometries were constructed by taking the SC-XRD structures of compound **157** and **158** and removing each CO ligand individually in turn. Additionally, the geometries of DCM and water-coordinated species (**PP2** and **PP3**) respectively were optimised with the new ligand in each site using a similar process (Scheme 78).

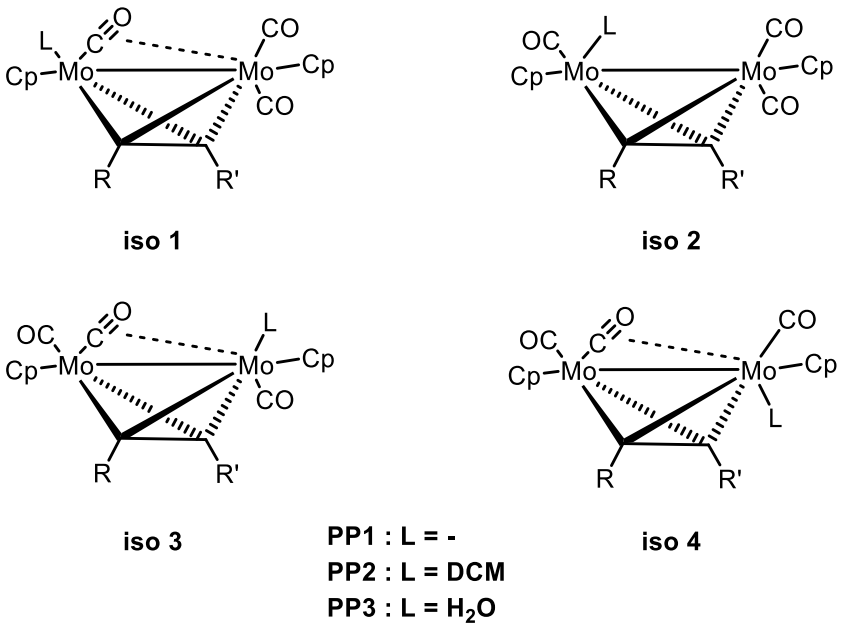

Scheme 78 - Structures of simulated photoproducts.

*Table 16 - Calculated Gibbs energies (with DFT-D3 dispersion correction and COSMO-DCM solvation correction of the proposed photoproducts for **157**.*

Photoproduct	Isomer	Relative Gibbs energy to other isomers / kJ mol^{-1}	Relative Gibbs energy to lowest-energy CO-loss product / kJ mol^{-1}
157 PP1	**iso1**	0.0	9.4
	iso2	13.1	22.5
	iso3	7.0	16.4
	iso4	-9.4	0.0
157 PP2	**iso1**	0.0	-24.9
	iso2	-6.5	-31.4
	iso3	0.3	-24.5
	iso4	-1.4	-26.2
157 PP3	**iso1**	0.0	-40.6
	iso2	-3.3	-43.8
	iso3	-7.5	-48.0
	iso4	-6.1	-46.6

For compound **157**, the most stable species was **iso4**, which is produced by the loss of a terminal carbonyl opposite the semibridging CO. This is the same carbonyl which undergoes MLCT in the HOMO -1 → LUMO +1 energy transition. It is likely, therefore, that this will be the site of photodissociation. The calculated vibrational spectrum of **157 PP1 iso4**, scaled by the scaling factor derived above, was compared to the difference spectrum at 50 ps following excitation. A sharp transient is observed at 1968 cm^{-1}, corresponding to the major band of the simulated spectrum.

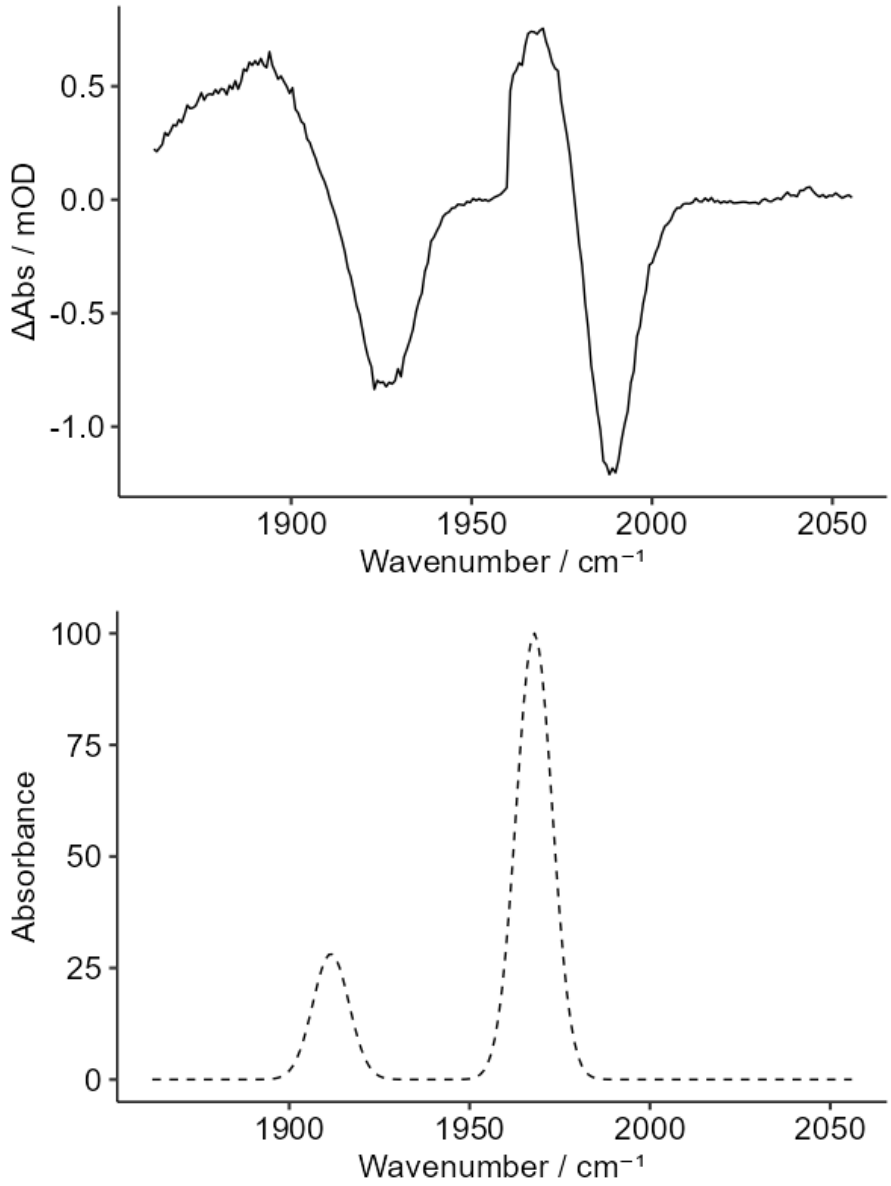

*Figure 90 - Top: difference spectrum of **157** 50 picoseconds after excitation at 355nm. Bottom: Simulated and scaled vibrational spectrum of **157 PP1 iso4**.*

When the energies for **157 PP2**, the DCM-coordinated complex, were compared four isomers were found to be within an 8 kJ mol^{-1} range, implying no particular energetic favourability for coordination in any one site over the others. IR absorption bands for the DCM-coordinated complex (**157 PP2**) are not observed in the ultrafast spectra. This may arise from the fact that the DCM-water exchange is likely to occur on the same timescale as the far more intense Mo-Mo homolysis behaviour, masking the bands of **157 PP2** in the difference spectra. Once the homolysis mode excited state has decayed, the long-lived transients arise from the water-

coordinated photoproduct, **157 PP3**. The bands correlate with the simulated vibrational spectrum of **157 PP3 iso3**, implying that a pseudorotation occurs during the ligand-exchange process, and water is coordinated at a different site to that from which the initial CO photodissociation is thought to take place (Figure 91). Additionally, the presence of a band at 1910 cm^{-1} in the simulated vibrational spectrum reveals the reason that the bleach bands in the long-term difference spectra of **157** are not proportional in size with the ground state FTIR bands. The interference of the long-lived transient overlapping with the bleach causes the overall magnitude of the negative peak to be decreased compared to the higher energy, un-overlapped band at 1990 cm^{-1}.

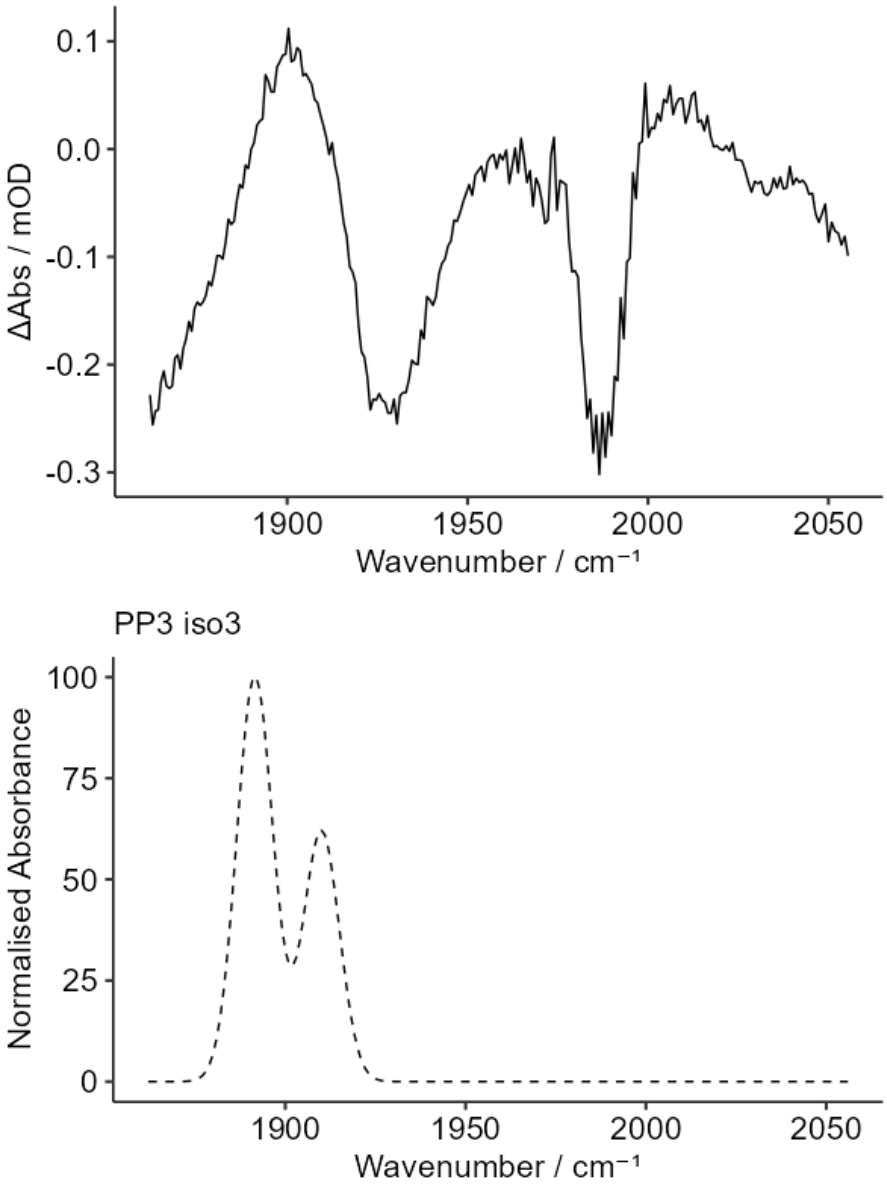

*Figure 91 - Top: Difference spectrum 10ns after excitation of **157** at 355nm.*
*Bottom: The scaled simulated spectrum of **157 PP3 iso3***

Energetically, the coordination of DCM to the tricarbonyl species **157 PP1** to form **157 PP2** represents a 26 kJ mol^{-1} stabilisation, and the displacement of DCM with water confers a further 21 kJ mol^{-1} energetic benefit.

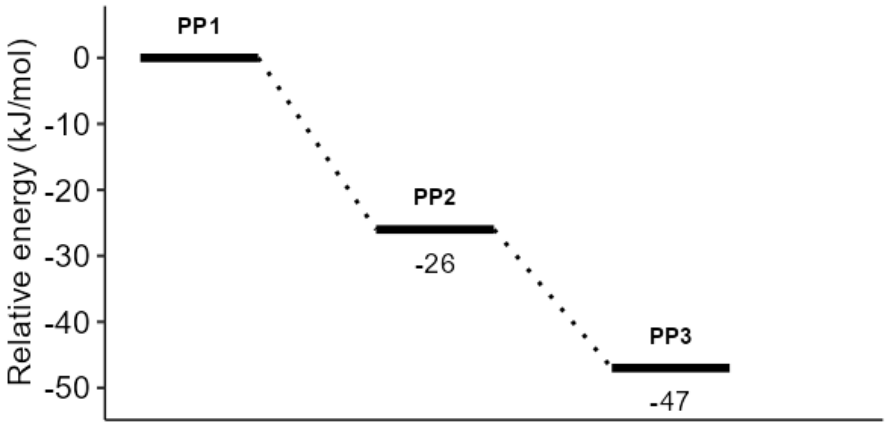

*Figure 92 - Calculated Gibbs energies (BP86-SV(P)) with DFT-D3 dispersion correction and COSMO-DCM solvent correction of the lowest energy isomers of photoproducts of **157** following excitation at 355nm.*

While CO-loss transients are observed following the 355nm excitation of **158**, the intensities of the long-lived peaks are lower. This is assigned to lower levels of CO dissociation due to the electron-withdrawing nature of the pyrone leading to the lower-lying virtual orbitals in **157** being unable to carry out MLCT. Energetic comparisons of the CO-loss products showed that once again the photodissociation of the terminal CO opposite the semi-bridging carbonyl ligand was most thermodynamically favourable.

Lower peak intensities made it less easy to identify peaks at later timepoints due to lower signal to detector noise ratio, however based on comparison between the transient peak position and the simulated vibrational spectra, the final water-coordinated photoproduct, **158 PP3**, was identified as having the water coordinated in the same site as the CO loss (**iso4**). The energetics of the post-photolysis pathway are very similar to those of**1 57**, demonstrating that while the altered complex structure has implications regarding CO photodissociation quantum yield, and the subsequent in-solution coordination behaviour, the energetics of the process are relatively consistent between the two complexes.

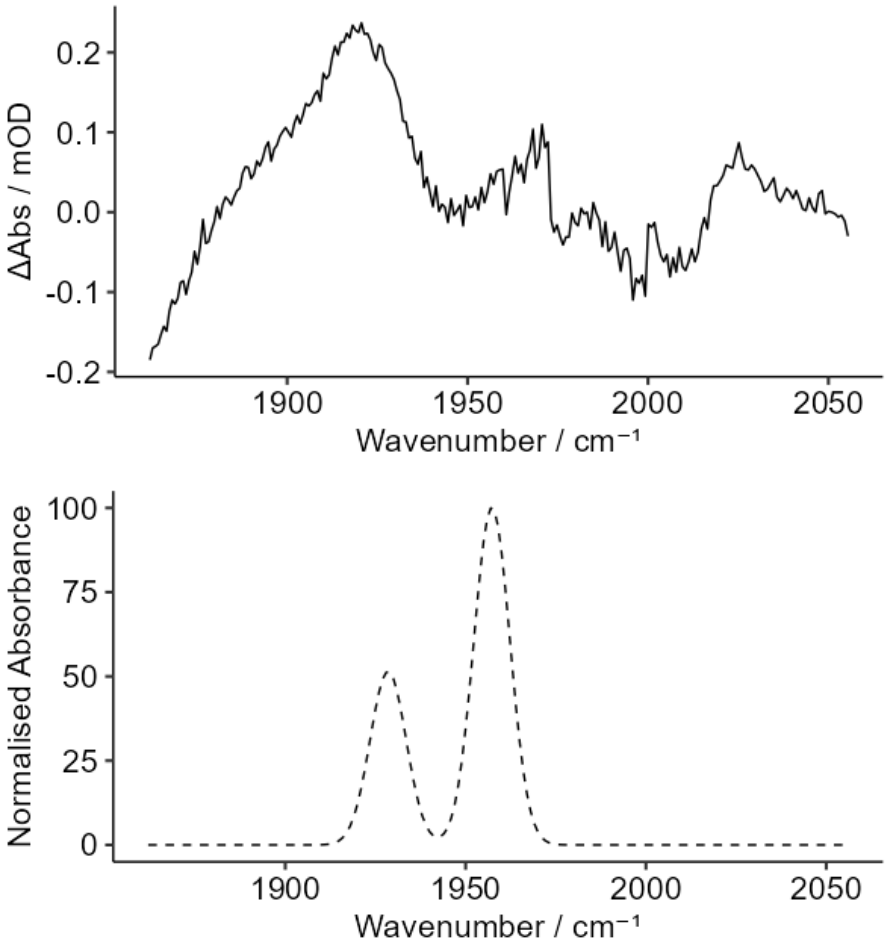

*Figure 93 - Top: Difference spectrum 10ns after excitation of **158** at 355nm.*
*Bottom: The scaled simulated spectrum of **158 PP3 iso4**.*

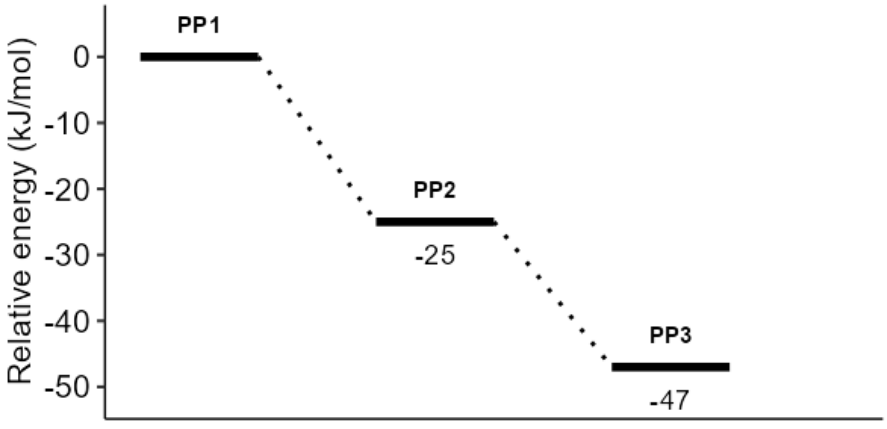

*Figure 94 - Calculated Gibbs energies (BP86-SV(P)) with DFT-D3 dispersion correction and COSMO-DCM solvent correction of the photoproducts of **158** following excitation at 355nm.*

Following the observation of CO photodissociation, further experiments were conducted by photolysing **157** with an excess of acetonitrile present in the DCM solution, to assess the binding behaviour of the CO-loss products. Acetonitrile acts as a more competitive ligand than water in the solution, leading to an acetonitrile-coordinated final product.

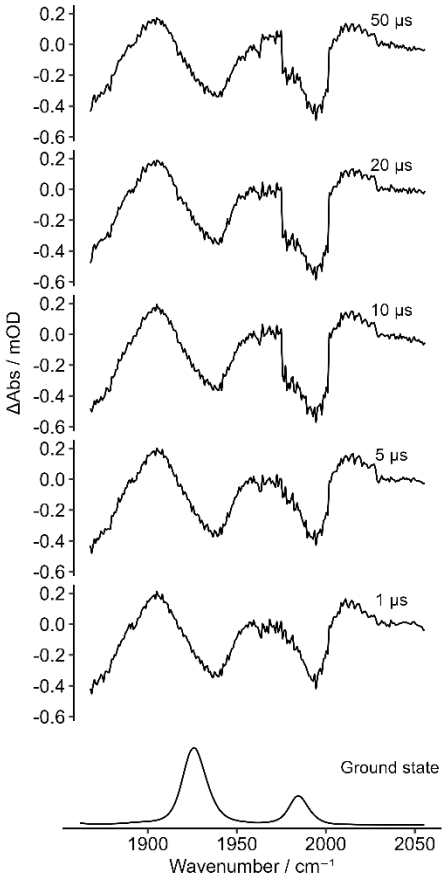

*Figure 95 – Longer-timescale difference peaks resulting from excitation of **157** in the presence of acetonitrile at 355nm.*

Reaction in the presence of an excess of acetonitrile led to the observation of new long-lived transients, demonstrating the presence of acetonitrile adducts bound in the metal-carbonyl environment (Figure 95). Comparison of the difference spectrum at 10 nanoseconds post-excitation of **157** with the vibrational spectra of simulated isomers of the acetonitrile-coordinated photoproduct **157 PP4** (Figure 96) showed that although CO-loss is understood to occur at the position opposite the semibridging carbonyl, the final structure of **157 PP4** features the acetonitrile at the alternate position on the same molybdenum centre, implying a pseudorotation occurs during the ultrafast process to give **157 PP4 iso3** as the final product.

As observed in the spectrum of **157 PP3 iso3**, there is a transient band overlapping the bleach at 1935cm^{-1}, attenuating the intensity of the bleach.

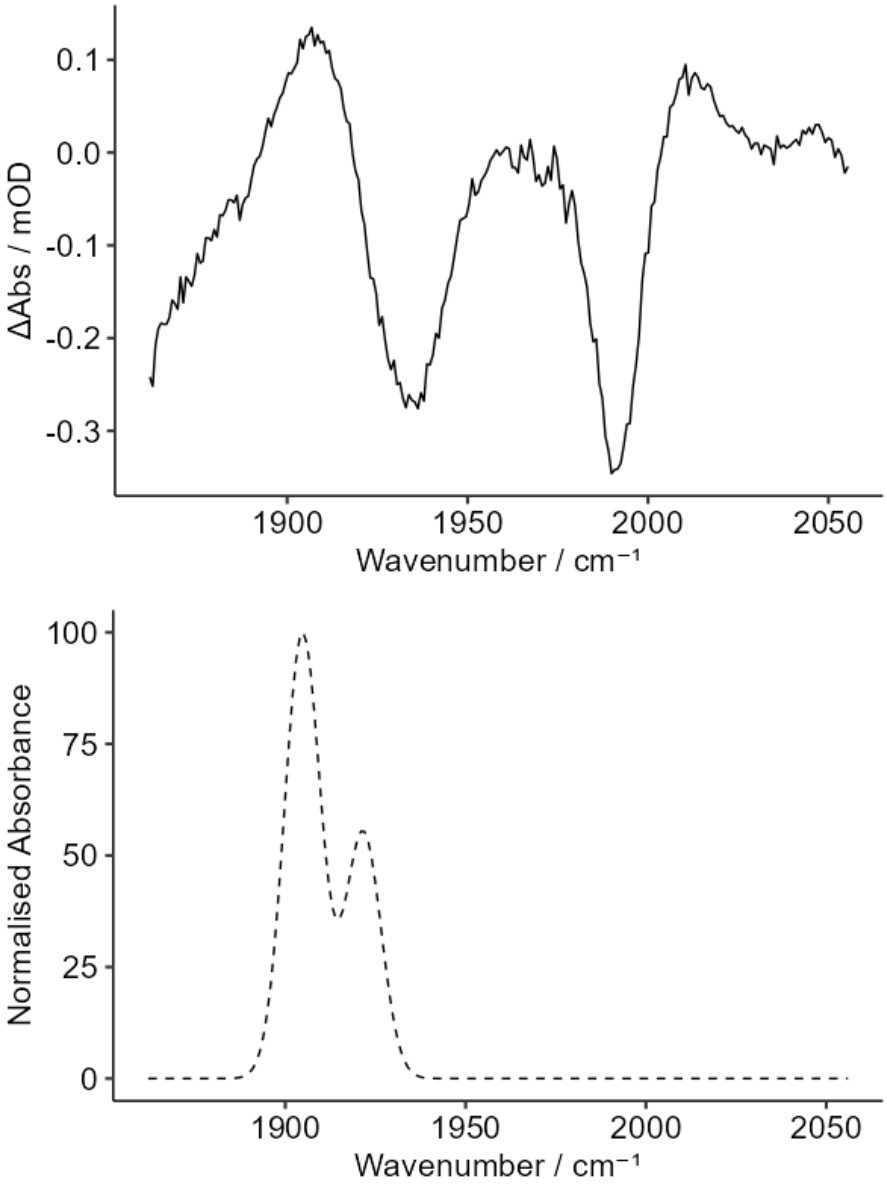

*Figure 96 - Top: Difference spectrum 10ns after excitation of **157** at 355nm in the presence of acetonitrile. Bottom: The scaled simulated spectrum of **157 PP4 iso3**.*

As expected, the formation of the acetonitrile adduct is more favourable than the water-coordination pathway, with the acetonitrile adduct demonstrating an energetic stabilisation of 52 kJ mol^{-1} compared to the DCM adduct **157 PP2**.

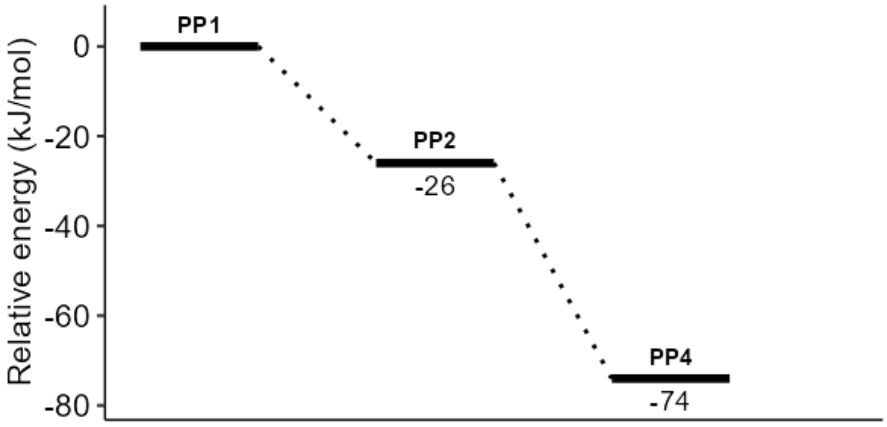

*Figure 97 - Calculated Gibbs energies (BP86-SV(P)) with DFT-D3 dispersion correction and COSMO-DCM solvent correction of the photoproducts of **157** following excitation at 355nm in the presence of acetonitrile.*

4.4. Summary and conclusions

A set of bimetallic carbonyl alkyne compounds were synthesised and studied by ultrafast IR methods. In all cases, metal-metal bond homolysis was observed, highlighting the labile nature of this interaction. The kinetics of bond homolysis in dimolybdenum species were found to be generally comparable to cobalt species studied here and previously described in the literature. Unlike cobalt species, dicyclopentadienyl molybdenum tetracarbonyl alkynyl dimers were able to undergo CO-loss when excited at high-energy wavelengths. The orbital transitions associated with this CO loss have been described for the first time for this system, deepening the understanding into a photochemically accessible regime. In particular, the nature of the alkyne has been shown to play a role on the available transitions facilitating MLCT for these molybdenum complexes, opening the way to tuneable photochemistry based on alkyne, which can to a certain extent be predicted using calculated orbital properties. The post-photolysis pathway has been described in detail, with observed long-lived products identified via vibrational spectrum simulation utilising a bespoke scaling factor for metal carbonyl frequencies.

Overall, this work offers insight into the depth of photochemistry available to dicyclopentadienyl dimolybdenum tetracarbonyl alkyne complexes, and their ability to undergo selective CO loss under irradiation. These finding suggest that these species may be active in photochemical PKR conditions, perhaps more so than cobalt analogues. Furthermore, demonstration of the similarly labile nature of the metal-metal bond across the full set of these complexes supports the reasoning that considering the intermetal interaction similarly to a single covalent bond is not an accurate description, and that PKR precursor complexes should sometimes be considered as singlet diradical species, especially in the context of theoretical computational studies. As shown by Pryce and co-workers, implication of radical cobalt centres in PKR mechanisms allows for alternate pathways to be considered.

Chapter 5: Conclusions and Future Work

5.1. Conclusions

The work described in this thesis has focused on the application of a range of techniques to understand the mechanism and regioselectivity of the PKR, with the overarching goal of gleaning mechanistic understanding which have historically been challenging to gather through other methods.

In Chapter 2, the question of regioselectivity concerning electronically imbalanced internal alkenes was investigated, and literature data was used to train a series of statistical models to draw a relationship between reagent parameters and reaction outcomes. This approach was able to successfully identify systematically unusual regioselectivities for a subset of the data, highlighting the disruptive influence of heterocyclic substituents containing donor functionalities at the 2-position on the regiochemical outcome of the reaction. In these cases, the proportion of β-heterocyclic product observed experimentally was higher than that predicted by the model. The exclusion of these cases from the dataset allowed for the building of a model with a good predictive ability for unseen test cases, with the best performing model able to achieve a Leave-One-Out Cross Validation (LOOCV) RMSE of 5.5%. Comparison between a multicomponent linear model and a Random Forest machine learning approach was undertaken, revealing that with the data surveyed, the methods were generally comparable in their predictive accuracy. The observed anomalous selectivity of heterocyclic substituents for the β position of the cyclopentenone ring led to the formation of a hypothesis that interactions from the heteroatom may play a part in non-symmetrically stabilising the alkene insertion transition state adjacent to the heterocyclic group, facilitating this insertion over that on the opposite side. This unsymmetrical stabilisation would have the effect of increasing the proportion of β product compared to that which would be predicted using the electronic and steric parameters available to the model.

This hypothesis was investigated in Chapter 3, where a model reaction system based on substrate **131** was employed. This substrate, which had previously been found in previous work to be fully β-pyridyl selective, was observed by *in-situ* IR spectroscopic methods, which enabled the observation of metal carbonyl species within the reaction mixture. Observation of a series of reactions with this model system yielded some unexpected observations. Firstly, following activation of the *in-situ* generated cobalt complex **141** with NMO, complex

regeneration was found to take place, beginning immediately after NMO addition with the bands associated with complex steadily increasing in intensity. As NMO is understood to oxidise CO to CO_2, this recombination of CO to the complex was unexpected. An experiment using a sample of **141** isolated and purified prior to the experiment showed that this complex re-formation did not take place when *in-situ* complexation was not performed, leading to the conclusion that residual CO that is released during complexation of **131** to $Co_2(CO)_8$ remained in the headspace of the reaction vessel and led to the re-formation of **141**. Secondly, following the addition of NMO and the decreasing in intensity of bands associated with the complex **141**, new bands were observed in the *in-situ* IR spectrum. These bands were proposed to arise from the cleavage of the cobalt-cobalt bond of complex **141** to ionic monocobalt species, in the form of cationic alkyne-coordinated cobalt complexes and the cobalt tetracarbonyl $[Co(CO)_4]^-$ anion in processes similar to those reported by Gibson[48] and by Lynam, Fairlamb and co-workers.[133] To further understand the reactivity of these proposed species, DFT potential energy surfaces of cyclopentenone formation pathways based on the proposed monocobalt species were constructed. It was found that in most cases the rate-determining states of the monocobalt pathways were the transition state to form the initial cobaltacycle and early coordinatively-saturated pre-cyclisation states, which represented an energy barrier of between 84 and 124 kJ mol^{-1} for the pathways surveyed. It was found that the highest barrier for the dicobalt-based Magnus mechanism was lower, at 76 kJ mol^{-1}. Therefore, if dicobalt-alkyne complexes were present in solution then this pathway would be favoured. In conclusion, it appears that the pathway followed may depend strongly on the cobalt complex speciation in solution.

Given the capacity for the newly-observed species to re-form complex **141** when CO was present in the system, it was hypothesised that re-combination of the proposed monocobalt intermediates into dicobalt species may be a pathway that would allow for the ionic species to form Magnus pathway intermediates. Conversely, if re-combination was not possible in the absence of CO, reactivity about a monocobalt centre would occur. More research to understand this speciation is required, as it could represent an underexplored facet of the reactivity of cobalt-alkyne compounds.

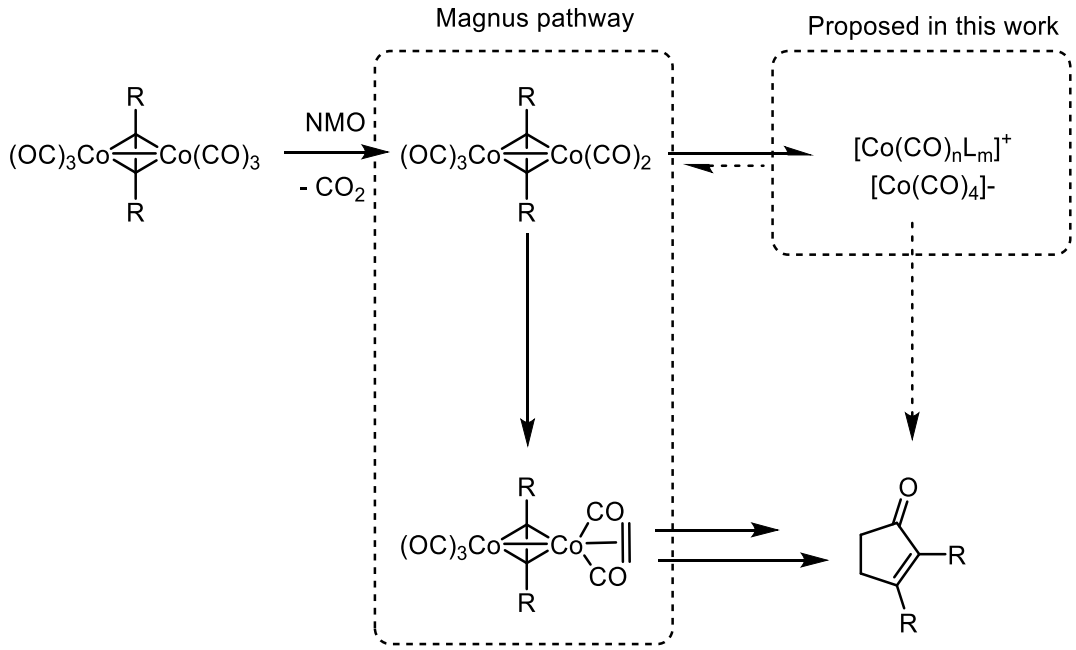

Scheme 79 - Suggested additional cobalt speciation discussed in Chapter 3.

Further investigation into metal-metal bonding in these complexes was undertaken in Chapter 4, where ultrafast time-resolved IR (TRIR) techniques were used to probe the bonding interaction. Excitation of compounds **141** and **146** at 400nm showed that cobalt-cobalt bond homolysis occurred on comparable timescales with literature investigations of similar compounds. Furthermore, in accordance with literature findings, carbonyl photodissociation was not observed. The use of the pyrone carbonyl as a reporting group was also able to provide information about the alkyne environment during and after the homolysis process, confirming the reversibility of the process.

A model molybdenum-based analogue system was developed and studied by TRIR. These studies revealed wavelength-dependent carbonyl photodissociation, with a similar molybdenum-molybdenum breathing mode present. DFT excited-state calculations allowed for the assignment of the transitions accessible at each wavelength, showing that excitation at 355nm allows for population of orbitals on carbonyl ligands, in a metal-ligand charge transfer (MCLT) process, promoting photodissociation. Differing levels of photodissociation were observed between complexes **157** and **158**, which was assigned to the pyrone group altering the structure of the virtual orbitals in the complex, hindering the MLCT process for **158**.

The post-photolysis reactivity of the complexes was investigated, with scaled simulated spectra used to assign the newly observed species in the TRIR as water-coordinated

tricarbonyl complexes. Acetonitrile was used a coordinating ligand and found to form the acetonitrile adduct of the tricarbonyl complex, which could be detected by an alteration in the metal carbonyl environments. This showed that the metal carbonyl environments can be used as diagnostic probes in this system for the coordination state at the metal centre and could in future be used to observe PKR intermediate events on an ultrafast timescale.

5.2. Future work

A reliable protocol for an intermolecular cobalt-catalysed PKR for complex substrates such as heterocyclic internal alkynes would represent a valuable synthetic tool, which would allow for highly efficient synthesis of functionalised materials. One of the obstacles to the development of such a process is the regiochemical uncertainty inherent in this type of intermolecular PKR.

Further studies to address this limitation could focus on the statistical methodology presented in this work. The expansion of this approach with a broader range of data would allow the model to provide better predictive judgement about a wider range of substrates, and with more accuracy. Specifically, the inclusion of a more sterically diverse dataset would allow for a better understanding of the fine balance between steric and electronic factors in the PKR for substrates for which regiochemistry is dictated by the balance of these effects, and go some way towards providing a unified predictive theory which could be applied to any intermolecular PKR system with a high degree of accuracy.

The application of *in-situ* IR has been shown to readily provide unique insights into the PKR reaction environment, and could be employed more widely on investigations into the reaction. While well-applied in the general field of the mechanistic study, in a PKR setting *in-situ* IR is underused for determining metal complex resting states and overall reaction kinetics. The application of this technique to the PKR could allow for more in-depth analysis of a rather difficult-to-study mechanism.

The proposed monocobalt speciation in this work has implications for the cobalt-mediated PKR which warrant further study. First and foremost, the exact nature and structure of these intermediates should be ascertained. Secondly, as detailed in Section 3.8, an important unknown factor limiting understanding of the reactivity taking place is the exact mechanism of the re-formation of complex **141** when CO is present in the system. Understanding the order of steps in this process would shed light on whether recombination to afford a pentacarbonyl intermediate is a possible, enabling Magnus reactivity from monocobalt starting materials, or if only monocobalt centred pathways are available following cobalt-cobalt bond cleavage.

Furthermore, as theoretical investigations have suggested that reaction about these cationic cobalt centres is possible (albeit with a higher energy barrier compared to Magnus reactivity), investigations should be undertaken into improving the capability of these species to perform the PKR. There may be advantages inherent to a monocobalt-centred pathway which are not accessible to a dicobalt pathway. For instance, the coordination-dependent selectivity detailed for a rhodium system by Baik, Evans and co-workers[69] would be difficult to attain with a dicobalt system, but more attainable with a monocobalt-centred pathway.

Finally, TRIR investigations with molybdenum-based systems have shown that measurable photodissociation is achievable at ultrafast timescales, demonstrating their suitability as models of PKR-relevant substrates which can be studied using ultrafast methods, potentially paving the way for further ultrafast investigations of the process. Similarly, these results would imply that a light-activated PKR using molybdenum may be more efficient than cobalt-based photochemical systems, as CO photodissociation is more accessible. This implication should be investigated further.

Chapter 6: Experimental

6.1. General experimental details

6.1.1. Solvents and reagents

Dry dichloromethane, toluene, hexane and pentane were collected from a Pure Solv MD-7 solvent purification system (SPS), and stored in oven dried ampoules under an atmosphere of N_2. Commercially available solvents and reagents were purchased from Sigma Aldrich, Acros Organics, Alfa Aesar, Apollo Scientific or Tokyo Chemical Industries, and were used without further purification unless stated otherwise.

6.1.2. Chromatography

Thin-layer chromatography was performed using Merck aluminium-backed 5554 silica plates. Fraction spots were visualised using short-wave UV irradiation (254nm). Flash column chromatography was carried out either following the established procedure[161] using Supelco 60 Å pore-size silica gel (purchased from Sigma Aldrich), or using a Teldyne ISCO CombiFlash Rf automated separations system, equipped with Teldyne RediSep pre-packed silica columns (4 or 12g silica).

6.1.3. IR spectroscopy

IR spectra were recorded on a Thermo-Nicolet Avatar 370 solution-phase FTIR, or a Bruker ALPHA FTIR system equipped with either a platinum ATR crystal module or a transmission solution phase FTIR model.

6.1.4. Nuclear magnetic resonance spectroscopy

^{1}H and ^{13}C NMR spectroscopic measurements were carried out using a Bruker AV500 spectrometer (500 MHz ^{1}H, 126 MHz ^{13}C) or a Bruker S600 spectrometer (600 MHz ^{1}H, 150 MHz ^{13}C). All spectra were recorded at a probe temperature of 298 K. Spectra were processed in MestReNova software version 14.3.2-32681. Chemical shifts are reported in ppm and referenced to residual proteo-solvent in the sample.

NMR signals were assigned using the following abbreviations: s (singlet), d (doublet), t (triplet), q (quartet), m (multiplet, unresolved), ph (phenyl), pyrid (pyridyl), Cp (cyclopentadienyl).

6.1.5. Mass spectrometry

Mass spectra were recorded using a Bruker Daltronics micrOTOF MS with electrospray ionisation (ESI) by Dr Karl Heaton (University of York). Data are quoted as mass-to-charge ratio (m/z) in Daltons, and are reported with ion assignment.

6.1.6. Single-crystal X-ray diffraction

Diffraction data were collected at 110 K on an Oxford Diffraction SuperNova diffractometer with Cu-Kα radiation (λ = 1.54184 Å) or Mo-Kα radiation (λ = 0.71073 Å), using an EOS CCD camera. The crystal was cooled with an Oxford Instruments Cryojet. Diffractometer control, data collection, initial unit cell determination, frame integration and unit-cell refinement was carried out with CrysAlisPro software. Face-indexed absorption corrections were applied using spherical harmonics, implemented in SCALE3 ABSPACK scaling algorithm. OLEX2 was used for overall structure solution and refinement.[162] Within OLEX2, the algorithm used for structure solution was "ShelXT dual-space".[163] Refinement was carried out by full-matrix least-squares used the SHELXL-97[164] algorithm within OLEX2. All non-hydrogen atoms were refined anisotropically, and hydrogen atoms were placed using a riding model.

6.1.7. UV-Visible spectroscopy

UV-visible spectroscopy was carried out using a Jasco V560 spectrometer, and quartz cuvettes with path length 10 mm. A background of the appropriate solvent was acquired before sample acquisition.

6.1.8. Time-Resolved Multiple Probe Spectroscopy (TR^MPS) measurements

TR^MPS measurements were carried out at the Central Laser Facility (CLF) at the Rutherford Appleton Laboratories. Experiments were conducted using conditions previously reported by the group[165], reproduced below:

For the LIFEtime spectrometer, the pump source was the output of a Yb:KGW amplifier providing 15W, 260 fs pulses at 1030 nm with a 100 kHz repetition rate (Pharos). This was

used to drive a BBO-based 515 nm pumped optical parametric amplifier (OPA) to deliver pulses at 355 nm. The pump beam was collimated, travelled over a computer programmable 0 - 16 ns optical delay (1200 mm long, double pass), and focused onto the sample. The pump energy at the sample was attenuated down to 500 nJ and focused down to a 120 × 120 µm2 spot. The probe source was the output of a Yb:KGW amplifier providing 6 W, 180 fs pulses at 1030 nm with a 100 kHz repetition rate (Pharos). This drove two 3 W BBO/KTA based OPAs. The two Pharos sources share a common 80 MHz oscillator to allow for pump-probe delay steps of 12.5 ns. The probe beam was split to provide probe and reference pulses. To go beyond pump-probe delays of 12.5 ns, subsequent seed pulses were selected from the 80 MHz oscillator. Data were collected using pump-probe delays ranging from 1 ps to 988.5 µs. The probe beams were collimated, synchronised by a fixed optical delay, and focused by a gold S19 parabolic mirror onto the sample. The three beams were overlapped on the sample using a 50 µm pinhole. The probe beams were measured by two separate 128-element detectors. To cover the full spectroscopic window required, data from different detector positions were combined to generate the required spectra.

Solutions of the cobalt complexes were prepared by dissolution of 19.5 mg of complex in 20 ml of DCE, in a thick walled Duran flask.

Solutions of molybdenum complexes were prepared by using 6-12 mg of complex in 12 mL of DCM, in a thick walled Duran flask

The solutions were then flowed (peristaltic pump) through a Harrick cell fitted with a 100 µm Teflon spacer. To ensure that the photoproducts were not themselves irradiated, data were acquired while continuously flowing and rastering the samples.

Collected spectra were initially processed in the ULTRA View 2 software, where negative timepoint spectra were subtracted, and a second-order polynomial baseline applied (in instances where detector drift which would perturb baseline fitting was not present). The data were exported as a text file which was further processed and plotted in Rstudio. Exponential fits for peak lifetimes were performed using the “nls()” (nonlinear-least-squares) function, and are reported as xx ± yy, where xx is the model parameter and yy is the parameter standard error.

6.2. Computational procedures for parameterisation

Geometries of alkynes for parameterisation were optimised at the BP86/SV(P) level of theory using the Turbomole V6.4 software package[166], employing the resolution of identity (RI) approximation. Following the (RI)BP86/SV(P) optimisation, single point energy calculations were performed at the B3LYP/DGTZVP level of theory using the Gaussian 09 software package to produce an NBO7 input file. The NBO7 program was used to generate atomic point charges and Lewis structure perturbation energies.

6.3. Computational procedures for the construction of potential energy surfaces (PESs)

All geometries were optimised at the (RI)BP86/SV(P) level of theory, with frequency calculation. Following geometry optimisation, single-point calculations were performed to apply dispersion correction (Grimme's DFT-D3[167]) and solvation energy correction (COSMO CH_2Cl_2, ε = 8.93 at 298 K) to the energy of the optimised geometry. Corrections were applied for thermal energies and entropies. Energies discussed are relative Gibbs energies, calculated using these corrections. For all calculated minima, vibrational frequency analysis confirmed the absence of negative "imaginary" frequencies.

Where charged cobalt complexes were investigated, the species were modelled as singlet-state cationic structures, with no explicit counterion.

Transition states were optimised using a constrained optimisation along the reaction coordinate, to identify imaginary frequencies corresponding to the target transformation. After the identification of the transition vector, a transition state optimisation was performed to follow the transition vector to the energy maximum saddle point. The identity of the resulting state was confirmed by the presence of a single imaginary frequency, corresponding to movement along the reaction coordinate.

6.4. General synthetic procedures

6.4.1. General Sonogashira coupling procedure

Aryl Bromide (1 eq.) was added to an evacuated and purged Schlenk flask under nitrogen, followed by dry acetonitrile (15 mL/mmol), dry triethylamine (10 eq.), $PdCl_2(PPh_3)_2$ (1 mol %) and CuI (3 mol %). The arylacetylene (1.2 eq) was added and the reaction heated at reflux for 16 h. On completion, the reaction mixture was diluted with water and extracted with ethyl acetate. The combined organic fractions were washed with brine, dried over $MgSO_4$ and the

solvent removed *in vacuo*. The products were purified by column chromatography on silica gel (hexane/ethyl acetate) to afford the pure alkyne.

6.4.2. General cobalt complexation procedure

An equimolar mixture of alkyne and dicobalt octacarbonyl were stirred in dry THF (6 mL per mmol) for 16 h. The solvent was removed *in vacuo*, and the crude product taken into DCM and filtered through Celite™. The filtrate was pre-adsorbed onto silica gel and concentrated by rotary evaporation. The pure product was eluted from the silica gel with ethyl acetate/hexane to afford the pure complex.

6.5. Synthetic procedures

6.5.1. Synthesis of 6-methyl-4-bromo-2-pyrone (159)[168]

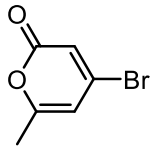

A two necked round-bottomed flask evacuated and backfilled three times with nitrogen, then was charged with 6-methyl-4-hydroxy-2-pyrone (10.58 mmol, 1.33 g), dry toluene (60 mL), phosphorus pentoxide (25.18 mmol, 3.57 g), tetrabutylammonium bromide (12.27 mmol, 3.95 g). A condenser was fitted and the reaction mixture brought to reflux. After 16 hours, the reaction mixture was cooled and diluted with water (50 mL), before being extracted with toluene (3 x 40 mL). The combined organic layers were washed with brine and dried over magnesium sulfate. The solvent was removed *in-vacuo*, and the crude material dissolved in boiling hexane to form a saturated solution. Cooling of the saturated solution gave the product as peach-coloured crystals (1.13 g, 56%).

δ H (600 MHz, $CDCl_3$) 2.25 (3 H, s, CH_3), 6.19 (1 H, d, J 1.7), 6.51 (1 H, d, J 1.7).

δ C (151 MHz, $CDCl_3$) 19.9 (CH_3), 108.6 (CH), 114.9 (CH), 141.3 (4^o), 160.8 (4^o), 162.2 (4^o).

ESI-MS: calcd for $C_6H_5BrNaO_2$ 210.9365, found 210.9368 [M+Na]

6.5.2. Synthesis of 6-methyl-4-(2-pyridylethynyl)-2-pyrone (131)[114]

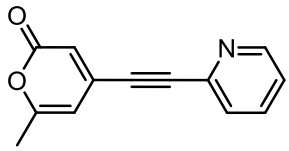

Synthesised according to general procedure 6.4.1, with 6-methyl-4-bromo-2-pyrone (4.74 mmol, 0.896 g) and 2-ethynylpyridine (5.86 mmol, 0.586 g). Column chromatography (silica, 60:30 EtOAc:hexane, R_f = 0.25) gave the product as an off-white powder (0.833 g, 83%)

δ H (600 MHz, CD_2Cl_2) 2.25 (3 H, s), 6.10 (1 H, s), 6.33 (1 H, s), 7.33 (1 H, dd, J 7.7, 4.9), 7.56 (1 H, d, J 7.8), 7.74 (1 H, td, J 7.7, 1.8), 8.63 (1 H, d, J 4.9).

δ C (151 MHz, CD_2Cl_2) 19.8 (CH_3), 83.9 (4°), 96.4 (4°), 104.8 (CH), 115.4 (CH), 124.1 (CH), 128.0 (CH), 136.3 (CH), 137.9 (4°), 141.7 (4°), 150.4 (CH), 161.5 (4°), 162.5 (4°).

ESI-MS calcd for $C_{13}H_{10}NO_2$: 212.0706, found 212.0714. [M+H]

Slow vapour diffusion of hexane into a DCM solution of the product gave crystals suitable for X-ray diffraction

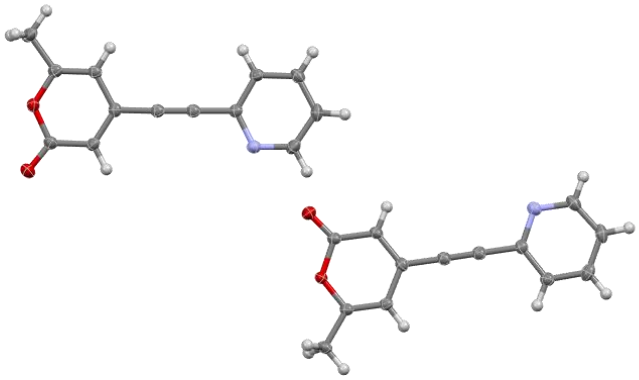

6.5.3. Synthesis of 6-methyl-4-(phenylethynyl)-2-pyrone (129)[112]

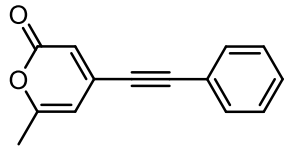

Synthesised according to general procedure 6.4.1, with 6-methyl-4-bromo-2-pyrone (2.38 mmol, 0.449 g) and phenylacetylene (2.85 mmol, 0.292 g). Column chromatography (silica, 20:80 EtOAc:hexane, R_f = 0.28) gave the product as a yellow powder (0.22 g, 44%)

δ H (600 MHz, CD_2Cl_2) 2.28 (3 H, s, CH_3), 6.10 (1 H, s, pyrone-H), 6.29 (1 H, s, pyrone-H), 7.41 – 7.47 (2 H, m, Ph), 7.45 – 7.51 (1 H, m, Ph), 7.57 – 7.62 (2 H, m, Ph).

δ C (151 MHz, CD_2Cl_2) 19.7 (4°), 85.3 (4°), 98.1 (CH), 105.1 (CH), 114.3 (CH), 121.3 (CH), 128.6 (CH), 129.9 (CH), 132.1 (CH), 138.7 (4°), 161.8 (4°), 162.2 (4°).

ESI-MS: Calcd for $C_{14}H_{11}O_2$: 211.0758, found 211.0754 [M+H]

Slow vapour diffusion of hexane into a DCM solution of the product gave crystals suitable for X-ray diffraction.

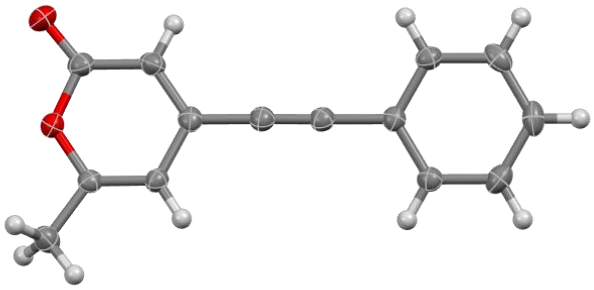

6.5.4. Synthesis of 2-(phenylethynyl) pyridine (123)[112]

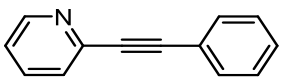

Synthesised according to general procedure 6.4.1, with 2-bromopyridine (1.12mmol, 0.175g) and phenylacetylene (1.34mmol, 0.139g). Column chromatography (silica, 20:80 EtOAc:hexane, R_f = 0.20) gave the product as a yellow oil (101mg, 50%)

δ H (600 MHz, $CDCl_3$) 7.23 – 7.25 (1 H, m, Ph), 7.37 (3 H, dd, J 5.2, 1.9, Ph), 7.54 (1 H, d, J 7.8, Ph), 7.61 (2 H, dd, J 7.1, 1.9, pyrid), 7.69 (1 H, td, J 7.7, 1.8, pyrid), 8.63 (1 H, s, pyrid).

δ C (151 MHz, $CDCl_3$) 88.6 (4°), 89.3 (4°), 122.3 (4°), 122.8 (CH), 127.2 (CH), 128.4 (CH), 129.0 (CH), 132.1 (CH), 136.2 (CH), 143.5 (4°), 150.1 (CH).

ESI-MS: Calcd for $C_{13}H_{10}N$: 180.0808, found 180.0809 [M+H]

6.5.5. Synthesis of η^2-[(6-Methyl-4-(2-pyridylethynyl))-2-pyrone]-hexacarbonyl dicobalt (141)[114]

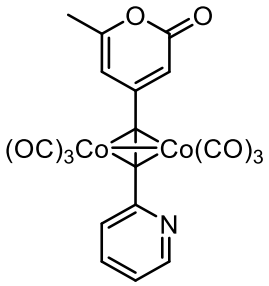

Synthesised according to general procedure 6.4.2, using 6-methyl-4-(2-pyridylethynyl)-2-pyrone (1 mmol, 0.213 g) and dicobalt octacarbonyl (1 mmol, 0.344 g). Column chromatography (silica, 20:80 EtOAc:hexane, R_f = 0.28) gave the product as a red crystalline solid (0.358 g, 72%).

δ H (600 MHz, CD_2Cl_2) 2.27 (3 H, s, CH_3), 6.26 (1 H, s, pyrone), 6.56 (1 H, s, pyrone), 7.24 – 7.29 (1 H, m, pyridyl), 7.55 (1 H, d, J 7.9, pyridyl), 7.72 (1 H, t, J 7.7, pyridyl), 8.63 (1 H, d, J 4.8, pyridyl).

δ C (151 MHz, CD_2Cl_2) 19.8 (CH_3), 84.4 (4°), 92.3 (4°), 105.1 (CH), 110.5 (CH), 122.4 (CH), 124.6 (CH), 136.8 (CH), 150.1 (CH), 156.1 (4°), 157.0 (4°), 161.6 (4°), 162.5 (4°), 198.2 (4°).

ESI-MS: calcd for $C_{19}H_{10}Co_2NO_8$: 497.9064, found 497.9065 [M+H]

FTIR (CH_2Cl_2, cm^{-1}): 2098, 2066, 2037 (M-CO), 1715 (org-CO)

Evaporation of DCM gave crystals suitable for X-ray diffraction.

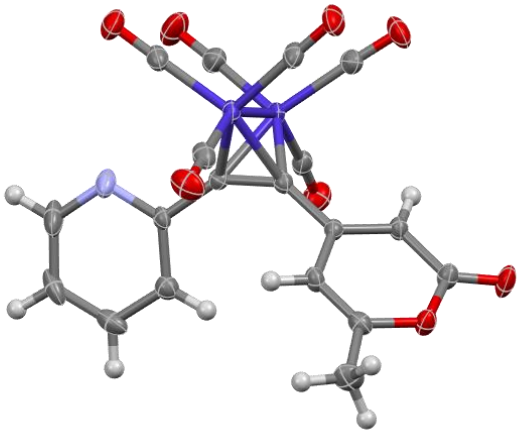

6.5.6. Synthesis of η²-[(6-Methyl-4-(2-(phenylethynyl))-2-pyrone]-hexacarbonyl dicobalt (146)[169]

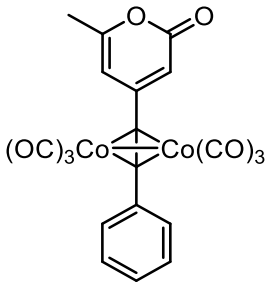

Synthesised according to general procedure 6.4.2, with 6-Methyl-4-(2-(phenylethynyl))-2H-pyran-2-one (1 mmol, 0.211 g) and dicobalt octacarbonyl (1 mmol, 0.345 g). Column chromatography (silica, 20:80 EtOAc:hexane, R_f = 0.44) gave the product as a black crystalline solid (0.264 g, 62%).

δ H (600 MHz, CD_2Cl_2) 2.25 (3 H, s, CH_3), 5.98 (1 H, s, pyrone), 6.31 (1 H, s, pyrone), 7.33 – 7.42 (3 H, m, Ph), 7.49 – 7.56 (2 H, m, Ph).

δ C (151 MHz, CD_2Cl_2) 19.8 (CH_3), 104.6 (CH), 110.0 (CH), 128.5 (CH), 129.2 (CH), 129.3 (CH), 137.1 (CH), 156.8 (CH), 161.8 (CH), 162.3 (CH) (Note: Signals for quaternary carbons could not be detected above the spectrum noise level for this compound)

ESI-MS: calcd for $C_{20}H_{11}Co_2O_8$: 496.9112, found 496.9108 [M+H]

FTIR (CH_2Cl_2, cm^{-1}): 2096, 2062, 2035 (M-CO) 1715 (Org-CO)

Slow vapour diffusion of hexane into a DCM solution of the product gave crystals suitable for X-ray diffraction.

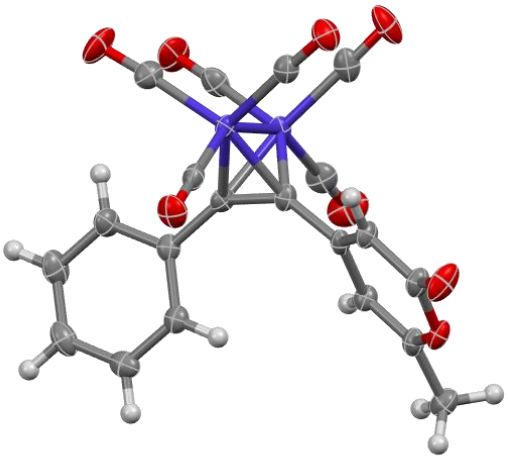

6.5.7. Synthesis of η²-[2-(phenylethynyl)pyridine)]-hexacarbonyl dicobalt (145)[169]

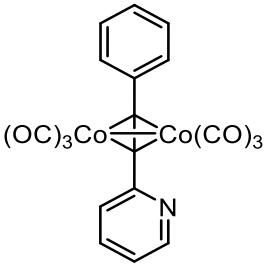

Synthesised according to general procedure 6.4.2, with 2-(phenylethynyl)pyridine (0.64 mmol, 0.115 g) and dicobalt octacarbonyl (0.64 mmol, 0.222 g). Column chromatography (silica, 10:90 EtOAc:hexane, R_f = 0.38) gave the product as a red crystalline solid, (0.152 g, 50%).

δ H (500 MHz, CD_2Cl_2) 7.24 (1 H, s, Ph), 7.37 (3 H, s, overlapped), 7.61 (1 H, s, Ph), 7.70 (1 H, s, pyrid), 7.82 (2 H, s, Ph), 8.65 (1 H, s, pyrid). (Note: Peak broadening from trace paramagnetic degradation products caused peak broadening, leading to overlapping of peaks and loss of splitting patterns)

δ C (126 MHz, CD2Cl2) 91.4 (4°), 91.8 (4°), 121.9 (CH), 122.9 (4°), 124.4 (CH), 128.0 (CH), 128.5 (4°), 128.8 (CH), 129.0 (4°), 129.8 (CH), 132.0 (4°), 136.1 (4°), 136.6 (CH), 138.0 (CH), 150.0 (CH), 158.2 (CH), 199.3 (4°).

ESI-MS: calcd for $C_{19}H_{10}Co_2NO_6$: 465.9167, found 465.9165 [M+H]

FTIR (DCM, cm^{-1}): 2092, 2057, 2029 (M-CO)

Cooling of a saturated heated hexane solution of the product gave crystals suitable for X-ray diffraction.

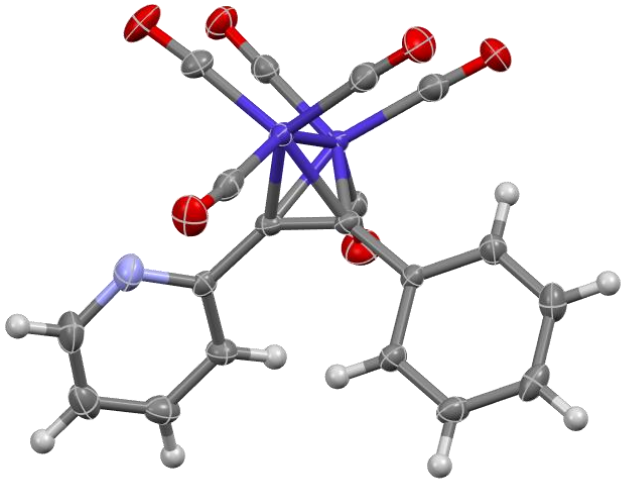

6.5.8. Synthesis of η^2-[diphenylacetylene]-hexacarbonyl dicobalt (142)[169]

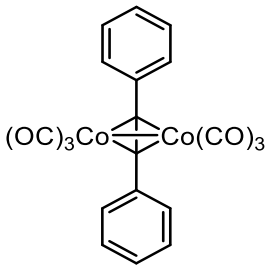

Synthesised according to general procedure 6.4.2, using diphenylacetylene (0.192 mmol, 0.034 g) and dicobalt octacarbonyl (0.192 mmol, 0.065 g). Column chromatography (silica, 10:90 EtOAc:hexane, R_f=0.63) gave the product as a black crystalline solid (56 mg, 56%).

δ H (500 MHz, CD_2Cl_2) 7.38 6 H, m, Ph), 7.63 – 7.71 (4 H, m, Ph).

δ C (126 MHz, CD_2Cl_2) 92.0 (4°), 127.9 (CH), 128.3 (4°), 128.4 (4°), 128.9 (CH), 129.2 (CH), 131.5 (4°), 138.3 (CH), 199.5 (M-CO, br).

Did not fly by ESI-MS

FTIR (DCM cm^{-1}): 2090, 2055, 2026 (M-CO)

Slow vapour diffusion of hexane into a DCM solution of the product gave crystals suitable for X-ray diffraction.

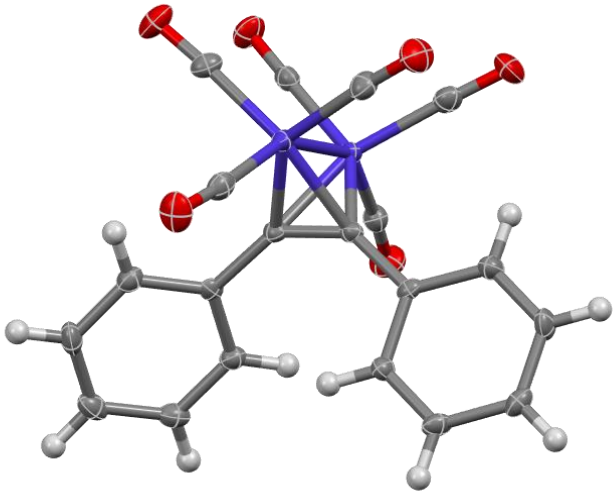

6.5.9. Synthesis of (140) using microwave promotion[114]

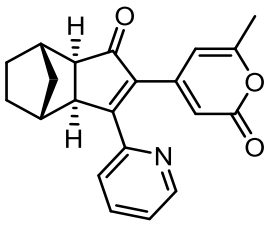

A microwave tube was fitted with a septum and purged with argon, before being charged with η^2-[2(6-Methyl-4-(2-(2-pyridylethynyl))-2-pyrone]-hexacarbonyl dicobalt (0.142 mmol, 0.071 g) and norbornene (0.716 mmol, 67.42 mg) and dichloroethane (1 mL). The reaction mixture was sparged with argon for 10 minutes, then the septum replaced with a microwave cap. The reaction mixture was then heated at 90 °C using microwave heating (95 W) for one

hour. The reaction mixture was then cooled and filtered through celite. The crude reaction mixture was purified by silica column chromatography (silica, 60:40 EtOAc:hexane, R_f = 0.22) to give the product as a waxy yellow solid, which solidified upon standing (0.029 g, 58%).

δ H (500 MHz, CD_2Cl_2) 1.03 (1 H, dt, J 10.7, 1.4), 1.11 – 1.17 (1 H, m), 1.36 – 1.48 (2 H, m), 1.59 – 1.73 (2 H, m), 2.15 (3 H, s), 2.22 (1 H, d, J 3.9), 2.48 (1 H, dd, J 5.5, 1.4), 2.53 (1 H, s), 3.42 (1 H, d, J 5.5), 5.69 (1 H, s), 6.01 (1 H, s), 7.32 (1 H, ddd, J 7.6, 4.8, 1.1), 7.37 (1 H, dt, J 7.9, 1.0), 7.70 (1 H, td, J 7.7, 1.8), 8.70 (1 H, ddd, J 4.8, 1.8, 1.0).

δ C (126 MHz, CD_2Cl_2) 19.8, 28.5, 29.0, 31.5, 38.7, 39.9, 50.4, 104.6, 112.1, 124.4, 124.7, 136.3, 140.0, 148.6, 150.1, 150.1, 152.6, 161.8, 162.4, 171.8, 206.7.

ESI-MS: calcd for $C_{21}H_{19}NNaO_3$: 356.1257 found 356.1269 [M+Na]

Slow vapour diffusion of pentane into a DCM solution of the product gave crystals suitable for X-ray diffraction.

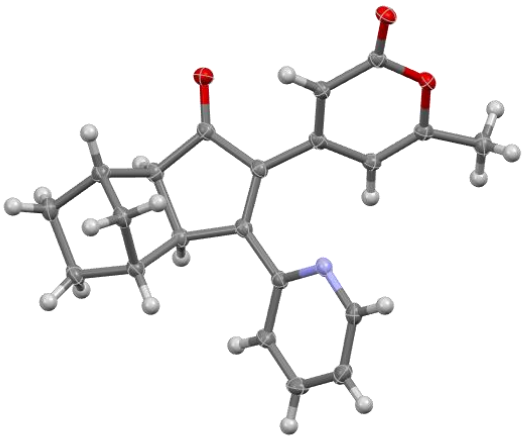

6.5.10. Synthesis of η^2-[diphenylacetylene]-bis-cyclopentadienyl tetracarbonyl dimolybdenum (157)

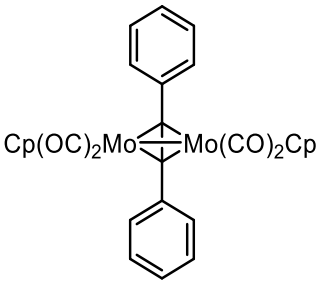

A Schlenk flask was evacuated and backfilled three times with nitrogen, before being charged with dimolybdenum bis-cyclopentadienyl hexacarbonyl (0.16 mmol, 0.076 g), diphenylacetylene (0.19 mmol, 0.034 g) and dry toluene (5 mL). The reaction mixture was brought to reflux and monitored by FTIR of reaction aliquots. When no further molybdenum starting material was detected, the reaction mixture was cooled and the solvent removed *in vacuo*. Column chromatography (silica, 10:90 EtOAc:hexane, R_f=0.35) gave the product as a red powder (0.034 g, 34%).

δ H (500 MHz, CD_2Cl_2) 5.21 (10 H, s, Cp), 7.00 – 7.05 (4 H, m, Ph), 7.07 – 7.13 (2 H, m, Ph), 7.19 – 7.25 (4 H, m, Ph).

δ C (126 MHz, CD_2Cl_2) 0.8 (4°), 31.6 (4°), 93.0 (CH – Cp), 125.3 (CH), 128.0 (CH), 129.4 (CH), 146.0 (CH), 230.6 (M-CO).

ESI-MS: calcd for $C_{28}H_{20}Mo_2O_4$: 615.9464, found 615.9432 [M^+]

FTIR (DCM, cm^{-1}): 1984, 1926, 1842 (M-CO)

Cooling of a hot toluene solution of the product gave crystals suitable for X-ray diffraction.

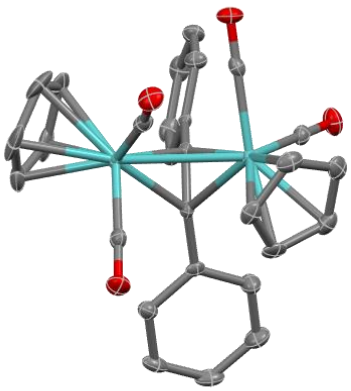

6.5.11. Synthesis of η^2-[(6-Methyl-4-(2-(2-pyridylethynyl))-2H-pyran-2-one]-bis-cyclopentadienyl tetracarbonyl dimolybdenum (158)

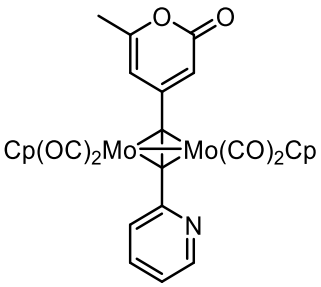

A two-necked round-bottom flask was evacuated and backfilled three times with nitrogen, before being charged with dimolybdenum bis-cyclopentadienyl hexacarbonyl (0.15 mmol, 0.079 g), and anhydrous toluene (5 mL). A Schlenk flask was evacuated and backfilled three times with nitrogen, and charged with 6-Methyl-4-(2-(2-pyridylethynyl))-2-pyrone (0.31 mmol, 0.065 g) and dry toluene (8 mL), and stirred to form an alkyne stock solution. A 2 mL aliquot of the alkyne stock was added to the reaction flask containing the molybdenum starting material, and the reaction mixture heated to reflux. Further aliquots of alkyne stock solution were added over the following 48 hours until the stock was exhausted. Following the final addition of the stock solution, the reaction was heated for a further 12 hours, before being cooled and the solvent removed *in vacuo*. Column chromatography (silica, 0:100 – 20:80 EtOAc:Hexane) give the product as a dark red powder (18mg, 18%).

δ H (500 MHz, CD_2Cl_2) 2.16 (3 H, s, CH_3), 5.24 (10 H, s, Cp), 5.69 (1 H, s, pyrone), 5.73 (1 H, s, pyrone), 6.79 (1 H, dt, J 8.1, 0.9, pyrid), 7.01 (1 H, ddd, J 7.5, 4.8, 1.1, pyrid), 7.52 (1 H, td, J 7.7, 1.9, pyrid), 8.54 (1 H, dq, J 4.9, 0.7, pyrid).

Due to low amounts of product, and long-term instability in solution, ^{13}C NMR data could not be collected for this compound.

ESI-MS: Calcd for $C_{27}H_{20}Mo_2NO_6$: 649.9393 found 649.9401. [M^+]

FTIR (DCM, cm^{-1}): 2011, 1938, 1848 (M-CO), 1705 (Org-CO)

Cooling of a saturated toluene solution of the product gave crystals suitable for X-ray diffraction.

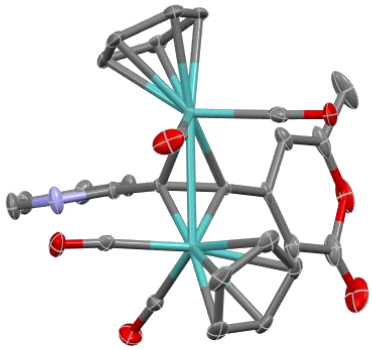

6.6. *In-situ* IR experiments

In-situ IR spectroscopy was performed using a Mettler Toledo ReactIR ic10 system, equipped with a K6 conduit SiComp probe and MCT detector. Data collection and initial processing was performed using Mettler-Toledo proprietary iCIR 7.2 software. Further data processing was carried out using Microsoft Excel and Rstudio.

6.6.1. Reaction of (131) with norbornene, using *in-situ* complexation and 6 equivalents NMO (TT57)

A three-necked round bottomed flask with stir bar was mounted on a clamp stand over a stirrer plate. The ReactIR probe was introduced through a screw-top seal ground glass adapter, and the flask attached to a Schlenk line. The flask was evacuated and backfilled three times with argon, and data collection commenced. DCM (4 mL) and THF (2 mL) were added to the flask, and a solvent background spectrum identified, which was subtracted from subsequent measurements. **131** (0.61 mmol, 0.130 g) and dicobalt octacarbonyl (0.61 mmol, 0.210 g) were added sequentially to the flask and stirred for 30 minutes, while complex formation was observed using the *in-situ* IR probe. After 10 minutes, complexation was seen to be complete, and norbornene (1.22 mmol, 114 mg) was added and the reaction stirred for 10 minutes. NMO (3.69 mmol, 0.432 g) was added to the reaction, and the reaction stirred for 20 hours at room temperature. The reaction mixture was diluted with DCM, and filtered through Celite. The crude material was separated by silica column chromatography (0-50% EtOAC in hexane). The product **140** was recovered as a yellow solid (0.031 g, 15%). NMR

spectroscopy showed that the product consisted of a mixture of two regioisomers in a 0.84:0.16 ratio by NMR. The major component of the product mixture was confirmed to be the β-pyridyl isomer by comparison to the product of the fully β-selective microwave reaction (confirmed by SCXRD).

6.6.2. Reaction of (131) with norbornene, using in-situ complexation and 2 equivalents NMO (TT58)

A three-necked round bottomed flask with stir bar was mounted on a clamp stand over a stirrer plate. The ReactIR probe was introduced through a screw-top seal ground glass adapter, and the flask attached to a Schlenk line. The flask was evacuated and backfilled three times with argon, and data collection commenced. DCM (4 mL) and THF (2 mL) were added to the flask, and a solvent background spectrum identified, which was subtracted from subsequent measurements. **131** (0.61 mmol, 0.129 g) and dicobalt octacarbonyl (0.61 mmol, 0.210 g) were added sequentially to the flask and stirred for 30 minutes, while complex formation was observed using the *in-situ* IR probe. After 10 minutes, complexation was seen to be complete, and norbornene (1.22 mmol, 114 mg) was added and the reaction stirred for 10 minutes. NMO (1.22 mmol, 0.144 g) was added to the flask and the reaction stirred for 20 hours at room temperature. The reaction mixture was diluted with DCM, and filtered through Celite. The crude material was separated by silica column chromatography (0-50% EtOAc in hexane). The product **140** was recovered as a yellow solid (0.027 g, 14%). NMR spectroscopy showed that the product consisted of a mixture of two regioisomers in a 0.81:0.19 ratio by NMR. The major component of the product mixture was confirmed to be the β-pyridyl isomer by comparison to the product of the fully β-selective microwave reaction (confirmed by SCXRD).

6.6.3. Reaction of (131) with norbornene, using in-situ complexation and 3 2 equivalent additions of NMO (TT61)

A three-necked round bottomed flask with stir bar was mounted on a clamp stand over a stirrer plate. The ReactIR probe was introduced through a screw-top seal ground glass adapter, and the flask attached to a Schlenk line. The flask was evacuated and backfilled three times with argon, and data collection commenced. DCM (4 mL) and THF (2 mL) were added to the flask, and a solvent background spectrum identified, which was subtracted from subsequent measurements. **131** (0.61 mmol, 0.129g) and dicobalt octacarbonyl (0.61 mmol,

0.210 g) were added sequentially to the flask and stirred for 30 minutes, while complex formation was observed using the *in-situ* IR probe. After 10 minutes, complexation was seen to be complete, and norbornene (1.22 mmol, 0.114 g) was added and the reaction stirred for 10 minutes. NMO (1.22 mmol, 0.144 g) was added, and the reaction stirred for one hour. Another dose of NMO (1.22 mmol, 0.144 g) was added, and the reaction stirred further for one hour. A final dose of NMO (1.22 mmol, 0.144 g) was added, and the reaction stirred for 20 hours. The reaction mixture was diluted with DCM, and filtered through Celite. Crude NMR spectroscopy showed that two isomers of the product **140** were present in a 0.82:0.18 ratio. The major component of the crude mixture was confirmed to be the β-pyridyl isomer by comparison to the product of the fully β-selective microwave reaction (confirmed by SCXRD). Silica column chromatography (0-50% EtOAc in hexane) yielded the β-pyridyl product as a yellow solid (0.071g, 35%)

6.6.4. Reaction of (141) with norbornene, with 3 2 equivalent additions of NMO (TT81)

A three-necked round bottomed flask with stir bar was mounted on a clamp stand over a stirrer plate. The ReactIR probe was introduced through a screw-top seal ground glass adapter, and the flask attached to a Schlenk line. The flask was evacuated and backfilled three times with argon, and data collection commenced. DCM (4 mL) and THF (2 mL) were added to the flask, and a solvent background spectrum identified, which was subtracted from subsequent measurements. **141** (0.6 mmol, 0.298 g) was added to the reaction flask and stirred for 30 minutes. Norbornene (1.2 mmol, 113 mg) was added to the reaction, and the reaction stirred for 10 minutes. NMO (1.22 mmol, 0.144 g) was added, and the reaction stirred for one hour. Another dose of NMO (1.22 mmol, 0.144 g) was added, and the reaction stirred further for one hour. A final dose of NMO (1.22 mmol, 0.144 g) was added, and the reaction stirred for 20 hours. The reaction mixture was diluted with DCM, and filtered through Celite. The crude material was separated by silica column chromatograpy (0-50% EtOAc in hexane). The product **140** was recovered as a yellow solid (0.037 g, 19%). NMR spectroscopy showed that the product consisted of a mixture of two regioisomers in a 0.85:0.15 ratio by NMR. The major component of the product mixture was confirmed to be the β-pyridyl isomer by comparison to the product of the fully β-selective microwave reaction (confirmed by SCXRD).

6.6.5. Reaction of (141) with norbornene, with 3 2 equivalent additions of NMO performed prior to alkene addition (TT101)

A three-necked round bottomed flask with stir bar was mounted on a clamp stand over a stirrer plate. The ReactIR probe was introduced through a screw-top seal ground glass adapter, and the flask attached to a Schlenk line. The flask was evacuated and backfilled three times with argon, and data collection commenced. DCM (4 mL) and THF (2 mL) were added to the flask, and a solvent background spectrum identified, which was subtracted from subsequent measurements. **141** (0.3 mmol, 0.149 g) was added to the reaction flask and stirred for 30 minutes. NMO (0.6 mmol, 0.070 g) was added, and the reaction stirred for one hour. NMO (0.6 mmol, 0.070 g) was added, and the reaction further stirred for one hour. A final dose of NMO (0.6 mmol, 0.070g) was added, and the reaction stirred for 30 minutes. Norbornene (0.6 mmol, 0.056 g) was added to the reaction, and the mixture stirred for 20 hours. The reaction mixture was diluted with DCM, and filtered through Celite. The crude material was separated by silica column chromatograpy (0-50% EtOAc in hexane). The product was recovered as a yellow solid (0.016 g, 16%). NMR spectroscopy showed that the product **140** consisted of a mixture of two regioisomers in a 0.78:0.23 ratio by NMR. The major component of the product mixture was confirmed to be the β-pyridyl isomer by comparison to the product of the fully β-selective microwave reaction (confirmed by SCXRD).

Appendix 1: Structures of commonly referenced compounds

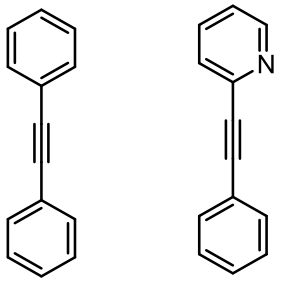

95

123

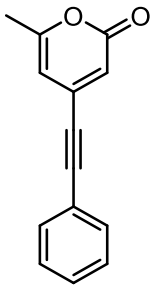

129

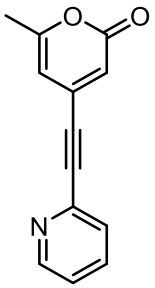

131

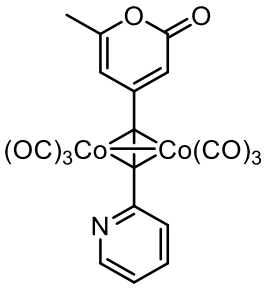

141

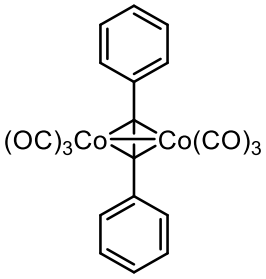

142

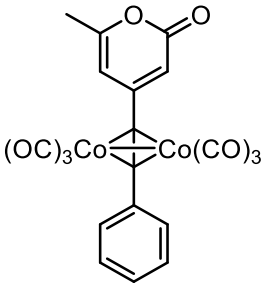

146

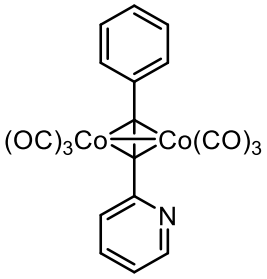

145

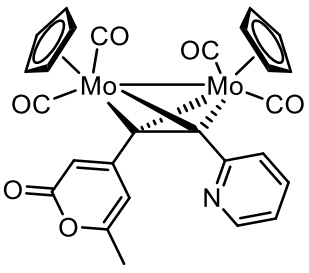

157

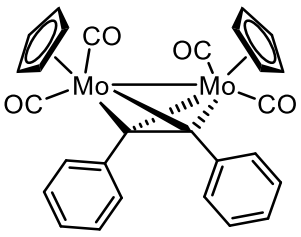

158

Appendix 2: Final dataset used for statistical modelling.

*Table 17 -The calculated parameters of alkynes **101-132** and the literature reported α product proportions, as used in statistical modelling in Chapter 2.*

Compound	deltaC1C4	deltaR	diff_sec	alphaprop
101	0.04	-1.51	100.25	0.43
102	-0.03	1.18	43.49	0.62
103	-0.01	0.54	25.79	0.55
104	-0.01	0.08	21.45	0.50
105	0.03	-1.02	48.86	0.44
106	0.03	-1.30	41.56	0.43
107	0.06	-2.24	83.19	0.40
108	0.04	-1.76	0.31	0.40
109	0.02	-1.22	80.80	0.42
110	0.03	-1.78	33.11	0.38
111	0.07	-2.96	-10.97	0.36
112	0.01	-0.03	12.10	0.48
113	0.03	-1.73	60.66	0.33
114	0.19	-0.19	70.71	0.67
115	0.14	1.02	1.77	0.74
116	0.29	-0.98	-6.52	0.23
117	0.41	-7.11	-0.75	0.05
118	-0.06	0.65	43.90	0.51
119	0.09	-2.95	37.80	0.35
120	0.06	5.95	-19.61	0.95
121	-0.23	5.17	-14.67	0.18
122	-0.13	1.93	-18.06	0.51
123	0.24	-2.68	-0.67	0.10
124	-0.03	-0.21	-0.39	0.36
125	0.04	-2.11	-0.22	0.29
126	0.26	-6.71	47.54	0.25
127	-0.13	0.33	-1.59	0.31
128	-0.04	-2.56	-4.08	0.33
129	-0.10	4.58	-12.44	0.79
130	0.12	2.09	-12.24	0.00
131	0.15	1.51	-12.19	0.00
132	-0.05	2.40	-12.66	0.50

Appendix 3: Characterisation data for compounds.

Spectral data for 6-methyl-4-bromo-2-pyrone (**159**)

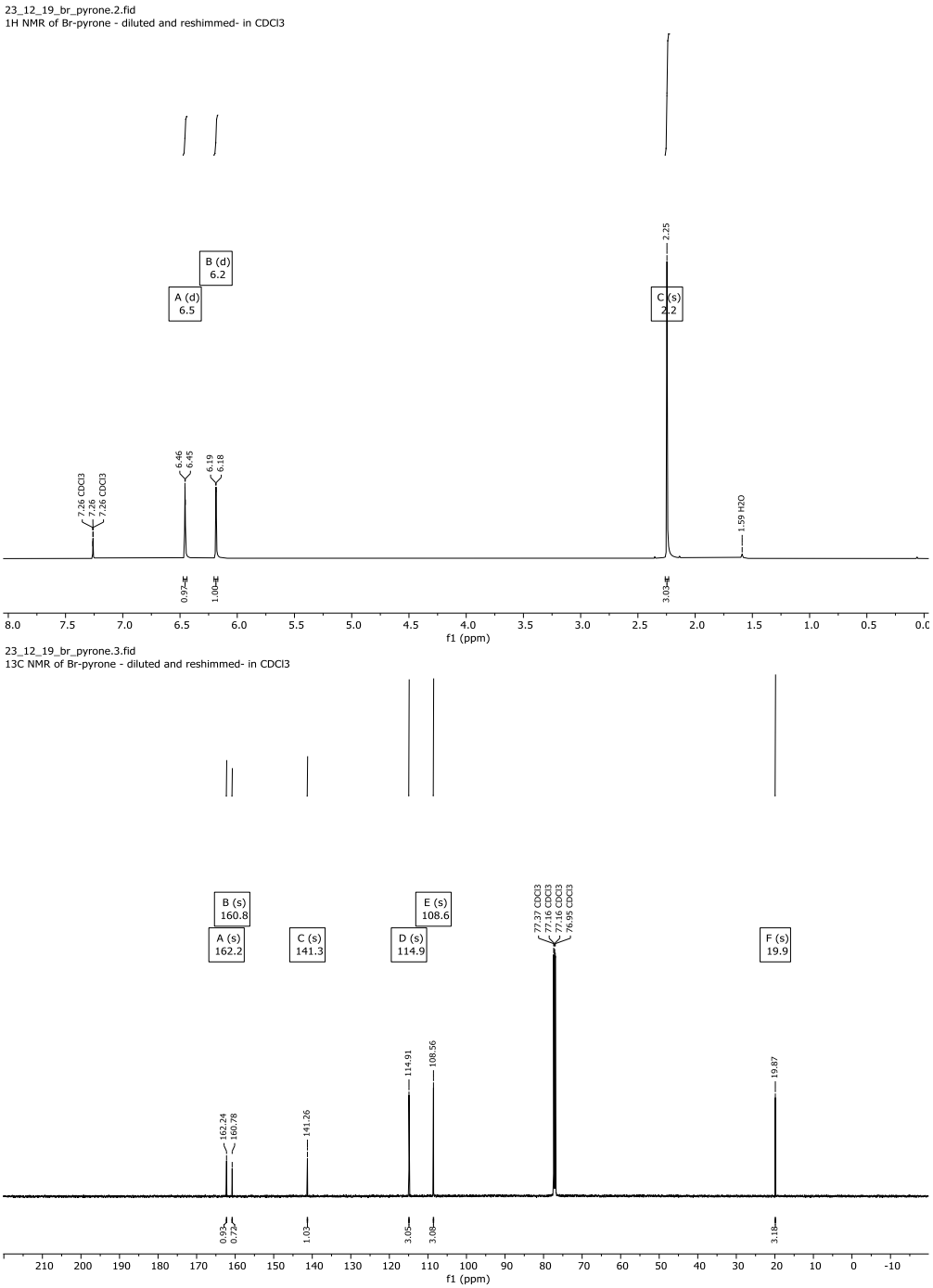

*Figure 98 – ^{1}H (top) and ^{13}C NMR (bottom) of **159** in $CDCl_3$.*

York - Chemistry - Mass Spectrometry Service Report

Br Pyrone_if106024tt

Analysis Information

Analysis Filename	if106024tt_P1-A-5_01_43644.d	Acquisition Date	01/09/2023 12:53:00
Method	ESI_low mass_2c1s.m	Instrument	compact
Submission Name	if106024tt	ESI	Positive

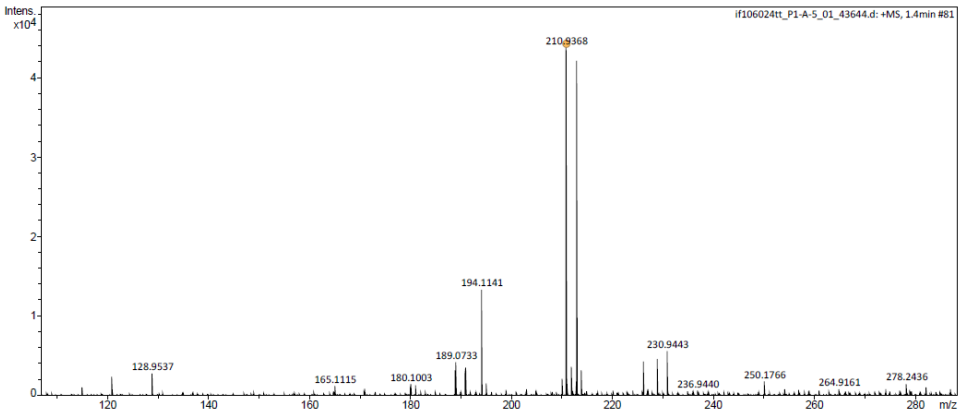

Meas. m/z	#	Ion Formula	m/z	err [ppm]	err [mDa]	mSigma	Mean err [ppm]
210.9368	1	C6H5BrNaO2	210.9365	-1.3	-0.3	12.1	-0.9

*Figure 99 - ESI-MS data for **131**.*

Spectral data for 6-methyl-4-(2-pyridylethynyl)-2-pyrone (**131**)

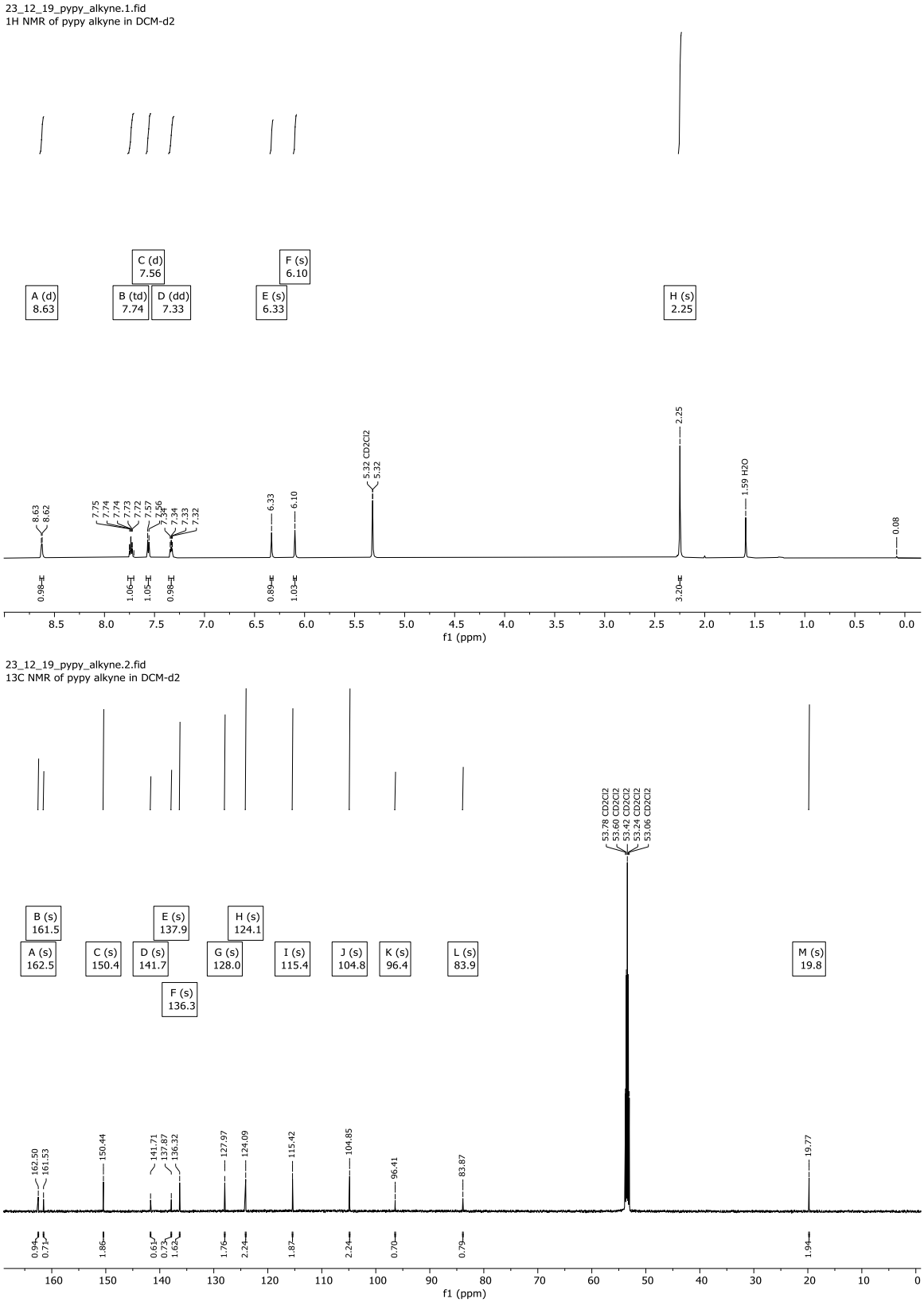

*Figure 100 – ^{1}H (top) and ^{13}C (bottom) NMR spectra of **131***

York - Chemistry - Mass Spectrometry Service Report

pyridine-2-cc-pyrone_if105974tt

Analysis Information

Analysis Filename	if105974tt_P1-D-2_01_43678.d	Acquisition Date	04/09/2023 15:43:33
Method	ESI_low mass_2c1s.m	Instrument	compact
Submission Name	if105974tt	ESI	Positive

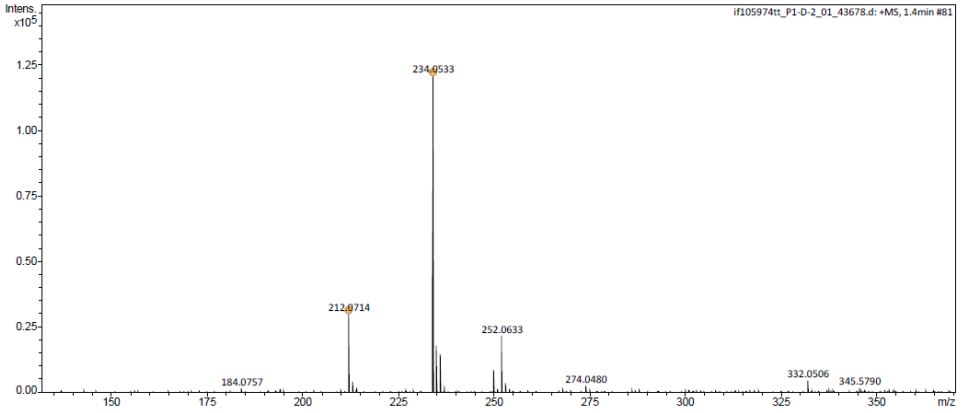

Meas. m/z	#	Ion Formula	m/z	err [ppm]	err [mDa]	mSigma	Mean err [ppm]
212.0714	1	C13H10NO2	212.0706	-3.9	-0.8	9.1	-2.4
234.0533	1	C13H9NNaO2	234.0525	-3.1	-0.7	8.2	-2.4

*Figure 101 - ESI-MS data for **131***

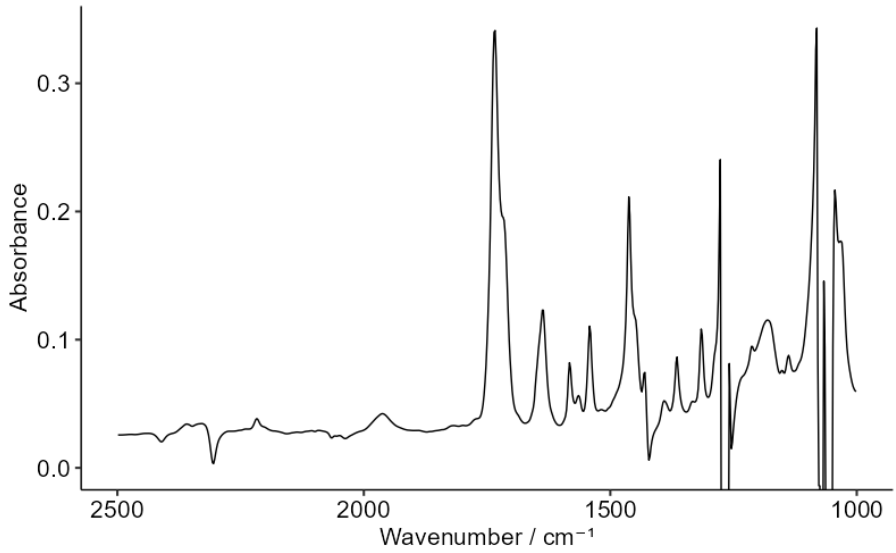

*Figure 102 - Solution-phase FTIR of **131** (2:1 DCM:THF).*

Spectral data for 6-methyl-4-(phenylethynyl)-2-pyrone (**129**)

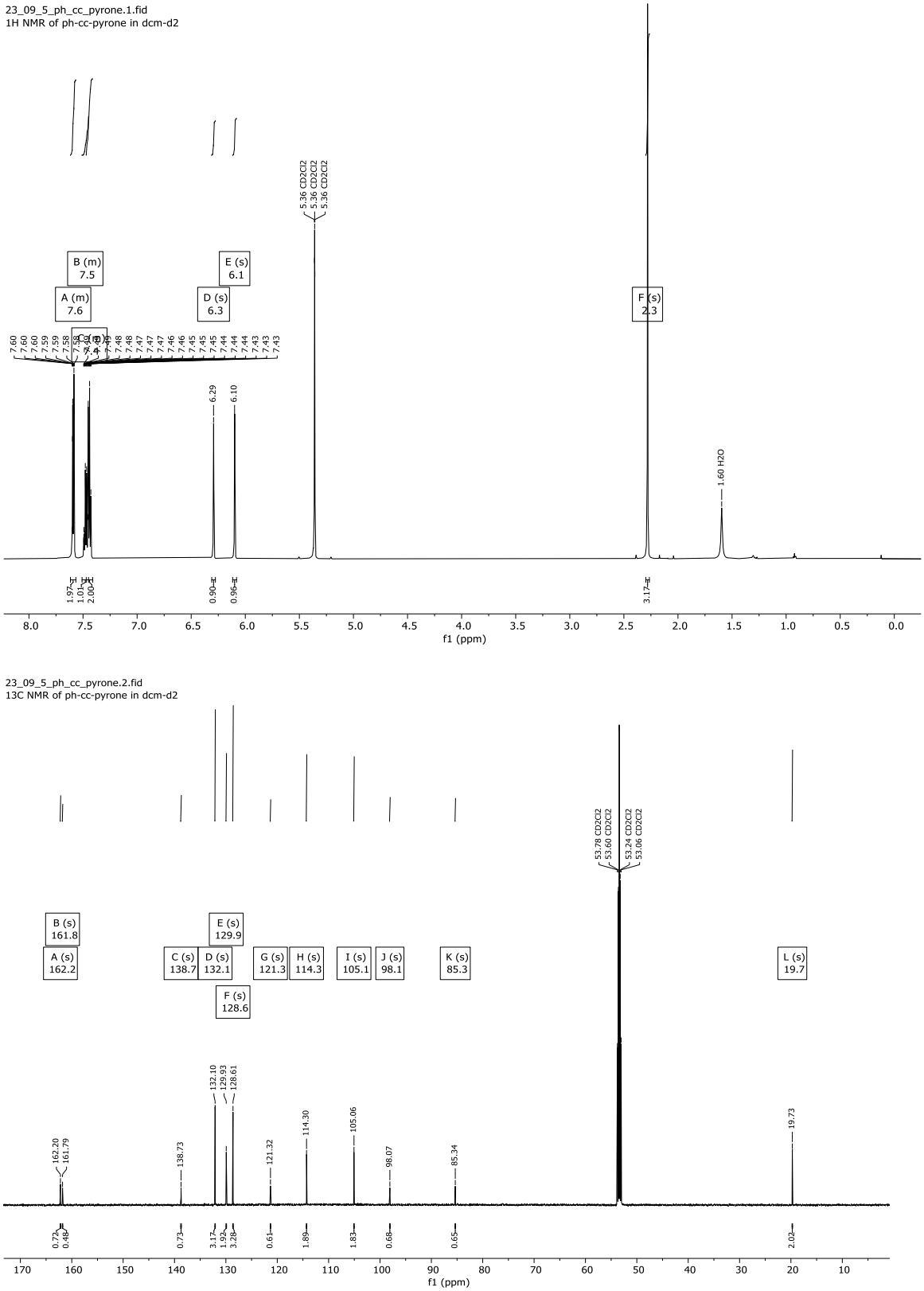

*Figure 103 - ^{1}H (top) and ^{13}C (bottom) NMR spectra of **129** in CD_2Cl_2.*

York - Chemistry - Mass Spectrometry Service Report

Ph-cc-pyrone_if105975tt

Analysis Information

Analysis Filename	if105975tt_P1-D-3_01_43679.d	Acquisition Date	04/09/2023 15:46:31
Method	ESI_low mass_2c1s.m	Instrument	compact
Submission Name	if105975tt	ESI	Positive

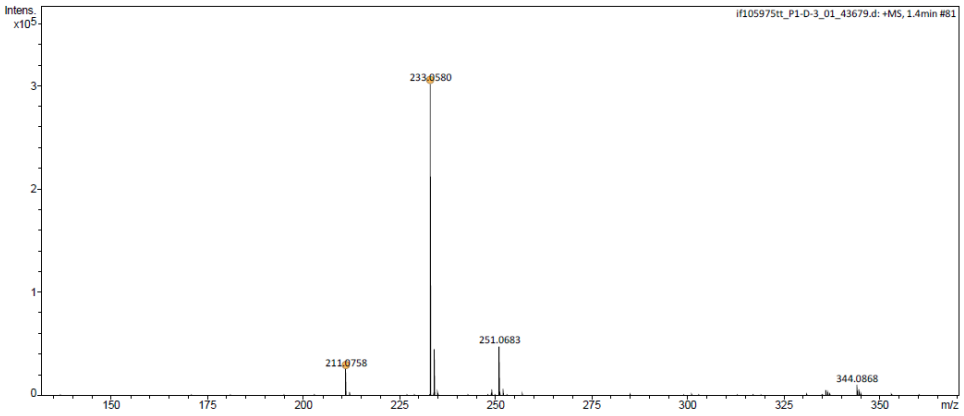

Meas. m/z	#	Ion Formula	m/z	err [ppm]	err [mDa]	mSigma	Mean err [ppm]
211.0758	1	C14H11O2	211.0754	-2.3	-0.5	3.4	-2.3
233.0580	1	C14H10NaO2	233.0573	-3.1	-0.7	3.2	-3.9

*Figure 104 - ESI-MS data for **129**.*

Spectral data for 2-phenylethynyl pyridine (**123**)

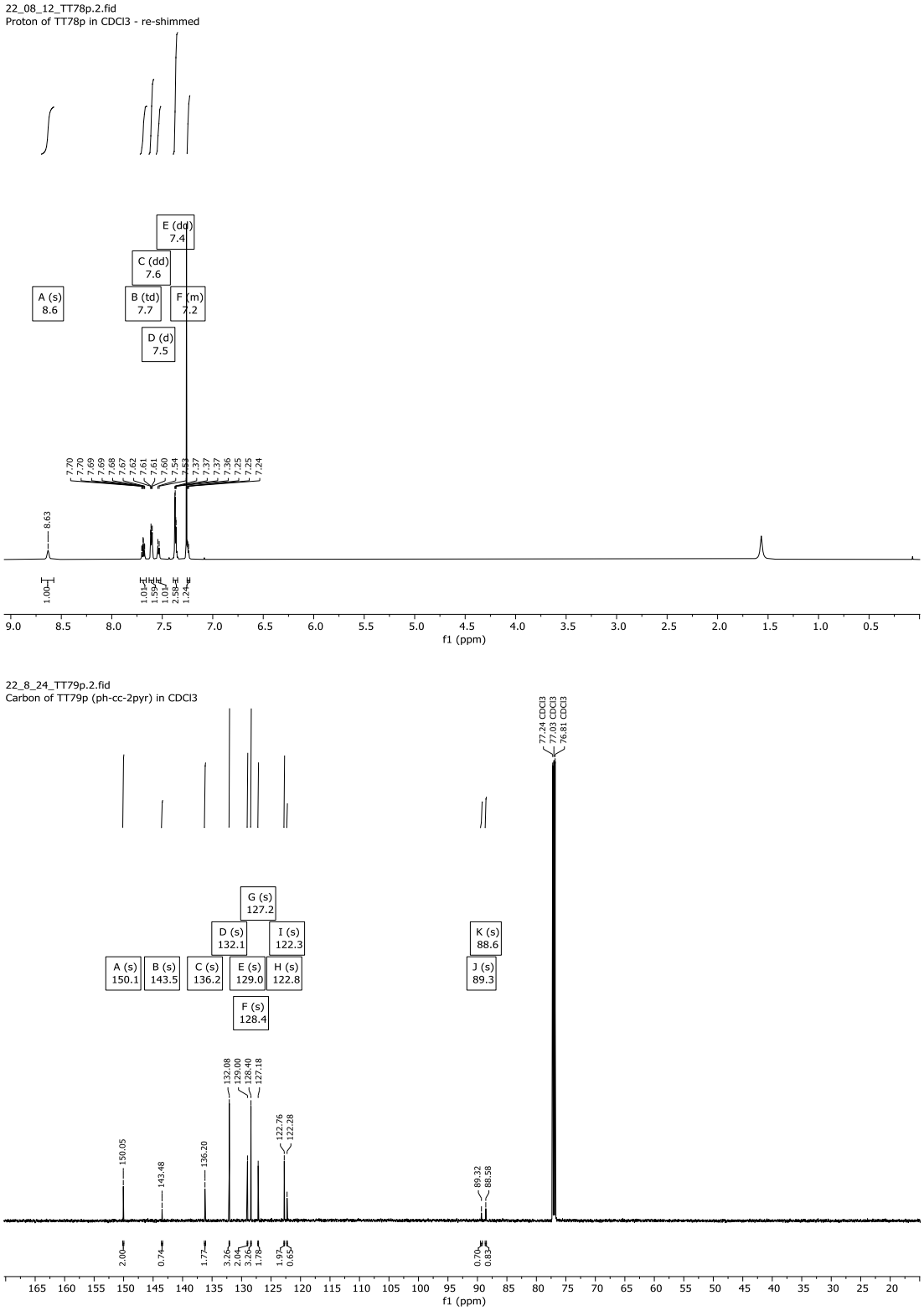

*Figure 105 -^{1}H (top) and ^{13}C (bottom) NMR spectra of **123** in CD_2Cl_2.*

York - Chemistry - Mass Spectrometry Service Report

TT77p_jms99001tt

Analysis Information

Analysis Filename	jms99001tt_P1-E-3_01_36344.d	Acquisition Date	24/08/2022 11:35:41
Method	ESI_low mass_2c1s.m	Instrument	compact
Submission Name	jms99001tt	ESI	Positive

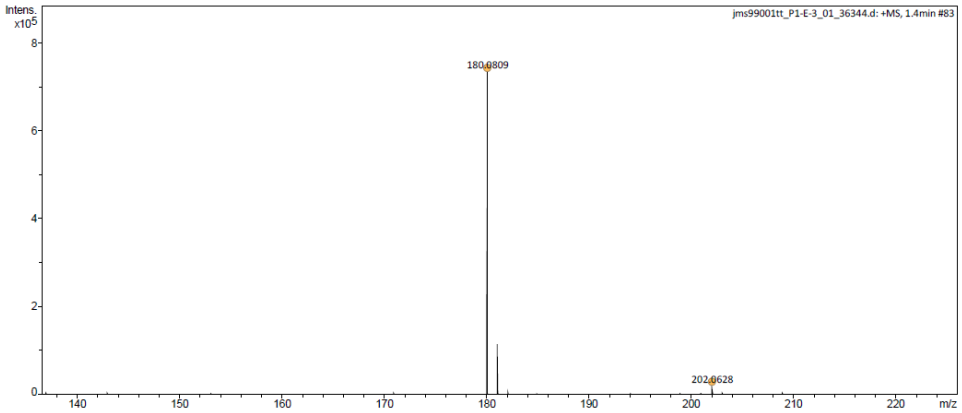

Meas. m/z	#	Ion Formula	m/z	err [ppm]	err [mDa]	mSigma	Mean err [ppm]
180.0809	1	C13H10N	180.0808	-0.8	-0.1	6.7	-2.2
202.0628	1	C13H9NNa	202.0627	-0.4	-0.1	7.4	-0.9

*Figure 106 - ESI-MS data for **123**.*

Spectral data for η^2-2(6-Methyl-4-(2-(2-pyridylethynyl))-2H-pyran-2-one]-hexacarbonyl dicobalt (**141**)

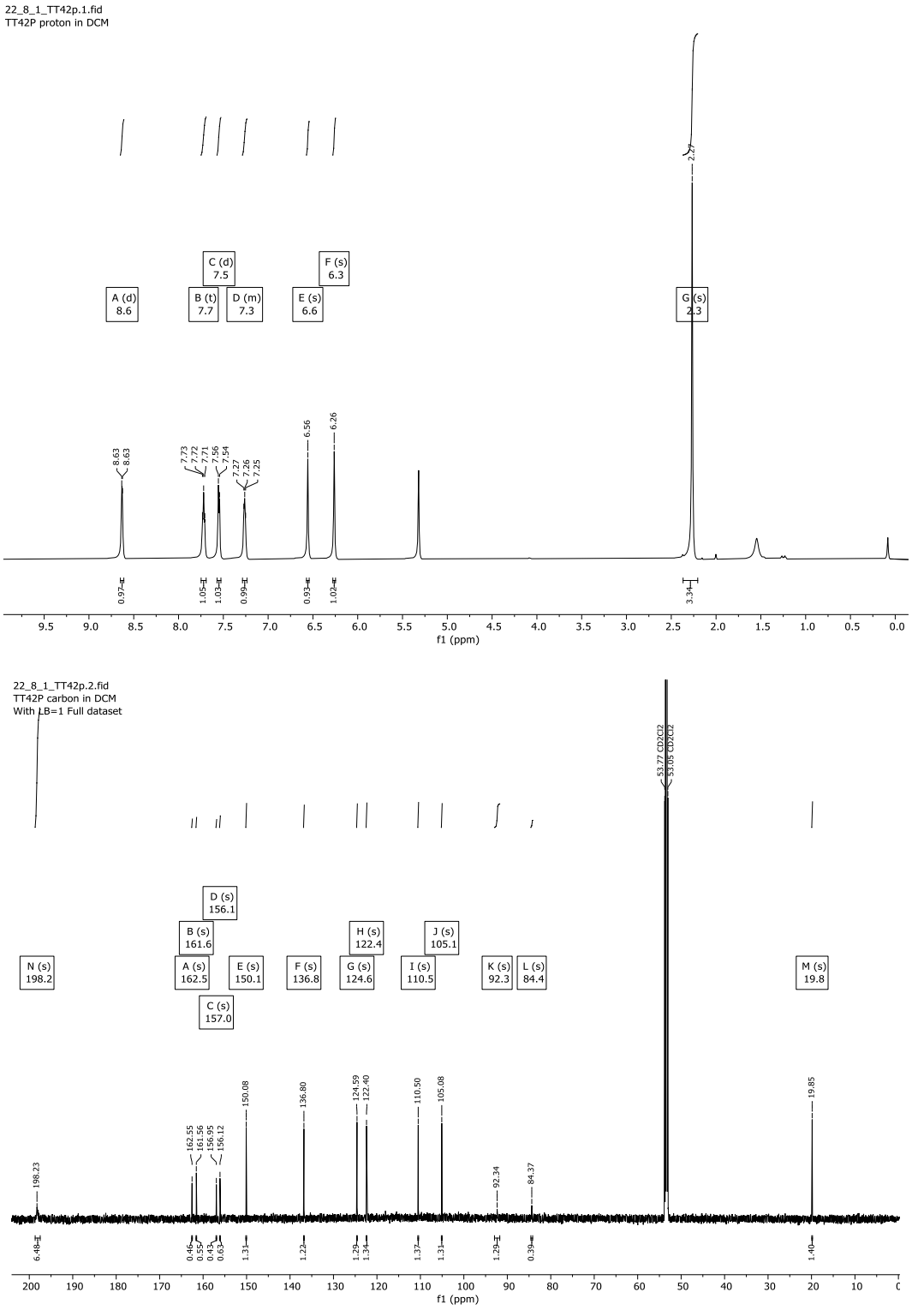

*Figure 107 - ^1H (top) and ^{13}C (bottom) NMR spectra of **123** in CD_2Cl_2.*

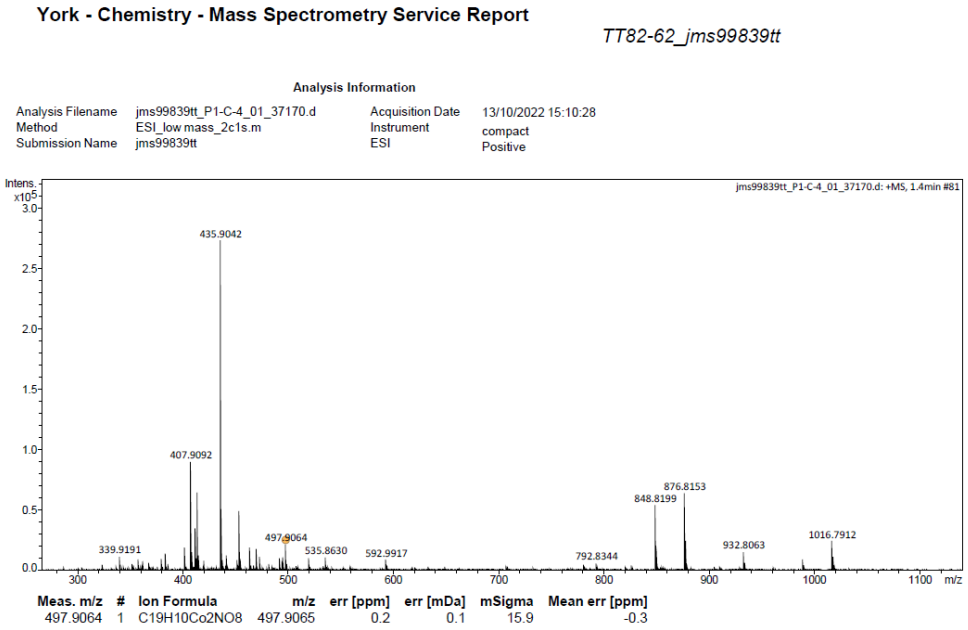

*Figure 108 - ESI-MS data for **141**.*

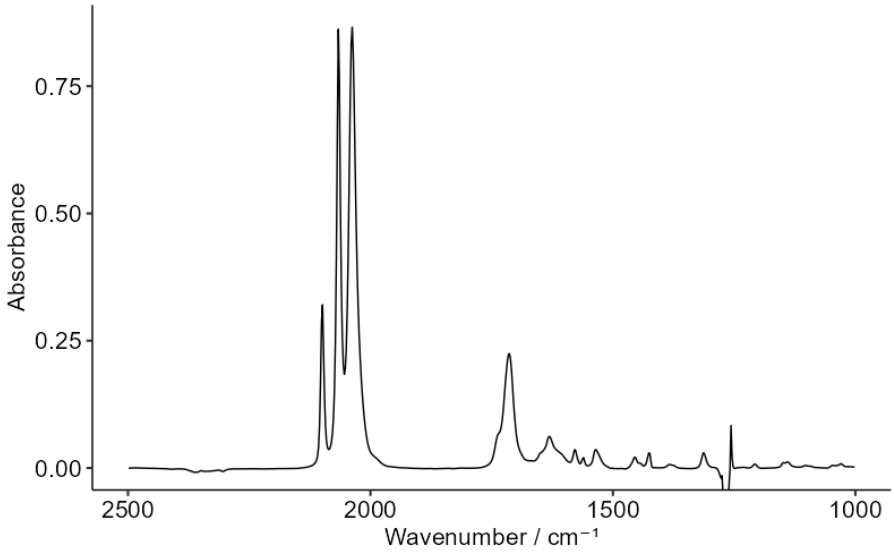

*Figure 109 - Solution-phase FTIR of **131** (2:1 DCM:THF)*

Spectral data for η^2-[2(6-Methyl-4-(2-(phenylethynyl))-2-pyrone]-hexacarbonyl dicobalt (**146)**

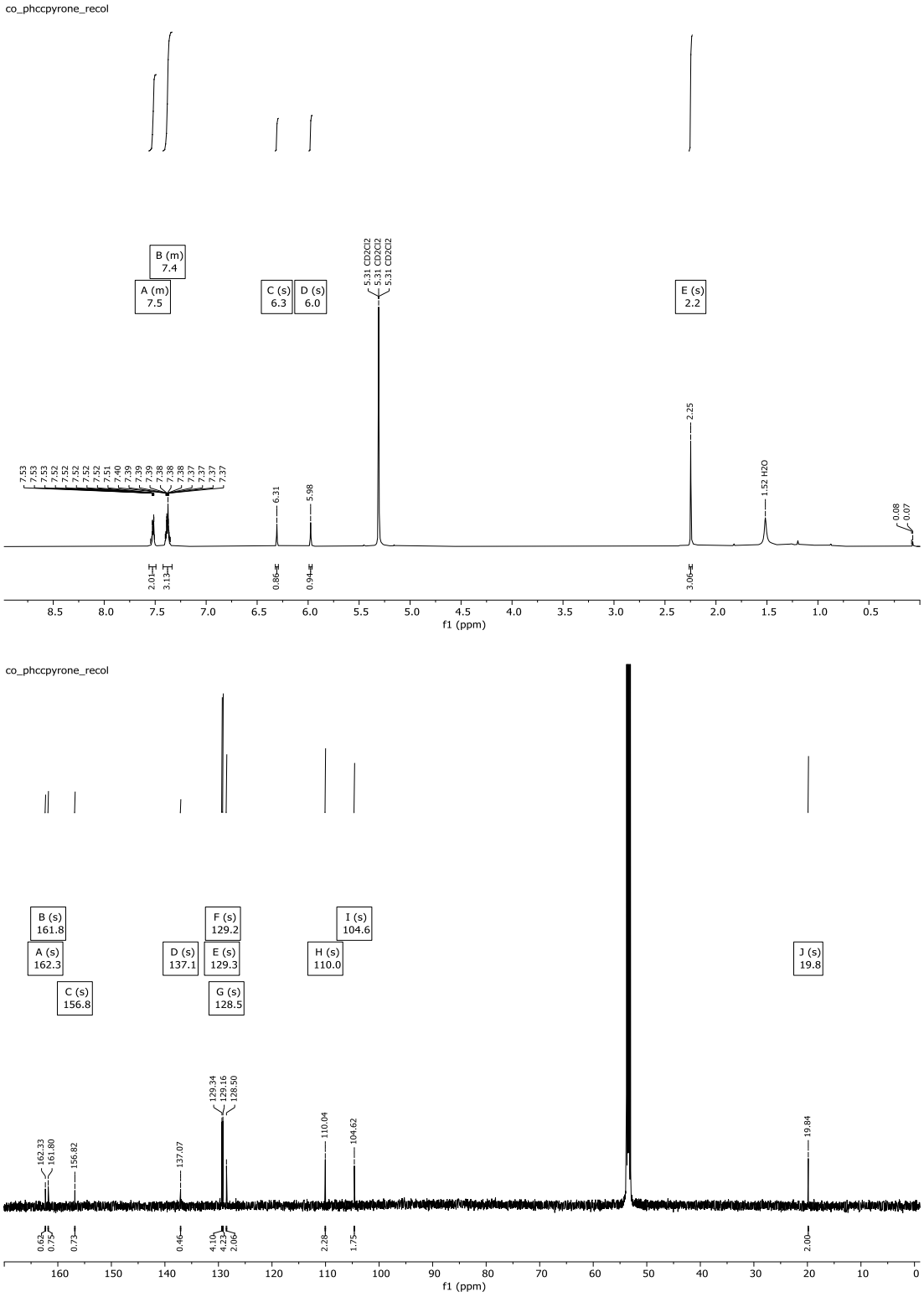

*Figure 110 - ^{1}H (top) and ^{13}C (bottom) NMR spectra of **146** in CD_2Cl_2.*

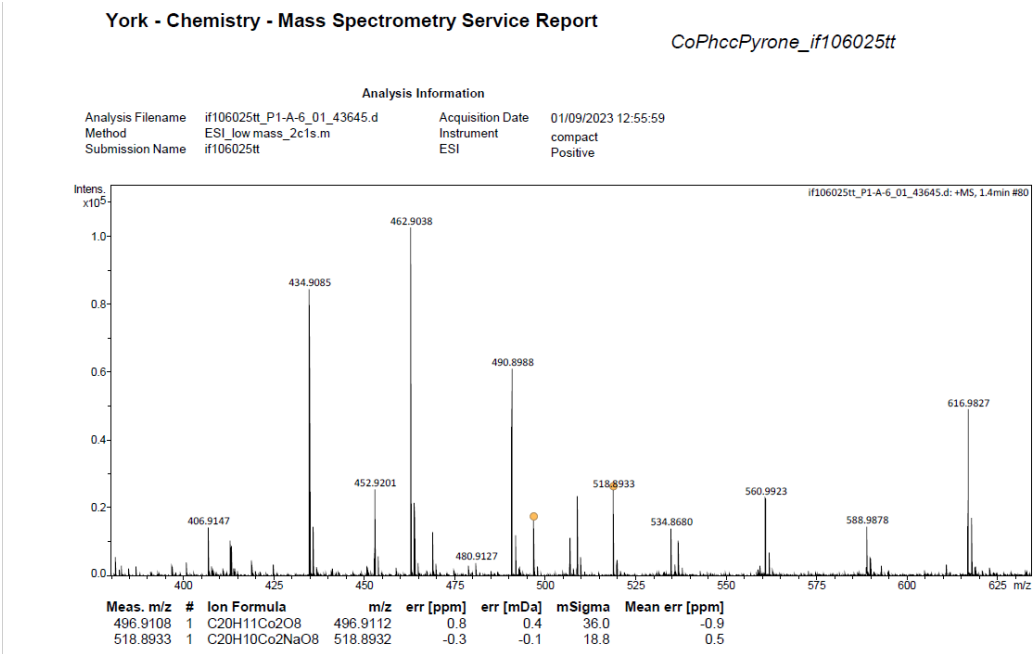

*Figure 111 - ESI-MS data for **146**.*

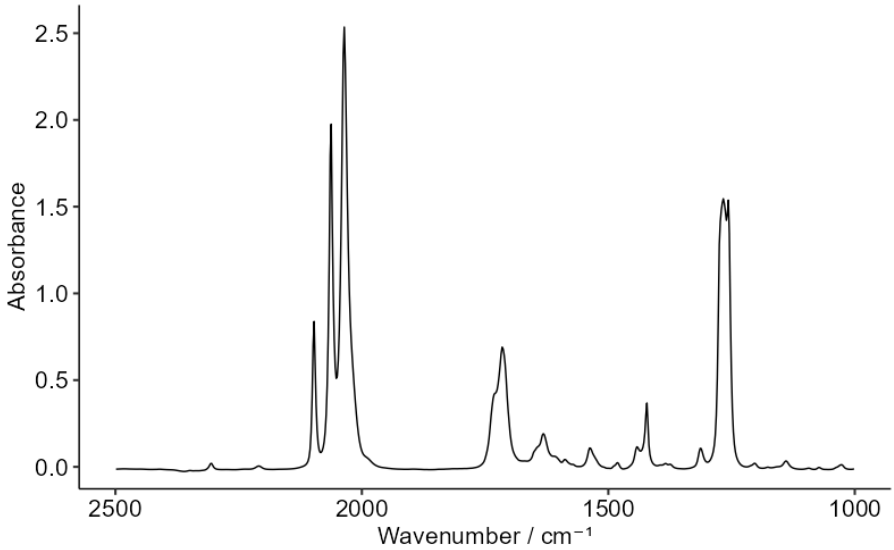

*Figure 112 - Solution-phase FTIR of **146** (DCM)*

Spectral data for η^2-[2-(phenylethynyl)pyridine)]-hexacarbonyl dicobalt (**145**)

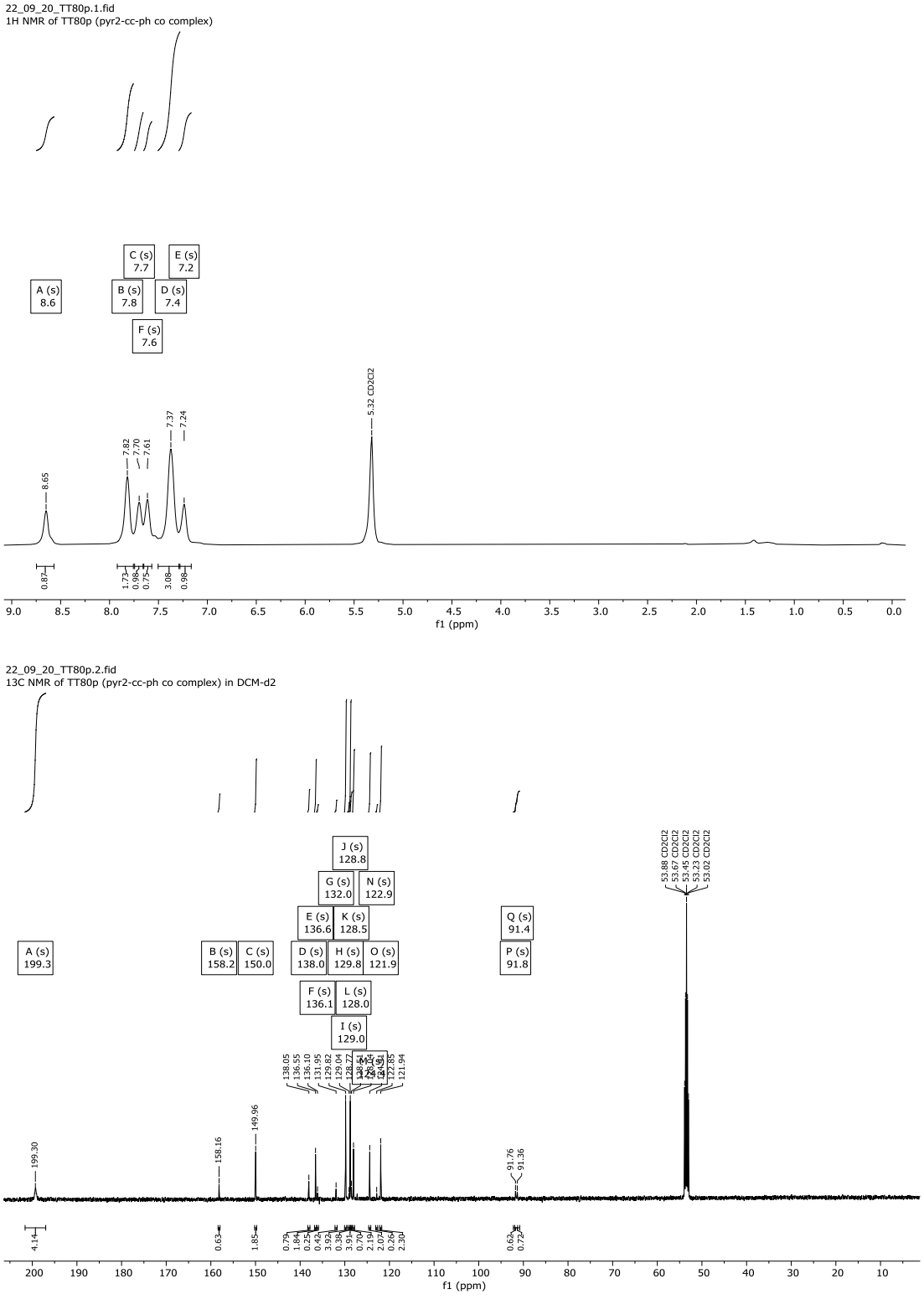

*Figure 113 - ^1H (top) and ^{13}C (bottom) NMR spectra of **145** in CD_2Cl_2.*

York - Chemistry - Mass Spectrometry Service Report

TT80P_jms99405tt

Analysis Information

Analysis Filename	jms99405tt_P1-A-2_01_36719.d	Acquisition Date	20/09/2022 14:33:42
Method	ESI_low mass_2c1s.m	Instrument	compact
Submission Name	jms99405tt	ESI	Positive

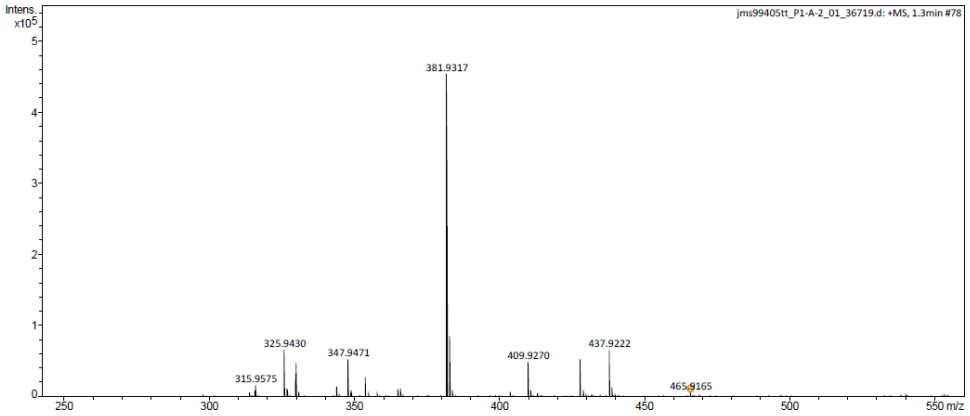

Meas. m/z	#	Ion Formula	m/z	err [ppm]	err [mDa]	mSigma	Mean err [ppm]
465.9165	1	C19H10Co2NO6	465.9167	0.4	0.2	32.6	4.3

*Figure 114 - ESI-MS data for **145***

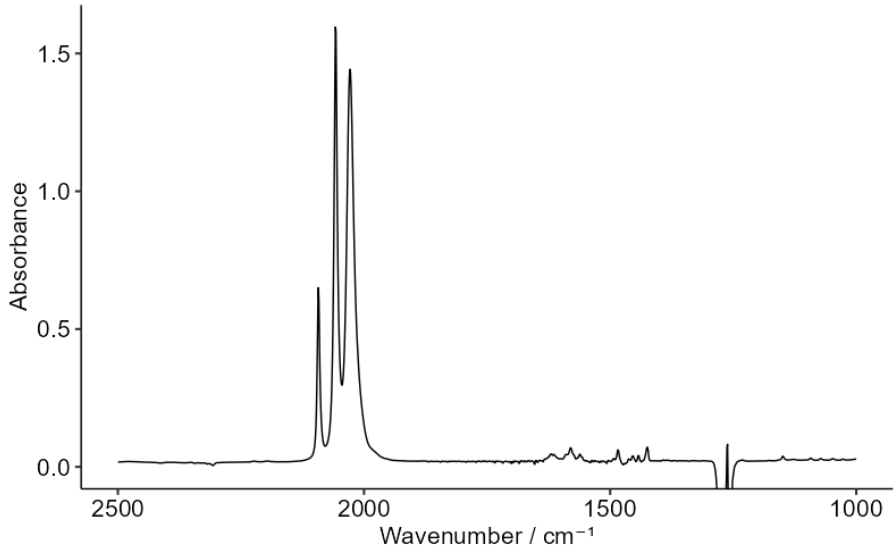

*Figure 115 - Solution-phase FTIR of **145** (DCM)*

Spectral data for η^2-[diphenylacetylene]-hexacarbonyl dicobalt (**142**)

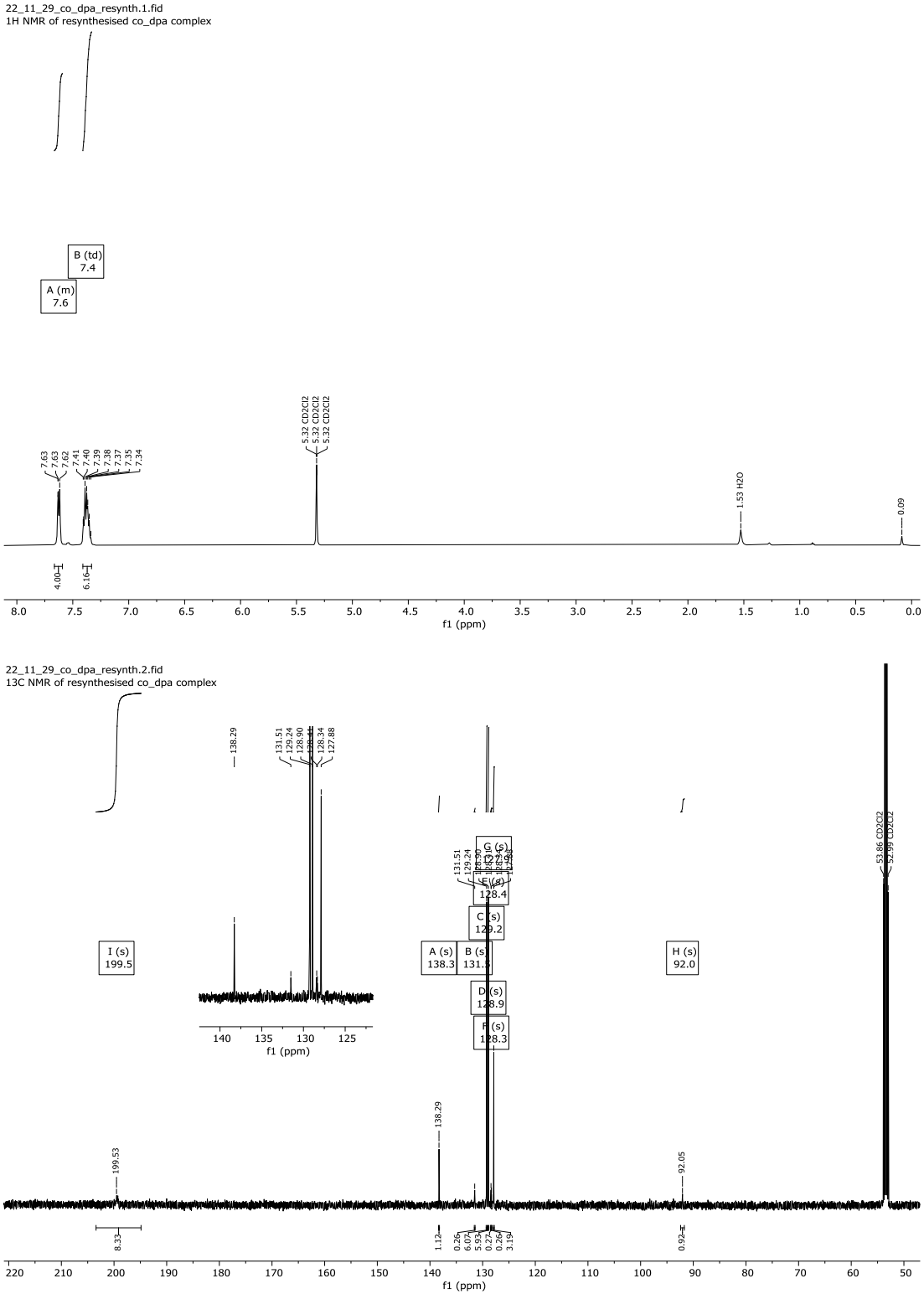

*Figure 116 -^{1}H (top) and ^{13}C (bottom) NMR spectra of **142** in CD_2Cl_2.*

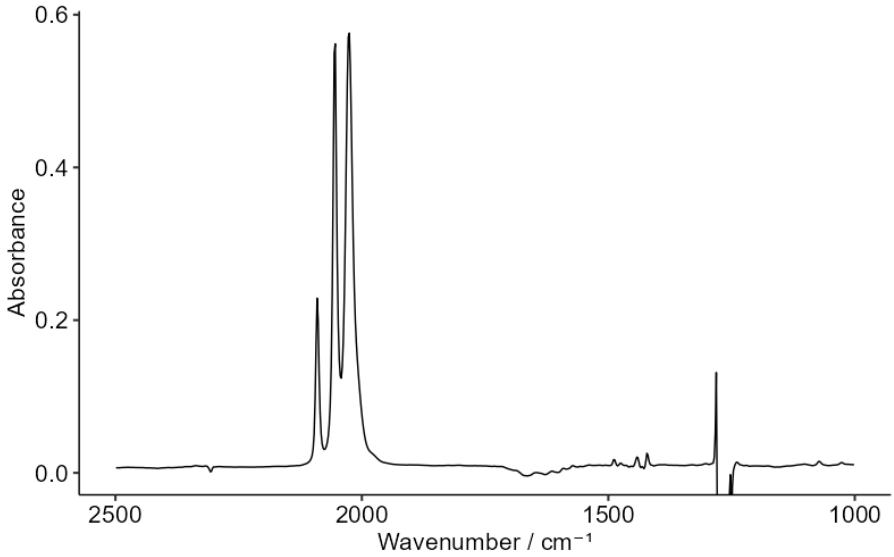

*Figure 117 - Solution phase FTIR of **142** (DCM)*

Spectral data for **140β**

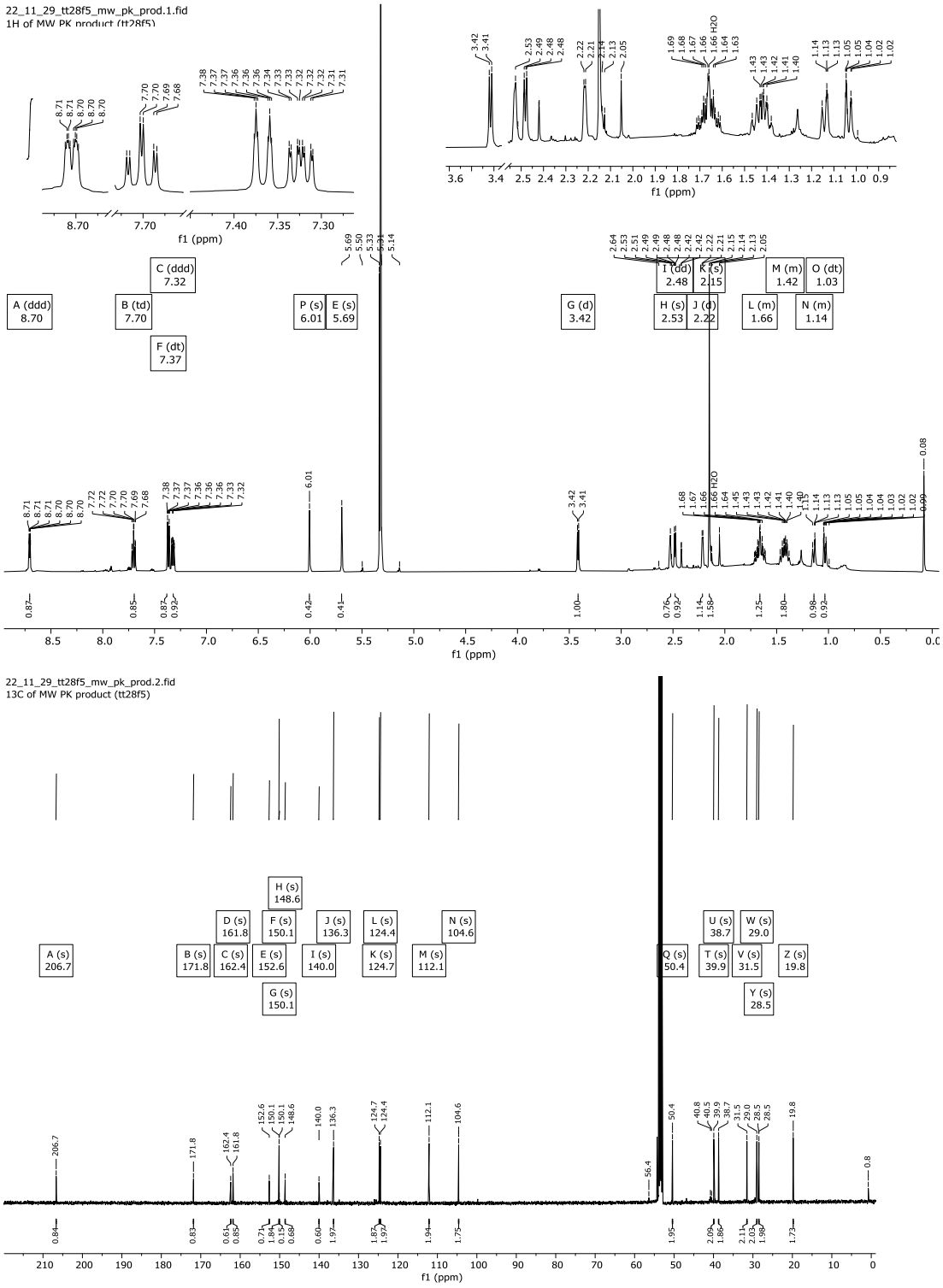

*Figure 118 - ^{1}H (top) and ^{13}C (bottom) NMR spectra of **140β** in CD_2Cl_2*

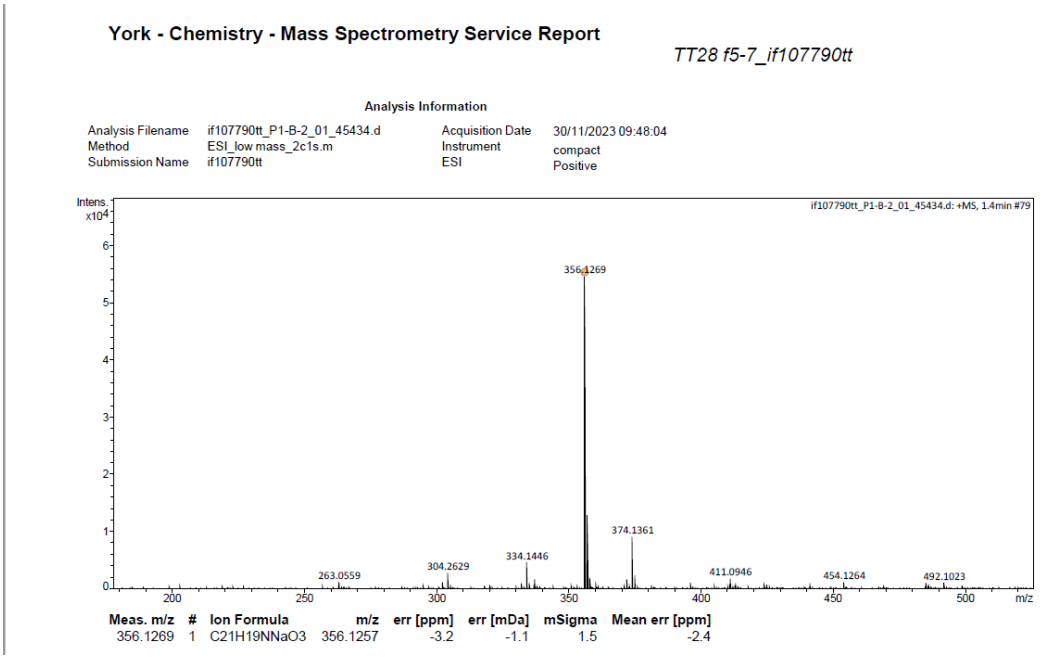

*Figure 119 - ESI-MS data for **1406.***

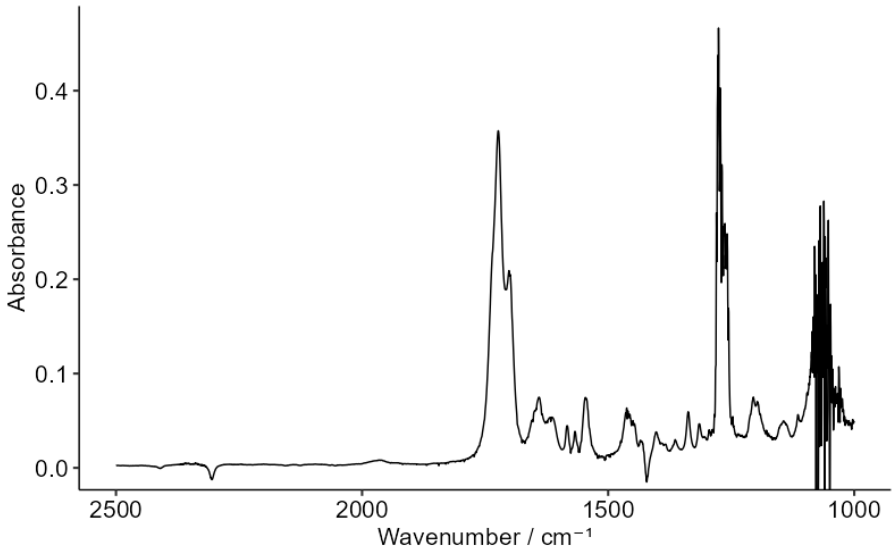

*Figure 120 – Solution FTIR data for **1406** (2:1 DCM:THF)*

Spectral data for η^2-[diphenylacetylene]-bis-cyclopentadienyl tetracarbonyl dimolybdenum (**157**)

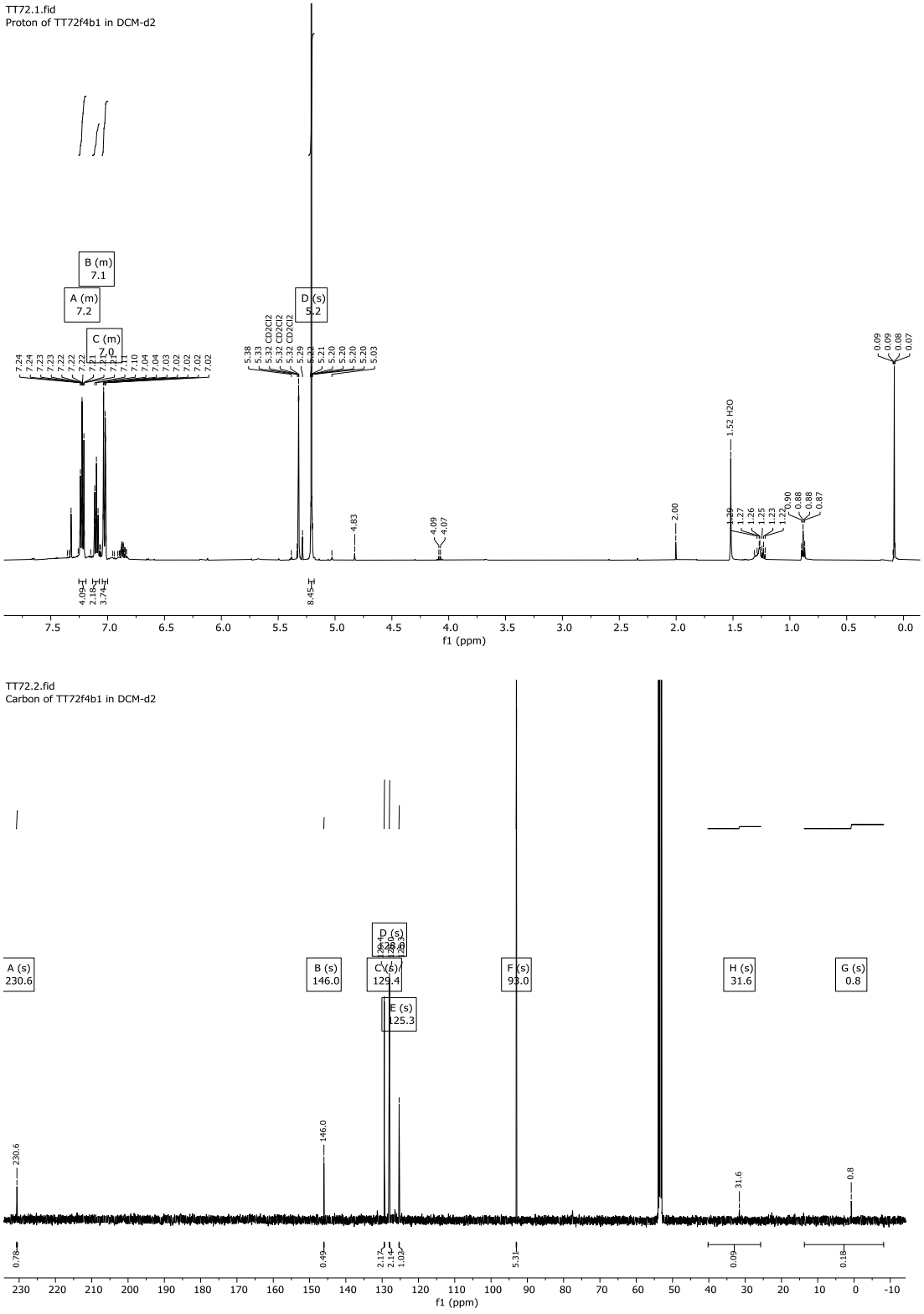

*Figure 121 -^{1}H (top) and ^{13}C (bottom) NMR spectra of **157** in CD_2Cl_2*

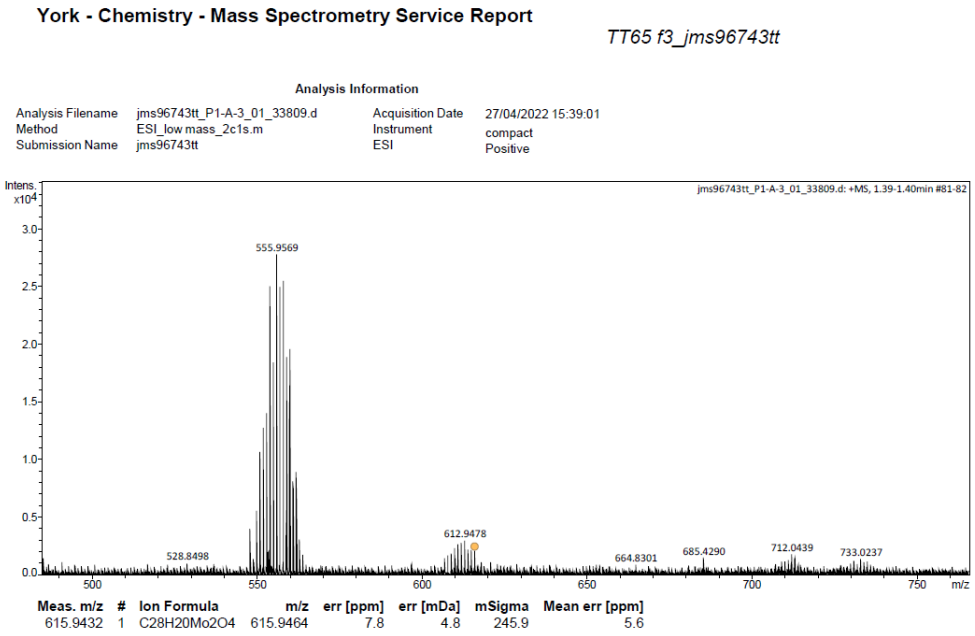

*Figure 122 - ESI-MS data for **157.***

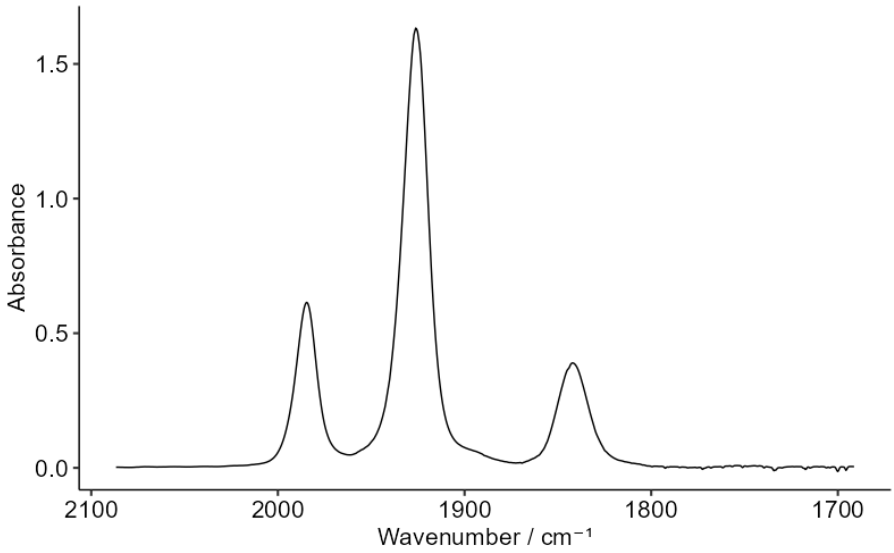

*Figure 123 - Solution FTIR of **157** (DCM)*

Spectral data for η^2-[(6-Methyl-4-(2-(2-pyridylethynyl))-2-pyrone]-bis-cyclopentadienyl tetracarbonyl dimolybdenum

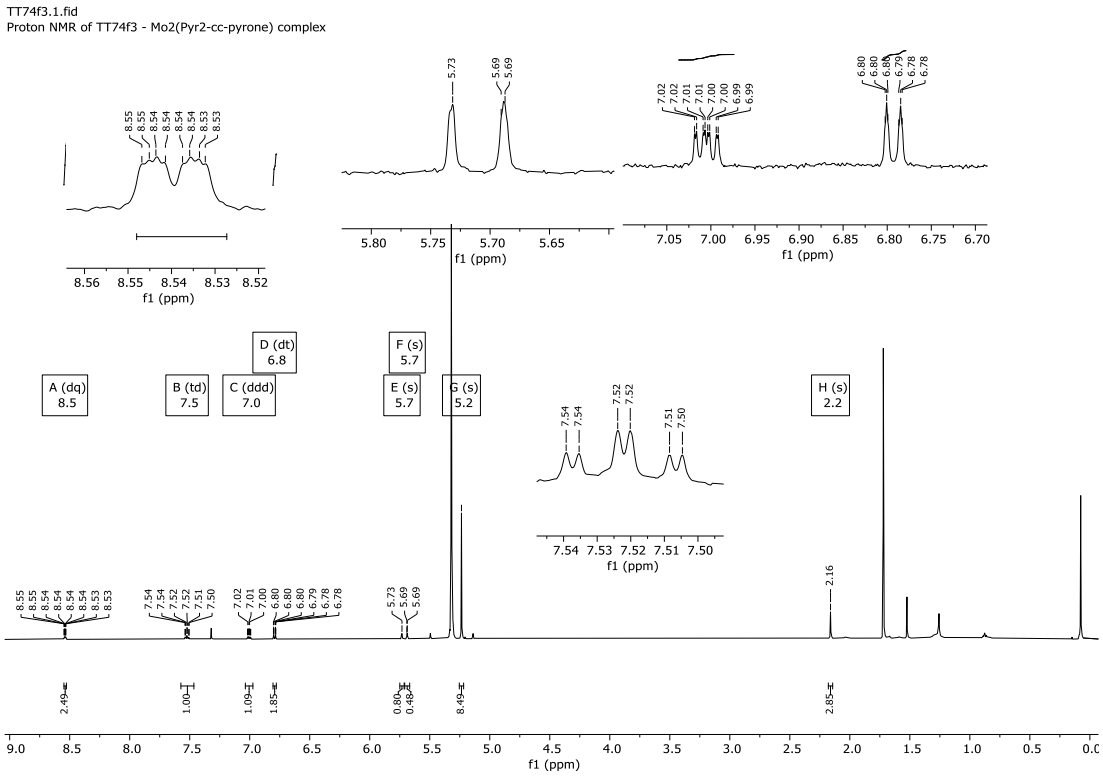

*Figure 124 - ^{1}H NMR of **158** in CD_2Cl_2.*

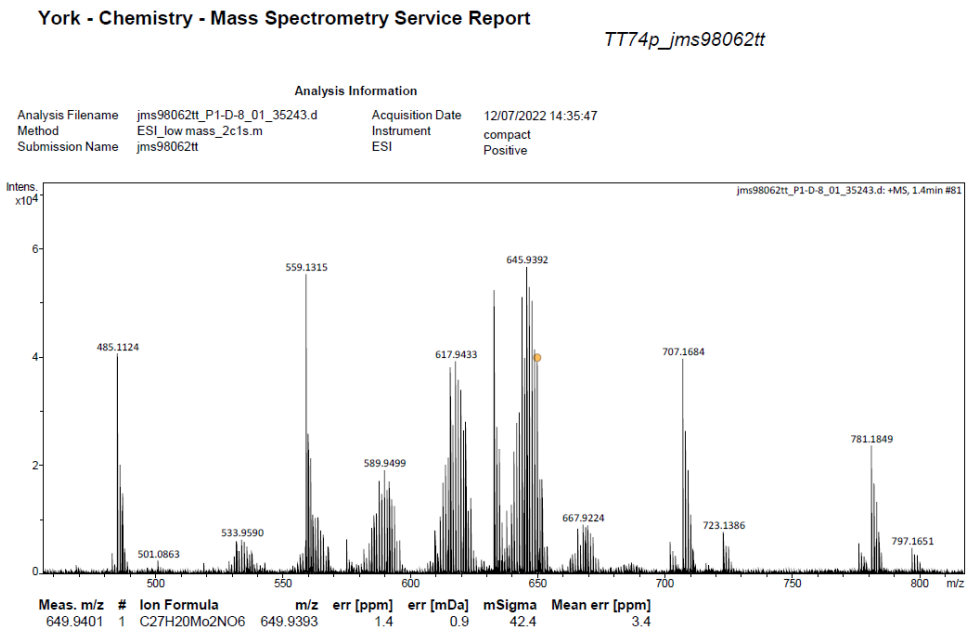

*Figure 125 - ESI-MS of **158**.*

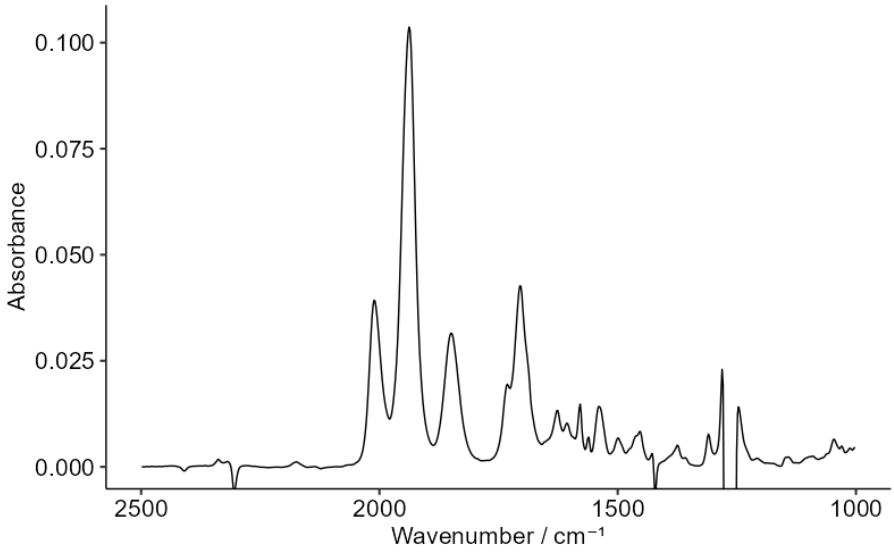

*Figure 126 - Solution FTIR of **158** (DCM).*

Appendix 4: Crystallographic data for compounds

X-ray diffraction data for compound **129**

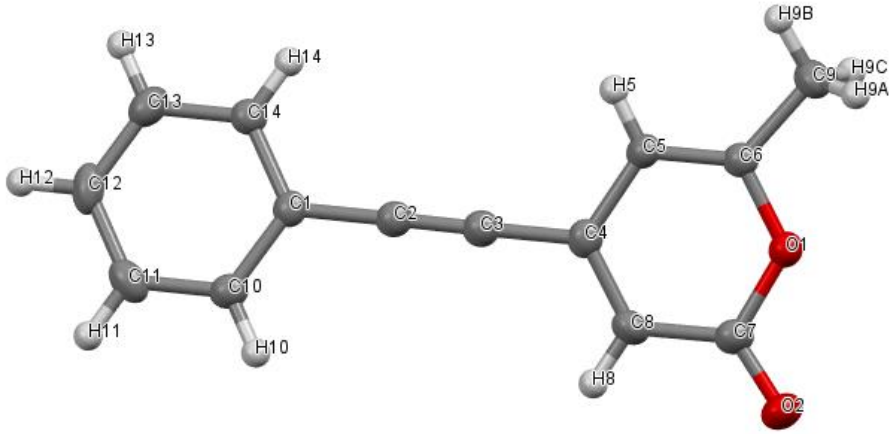

*Figure 127 - SCXRD structure of compound **129.** Thermal ellipsoids shown with 50% probability.*

Selected bond lengths (Å): C1-C2: 1.436(2), C2-C3: 1.201(2), C3-C4: 1.432(2), C6-C9:1.488(2) . Selected bond angles (°): C14-C1-C2: 120.4(1), C3-C4-C5: 119.0(1). Selected dihedrals (°): C14-C2-C3-C5: 13.5(5)

*Table 18 - Crystal data and structure refinement for compound **129***

Identification code	jms2002a
Empirical formula	$C_{14}H_{10}O_2$
Formula weight	210.22
Temperature/K	110.00(10)
Crystal system	monoclinic
Space group	$P2_1/n$
a/Å	7.8264(4)
b/Å	10.2109(5)
c/Å	13.4415(7)
α/°	90
β/°	95.816(5)
γ/°	90
Volume/Å^3	1068.64(9)
Z	4
ρ_{calc}g/cm^3	1.307
μ/mm^{-1}	0.701
F(000)	440.0
Crystal size/mm^3	0.257 × 0.06 × 0.048
Radiation	Cu Kα (λ = 1.54184)
2Θ range for data collection/°	10.902 to 142.152
Index ranges	$-9 \leq h \leq 9$, $-9 \leq k \leq 12$, $-16 \leq l \leq 13$
Reflections collected	5791
Independent reflections	2040 [R_{int} = 0.0258, R_{sigma} = 0.0318]
Data/restraints/parameters	2040/0/146
Goodness-of-fit on F^2	1.046
Final R indexes [I>=2σ (I)]	R_1 = 0.0464, wR_2 = 0.1123
Final R indexes [all data]	R_1 = 0.0587, wR_2 = 0.1224
Largest diff. peak/hole / e Å^{-3}	0.38/-0.18

X-ray diffraction data for compound **131**

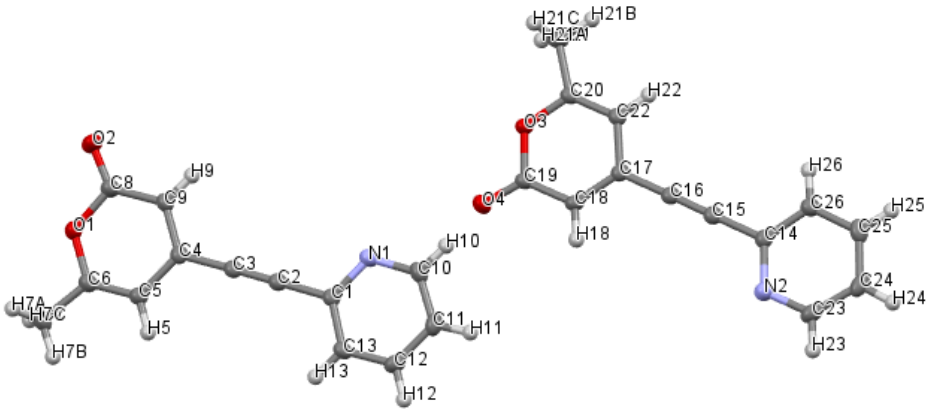

*Figure 128 - SCXRD structure of compound **129.** Thermal ellipsoids shown with 50% probability.*

Selected bond lengths (Å): C1-C2: 1.435(2), C2-C3: 1.202(2), C3-C4: 1.202(2), C6-C7: 1.487(2), C1-N1: 1.351(2), C14-C15: 1.437(2), C15-C16: 1.437(2), C16-C17: 1.429(2), C14-N2: 1.351(2). Selected bond angles (°): N1-C1-C2: 116.4(1), C9-C4-C3: 121.5(1), N2-C14-C15: 116.8(1), C18-C17-C16: 120.9(1). Selected dihedrals (°): N1-C2-C3-C9: -7.0(4), N2-C15-C16-C18: -2.6(4)

*Table 19 - Crystal data and structure refinement for compound **129***

Identification code	tt23002
Empirical formula	$C_{13}H_9NO_2$
Formula weight	211.21
Temperature/K	109.9(3)
Crystal system	monoclinic
Space group	$P2_1/c$
a/Å	12.2837(3)
b/Å	23.6744(4)
c/Å	7.2338(2)
α/°	90
β/°	101.556(2)
γ/°	90
Volume/Å^3	2061.01(8)
Z	8
ρ_{calc}g/cm^3	1.191
μ/mm^{-1}	0.664
F(000)	770.0
Crystal size/mm^3	0.21 × 0.07 × 0.06
Radiation	Cu Kα (λ = 1.54184)
2Θ range for data collection/°	7.346 to 154.312
Index ranges	$-15 \leq h \leq 15$, $-29 \leq k \leq 11$, $-9 \leq l \leq 8$
Reflections collected	12464
Independent reflections	4194 [R_{int} = 0.0288, R_{sigma} = 0.0367]
Data/restraints/parameters	4194/0/291
Goodness-of-fit on F^2	1.055
Final R indexes [I>=2σ (I)]	R_1 = 0.0403, wR_2 = 0.1091
Final R indexes [all data]	R_1 = 0.0473, wR_2 = 0.1145
Largest diff. peak/hole / e Å^{-3}	0.22/-0.21

X-ray diffraction data for compound **140β**

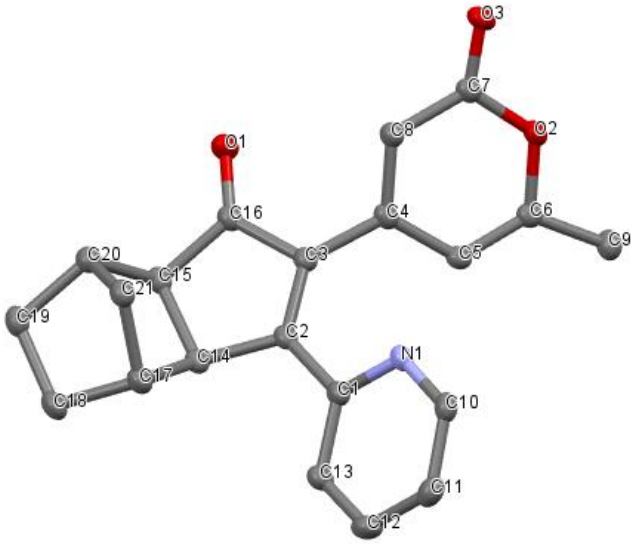

*Figure 129 - SCXRD structure of compound **140β.** Thermal ellipsoids shown with 50% probability. Hydrogen atoms omitted for clarity.*

Selected bond lengths (Å): C1-C2: 1.472(2), C2-C3: 1.358(2), C3-C4: 1.475(2), C14-C15: 1.547(2), C16-O1: 1.215(2), C17-C21: 1.539(2), C21-C20: 1.535(2), C18-C19: 1.554(2), C6-C9: 1.485(2). Selected bond angles (°): C1-C2-C3: 126.7(1), C4-C3-C2: 130.1(1), C2-C14-C17: 115.5(1), C15-C16-C20: 32.98(6), C20-C21-C17: 94.5(1). Selected dihedrals (°): C1-C2-C3-C4: 13.0(2), C1-C2-C14-C17: 57.5(2).

*Table 20 Crystal data and structure refinement for compound **1408***

Identification code	jms21015
Empirical formula	$C_{21}H_{19}NO_3$
Formula weight	333.37
Temperature/K	110.00(10)
Crystal system	monoclinic
Space group	$P2_1/n$
a/Å	10.2821(3)
b/Å	10.6410(2)
c/Å	14.8441(3)
α/°	90
β/°	99.064(2)
γ/°	90
Volume/Å^3	1603.84(7)
Z	4
ρ_{calc}g/cm^3	1.381
μ/mm^{-1}	0.745
F(000)	704.0
Crystal size/mm^3	0.251 × 0.209 × 0.087
Radiation	Cu Kα (λ = 1.54184)
2Θ range for data collection/°	9.784 to 142.224
Index ranges	$-12 \leq h \leq 9$, $-9 \leq k \leq 12$, $-18 \leq l \leq 16$
Reflections collected	5761
Independent reflections	3042 [R_{int} = 0.0172, R_{sigma} = 0.0233]
Data/restraints/parameters	3042/0/227
Goodness-of-fit on F^2	1.031
Final R indexes [I>=2σ (I)]	R_1 = 0.0357, wR_2 = 0.0883
Final R indexes [all data]	R_1 = 0.0406, wR_2 = 0.0924
Largest diff. peak/hole / e Å^{-3}	0.26/-0.20

X-ray diffraction data for compound **141**

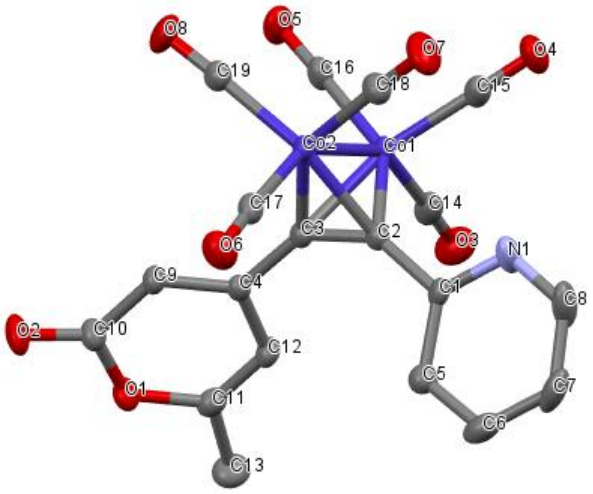

*Figure 130 - SCXRD structure of compound **141.** Thermal ellipsoids shown with 50% probability. Hydrogen atoms omitted for clarity.*

Selected bond lengths (Å): C1-C2: 1.462(4), C2-C3: 1.353(3), C3-C4: 1.450(4), C2-Co2: 1.964(4), C2-Co1: 1.933(3), C3-Co2: 1.940(3), C3-Co1: 1.981(3), Co2-Co1: 2.4658(8), Co1-C15: 1.830(3), Co1-C14: 1.808(4), Co1-C16: 1.817(3), Co2-C19: 1.832(3), Co2-C17: 1.795(3). Selected bond angles (°): C1-C2-C3: 144.6(3), C4-C3-C2: 142.2(3), C1-C2-Co2: 130.2(2), C1-C2-Co1: 135.0(2), C4-C3-Co1: 132.1(2), C4-C3-Co2: 137.0(2), Co1-Co2-C18: 99.9(1), Co1-Co2-C17: 147.3(1), Co1-Co2-C19: 99.0(1), Co2-Co1-C15: 98.7(1), Co2-Co1-C14: 150.2(1), Co2-Co1-C16: 98.0(1). Selected dihedrals (°): C1-C2-C3-C4: -14.0(8), C14-Co1-Co2-C17: 3.3(3), N1-C2-C3-C9: 37(3).

*Table 21 - Crystal data and structure refinement for compound **141***

Identification code	jms21001
Empirical formula	$C_{19}H_9Co_2NO_8$
Formula weight	497.13
Temperature/K	110.05(10)
Crystal system	triclinic
Space group	P-1
a/Å	8.2627(9)
b/Å	9.0904(8)
c/Å	13.9309(11)
α/°	78.168(7)
β/°	78.428(8)
γ/°	72.895(9)
Volume/Å^3	967.77(17)
Z	2
ρ_{calc}g/cm^3	1.706
μ/mm^{-1}	13.871
F(000)	496.0
Crystal size/mm^3	0.196 × 0.043 × 0.031
Radiation	Cu Kα (λ = 1.54184)
2Θ range for data collection/°	10.308 to 142.386
Index ranges	$-9 \leq h \leq 9$, $-11 \leq k \leq 11$, $-17 \leq l \leq 13$
Reflections collected	6267
Independent reflections	3619 [R_{int} = 0.0335, R_{sigma} = 0.0489]
Data/restraints/parameters	3619/0/272
Goodness-of-fit on F^2	1.025
Final R indexes [I>=2σ (I)]	R_1 = 0.0373, wR_2 = 0.0920
Final R indexes [all data]	R_1 = 0.0470, wR_2 = 0.0990
Largest diff. peak/hole / e Å^{-3}	0.49/-0.59

X-ray diffraction data for compound **142**

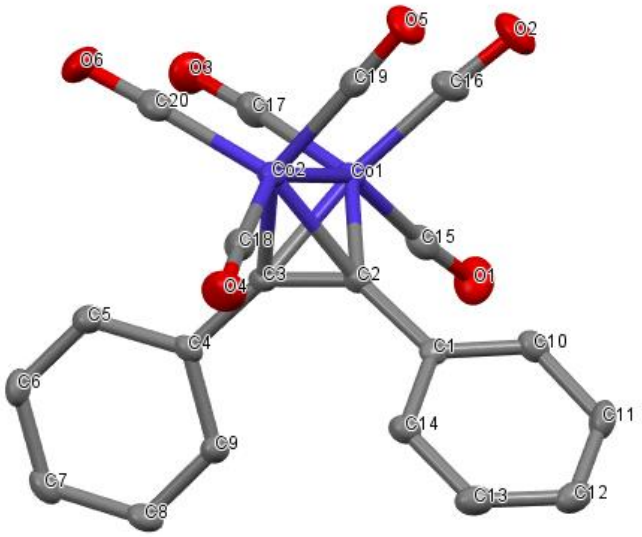

*Figure 131 - SCXRD structure of compound **142.** Thermal ellipsoids shown with 50% probability. Hydrogen atoms omitted for clarity.*

Selected bond lengths (Å): C1-C2: 1.465(6), C2-C3: 1.352(5), C3-C4: 1.449(6), C2-Co2: 1.990(5), C2-Co1: 1.945(5), C3-Co1: 1.988(5), C3-Co2: 1.957(5), Co2-Co1: 2.4684(8), Co1-C17: 1.836(5), Co1-C16: 1.808(4), Co1-C15: 1.807(5), Co2-C20: 1.819(4), Co2-C19: 1.825(4), Co2-C18: 1.789(5). Selected bond angles (°): C1-C2-C3: 139.5(4), C4-C3-C2: 140.3(4), C1-C2-Co2: 134.4(3), C1-C2-Co1: 136.5(3), C4-C3-Co2: 137.5(3), C4-C3-Co1: 133.3(3), Co1-C2-Co2: 77.7(2), Co1-C3-Co2: 77.5(2). Selected dihedrals (°): C1-C2-C3-C4: -10(1), C14-C2-C3-C9: -39.0(4), C18-Co2-Co1-C15: -5.4(4).

*Table 22 - Crystal data and structure refinement for compound **142***

Identification code	jms2003
Empirical formula	$C_{20}H_{10}O_6Co_2$
Formula weight	464.14
Temperature/K	110.00(14)
Crystal system	monoclinic
Space group	Ia
a/Å	7.80226(18)
b/Å	15.7808(4)
c/Å	15.3029(3)
α/°	90
β/°	100.816(2)
γ/°	90
Volume/Å^3	1850.71(7)
Z	4
ρ_{calc}g/cm^3	1.666
μ/mm^{-1}	1.827
F(000)	928.0
Crystal size/mm^3	0.178 × 0.112 × 0.067
Radiation	Mo Kα (λ = 0.71073)
2Θ range for data collection/°	7.316 to 58.122
Index ranges	$-10 \leq h \leq 10$, $-21 \leq k \leq 19$, $-18 \leq l \leq 20$
Reflections collected	4044
Independent reflections	2753 [R_{int} = 0.0234, R_{sigma} = 0.0407]
Data/restraints/parameters	2753/2/253
Goodness-of-fit on F^2	1.054
Final R indexes [I>=2σ (I)]	R_1 = 0.0271, wR_2 = 0.0635
Final R indexes [all data]	R_1 = 0.0287, wR_2 = 0.0648
Largest diff. peak/hole / e Å^{-3}	0.33/-0.26
Flack parameter	0.005(18)

X-ray diffraction data for compound **145**

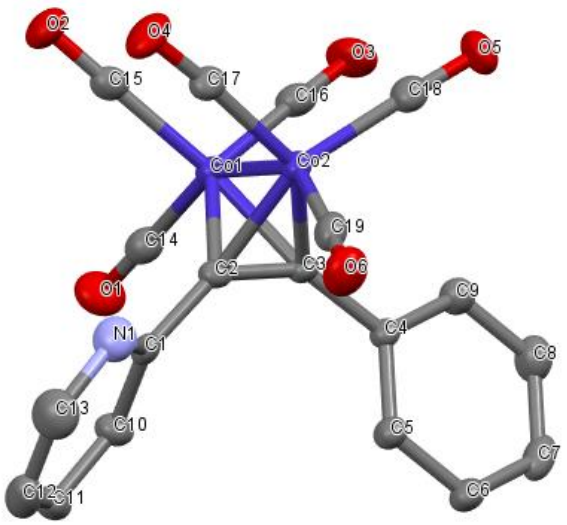

*Figure 132 - SCXRD structure of compound **145**. Thermal ellipsoids shown with 50% probability. Hydrogen atoms omitted for clarity.*

Selected bond lengths (Å): C1-C2: 1.462(5), C2-C3: 1.344(5), C3-C4: 1.460(4), C2-Co1: 1.981(3), C2-Co2: 1.946(4), C3-Co2: 1.975(3), C3-Co1: 1.948(3), Co1-Co2: 2.4715(8), Co1-C14: 1.804(5), Co1-C15: 1.825(3), Co1-C16: 1.813(4), Co2-C17: 1.815(3), Co2-C18: 1.827(4), Co2-C19: 1.806(4). Selected bond angles (°): C1-C2-C3: 139.6(3), C4-C3-C2: 141.4(3), C1-C2-Co1: 136.0(2), C1-C2-Co2: 135.1(2), C4-C3-Co1: 136.4(2), C4-C3-Co2: 132.6(2), Co1-C3-Co2: 78.1(1), Co1-C2-Co2: 78.0(1). Selected dihedrals (°): C1-C2-C3-C4: -6.2(8), N1-C2-C3-C9: 70(2), C14-Co1-Co2-C19: -4.2(3).

*Table 23 - Crystal data and structure refinement for compound **145***

Identification code	jms22016
Empirical formula	$C_{19}H_9Co_2NO_6$
Formula weight	465.13
Temperature/K	110.00(10)
Crystal system	monoclinic
Space group	Ia
a/Å	7.77500(10)
b/Å	15.7600(2)
c/Å	15.1950(2)
α/°	90
β/°	100.7250(10)
γ/°	90
Volume/Å^3	1829.38(4)
Z	4
ρ_{calc}g/cm^3	1.689
μ/mm^{-1}	14.543
F(000)	928.0
Crystal size/mm^3	0.1 × 0.06 × 0.05
Radiation	Cu Kα (λ = 1.54184)
2Θ range for data collection/°	8.158 to 153.452
Index ranges	$-9 \leq h \leq 8$, $-19 \leq k \leq 19$, $-18 \leq l \leq 18$
Reflections collected	8193
Independent reflections	2566 [R_{int} = 0.0246, R_{sigma} = 0.0234]
Data/restraints/parameters	2566/2/253
Goodness-of-fit on F^2	1.081
Final R indexes [I>=2σ (I)]	R_1 = 0.0236, wR_2 = 0.0651
Final R indexes [all data]	R_1 = 0.0245, wR_2 = 0.0655
Largest diff. peak/hole / e Å^{-3}	0.25/-0.29
Flack parameter	-0.010(4)

X-ray diffraction data for compound **146**

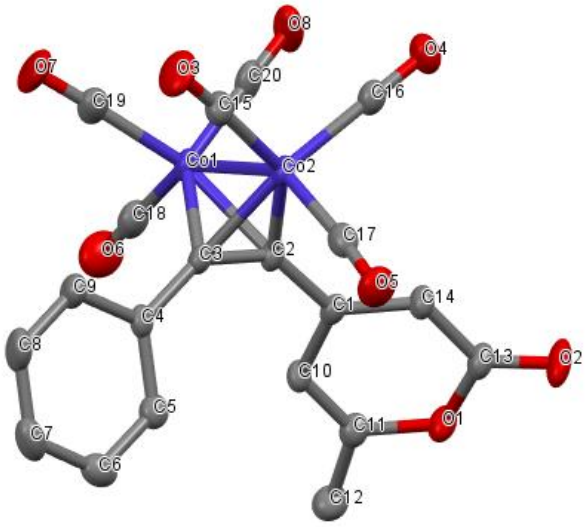

*Figure 133 - SCXRD structure of compound **146**. Thermal ellipsoids shown with 50% probability. Hydrogen atoms omitted for clarity.*

Selected bond lengths (Å): C1-C2: 1.454(4), C2-C3: 1.360(4), C3-C4: 1.455(4), C2-Co1: 1.974(3), C2-Co2: 1.947(4), Co1-Co2: 2.4727(9), C3-Co1: 1.956(3), C3-Co2: 1.972(4), Co1-C18: 1.805(5), Co1-C19: 1.817(4), Co1-C20: 1.828(4), Co2-C15: 1.820(3), Co2-C16: 1.841(4), Co2-C17: 1.812(4). Selected bond angles (°): C1-C2-C3: 141.8(3), C4-C3-C2: 142.5(3), C1-C2-Co1: 133.9(2), C1-C2-Co2: 135.0(2), C4-C3-Co1: 135.6(2), C4-C3-Co2: 133.0(2). Selected dihedrals (°): C1-C2-C3-C4: 6.1(8), C14-C2-C3-C9: -30(2), C18-Co1-Co2-C17: -9.3(4).

*Table 24 - Crystal data and structure refinement for compound **146***

Identification code	tt23004
Empirical formula	$C_{20}H_{10}Co_2O_8$
Formula weight	496.14
Temperature/K	110.05(10)
Crystal system	triclinic
Space group	P-1
a/Å	8.5483(3)
b/Å	8.5830(3)
c/Å	14.2565(5)
α/°	80.913(3)
β/°	77.699(3)
γ/°	75.855(3)
Volume/Å^3	984.79(6)
Z	2
ρ_{calc}g/cm^3	1.673
μ/mm^{-1}	13.614
F(000)	496.0
Crystal size/mm^3	0.21 × 0.09 × 0.05
Radiation	Cu Kα (λ = 1.54184)
2Θ range for data collection/°	10.696 to 153.31
Index ranges	$-8 \leq h \leq 10$, $-10 \leq k \leq 10$, $-17 \leq l \leq 17$
Reflections collected	9040
Independent reflections	3892 [R_{int} = 0.0467, R_{sigma} = 0.0533]
Data/restraints/parameters	3892/0/272
Goodness-of-fit on F^2	1.055
Final R indexes [I>=2σ (I)]	R_1 = 0.0466, wR_2 = 0.1059
Final R indexes [all data]	R_1 = 0.0582, wR_2 = 0.1122
Largest diff. peak/hole / e Å^{-3}	0.69/-0.40

X-ray diffraction data for compound **157**

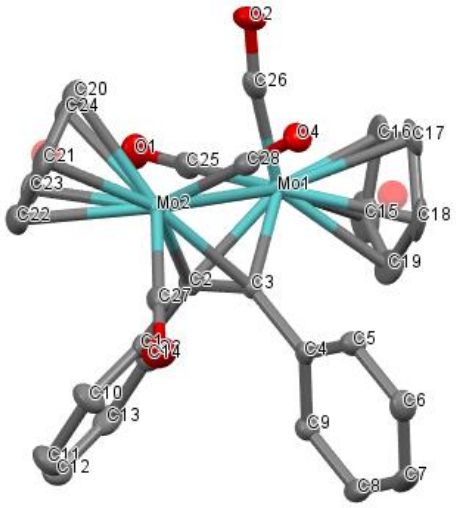

*Figure 134 - SCXRD structure of compound **157**. Thermal ellipsoids shown with 50% probability. Hydrogen atoms omitted for clarity.*

Selected bond lengths (Å): C1-C2: 1.476(3), C2-C3: 1.358(4), C3-C4: 1.473(3), C2-Mo1: 2.188(2), C2-Mo2: 2.196(3), C3-Mo1: 2.159(2), C3-Mo2: 2.204(2), Mo1-C26: 1.949(2), Mo1-C25: 1.958(3), Mo1-centroid: C15 C19 C18 C17 C16: 2.021, Mo2-C27: 1.970(2), Mo2-C28: 1.996(3), Mo2-centroid: C23 C20 C24 C22 C21: 2.001, Mo2-C26: 2.877(2), C1-C2: 1.476(3), C1-C2: 1.476(3), C1-C2: 1.476(3), C1-C2: 1.476(3), Mo1-Mo2: 2.9679(3). Selected bond angles (°): C1-C2-C3: 134.1(2), C4-C3-C2: 134.7(2), C1-C2-Mo1: 138.3(2), C1-C2-Mo2: 130.1(2), C4-C3-Mo1: 130.7(2), C4-C3-Mo2: 136.2(2), Mo1-Mo2-C28: 83.45(7), Mo1-Mo2-C27: 122.33(8), Mo2-Mo1-C25: 88.00(8), Mo2-Mo1-C26: 68.01(7), Mo1-C26-O2: 170.2(2), Mo2-Mo1-centroid: C15 C19 C18 C17 C16: 152.47, Mo1-Mo2-centroid: C23 C20 C24 C22 C21: 122.43. Selected dihedrals (°): C1-C2-C3-C4: 8.6(5), C9-C3-C2-C14: -24.4(3), centroid: C15 C19 C18 C17 C16-Mo1-Mo2-centroid: C23 C20 C24 C22 C21: 163.57.

*Table 25- Crystal data and structure refinement for compound **157***

Identification code	jms22008
Empirical formula	$C_{28}H_{20}O_4Mo_2$
Formula weight	612.32
Temperature/K	109.8(3)
Crystal system	monoclinic
Space group	I2/a
a/Å	16.1306(3)
b/Å	8.93680(10)
c/Å	32.4119(5)
α/°	90
β/°	97.116(2)
γ/°	90
Volume/Å^3	4636.38(13)
Z	8
ρ_{calc}g/cm^3	1.754
μ/mm^{-1}	1.115
F(000)	2432.0
Crystal size/mm^3	0.35 × 0.16 × 0.14
Radiation	MoKα (λ = 0.71073)
2Θ range for data collection/°	6.724 to 57.918
Index ranges	$-21 \leq h \leq 20$, $-11 \leq k \leq 11$, $-43 \leq l \leq 43$
Reflections collected	10239
Independent reflections	5265 [R_{int} = 0.0217, R_{sigma} = 0.0372]
Data/restraints/parameters	5265/0/308
Goodness-of-fit on F^2	1.051
Final R indexes [I>=2σ (I)]	R_1 = 0.0269, wR_2 = 0.0547
Final R indexes [all data]	R_1 = 0.0349, wR_2 = 0.0603
Largest diff. peak/hole / e Å^{-3}	0.37/-0.41

X-ray diffraction data for compound **158**

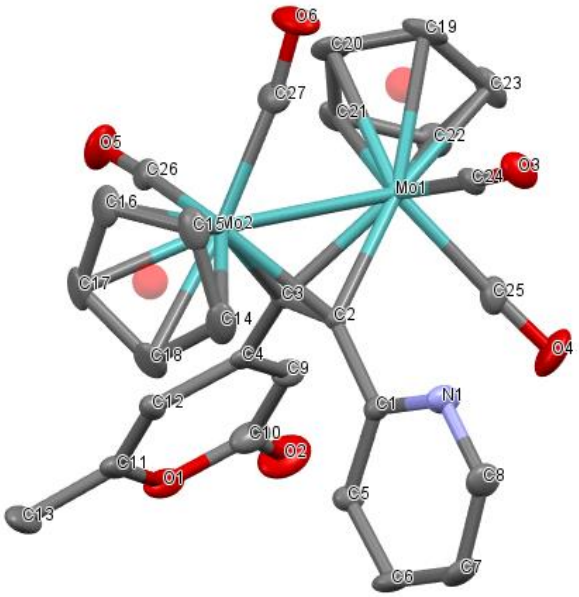

*Figure 135 - SCXRD structure of compound **158**. Thermal ellipsoids shown with 50% probability. Hydrogen atoms omitted for clarity.*

Selected bond lengths (Å): C1-C2: 1.466(2), C2-C3: 1.383(3), C3-C4: 1.461(3), C2-Mo1: 2.186(2), C2-Mo2: 2.134(2), Mo1-centroid: C22 C23 C19 C20 C21: 2.003, Mo1-C25: 1.984(2), Mo1-C24: 2.006(2), Mo2-C26: 1.978(2), Mo2-C27: 1.969(2), Mo2-centroid: C18 C17 C16 C15 C14: 2.013, C27-Mo1: 2.915(2). Selected bond angles (°): C1-C2-C3: 134.1(2), C4-C3-C2: 132.1(2), C9-C2-Mo2: 106.64(8), C1-C2-Mo1: 133.4(1), C4-C3-Mo1: 135.0(1), C4-C3-Mo2: 135.2(1), Mo1-Mo2-C27: 68.88(7), Mo1-Mo2-centroid: C18 C17 C16 C15 C14: 153.48, Mo1-Mo2-C26: 87.03(7), Mo2-Mo1-C24: 88.12(6), Mo2-Mo1-C25: 122.12(7), Mo2-Mo1-centroid: C22 C23 C19 C20 C21: 121.54, Mo2-C27-O6: 170.1(2). Selected dihedrals (°): centroid: C22 C23 C19 C20 C21-Mo1-Mo2-centroid: C18 C17 C16 C15 C14: -159.47, C1-C2-C3-C4: 2.9(4), C9-C3-C2-C5: -40.0(2).

*Table 26 - Crystal data and structure refinement for compound **158***

Identification code	jms22011
Empirical formula	$C_{27}H_{19}Mo_2NO_6$
Formula weight	645.31
Temperature/K	110.00(10)
Crystal system	triclinic
Space group	P-1
a/Å	8.6500(4)
b/Å	9.7066(4)
c/Å	16.6660(7)
α/°	91.767(4)
β/°	102.166(4)
γ/°	105.286(4)
Volume/Å^3	1313.94(10)
Z	2
ρ_{calc}g/cm^3	1.631
μ/mm^{-1}	8.164
F(000)	640.0
Crystal size/mm^3	0.18 × 0.15 × 0.13
Radiation	Cu Kα (λ = 1.54184)
2Θ range for data collection/°	9.486 to 143.204
Index ranges	-10 ≤ h ≤ 10, -11 ≤ k ≤ 11, -20 ≤ l ≤ 16
Reflections collected	9050
Independent reflections	5009 [R_{int} = 0.0163, R_{sigma} = 0.0234]
Data/restraints/parameters	5009/0/327
Goodness-of-fit on F^2	1.038
Final R indexes [I>=2σ (I)]	R_1 = 0.0188, wR_2 = 0.0447
Final R indexes [all data]	R_1 = 0.0214, wR_2 = 0.0460
Largest diff. peak/hole / e Å^{-3}	0.44/-0.41

Disordered toluene in the structure was modelled implicitly using a BYPASS/SQUEEZE solvent mask.

Appendix 5: Nomenclature for PES isomers

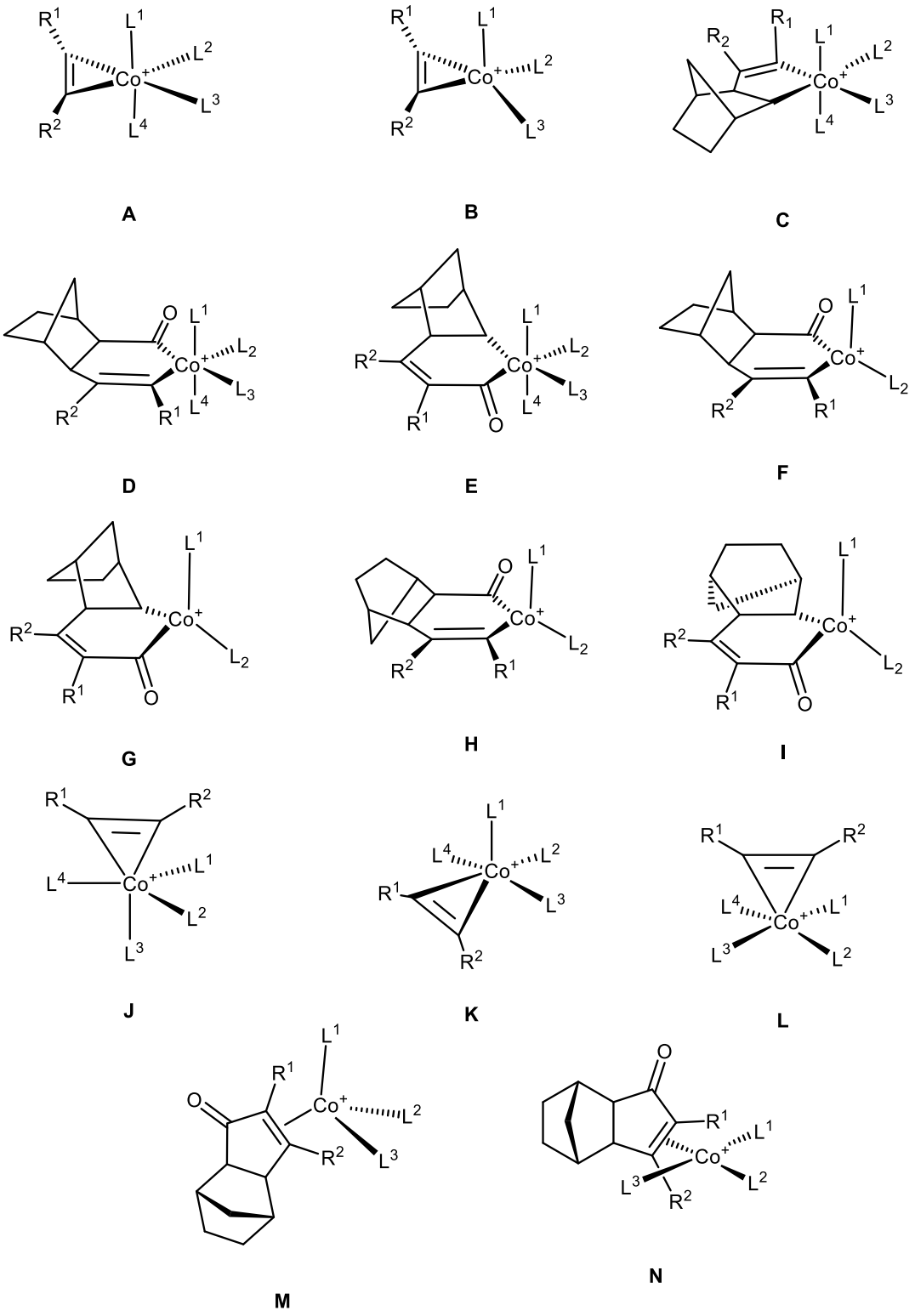

*Figure 136 - General structures for states in the **MC** and **DC** pathways.*

*Table 27 – Structural information for intermediates on the monocarbonyl (**MC)** pathway.*

Intermediate	Isomer	Base geometry	R1	R2	L1	L2	L3	L4
MC1 CO THF3	**iso1**	**A**	Pyrone	2-pyridyl	CO	THF	THF	THF
	iso2	**A**	Pyrone	2-pyridyl	THF	CO	THF	THF
	iso3	**A**	Pyrone	2-pyridyl	THF	THF	THF	CO
	iso4	**A**	Pyrone	2-pyridyl	THF	THF	CO	THF
MC1 CO THF2	**iso1**	**B**	Pyrone	2-pyridyl	THF	CO	THF	
	iso2	**B**	Pyrone	2-pyridyl	THF	THF	CO	
	iso3	**B**	Pyrone	2-pyridyl	CO	THF	THF	
	iso4	**A**	Pyrone	2-pyridyl	THF	THF	CO	-
	iso5	**A**	Pyrone	2-pyridyl	THF	CO	THF	-
	iso6	**A**	Pyrone	2-pyridyl	CO	THF	THF	-
MC2 CO THF2	**iso1**	**A**	Pyrone	2-pyridyl	CO	THF	NBE	THF
	iso2	**A**	Pyrone	2-pyridyl	CO	NBE	THF	THF
	iso3	**A**	Pyrone	2-pyridyl	NBE	THF	THF	CO
	iso4	**A**	Pyrone	2-pyridyl	NBE	THF	CO	THF
MC3 CO THF2	**iso1**	**C**	Pyrone	2-pyridyl	CO	-	THF	THF
	iso2	**C**	Pyrone	2-pyridyl	CO	THF	THF	-
	iso3	**C**	Pyrone	2-pyridyl	THF	-	CO	THF
	iso4	**C**	2-pyridyl	Pyrone	CO	-	THF	THF
	iso5	**C**	2-pyridyl	Pyrone	CO	THF	THF	-
	iso6	**C**	2-pyridyl	Pyrone	THF	-	CO	THF
	iso7	**C**	Pyrone	2-pyridyl	THF	CO	THF	-
	iso8	**C**	Pyrone	2-pyridyl	THF	THF	CO	-
	iso9	**C**	2-pyridyl	Pyrone	THF	CO	THF	-
	iso10	**C**	2-pyridyl	Pyrone	THF	THF	CO	-

Intermediate	Isomer	Base geometry	R1	R2		L1	L2	L3	L4
MC3 CO THF3	**iso1**	**C**	Pyrone	2-pyridyl		CO	THF	THF	THF
	iso2	**C**	Pyrone	2-pyridyl		THF	CO	THF	THF
	iso3	**C**	Pyrone	2-pyridyl		THF	THF	CO	THF
	iso4	**C**	Pyrone		2-pyridyl	THF	THF	THF	CO
	iso5	**C**	2-pyridyl		Pyrone	CO	THF	THF	THF
	iso6	**C**	2-pyridyl		Pyrone	THF	CO	THF	THF
	iso7	**C**	2-pyridyl		Pyrone	THF	THF	CO	THF
	iso8	**C**	2-pyridyl		Pyrone	THF	THF	THF	CO
MC4 THF2	**iso1**	**E**	Pyrone		2-pyridyl	-	THF	THF	-
	iso2	**D**	Pyrone		2-pyridyl	-	THF	THF	-
	iso3	**G**	Pyrone		2-pyridyl	THF	THF	-	-
	iso4	**F**	Pyrone		2-pyridyl	THF	THF	-	-
	iso5	**E**	2-pyridyl		Pyrone	-	THF	THF	-
	iso6	**D**	2-pyridyl		Pyrone	-	THF	THF	-
	iso7	**G**	2-pyridyl		Pyrone	THF	THF	-	-
	iso8	**F**	2-pyridyl		Pyrone	THF	THF	-	-
MC4 THF3	**iso1**	**E**	Pyrone		2-pyridyl	THF	THF	THF	-
	iso2	**E**	Pyrone		2-pyridyl	THF	THF	-	THF
	iso3	**E**	Pyrone		2-pyridyl	THF	-	THF	THF
	iso4	**D**	Pyrone		2-pyridyl	THF	THF	THF	-
	iso5	**D**	Pyrone		2-pyridyl	THF	-	THF	THF
	iso6	**D**	Pyrone		2-pyridyl	THF	THF	-	THF
	iso7	**E**	2-pyridyl		Pyrone	THF	THF	THF	-
	iso8	**E**	2-pyridyl		Pyrone	THF	THF	-	THF

Intermediate	Isomer	Base geometry	R1	R2		L1	L2	L3	L4
	iso9	**E**	2-pyridyl		Pyrone	THF	-	THF	THF
	iso10	**D**	2-pyridyl		Pyrone	THF	THF	THF	-
	iso11	**D**	2-pyridyl		Pyrone	THF	-	THF	THF
	iso12	**D**	2-pyridyl		Pyrone	THF	THF	-	THF
MC5 THF3	**iso1**	**M**	Pyrone		2-pyridyl	THF	THF	THF	
	iso2	**N**	Pyrone		2-pyridyl	THF	THF	THF	
	iso3	**M**	2-pyridyl		Pyrone	THF	THF	THF	
	iso4	**N**	2-pyridyl		Pyrone	THF	THF	THF	

Intermediate	Isomer	Base geometry	R1	R2	L1	L2	L3	L4
DC1 CO2 THF2	iso1	A	Pyrone	2-pyridine	CO	THF	THF	CO
	iso2	A	Pyrone	2-pyridine	CO	THF	CO	THF
	iso3	A	Pyrone	2-pyridine	CO	CO	THF	THF
	iso4	A	Pyrone	2-pyridine	THF	CO	CO	THF
	iso5	J	Pyrone	2-pyridine	CO	CO	THF	THF
	iso6	J	Pyrone	2-pyridine	THF	CO	THF	THF
	iso7	K	Pyrone	2-pyridine	CO	THF	THF	CO
	iso8	K	Pyrone	2-pyridine	CO	CO	THF	THF
	iso9	K	Pyrone	2-pyridine	CO	THF	CO	THF
	iso10	K	Pyrone	2-pyridine	THF	THF	CO	CO
	iso11	K	Pyrone	2-pyridine	THF	THF	CO	CO
	iso12	K	Pyrone	2-pyridine	THF	CO	THF	CO
	iso13	L	Pyrone	2-pyridine	THF	THF	CO	CO
	iso14	L	Pyrone	2-pyridine	CO	THF	CO	THF
DC1 CO2 THF	iso1	B	Pyrone	2-pyridine	CO	CO	THF	
	iso2	B	2-pyridine	pyrone	CO	CO	THF	
	iso3	B	Pyrone	2-pyridine	CO	THF	THF	
DC2 CO2 THF	iso1	A	Pyrone	2-pyridine	CO	NBE	THF	CO
	iso2	A	Pyrone	2-pyridine	CO	THF	NBE	CO
	iso3	A	Pyrone	2-pyridine	CO	NBE	CO	THF
	iso4	A	Pyrone	2-pyridine	CO	THF	CO	NBE
	iso5	A	Pyrone	2-pyridine	CO	CO	NBE	THF
	iso6	A	Pyrone	2-pyridine	CO	CO	THF	NBE

Intermediate	Isomer	Base geometry	R1	R2	L1	L2	L3	L4
	iso7	A	Pyrone	2-pyridine	THF	CO	CO	NBE
	iso8	A	Pyrone	2-pyridine	NBE	CO	CO	THF
	iso9	A	Pyrone	2-pyridine	THF	CO	NBE	CO
	iso10	A	Pyrone	2-pyridine	NBE	CO	THF	CO
DC3 CO2 THF	iso1	C	Pyrone	2-pyridine	CO	THF	CO	-
	iso2	C	Pyrone	2-pyridine	-	CO	THF	CO
	iso3	C	2-pyridine	pyrone	CO	THF	CO	-
	iso4	C	2-pyridine	pyrone	-	CO	THF	CO
	iso5	C	Pyrone	2-pyridine	CO	-	THF	CO
	iso6	C	Pyrone	2-pyridine	CO	-	THF	CO
	iso7	C	2-pyridine	pyrone	CO	-	THF	CO
	iso8	C	2-pyridine	pyrone	CO	-	THF	CO
	iso9	C	Pyrone	2-pyridine	THF	-	CO	THF
	iso10	C	Pyrone	2-pyridine	CO	-	CO	THF
	iso11	C	2-pyridine	pyrone	THF	-	CO	THF
	iso12	C	2-pyridine	pyrone	CO	-	CO	THF
	iso13	C	Pyrone	2-pyridine	THF	CO	CO	-
	iso14	C	Pyrone	2-pyridine	-	CO	CO	THF
	iso15	C	2-pyridine	pyrone	THF	CO	CO	-
	iso16	C	2-pyridine	pyrone	-	CO	CO	THF
	iso17	C	Pyrone	2-pyridine	CO	CO	-	THF
	iso18	C	Pyrone	2-pyridine	THF	CO	-	CO
	iso19	C	2-pyridine	pyrone	CO	CO	-	THF

Intermediate	Isomer	Base geometry	R1	R2	L1	L2	L3	L4
	iso20	C	2-pyridine	pyrone	THF	CO	-	CO
DC3 CO THF2	iso1	C	Pyrone	2-pyridine	CO	CO	THF	THF
	iso2	C	Pyrone	2-pyridine	THF	CO	THF	CO
	iso3	C	2-pyridine	pyrone	CO	CO	THF	THF
	iso4	C	2-pyridine	pyrone	THF	CO	THF	CO
	iso5	C	Pyrone	2-pyridine	CO	THF	CO	THF
	iso6	C	Pyrone	2-pyridine	THF	THF	CO	CO
	iso7	C	2-pyridine	pyrone	CO	THF	CO	THF
	iso8	C	2-pyridine	pyrone	THF	THF	CO	CO
	iso9	C	Pyrone	2-pyridine	CO	THF	THF	CO
	iso10	C	Pyrone	2-pyridine	CO	THF	THF	CO
	iso11	C	2-pyridine	pyrone	CO	THF	THF	CO
	iso12	C	2-pyridine	pyrone	CO	THF	THF	CO
	iso13	C	Pyrone	2-pyridine	THF	CO	CO	THF
	iso14	C	Pyrone	2-pyridine	THF	CO	CO	THF
	iso15	C	2-pyridine	pyrone	THF	CO	CO	THF
	iso16	C	2-pyridine	pyrone	THF	CO	CO	THF
DC4 CO THF	iso1	E	Pyrone	2-pyridine	-	THF	CO	-
	iso2	E	Pyrone	2-pyridine	-	THF	CO	-
	iso3	E	2-pyridine	pyrone	-	THF	CO	-
	iso4	E	2-pyridine	pyrone	-	THF	CO	-
	iso5	E	Pyrone	2-pyridine	-	CO	THF	-
	iso6	E	Pyrone	2-pyridine	-	CO	THF	-

Intermediate	Isomer	Base geometry	R1	R2	L1	L2	L3	L4
	iso7	E	2-pyridine	pyrone	-	CO	THF	-
	iso8	E	2-pyridine	pyrone	-	CO	THF	-
	iso9	G	Pyrone	2-pyridine	THF	CO		
	iso10	I	Pyrone	2-pyridine	THF	CO		
	iso11	G	2-pyridine	pyrone	THF	CO		
	iso12	I	2-pyridine	pyrone	THF	CO		
	iso13	G	Pyrone	2-pyridine	CO	THF		
	iso14	I	Pyrone	2-pyridine	CO	THF		
	iso15	G	2-pyridine	pyrone	CO	THF		
	iso16	I	2-pyridine	pyrone	CO	THF		
	iso17	D	Pyrone	2-pyridine	-	THF	CO	-
	iso18	D	Pyrone	2-pyridine	-	THF	CO	-
	iso19	D	2-pyridine	pyrone	-	THF	CO	-
	iso20	D	2-pyridine	pyrone	-	THF	CO	-
	iso21	D	Pyrone	2-pyridine	-	CO	THF	-
	iso22	D	Pyrone	2-pyridine	-	CO	THF	-
	iso23	D	2-pyridine	pyrone	-	CO	THF	-
	iso24	D	2-pyridine	pyrone	-	CO	THF	-
	iso25	H	Pyrone	2-pyridine	THF	CO		
	iso26	I	Pyrone	2-pyridine	THF	CO		
	iso27	H	2-pyridine	pyrone	THF	CO		
	iso28	I	2-pyridine	pyrone	THF	CO		
	iso29	H	Pyrone	2-pyridine	CO	THF		

Intermediate	Isomer	Base geometry	R1	R2	L1	L2	L3	L4
	iso30	I	Pyrone	2-pyridine	CO	THF		
	iso31	H	2-pyridine	pyrone	CO	THF		
	iso32	I	2-pyridine	pyrone	CO	THF		
DC4 CO THF2	iso1	E	Pyrone	2-pyridine	-	THF	CO	THF
	iso2	E	Pyrone	2-pyridine	-	CO	THF	THF
	iso3	E	2-pyridine	pyrone	-	THF	CO	THF
	iso4	E	2-pyridine	pyrone	-	CO	THF	THF
	iso5	E	Pyrone	2-pyridine	`	THF	THF	CO
	iso6	E	Pyrone	2-pyridine	CO	THF	THF	-
	iso7	E	2-pyridine	pyrone	`	THF	THF	CO
	iso8	E	2-pyridine	pyrone	CO	THF	THF	-
	iso9	E	Pyrone	2-pyridine	THF	THF	-	CO
	iso10	E	Pyrone	2-pyridine	CO	THF	-	THF
	iso11	E	2-pyridine	pyrone	THF	THF	-	CO
	iso12	E	2-pyridine	pyrone	CO	THF	-	THF
	iso13	E	Pyrone	2-pyridine	THF	CO	-	THF
	iso14	E	Pyrone	2-pyridine	THF	THF	CO	-
	iso15	E	2-pyridine	pyrone	THF	CO	-	THF
	iso16	E	2-pyridine	pyrone	THF	THF	CO	-
	iso17	E	Pyrone	2-pyridine	THF	-	CO	THF
	iso18	E	Pyrone	2-pyridine	CO	-	THF	THF
	iso19	E	2-pyridine	pyrone	THF	-	CO	THF
	iso20	E	2-pyridine	pyrone	CO	-	THF	THF

Intermediate	Isomer	Base geometry	R1	R2	L1	L2	L3	L4
	iso21	E	Pyrone	2-pyridine	THF	-	THF	CO
	iso22	D	Pyrone	2-pyridine	-	THF	CO	THF
	iso23	D	Pyrone	2-pyridine	-	CO	THF	THF
	iso24	D	2-pyridine	pyrone	-	THF	CO	THF
	iso25	D	2-pyridine	pyrone	-	CO	THF	THF
	iso26	D	Pyrone	2-pyridine	-	THF	THF	CO
	iso27	D	Pyrone	2-pyridine	CO	THF	THF	-
	iso28	D	2-pyridine	pyrone	-	THF	THF	CO
	iso29	D	2-pyridine	pyrone	CO	THF	THF	-
	iso30	D	Pyrone	2-pyridine	THF	THF	-	CO
	iso31	D	Pyrone	2-pyridine	CO	THF	-	THF
	iso32	D	2-pyridine	pyrone	THF	THF	-	CO
	iso33	D	2-pyridine	pyrone	CO	THF	-	THF
	iso34	D	Pyrone	2-pyridine	THF	CO	-	THF
	iso35	D	Pyrone	2-pyridine	THF	THF	CO	-
	iso36	D	2-pyridine	pyrone	THF	CO	-	THF
	iso37	D	2-pyridine	pyrone	THF	THF	CO	-
	iso38	D	Pyrone	2-pyridine	THF	-	CO	THF
	iso39	D	Pyrone	2-pyridine	CO	-	THF	THF
	iso40	D	2-pyridine	pyrone	THF	-	CO	THF
	iso41	D	2-pyridine	pyrone	CO	-	THF	THF
	iso42	D	Pyrone	2-pyridine	THF	-	THF	CO
	iso43	D	2-pyridine	pyrone	THF	-	THF	CO

Intermediate	Isomer	Base geometry	R1	R2	L1	L2	L3	L4
	iso44	E	2-pyridine	pyrone	THF	-	THF	CO
DC5 CO THF2	iso1	N	Pyrone	2-pyridine	THF	CO	THF	
	iso2	N	Pyrone	2-pyridine	CO	THF	THF	
	iso3	N	2-pyridine	pyrone	THF	CO	THF	
	iso4	N	2-pyridine	pyrone	CO	THF	THF	
	iso5	M	Pyrone	2-pyridine	THF	CO	THF	
	iso6	M	Pyrone	2-pyridine	CO	THF	THF	
	iso7	M	2-pyridine	pyrone	THF	CO	THF	
	iso8	M	2-pyridine	pyrone	CO	THF	THF	

Appendix 6: Potential energy surface calculation results

Calculation results for the monocarbonyl pathway states **MC1** and **MC2**

*Table 28 - Calculation results (BP86/SV(P)) for isomers of intermediates **MC1** and **MC2***

Intermediate	Isomer	SCF (a.u.)	DFT-D3 corr. (a.u.)	COSMO (CH2Cl2) (a.u.)	ZPE (a.u.)	Chem. Pot. (kJ/mol)	Energy (kJ/mol)	Entropy (kJ/K/mol)
MC1 CO THF3	iso1	-2898.267967	-0.15	-2898.32	0.54	1217.72	1507.90	0.98
	iso2	-2898.259333	-0.15	-2898.32	0.54	1217.99	1507.53	0.98
	iso3	-2898.267051	-0.15	-2898.32	0.54	1222.38	1501.95	0.95
	iso4	-2898.256496	-0.15	-2898.31	0.54	1222.02	1507.94	0.97
MC1 CO THF2	iso1	-2665.958208	-0.12	-2666.02	0.42	929.81	1186.93	0.87
	iso2	-2665.976482	-0.12	-2666.03	0.42	932.70	1187.96	0.86
	iso3	-2665.976162	-0.12	-2666.03	0.42	933.50	1188.00	0.86
	iso4	-2665.973245	-0.12	-2666.03	0.42	935.05	1184.66	0.85
	iso5	-2665.973136	-0.11	-2666.03	0.42	930.18	1187.59	0.87
	iso6	-2665.974996	-0.12	-2666.03	0.42	930.36	1187.19	0.87
MC2 CO THF2	iso1	-2938.510269	-0.17	-2938.56	0.57	1312.65	1600.10	0.97
	iso2	-2938.514633	-0.17	-2938.57	0.57	1320.21	1601.89	0.95
	iso3	-2938.497119	-0.17	-2938.55	0.57	1312.77	1599.67	0.97
	iso4	-2938.50867	-0.17	-2938.56	0.57	1314.93	1600.66	0.97

*Table 29 - Calculated energies of isomers for intermediates **MC1** and **MC2** with solvation and dispersion energetic corrections.*

		Entropy at 1 mol/dm3 (kJ/K/mol)	Electronic E gas (kJ/mol)	Electronic E+D gas (kJ/mol)	Electronic E CH2Cl2 (kJ/mol)	Electronic E+D CH2Cl2 (kJ/mol)
MC1 CO THF3	iso1	0.9549	-120	-175	-100	-155
	iso2	0.9527	-97	-158	-78	-139
	iso3	0.9193	-118	-170	-97	-150
	iso4	0.9406	-90	-150	-72	-132
MC1 CO THF2	iso1	0.8440	0	0	0	0
	iso2	0.8378	-48	-43	-46	-41
	iso3	0.8352	-47	-43	-44	-40
	iso4	0.8188	-39	-31	-34	-26
	iso5	0.8450	-39	-29	-34	-24
	iso6	0.8431	-44	-37	-37	-30
MC2 CO THF2	iso1	0.9458	-84	-147	-67	-130
	iso2	0.9264	-96	-162	-76	-142
	iso3	0.9439	-50	-122	-31	-103
	iso4	0.9400	-80	-151	-64	-135

*Table 30 - Calculated Gibbs energies for isomers of intermediates **MC1** and **MC2** with solvation and dispersion energetic corrections.*

		Gas Phase 298.15 K			COSMO CH2Cl2 298.15 K			DFT-D3 COSMO CH2Cl2 298.15 K			
Intermediate	**Isomer**	Rel H (kJ/mol)	Rel S (J/K/mol)	Rel G (kJ/mol)	Rel H (kJ/mol)	Rel S (J/K/mol)	Rel G (kJ/mol)	Rel H (kJ/mol)	Rel S (J/K/mol)	Rel G (kJ/mol)	Relative Pathway energy
MC1 CO THF3	iso1	-108	-165	-58	-88	-138	-47	-143	-138	-101	0
	iso2	-85	-167	-35	-66	-141	-24	-127	-141	-85	16
	iso3	-111	-201	-51	-91	-174	-39	-143	-174	-91	10
	iso4	-77	-179	-24	-59	-153	-14	-119	-153	-74	27
MC1 CO THF2	iso1	0	0	0	0	0	0	0	0	0	100
	iso2	-47	-6	-45	-45	-6	-43	-40	-6	-38	62
	iso3	-46	-9	-43	-43	-9	-41	-39	-9	-36	64
	iso4	-42	-25	-34	-37	-25	-29	-29	-25	-21	79
	iso5	-39	1	-39	-33	1	-34	-23	1	-24	76
	iso6	-44	-1	-44	-36	-1	-36	-30	-1	-29	70
MC2 CO THF2	iso1	-77	-206	-15	-60	-180	-6	-123	-180	-69	30
	iso2	-86	-226	-19	-67	-199	-7	-133	-199	-73	27
	iso3	-43	-208	19	-24	-182	30	-96	-182	-42	58
	iso4	-72	-212	-9	-56	-185	-1	-127	-185	-72	28

Calculation results for the monocarbonyl pathway states **MC TS23** to **MC5** to give **140β** (monocarbonyl β-pyridyl pathway)

*Table 31 - Calculation results (BP86/SV(P)) for isomers of intermediates **TS32** and **MC3** on the β-pyridyl pathway.*

Intermediate	Isomer	SCF (a.u.)	DFT-D3 corr. (a.u.)	COSMO (CH2Cl2) (a.u.)	ZPE (a.u.)	Chem. Pot. (kJ/mol)	Energy (kJ/mol)	Entropy (kJ/K/mol)
TS23	iso1	-2938.468312	-0.1708	-2938.527333	0.572165	1316.69	1596.44	0.94663
MC3 CO THF2	iso1	-2938.546072	-0.17529	-2938.604529	0.574738	1323.96	1602.73	0.94332
	iso2	-2938.545959	-0.17513	-2938.604679	0.574424	1325.8	1599.91	0.92768
	iso3	-2938.520134	-0.17904	-2938.576776	0.575085	1330.05	1603.02	0.92383
	iso11	-2938.543387	-0.17349	-2938.601888	0.574372	1318.74	1602.15	0.95887
MC3 CO THF3	iso1	-3170.834864	-0.21444	-3170.890866	0.691344	1617.15	1924.19	1.03812
	iso2	-3170.797979	-0.21528	-3170.854749	0.690926	1617.36	1922.94	1.03324
	iso3	-3170.802641	-0.2091	-3170.855129	0.689772	1600.96	1922.08	1.08537
	iso4	-3170.825017	-0.21557	-3170.879785	0.691611	1618.02	1924.92	1.03769

*Table 32 - Calculated energies of states **TS23** and **MC3** on the β-pyridyl pathway, with dispersion and solvation corrections.*

		Entropy at 1 mol/dm3 (kJ/K/mol)	Electronic E gas (kJ/mol)	Electronic E+D gas (kJ/mol)	Electronic E CH2Cl2 (kJ/mol)	Electronic E+D CH2Cl2 (kJ/mol)
TS23	iso1	0.9199	26	-45	30	-41
MC3 CO THF2	iso1	0.9166	-178	-261	-172	-255
	iso2	0.9010	-178	-260	-173	-255
	iso3	0.8971	-110	-203	-100	-192
	iso11	0.9322	-171	-249	-166	-244
MC3 CO THF3	iso1	1.0114	-241	-392	-219	-370
	iso2	1.0065	-144	-297	-124	-277
	iso3	1.0587	-156	-293	-125	-262
	iso4	1.0110	-215	-369	-190	-344

*Table 33 – Calculated Gibbs energies of states **TS23** and **MC3** on the β-pyridyl pathway, with dispersion and solvation corrections.*

		Gas Phase 298.15 K			COSMO CH2Cl2 298.15 K			DFT-D3 COSMO CH2Cl2 298.15 K			
		Rel H (kJ/mol)	Rel S (J/K/mol)	Rel G (kJ/mol)	Rel H (kJ/mol)	Rel S (J/K/mol)	Rel G (kJ/mol)	Rel H (kJ/mol)	Rel S (J/K/mol)	Rel G (kJ/mol)	Relative Pathway energy
TS23	iso1	30	-232	99	34	-206	95	-37	-206	24	124
MC3 CO THF2	iso1	-168	-236	-98	-163	-209	-100	-246	-209	-183	-83
	iso2	-171	-251	-96	-166	-224	-99	-248	-224	-181	-82
	iso3	-100	-255	-24	-89	-228	-21	-182	-228	-114	-14
	iso11	-162	-220	-96	-156	-193	-99	-234	-193	-177	-77
MC3 CO THF3	iso1	-218	-411	-96	-196	-357	-89	-347	-357	-240	-140
	iso2	-122	-416	1	-102	-362	6	-255	-362	-148	-48
	iso3	-136	-363	-27	-104	-310	-12	-241	-310	-149	-49
	iso4	-192	-411	-69	-166	-358	-59	-320	-358	-213	-113

*Table 34 - Calculation results (BP86/SV(P)) for isomers of intermediates **TS34** and **MC4** and **MC5** on the β-pyridyl pathway.*

	Isomer	SCF (a.u.)	DFT-D3 corr. (a.u.)	COSMO (CH2Cl2) (a.u.)	ZPE (a.u.)	Chem. Pot. (kJ/mol)	Energy (kJ/mol)	Entropy (kJ/K/mol)	ln q(vib)
TS34 THF3	iso1	-3170.80664	-0.21236	-3170.864752	0.690268	1614.05	1920.25	1.03532	42.34
MC4 THF2	iso1	-2938.518985	-0.16285	-2938.574058	0.573818	1319.11	1599.6	0.94907	38.25
	iso2	-2938.510799	-0.17005	-2938.566163	0.575654	1323.14	1604.6	0.95233	38.72
	iso3	-2938.511182	-0.16545	-2938.56952	0.573336	1317.95	1598.46	0.94916	38.25
	iso4	-2938.552712	-0.17237	-2938.606886	0.575979	1331.22	1604.54	0.92504	35.89
MC4 THF3	iso1	-3170.817517	-0.20169	-3170.872502	0.6908	1609.81	1921.33	1.05315	44.47
	iso2	-3170.81619	-0.20489	-3170.87419	0.692334	1613.84	1926.03	1.05539	44.5
	iso3	-3170.822343	-0.20768	-3170.880483	0.691536	1612.12	1924.28	1.0553	44.37
	iso4	-3170.832491	-0.21211	-3170.888797	0.691478	1618.62	1920.16	1.01968	41.79
	iso5	-3170.826261	-0.21129	-3170.880724	0.692599	1620.87	1924.39	1.02632	42.06
	iso6	-3170.834297	-0.21328	-3170.889605	0.692565	1620.39	1926.37	1.03459	42.23
MC5_THF3	iso1	-3170.823593	-0.21579	-3170.886883	0.693421	1623.33	1927.31	1.02787	41.99
	iso2	-3170.823689	-0.21582	-3170.886975	0.693491	1625.03	1927.27	1.02203	41.38

*Table 35 - Calculated energies of states **TS34** and **MC4** and **MC5** on the β-pyridyl pathway, with dispersion and solvation corrections..*

	Isomer	Entropy at 1 mol/dm3 (kJ/K/mol)	Electronic E gas (kJ/mol)	Electronic E+D gas (kJ/mol)	Electronic E CH2Cl2 (kJ/mol)	Electronic E+D CH2Cl2 (kJ/mol)
TS34 THF3	iso1	1.0086	-167	-312	-150	-296
MC4 THF2	iso1	0.9224	-107	-157	-92	-143
	iso2	0.9256	-85	-155	-72	-141
	iso3	0.9225	-86	-144	-81	-138
	iso4	0.8983	-196	-271	-179	-254
MC4 THF3	iso1	1.0265	-195	-313	-171	-288
	iso2	1.0287	-192	-318	-175	-301
	iso3	1.0286	-208	-341	-191	-325
	iso4	0.9930	-235	-380	-213	-358
	iso5	0.9996	-218	-361	-192	-335
	iso6	1.0079	-239	-387	-215	-363
MC5_THF3	iso1	1.0012	-211	-366	-208	-363
	iso2	0.9953	-212	-366	-209	-363

*Table 36 - Calculated Gibbs energies of states **TS34** and **MC4** and **MC5** on the β-pyridyl pathway, with dispersion and solvation corrections.*

		Gas Phase 298.15 K			COSMO CH2Cl2 298.15 K			DFT-D3 COSMO CH2Cl2 298.15 K			
		Rel H (kJ/mol)	Rel S (J/K/mol)	Rel G (kJ/mol)	Rel H (kJ/mol)	Rel S (J/K/mo)l	Rel G (kJ/mol)	Rel H (kJ/mol)	Rel S (J/K/mol)	Rel G (kJ/mol)	Pathway Relative energy.
TS34											
THF3	iso1	-148	-413	-25	-131	-360	-24	-277	-360	-169	-70
MC4											
THF2	iso1	-100	-230	-32	-86	-203	-25	-136	-203	-75	24
	iso2	-74	-227	-6	-60	-200	0	-129	-200	-70	30
	iso3	-81	-230	-12	-75	-203	-14	-132	-203	-72	28
	iso4	-184	-254	-108	-167	-227	-99	-242	-227	-175	-75
MC4											
THF3	iso1	-175	-396	-57	-151	-342	-48	-268	-342	-166	-66
	iso2	-167	-393	-50	-150	-340	-49	-276	-340	-175	-75
	iso3	-185	-393	-68	-169	-340	-67	-302	-340	-200	-101
	iso4	-216	-429	-88	-194	-376	-82	-339	-376	-227	-127
	iso5	-195	-422	-69	-169	-369	-59	-312	-369	-202	-102
	iso6	-214	-414	-91	-190	-361	-83	-338	-361	-231	-131
MC5											
THF3	iso1	-185	-421	-60	-182	-368	-73	-337	-368	-227	-127
	iso2	-186	-427	-58	-183	-373	-71	-337	-373	-226	-126

Calculation results for the monocarbonyl pathway states **MC TS23** to **MC5** to give **140α** (monocarbonyl α-pyridyl pathway)

*Table 37 - Calculation results (BP86/SV(P)) for isomers of intermediates **TS32** and **MC3** on the α-pyridyl pathway.*

Intermediate	Isomer	SCF (a.u.)	DFT-D3 corr. (a.u.)	COSMO (CH2Cl2) (a.u.)	ZPE (a.u.)	Chem. Pot. (kJ/mol)	Energy (kJ/mol)	Entropy (kJ/K/mol)
TS23	iso4	-2938.47	-0.17	-2938.53	0.57	1319.50	1597.16	0.94
MC3 CO THF2	iso4	-2938.57	-0.17	-2938.62	0.58	1323.89	1604.51	0.95
	iso5	-2938.57	-0.17	-2938.62	0.58	1328.52	1604.24	0.93
	iso6	-2938.54	-0.18	-2938.59	0.58	1332.21	1604.24	0.92
MC3 CO THF3	iso5	-3170.83	-0.21	-3170.89	0.69	1614.48	1923.56	1.04
	iso6	-3170.80	-0.21	-3170.86	0.69	1621.94	1917.38	1.00
	iso7	-3170.80	-0.21	-3170.86	0.69	1621.53	1921.40	1.01
	iso8	-3170.83	-0.21	-3170.88	0.69	1613.11	1924.42	1.05

*Table 38 - Calculated energies of states **TS23** and **MC3** on the β-pyridyl pathway, with dispersion and solvation corrections*

Intermediate	Isomer	Entropy at 1 mol/dm3 (kJ/K/mol)	Electronic E gas (kJ/mol)	Electronic E+D gas (kJ/mol)	Electronic E CH2Cl2 (kJ/mol)	Electronic E+D CH2Cl2 (kJ/mol)
TS23	iso4	0.9129	12	-61	26	-47
MC3 CO THF2	iso4	0.9228	-230	-309	-221	-301
	iso5	0.9064	-229	-309	-221	-300
	iso6	0.8940	-154	-237	-146	-230
MC3 CO THF3	iso5	1.0183	-241	-390	-222	-371
	iso6	0.9725	-153	-300	-130	-277
	iso7	0.9874	-154	-305	-131	-282
	iso8	1.0258	-217	-366	-197	-346

*Table 39 - Calculated Gibbs energies of states **TS23** and **MC3** on the α-pyridyl pathway, with dispersion and solvation corrections.*

		Gas Phase 298.15 K			COSMO CH2Cl2 298.15 K			DFT-D3 COSMO CH2Cl2 298.15 K			
Intermediate	**Isomer**	Rel H (kJ/mol)	Rel S (J/K/mol)	Rel G (kJ/mol)	Rel H (kJ/mol)	Rel S (J/K/mol)	Rel G (kJ/mol)	Rel H (kJ/mol)	Rel S (J/K/mol)	Rel G (kJ/mol)	Relative Pathway energy
TS23	iso4	17	-239	88	30	-213	93	-43	-213	21	121
MC3 CO THF2	iso4	-218	-229	-149	-210	-203	-149	-289	-203	-229	-129
	iso5	-218	-246	-145	-209	-219	-144	-289	-219	-224	-124
	iso6	-142	-258	-65	-135	-231	-66	-218	-231	-149	-49
MC3 CO THF3	iso5	-218	-404	-98	-200	-350	-95	-349	-350	-245	-145
	iso6	-137	-450	-3	-114	-396	4	-260	-396	-142	-43
	iso7	-134	-435	-4	-111	-381	3	-262	-381	-148	-49
	iso8	-194	-396	-76	-174	-343	-72	-322	-343	-220	-120

*Table 40 - Calculation results (BP86/SV(P)) for isomers of intermediates **TS34** and **MC4** and **MC5** on the α-pyridyl pathway.*

Intermediate	Isomer	SCF (a.u.)	DFT-D3 corr. (a.u.)	COSMO (CH2Cl2) (a.u.)	ZPE (a.u.)	Chem. Pot. (kJ/mol)	Energy (kJ/mol)	Entropy (kJ/K/mol)
TS34	iso4	-3170.81	-0.21	-3170.87	0.69	1605.38	1920.05	1.06
MC4 THF2	iso5	-2938.51	-0.16	-2938.57	0.57	1319.13	1599.70	0.95
	iso6	-2938.53	-0.17	-2938.59	0.58	1331.12	1606.56	0.93
	iso7	-2938.51	-0.17	-2938.57	0.57	1318.05	1598.57	0.95
	iso8	-2938.55	-0.18	-2938.61	0.58	1335.47	1603.85	0.91
MC4 THF3	iso7	-3170.82	-0.20	-3170.87	0.69	1610.86	1921.70	1.05
	iso8	-3170.82	-0.21	-3170.88	0.69	1612.72	1926.00	1.06
	iso9	-3170.82	-0.21	-3170.88	0.69	1613.42	1924.24	1.05
	iso10	-3170.83	-0.21	-3170.89	0.69	1610.60	1926.06	1.07
	iso11	-3170.84	-0.21	-3170.90	0.69	1618.23	1924.16	1.03
	iso12	-3170.84	-0.21	-3170.90	0.69	1622.29	1924.21	1.02
MC5_THF3	iso3	-3170.82	-0.21	-3170.88	0.69	1617.98	1925.73	1.04
	iso4	-3170.82	-0.21	-3170.89	0.69	1625.85	1928.09	1.02

*Table 41 -Calculated energies for isomers of intermediates **TS34** and **MC4** and **MC5** on the α-pyridyl pathway with dispersion and solvation corrections.*

Intermediate	Isomer	Entropy at 1 mol/dm3 (kJ/K/mol)	Electronic E gas (kJ/mol)	Electronic E+D gas (kJ/mol)	Electronic E CH2Cl2 (kJ/mol)	Electronic E+D CH2Cl2 (kJ/mol)
TS34	iso4	1.0370	-172	-313	-158	-299
MC4 THF2	iso5	0.9226	-96	-146	-86	-137
	iso6	0.9054	-146	-218	-141	-214
	iso7	0.9225	-91	-151	-83	-143
	iso8	0.8817	-192	-275	-186	-269
MC4 THF3	iso7	1.0242	-193	-310	-168	-285
	iso8	1.0324	-198	-324	-179	-305
	iso9	1.0241	-194	-320	-185	-311
	iso10	1.0397	-223	-362	-209	-348
	iso11	1.0077	-263	-399	-241	-377
	iso12	0.9943	-267	-403	-246	-382
MC5_THF3	iso3	1.0138	-208	-348	-190	-331
	iso4	0.9953	-212	-362	-204	-354

*Table 42 – Calculated Gibbs energies for isomers of intermediates **TS34** and **MC4** and **MC5** on the α-pyridyl pathway with dispersion and solvation corrections.*

Intermediate	Isomer	Rel H (kJ/mol)	Rel S (J/K/mol)	Rel G (kJ/mol)	Rel H (kJ/mol)	Rel S (J/K/mol)	Rel G (kJ/mol)	Rel H (kJ/mol)	Rel S (J/K/mol)	Rel G (kJ/mol)	Relative Pathway energy
TS34	iso4	-153	-385	-38	-139	-332	-40	-280	-332	-182	-82
MC4 THF2	iso5	-89	-230	-20	-79	-203	-19	-130	-203	-70	30
	iso6	-132	-247	-58	-127	-220	-62	-200	-220	-134	-35
	iso7	-85	-230	-17	-77	-203	-16	-137	-203	-77	23
	iso8	-181	-270	-100	-175	-244	-102	-257	-244	-185	-85
MC4 THF3	iso7	-172	-398	-53	-148	-344	-45	-265	-344	-162	-62
	iso8	-173	-390	-57	-154	-336	-54	-280	-336	-180	-80
	iso9	-171	-398	-52	-162	-345	-59	-288	-345	-186	-86
	iso10	-198	-382	-84	-184	-329	-86	-323	-329	-225	-126
	iso11	-240	-414	-117	-219	-361	-111	-354	-361	-246	-147
	iso12	-244	-428	-116	-223	-374	-111	-359	-374	-247	-148
MC5_THF3	iso3	-184	-408	-62	-166	-355	-60	-306	-355	-200	-100
	iso4	-185	-427	-58	-177	-373	-65	-327	-373	-216	-116

Calculation results for the dicarbonyl pathway states **DC1** and **DC2**

*Table 43 – Calculation results (BP86/SV(P)) for isomers of intermediates **DC1** and **DC2***

Intermediate	Isomer	SCF (a.u.)	DFT-D3 corr. (a.u.)	COSMO (CH2Cl2) (a.u.)	ZPE (a.u.)	Chem. Pot. (kJ/mol)	Energy (kJ/mol)	Entropy (kJ/K/mol)
DC1 CO2 THF2	iso1	-2779.232542	-0.1272	-2779.287768	0.429568	945.5	1214.45	0.9104
	iso2	-2779.243544	-0.1285	-2779.300118	0.429972	950.03	1212.88	0.8899
	iso3	-2779.241702	-0.1282	-2779.298224	0.430141	945.74	1215.75	0.9139
	iso4	-2779.230122	-0.1272	-2779.288707	0.429559	955.4	1209.55	0.8607
	iso5	-2779.243177	-0.1274	-2779.300723	0.429909	951.35	1212.68	0.8848
	iso6	-2779.246355	-0.1271	-2779.303634	0.430532	953.1	1215.75	0.8893
	iso7	-2779.245490	-0.1274	-2779.302467	0.430192	950.29	1215.27	0.8971
	iso8	-2779.231409	-0.1298	-2779.289500	0.430337	952.53	1215.29	0.8896
	iso9	-2779.232552	-0.1272	-2779.287812	0.429567	946.64	1214.33	0.9062
	iso10	-2779.245499	-0.1274	-2779.302503	0.430119	948.14	1215.26	0.9042
DC1 CO2 THF	iso1	-2546.944725	-0.0945	-2547.003432	0.314525	664.85	895.45	0.7818
	iso2	-2546.944902	-0.0937	-2546.929030	0.314791	668.22	895.61	0.7710
	iso3	-2546.945729	-0.0940	-2546.924987	0.314461	663.34	895.14	0.7858
	iso4	-2546.935498	-0.09555	-2546.9960	0.314157	666.41	894.93	0.7748
DC2 CO2 THF	iso1	-2819.478205	-0.1431	-2819.533907	0.464966	1047.56	1305.40	0.8731
	iso2	-2819.480397	-0.1440	-2819.536248	0.464865	1040.79	1307.60	0.9032
	iso3	-2819.492548	-0.14423	-2819.548443	0.465021	1042.2	1307.54	0.89827
	iso4	-2819.478111	-0.14611	-2819.53328	0.464933	1037.43	1308.05	0.91597
	iso5	-2819.474502	-0.14561	-2819.530978	0.463862	1035.76	1305.62	0.9134
	iso6	-2819.485335	-0.14536	-2819.542222	0.464661	1046.36	1304.96	0.87564
	iso7	-2819.485335	-0.1454	-2819.542222	0.464661	1046.36	1304.96	0.8756
	iso8	-2819.470733	-0.1400	-2819.525957	0.462941	1029.11	1301.74	0.9227
	iso9	-2819.493725	-0.1442	-2819.549924	0.465427	1046.01	1308.46	0.8886
	iso10	-2819.467926	-0.1240	-2819.524088	0.462747	1013.44	1302.75	0.9787

*Table 44 - Calculated energies for isomers of **DC1** and **DC2** with dispersion and solvent correction*

Intermediate	Isomer	Entropy at 1 mol/dm3 (kJ/K/mol)	Electronic E gas (kJ/mol)	Electronic E+D gas (kJ/mol)	Electronic E CH2Cl2 (kJ/mol)	Electronic E+D CH2Cl2 (kJ/mol)
DC1 CO2 THF2	iso1	0.8837	-60	-111	-41	-92
	iso2	0.8632	-89	-111	-73	-128
	iso3	0.8872	-84	-106	-69	-122
	iso4	0.8340	-54	-73	-44	-95
	iso5	0.8581	-88	-108	-75	-127
	iso6	0.8626	-97	-115	-83	-134
	iso7	0.8704	-94	-114	-80	-131
	iso8	0.8629	-57	-83	-46	-103
	iso9	0.8795	-60	-79	-41	-92
	iso10	0.8775	-94	-114	-80	-131
DC1 CO2 THF	iso1	0.7551	0	0	0	0
	iso2	0.7443	0	2	195	197
	iso3	0.7591	-3	-1	206	207
	iso4	0.7481	24	21	19	17
DC2 CO2 THF	iso1	0.8464	-35	-96	-23	-84
	iso2	0.8765	-41	-102	-29	-93
	iso3	0.8716	-73	-134	-62	-125
	iso4	0.8893	-35	-96	-22	-90
	iso5	0.8867	-26	-86	-16	-83
	iso6	0.8489	-54	-115	-45	-112
	iso7	0.8489	-54	-115	-45	-112
	iso8	0.8960	-16	-76	-2	-55
	iso9	0.8619	-76	-137	-65	-129
	iso10	0.9520	-8	-69	2	-8

		Gas Phase 298.15 K			COSMO CH2Cl2 298.15 K			DFT-D3 COSMO CH2Cl2 298.15 K			
Intermediate	**Isomer**	Rel H (kJ/mol)	Rel S (J/K/mol)	Rel G (kJ/mol)	Rel H (kJ/mol)	Rel S (J/K/mol)	Rel G (kJ/mol)	Rel H (kJ/mol)	Rel S (J/K/mol)	Rel G (kJ/mol)	Relative Pathway energy
DC1 CO2 THF2	iso1	-50	-141	-8	-31	-115	4	-82	-115	-48	36
	iso2	-80	-162	-32	-65	-135	-24	-119	-135	-79	5
	iso3	-73	-138	-32	-57	-111	-24	-111	-111	-77	7
	iso4	-48	-191	9	-38	-164	11	-89	-164	-40	44
	iso5	-80	-167	-30	-66	-140	-25	-118	-140	-76	8
	iso6	-85	-162	-36	-71	-136	-30	-122	-136	-81	3
	iso7	-83	-155	-37	-68	-128	-30	-120	-128	-82	2
	iso8	-46	-162	2	-34	-135	6	-92	-135	-52	32
	iso9	-50	-146	-7	-31	-119	5	-82	-119	-46	38
	iso10	-83	-147	-39	-68	-121	-32	-120	-121	-84	0
DC1 CO2 THF	iso1	0	0	0	0	0	0	0	0	0	84
	iso2	0	-11	3	196	-11	199	198	-11	201	285
	iso3	-3	4	-4	206	4	204	207	4	206	290
	iso4	24	-7	26	19	-7	21	16	-7	18	102
DC2 CO2 THF	iso1	-31	-217	33	-19	-190	37	-80	-190	-23	61
	iso2	-35	-187	21	-23	-160	25	-86	-160	-39	46
	iso3	-67	-192	-10	-55	-165	-6	-119	-165	-70	14
	iso4	-28	-174	24	-15	-147	29	-84	-147	-40	44
	iso5	-21	-177	31	-11	-150	33	-79	-150	-34	50
	iso6	-50	-214	14	-42	-188	14	-108	-188	-52	32
	iso7	-50	-214	14	-42	-188	14	-108	-188	-52	32
	iso8	-15	-167	35	-2	-140	40	-55	-140	-13	71
	iso9	-69	-201	-9	-58	-175	-6	-122	-175	-70	14
	iso10	-7	-111	26	4	-85	29	-7	-85	18	103

Calculation results for the dicarbonyl pathway states **DC TS23** to **DC5** to give **140β** (dicarbonyl β-pyridyl pathway)

*Table 45 – Calculation results (BP86/SV(P)) for isomers of intermediates **DC TS23** and **DC3** on the β-pyridyl dicarbonyl pathway.*

Intermediate	Isomer	SCF (a.u.)	DFT-D3 corr. (a.u.)	COSMO (CH2Cl2) (a.u.)	ZPE (a.u.)	Chem. Pot. (kJ/mol)	Energy (kJ/mol)	Entropy (kJ/K/mol)
DC TS23	iso1	-2819.47	-0.1488	-2819.53	0.465535	1051.75	1305.79	0.86037
DC3 CO2 THF	iso1	-2819.5	-0.14671	-2819.56	0.465547	1051.19	1305.11	0.85998
	iso2	-2819.5	-0.15107	-2819.56	0.466291	1049.67	1308.84	0.87755
	iso5	-2819.51	-0.14904	-2819.56	0.466433	1047.6	1309.26	0.88593
	iso6	-2819.51	-0.1496	-2819.56	0.466255	1047.03	1308.9	0.8866
	iso9	-2819.51	-0.15291	-2819.57	0.467487	1057.68	1310.86	0.85747
	iso10	-2819.51	-0.15168	-2819.57	0.466986	1053.07	1310.09	0.87035
	iso13	-2819.47	-0.14962	-2819.53	0.464112	1045.59	1303.18	0.8723
	iso14	-2819.47	-0.15141	-2819.53	0.465731	1045.94	1307.84	0.8867
	iso17	-2819.5	-0.14947	-2819.56	0.466529	1046.51	1309.66	0.89093
	iso18	-2819.5	-0.15083	-2819.56	0.466184	1045.58	1309.23	0.8926
DC3 CO2 THF2	iso1	-3051.8	-0.18602	-3051.86	0.58314	1340.22	1631.17	0.98417
	iso2	-3051.79	-0.18674	-3051.85	0.582861	1337.83	1630.86	0.99113
	iso5	-3051.82	-0.18429	-3051.88	0.58485	1342.98	1634.26	0.98527
	iso6	-3051.81	-0.18647	-3051.87	0.584739	1344.72	1634.3	0.97956
	iso9	-3051.8	-0.18707	-3051.86	0.58248	1334.36	1630.36	1.00113
	iso10	-3051.8	-0.1868	-3051.86	0.582289	1332.32	1630.01	1.00677
	iso13	-3051.77	-0.18919	-3051.83	0.582123	1342.34	1626.85	0.96258
	iso14	-3051.76	-0.18899	-3051.82	0.582927	1338.72	1630.53	0.98707

*Table 46 - Calculated energies of isomers of **DC TS23** and **DC3** on the β-pyridyl pathway, with dispersion and solvation corrections*

Intermediate	Isomer	Entropy at 1 mol/dm3 (kJ/K/mol)	Electronic E gas (kJ/mol)	Electronic E+D gas (kJ/mol)	Electronic E CH2Cl2 (kJ/mol)	Electronic E+D CH2Cl2 (kJ/mol)
DC TS23	iso1	-8.3318	16	-60	17	-59
DC3 CO2 THF	iso1	0.8333	-104	-174	-98	-168
	iso2	0.8509	-101	-183	-96	-178
	iso5	0.8592	-106	-182	-102	-178
	iso6	0.8599	-107	-185	-100	-178
	iso9	0.8308	-116	-203	-115	-202
	iso10	0.8437	-122	-205	-116	-199
	iso13	0.8456	-7	-85	-7	-85
	iso14	0.8600	-26	-109	-22	-105
	iso17	0.8642	-103	-180	-97	-175
	iso18	0.8659	-87	-168	-83	-164
DC3 CO2 THF2	iso1	0.9575	-194	-332	-174	-312
	iso2	0.9644	-164	-305	-147	-288
	iso5	0.9586	-244	-378	-219	-353
	iso6	0.9529	-216	-356	-191	-330
	iso9	0.9744	-189	-330	-170	-311
	iso10	0.9801	-180	-321	-165	-306
	iso13	0.9359	-107	-254	-91	-238
	iso14	0.9604	-92	-238	-76	-222

*Table 47 – Calculated Gibbs energies of isomers of **DC TS23** and **DC3** on the β-pyridyl pathway with dispersion and solvation correction.*

		Gas Phase 298.15 K			COSMO CH2Cl2 298.15 K			DFT-D3 COSMO CH2Cl2 298.15 K			
Intermediate	**Isomer**	Rel H (kJ/mol)	Rel S (J/K/mol)	Rel G (kJ/mol)	Rel H (kJ/mol)	Rel S (J/K/mol)	Rel G (kJ/mol)	Rel H (kJ/mol)	Rel S (J/K/mol)	Rel G (kJ/mol)	Relative Pathway energy
DC TS23	iso1	22	-208	84	23	-181	77	-53	-181	1	85
DC3 CO2 THF	iso1	-100	-230	-31	-94	-203	-34	-165	-203	-104	-20
	iso2	-94	-212	-31	-88	-186	-33	-170	-186	-115	-31
	iso5	-98	-204	-37	-94	-177	-41	-170	-177	-118	-33
	iso6	-100	-203	-39	-93	-177	-40	-170	-177	-118	-34
	iso9	-107	-232	-38	-106	-206	-44	-192	-206	-131	-47
	iso10	-113	-220	-48	-107	-193	-49	-190	-193	-132	-48
	iso13	-5	-218	60	-5	-191	52	-83	-191	-26	58
	iso14	-20	-203	41	-16	-177	37	-98	-177	-46	38
	iso17	-94	-199	-35	-89	-172	-38	-167	-172	-115	-31
	iso18	-79	-197	-20	-75	-171	-24	-156	-171	-105	-21
DC3 CO2 THF2	iso1	-173	-106	-141	-152	-322	-56	-291	-322	-195	-111
	iso2	-143	-99	-114	-126	-315	-32	-267	-315	-173	-89
	iso5	-220	-105	-189	-194	-321	-99	-328	-321	-233	-149
	iso6	-192	-110	-159	-166	-327	-69	-306	-327	-208	-124
	iso9	-168	-89	-142	-149	-305	-58	-291	-305	-200	-115
	iso10	-160	-83	-135	-145	-300	-56	-286	-300	-196	-112
	iso13	-90	-127	-52	-74	-344	29	-221	-344	-118	-34
	iso14	-71	-103	-40	-55	-319	40	-201	-319	-106	-22

*Table 48 - Calculation results (BP86/SV(P)) for **DC TS34** to **DC5** on the β-pyridyl pathway*

Intermediate	Isomer	SCF (a.u.)	DFT-D3 corr. (a.u.)	COSMO (CH2Cl2) (a.u.)	ZPE (a.u.)	Chem. Pot. (kJ/mol)	Energy (kJ/mol)	Entropy (kJ/K/mol)
DC TS34 CO THF2	iso1	-3051.78	-0.18647	-3051.84	0.582112	1337.94	1627.22	0.97859
DC4 CO THF2	iso1	-3051.79	-0.17862	-3051.84	0.583365	1334.6	1631.71	1.00483
	iso2	-3051.79	-0.17775	-3051.85	0.583505	1342.74	1629.42	0.96984
	iso5	-3051.81	-0.17712	-3051.87	0.58427	1343.97	1631.17	0.9716
	iso6	-3051.82	-0.18482	-3051.88	0.58473	1344.54	1633.9	0.97882
	iso9	-3051.81	-0.17901	-3051.87	0.584481	1339.95	1633.35	0.99238
	iso10	-3051.82	-0.17846	-3051.88	0.584622	1340.95	1633.5	0.98953
	iso13	-3051.79	-0.18096	-3051.84	0.584346	1341.22	1633.06	0.98718
	iso14	-3051.8	-0.18381	-3051.86	0.58363	1350.88	1626.91	0.93411
	iso17	-3051.8	-0.18307	-3051.85	0.583671	1341.18	1631.33	0.9815
	iso18	-3051.81	-0.17654	-3051.87	0.584229	1337.54	1633.22	1.00004
	iso21	-3051.81	-0.17756	-3051.87	0.584681	1340.89	1633.91	0.99112
	iso22	-3051.79	-0.18207	-3051.85	0.58393	1339.57	1632.46	0.99069
	iso23	-3051.79	-0.18635	-3051.85	0.584527	1341.08	1633.81	0.99015
	iso26	-3051.82	-0.18251	-3051.87	0.584762	1344.41	1633.89	0.97924
	iso27	-3051.82	-0.18337	-3051.88	0.585023	1337.58	1635.03	1.00597
	iso30	-3051.82	-0.1834	-3051.88	0.584566	1340.35	1633.83	0.99264
	iso31	-3051.82	-0.18329	-3051.88	0.585004	1342	1634.87	0.9906
	iso34	-3051.79	-0.18886	-3051.85	0.585136	1351.36	1633.82	0.9557
	iso35	-3051.79	-0.18171	-3051.85	0.582975	1340.99	1628.42	0.97237
	iso38	-3051.79	-0.18553	-3051.84	0.583887	1339.72	1632.48	0.99025
	iso39	-3051.82	-0.18327	-3051.88	0.584599	1342.95	1632.02	0.97786
	iso42	-3051.82	-0.18273	-3051.88	0.584714	1343.66	1633.67	0.98101
DC5 CO THF2	iso1	-3051.81	-0.19026	-3051.87	0.585571	1351.51	1634.53	0.9576
	iso2	-3051.84	-0.18237	-3051.9	0.58729	1359.17	1635.4	0.93479
	iso5	-3051.85	-0.1873	-3051.9	0.586185	1352.55	1635.95	0.95887
	iso6	-3051.84	-0.18238	-3051.9	0.587484	1358.5	1637.46	0.94396

*Table 49 – Calculated energies for isomers of **DC TS34** to **DC5** on the β-pyridyl pathway with solvation and dispersion correction.*

Intermediate	Isomer	Entropy at 1 mol/dm3 (kJ/K/mol)	Electronic E gas (kJ/mol)	Electronic E+D gas (kJ/mol)	Electronic E CH2Cl2 (kJ/mol)	Electronic E+D CH2Cl2 (kJ/mol)
DC TS34 CO THF2	iso1	0.9519	-128	-268	-116	-255
DC4 CO THF2	iso1	0.9781	-146	-265	-123	-242
	iso2	0.9431	-162	-279	-137	-254
	iso5	0.9449	-224	-339	-203	-318
	iso6	0.9521	-247	-382	-221	-357
	iso9	0.9657	-214	-334	-199	-320
	iso10	0.9628	-231	-349	-214	-333
	iso13	0.9605	-151	-276	-134	-259
	iso14	0.9074	-186	-319	-161	-294
	iso17	0.9548	-172	-303	-154	-285
	iso18	0.9733	-221	-335	-204	-318
	iso21	0.9644	-211	-328	-198	-314
	iso22	0.9640	-162	-290	-142	-270
	iso23	0.9635	-169	-309	-149	-289
	iso26	0.9525	-226	-355	-209	-338
	iso27	0.9793	-242	-373	-220	-352
	iso30	0.9659	-242	-374	-225	-356
	iso31	0.9639	-242	-373	-220	-351
	iso34	0.9290	-167	-313	-151	-297
	iso35	0.9457	-171	-298	-141	-268
	iso38	0.9636	-147	-284	-135	-272
	iso39	0.9512	-241	-373	-220	-351
	iso42	0.9543	-237	-367	-222	-352
DC5 CO THF2	iso1	0.9309	-208	-358	-204	-353
	iso2	0.9081	-293	-422	-287	-416
	iso5	0.9322	-311	-453	-284	-425
	iso6	0.9173	-298	-427	-290	-419

*Table 50 – Calculated Gibbs energies for isomers of **DC TS34** to **DC5** on the β-pyridyl pathway with dispersion and solvation correction*

		Gas Phase 298.15 K			COSMO CH2Cl2 298.15 K			DFT-D3 COSMO CH2Cl2 298.15 K			
Intermediate	**Isomer**	Rel H (kJ/mol)	Rel S (J/K/mol)	Rel G (kJ/mol)	Rel H (kJ/mol)	Rel S (J/K/mol)	Rel G (kJ/mol)	Rel H (kJ/mol)	Rel S (J/K/mol)	Rel G (kJ/mol)	Relative Pathway energy
DC TS34 CO THF2	iso1	-111	-111	-77	-98	-328	-1	-238	-328	-140	-56
DC4 CO THF2	iso1	-124	-85	-99	-101	-302	-11	-220	-302	-130	-46
	iso2	-143	-120	-107	-117	-337	-17	-234	-337	-134	-50
	iso5	-203	-388	-87	-182	-335	-82	-297	-335	-197	-113
	iso6	-223	-111	-190	-197	-328	-100	-333	-328	-235	-151
	iso9	-190	-98	-161	-176	-314	-82	-296	-314	-202	-118
	iso10	-207	-100	-177	-190	-317	-96	-309	-317	-214	-130
	iso13	-128	-103	-97	-111	-319	-15	-236	-319	-141	-56
	iso14	-169	-156	-123	-144	-372	-33	-277	-372	-166	-82
	iso17	-151	-108	-119	-133	-325	-36	-264	-325	-167	-83
	iso18	-198	-90	-171	-181	-306	-90	-295	-306	-203	-119
	iso21	-187	-99	-158	-174	-315	-80	-290	-315	-196	-112
	iso22	-140	-99	-110	-119	-316	-25	-247	-316	-153	-69
	iso23	-146	-100	-116	-125	-316	-31	-265	-316	-171	-86
	iso26	-202	-111	-169	-185	-327	-87	-314	-327	-216	-132
	iso27	-217	-84	-191	-195	-300	-106	-327	-300	-237	-153
	iso30	-218	-97	-189	-201	-314	-107	-332	-314	-239	-155
	iso31	-217	-99	-187	-195	-316	-101	-326	-316	-232	-148
	iso34	-143	-134	-103	-127	-351	-23	-273	-351	-169	-85
	iso35	-152	-118	-117	-123	-334	-23	-250	-334	-150	-66
	iso38	-124	-100	-95	-112	-316	-18	-249	-316	-155	-71
	iso39	-219	-112	-186	-198	-329	-100	-329	-329	-231	-147
	iso42	-213	-109	-181	-198	-325	-101	-328	-325	-231	-147
DC5 CO THF2	iso1	-183	-402	-63	-179	-349	-75	-329	-349	-225	-141
	iso2	-268	-425	-141	-262	-372	-151	-391	-372	-280	-196
	iso5	-285	-401	-166	-257	-348	-154	-399	-348	-296	-212
	iso6	-271	-416	-147	-263	-362	-155	-392	-362	-284	-200

Calculation results for the dicarbonyl pathway states **DC TS23** to **DC5** to give **140α** (dicarbonyl α-pyridyl pathway)

*Table 51 - Calculation results (BP86/SV(P)) for isomers of **DC TS23** and **DC3** on the α-pyridyl pathway*

Intermediate	Isomer	SCF (a.u.)	DFT-D3 corr. (a.u.)	COSMO (CH2Cl2) (a.u.)	ZPE (a.u.)	Chem. Pot. (kJ/mol)	Energy (kJ/mol)	Entropy (kJ/K/mol)
DC TS23	iso4	-2819.46	-0.14926	-2819.52	0.46549	1051.3	1305.7	0.86156
DC3 CO2 THF	iso3	-2819.5	-0.14754	-2819.56	0.465392	1050.5	1304.61	0.86061
	iso4	-2819.5	-0.14942	-2819.56	0.466666	1049.4	1309.84	0.88182
	iso7	-2819.53	-0.14697	-2819.59	0.4681	1055.57	1312.63	0.8705
	iso8	-2819.53	-0.14709	-2819.59	0.467715	1061.48	1309.29	0.83947
	iso11	-2819.53	-0.15156	-2819.59	0.46908	1066.61	1313.67	0.83694
	iso12	-2819.51	-0.15101	-2819.57	0.466817	1052.16	1309.62	0.87184
	iso15	-2819.47	-0.15011	-2819.53	0.464517	1049.55	1303.71	0.86078
	iso16	-2819.49	-0.14718	-2819.55	0.466311	1052.57	1308.72	0.86745
	iso19	-2819.52	-0.15066	-2819.58	0.468648	1062.65	1311.71	0.84368
	iso20	-2819.5	-0.15159	-2819.56	0.466355	1050.29	1309.13	0.87646
DC3 CO2 THF2	iso3	-3051.81	-0.18425	-3051.87	0.584434	1351.46	1627.73	0.93494
	iso4	-3051.81	-0.1871	-3051.87	0.584862	1350.22	1632.74	0.95589
	iso7	-3051.81	-0.1884	-3051.87	0.582927	1343.76	1628.33	0.96275
	iso8	-3051.8	-0.18857	-3051.86	0.583689	1342.52	1632.27	0.98014
	iso11	-3051.8	-0.18593	-3051.86	0.582721	1336.74	1630.66	0.99412
	iso12	-3051.8	-0.18562	-3051.86	0.582576	1334.96	1630.54	0.99968
	iso15	-3051.78	-0.18635	-3051.84	0.584059	1347.16	1631.42	0.96172
	iso16	-3051.78	-0.1862	-3051.84	0.584214	1347.56	1631.78	0.96157

*Table 52 – Calculated energies for isomers of **DC TS23** and **DC3** on the α-pyridyl pathway with dispersion and solvation correction*

Intermediate	Isomer	Entropy at 1 mol/dm3 (kJ/K/mol)	Electronic E gas (kJ/mol)	Electronic E+D gas (kJ/mol)	Electronic E CH2Cl2 (kJ/mol)	Electronic E+D CH2Cl2 (kJ/mol)
DC TS23	iso4	0.8349	2	-74	10	-67
DC3 CO2 THF	iso3	0.8339	-103	-175	-99	-172
	iso4	0.8551	-105	-182	-99	-176
	iso7	0.8438	-176	-246	-169	-240
	iso8	0.8128	-175	-247	-169	-240
	iso11	0.8102	-175	-258	-169	-252
	iso12	0.8451	-109	-190	-109	-190
	iso15	0.8341	-13	-92	-11	-90
	iso16	0.8408	-76	-147	-65	-136
	iso19	0.8170	-149	-229	-144	-224
	iso20	0.8498	-95	-178	-94	-177
DC3 CO2 THF2	iso3	0.9082	-221	-355	-204	-338
	iso4	0.9292	-213	-354	-192	-334
	iso7	0.9361	-205	-350	-188	-333
	iso8	0.9534	-190	-335	-170	-315
	iso11	0.9674	-194	-332	-174	-312
	iso12	0.9730	-193	-330	-174	-311
	iso15	0.9350	-141	-281	-126	-265
	iso16	0.9349	-141	-280	-126	-265

*Table 53 – Calculated Gibbs energies for isomers of **DC TS23** and **DC3** on the α-pyridyl pathway with dispersion and solvation correction*

		Gas Phase 298.15 K			COSMO CH2Cl2 298.15 K			DFT-D3 COSMO CH2Cl2 298.15 K			
Intermediate	**Isomer**	Rel H (kJ/mol)	Rel S (J/K/mol)	Rel G (kJ/mol)	Rel H (kJ/mol)	Rel S (J/K/mol)	Rel G (kJ/mol)	Rel H (kJ/mol)	Rel S (J/K/mol)	Rel G (kJ/mol)	Relative Pathway energy
DC TS23	iso4	9	-228	77	16	-202	77	-60	-202	0	84
DC3 CO2 THF	iso3	-100	-229	-31	-96	-203	-36	-168	-203	-108	-24
	iso4	-96	-208	-34	-90	-181	-36	-168	-181	-113	-29
	iso7	-164	-219	-99	-158	-193	-100	-228	-193	-171	-87
	iso8	-167	-250	-93	-161	-224	-94	-232	-224	-165	-81
	iso11	-163	-253	-87	-157	-226	-89	-240	-226	-172	-88
	iso12	-101	-218	-36	-101	-191	-44	-182	-191	-125	-41
	iso15	-11	-229	58	-9	-202	52	-88	-202	-27	57
	iso16	-68	-222	-2	-57	-196	1	-129	-196	-71	14
	iso19	-138	-246	-65	-133	-220	-68	-214	-220	-148	-64
	iso20	-87	-213	-23	-87	-187	-31	-170	-187	-114	-30
DC3 CO2 THF2	iso3	-203	-155	-157	-186	-372	-75	-320	-372	-209	-125
	iso4	-190	-134	-150	-170	-351	-65	-311	-351	-206	-122
	iso7	-187	-127	-149	-169	-344	-67	-314	-344	-212	-128
	iso8	-167	-110	-135	-147	-326	-50	-293	-326	-195	-111
	iso11	-173	-96	-144	-153	-312	-60	-292	-312	-198	-114
	iso12	-172	-90	-145	-153	-307	-62	-290	-307	-199	-115
	iso15	-120	-128	-81	-104	-345	-2	-244	-345	-141	-57
	iso16	-119	-128	-81	-104	-345	-1	-243	-345	-140	-56

*Table 54 – Calculation results (BP86-SV(P) for isomers of **DC TS34 THF** and **DC4 CO THF** on the α-pyridyl pathway*

Intermediate	Isomer	SCF (a.u.)	DFT-D3 corr. (a.u.)	COSMO (CH2Cl2) (a.u.)	ZPE (a.u.)	Chem. Pot. (kJ/mol)	Energy (kJ/mol)	Entropy (kJ/K/mol)
DC TS34 THF	iso1	-2819.51	-0.14694	-2819.56	0.467732	1059.66	1309.45	0.84611
DC4 CO THF	iso3	-2819.53	-0.1366	-2819.59	0.470291	1063.28	1314.03	0.84933
	iso4	-2819.48	-0.14143	-2819.54	0.467191	1051.81	1309.61	0.87298
	iso7	-2819.52	-0.14321	-2819.58	0.468766	1054.48	1313.62	0.87748
	iso8	-2819.51	-0.14192	-2819.57	0.467811	1052.2	1311.22	0.87706
	iso11	-2819.52	-0.14315	-2819.58	0.468868	1057.04	1313.65	0.86897
	iso12	-2819.52	-0.14231	-2819.57	0.468286	1055.83	1312.18	0.8681
	iso15	-2819.52	-0.14242	-2819.57	0.468357	1056.56	1312.29	0.86603
	iso16	-2819.47	-0.14309	-2819.53	0.465643	1047.99	1306.02	0.87375
	iso19	-2819.51	-0.14747	-2819.57	0.468584	1059.38	1312.78	0.85821
	iso20	-2819.52	-0.14748	-2819.57	0.468107	1049.44	1312.47	0.89052
	iso23	-2819.49	-0.15136	-2819.56	0.467643	1061.77	1310	0.84088
	iso24	-2819.51	-0.14789	-2819.56	0.468266	1055.96	1312.62	0.86915
	iso27	-2819.54	-0.14863	-2819.6	0.469655	1063.26	1314.8	0.85197
	iso28	-2819.51	-0.14869	-2819.57	0.469111	1060.36	1314	0.85903
	iso31	-2819.54	-0.14421	-2819.6	0.470141	1064.85	1315.84	0.85015
	iso32	-2819.55	-0.14602	-2819.61	0.469403	1059.88	1314.82	0.8634

*Table 55 – Calculated energies for isomers of **DC TS34 THF** and **DC4 CO THF** on the α-pyridyl pathway with dispersion and solvation correction*

Intermediate	Isomer	Entropy at 1 mol/dm3 (kJ/K/mol)	Electronic E gas (kJ/mol)	Electronic E+D gas (kJ/mol)	Electronic E CH2Cl2 (kJ/mol)	Electronic E+D CH2Cl2 (kJ/mol)
DC TS34 THF	iso1	0.8194	-107	-178	-103	-174
DC4 CO THF	iso3	0.8226	-160	-203	-163	-207
	iso4	0.8463	-51	-107	-47	-103
	iso7	0.8508	-137	-198	-134	-195
	iso8	0.8504	-122	-179	-123	-180
	iso11	0.8423	-137	-198	-134	-195
	iso12	0.8414	-136	-194	-130	-188
	iso15	0.8393	-134	-193	-129	-188
	iso16	0.8471	-9	-69	-13	-74
	iso19	0.8315	-125	-197	-123	-196
	iso20	0.8638	-134	-206	-127	-199
	iso23	0.8142	-74	-157	-80	-162
	iso24	0.8425	-108	-181	-104	-177
	iso27	0.8253	-185	-260	-184	-260
	iso28	0.8323	-131	-206	-131	-206
	iso31	0.8235	-207	-270	-200	-263
	iso32	0.8367	-226	-294	-221	-289

*Table 56 - Calculated Gibbs energies for isomers of **DC TS34 THF** and **DC4 CO THF** on the α-pyridyl pathway with dispersion and solvation correction*

		Gas Phase 298.15 K			COSMO CH2Cl2 298.15 K			DFT-D3 COSMO CH2Cl2 298.15 K			
Intermediate	**Isomer**	Rel H (kJ/mol)	Rel S (J/K/mol)	Rel G (kJ/mol)	Rel H (kJ/mol)	Rel S (J/K/mol)	Rel G (kJ/mol)	Rel H (kJ/mol)	Rel S (J/K/mol)	Rel G (kJ/mol)	Relative Pathway energy
DC TS34 THF	iso1	-99	-244	-26	-95	-217	-30	-166	-217	-101	-17
DC4 CO THF	iso3	-147	-241	-75	-150	-214	-87	-194	-214	-130	-46
	iso4	-43	-217	22	-38	-190	18	-95	-190	-38	46
	iso7	-125	-212	-61	-122	-186	-67	-183	-186	-128	-44
	iso8	-112	-213	-48	-113	-186	-57	-170	-186	-115	-31
	iso11	-125	-221	-59	-122	-194	-64	-183	-194	-125	-41
	iso12	-125	-222	-59	-119	-195	-60	-177	-195	-119	-35
	iso15	-123	-224	-57	-118	-197	-60	-177	-197	-119	-34
	iso16	-4	-216	60	-8	-189	48	-69	-189	-13	71
	iso19	-114	-232	-45	-112	-205	-51	-184	-205	-123	-39
	iso20	-122	-199	-63	-115	-173	-64	-188	-173	-136	-52
	iso23	-66	-249	9	-71	-222	-5	-153	-222	-87	-3
	iso24	-96	-221	-30	-92	-194	-34	-166	-194	-108	-24
	iso27	-172	-238	-101	-171	-211	-108	-246	-211	-183	-99
	iso28	-118	-231	-49	-118	-204	-57	-194	-204	-133	-49
	iso31	-192	-240	-121	-185	-213	-121	-249	-213	-185	-101
	iso32	-212	-227	-145	-208	-200	-148	-276	-200	-216	-132

*Table 57 - Calculation results (BP86-SV(P) for isomers of **DC4 CO THF2** and **DC5 CO THF2** on the α-pyridyl pathway*

Intermediate	Isomer	SCF (a.u.)	DFT-D3 corr. (a.u.)	COSMO (CH2Cl2) (a.u.)	ZPE (a.u.)	Chem. Pot. (kJ/mol)	Energy (kJ/mol)	Entropy (kJ/K/mol)
DC4 CO THF2	iso3	-3051.78	-0.18272	-3051.84	0.582802	1330.97	1630.05	1.01144
	iso4	-3051.79	-0.17849	-3051.84	0.584475	1340.88	1633.7	0.99045
	iso7	-3051.82	-0.17873	-3051.87	0.584698	1346.7	1631.89	0.96486
	iso8	-3051.81	-0.184	-3051.87	0.584259	1342.29	1632.91	0.98307
	iso11	-3051.81	-0.18038	-3051.87	0.585319	1346.91	1634.85	0.97406
	iso12	-3051.81	-0.17817	-3051.87	0.584647	1341.04	1633.74	0.99004
	iso15	-3051.78	-0.18061	-3051.84	0.583859	1342.34	1630.24	0.97391
	iso16	-3051.77	-0.18033	-3051.83	0.582048	1334.89	1627.81	0.99078
	iso19	-3051.8	-0.18343	-3051.85	0.583776	1342.41	1631.32	0.97734
	iso20	-3051.82	-0.17901	-3051.87	0.58463	1343.97	1633.68	0.97999
	iso24	-3051.79	-0.17758	-3051.85	0.585573	1351.79	1633.87	0.95441
	iso25	-3051.81	-0.18269	-3051.87	0.585429	1349.3	1634.47	0.96479
	iso28	-3051.82	-0.18225	-3051.88	0.584963	1342.86	1634.42	0.9862
	iso29	-3051.84	-0.18141	-3051.89	0.58575	1346.89	1635.77	0.97723
	iso32	-3051.82	-0.18223	-3051.88	0.585334	1346.89	1635.02	0.9747
	iso33	-3051.84	-0.18143	-3051.89	0.585951	1347.7	1636.05	0.97544
	iso36	-3051.81	-0.18297	-3051.87	0.585601	1347.78	1635.57	0.97355
	iso41	-3051.84	-0.1813	-3051.89	0.58572	1345.12	1635.69	0.9829
	iso43	-3051.84	-0.18154	-3051.9	0.585325	1351.66	1632.46	0.95012
	iso44	-3051.81	-0.17897	-3051.87	0.585019	1343.27	1634.72	0.98584
DC5 CO THF2	iso4	-3051.82	-0.18473	-3051.88	0.585257	1343.63	1634.38	0.9835
	iso7	-3051.82	-0.18757	-3051.88	0.586276	1351.84	1636.47	0.96297
	iso8	-3051.82	-0.18467	-3051.88	0.585396	1345.39	1634.77	0.97889

*Table 58 -Calculated energies for isomers of **DC4 CO THF2** and **DC5 CO THF2** on the α-pyridyl pathway with dispersion and solvation correction*

Intermediate	Isomer	Entropy at 1 mol/dm3 (kJ/K/mol)	Electronic E gas (kJ/mol)	Electronic E+D gas (kJ/mol)	Electronic E CH2Cl2 (kJ/mol)	Electronic E+D CH2Cl2 (kJ/mol)
DC4 CO THF2	iso3	0.9847	-121	-251	-112	-242
	iso4	0.9638	-158	-277	-134	-252
	iso7	0.9382	-226	-345	-202	-321
	iso8	0.9564	-218	-351	-204	-337
	iso11	0.9474	-210	-334	-193	-317
	iso12	0.9633	-218	-336	-205	-323
	iso15	0.9472	-134	-258	-116	-241
	iso16	0.9641	-115	-238	-100	-223
	iso19	0.9506	-176	-308	-160	-292
	iso20	0.9533	-229	-349	-208	-328
	iso24	0.9277	-161	-278	-145	-261
	iso25	0.9381	-222	-352	-205	-335
	iso28	0.9595	-248	-377	-230	-359
	iso29	0.9505	-285	-412	-265	-392
	iso32	0.9480	-248	-377	-231	-359
	iso33	0.9487	-286	-412	-266	-392
	iso36	0.9469	-213	-344	-198	-328
	iso41	0.9562	-285	-412	-266	-392
	iso43	0.9234	-296	-422	-275	-402
	iso44	0.9591	-209	-329	-192	-312
DC5 CO THF2	iso4	0.9568	-240	-375	-239	-374
	iso7	0.9363	-241	-384	-230	-372
	iso8	0.9522	-240	-375	-239	-374

*Table 59 - Calculated Gibbs energies for isomers of **DC4 CO THF2** and **DC5 CO THF2** on the α-pyridyl pathway with dispersion and solvation correction*

		Gas Phase 298.15 K			COSMO CH2Cl2 298.15 K			DFT-D3 COSMO CH2Cl2 298.15 K			
Intermediate	**Isomer**	Rel H (kJ/mol)	Rel S (J/K/mol)	Rel G (kJ/mol)	Rel H (kJ/mol)	Rel S (J/K/mol)	Rel G (kJ/mol)	Rel H (kJ/mol)	Rel S (J/K/mol)	Rel G (kJ/mol)	Relative Pathway energy
DC4 CO THF2	iso3	-101	-78	-77	-92	-295	-4	-221	-295	-134	-49
	iso4	-134	-99	-105	-110	-316	-15	-228	-316	-134	-50
	iso7	-204	-395	-86	-180	-342	-78	-299	-342	-197	-113
	iso8	-194	-107	-163	-181	-323	-84	-314	-323	-218	-134
	iso11	-185	-116	-151	-168	-332	-69	-292	-332	-192	-108
	iso12	-194	-100	-164	-181	-316	-86	-299	-316	-204	-120
	iso15	-113	-116	-79	-96	-333	3	-220	-333	-121	-37
	iso16	-97	-99	-67	-82	-316	12	-205	-316	-111	-27
	iso19	-155	-113	-121	-138	-329	-40	-270	-329	-172	-88
	iso20	-205	-110	-172	-184	-326	-86	-304	-326	-207	-122
	iso24	-137	-135	-97	-121	-352	-16	-237	-352	-132	-48
	iso25	-197	-125	-160	-180	-342	-78	-310	-342	-208	-124
	iso28	-223	-104	-192	-206	-320	-110	-334	-320	-239	-155
	iso29	-259	-113	-226	-239	-329	-141	-366	-329	-268	-184
	iso32	-223	-115	-189	-205	-332	-107	-334	-332	-235	-151
	iso33	-259	-114	-225	-240	-331	-141	-366	-331	-267	-183
	iso36	-187	-116	-153	-172	-333	-73	-302	-333	-203	-119
	iso41	-260	-107	-228	-240	-324	-143	-366	-324	-270	-185
	iso43	-273	-140	-231	-253	-356	-147	-380	-356	-273	-189
	iso44	-184	-104	-153	-168	-321	-72	-288	-321	-192	-108
DC5 CO THF2	iso4	-216	-376	-103	-214	-323	-118	-349	-323	-253	-169
	iso7	-215	-397	-96	-203	-343	-100	-345	-343	-243	-159
	iso8	-215	-381	-102	-214	-328	-117	-349	-328	-252	-167

Calculation results for the Magnus mechanism to give **140β** (β-pyridyl Magnus pathway)

Table 60 -Calculation results (BP86/SV(P)) for the β-pyridyl Magnus pathway

Intermediate	Isomer	SCF (a.u.)	DFT-D3 corr. (a.u.)	COSMO (CH2Cl2) (a.u.)	ZPE (a.u.)	Chem. Pot. (kJ/mol)	Energy (kJ/mol)	Entropy (kJ/K/mol)
CP1	iso1	-4150.93	-0.10949	-4150.95	0.233016	434.67	693.52	0.8765
CP2	iso1	-4037.65	-0.09993	-4037.66	0.2245792	419.91	665.59	0.83233
	iso2	-4037.63	-0.10096	-4037.64	0.2240438	416.47	664.64	0.84069
	iso3	-4037.65	-0.09976	-4037.66	0.2244677	418.11	665.45	0.83788
CP3	iso1	-4310.19	-0.15154	-4310.2	0.3747749	793.48	1076.98	0.95915
	iso2	-4310.2	-0.15023	-4310.21	0.375497	801.16	1077.9	0.9365
	iso3	-4310.18	-0.15038	-4310.19	0.3750446	799.16	1077.3	0.9412
TS34	iso1	-4310.17	-0.15576	-4310.18	0.3755166	806.98	1075.02	0.9073
CP4	iso1	-4310.19	-0.1611	-4310.2	0.3772355	815.07	1079.83	0.8963
CP5	iso1	-4423.45	-0.17176	-4423.47	0.3860022	832.12	1108.81	0.93634
TS56	iso1	-4423.44	-0.17129	-4423.45	0.3857944	833.88	1106.36	0.92222
CP6	iso1	-4423.47	-0.17075	-4423.48	0.387355	836.56	1110.82	0.92817
	iso3	-4423.44	-0.16887	-4423.46	0.3865236	832.42	1109.14	0.93645
CP7	iso1	-4536.72	-0.17973	-4536.74	0.3965675	856.89	1139.47	0.9561
	iso3	-4536.7	-0.17984	-4536.71	0.394851	848.23	1137.14	0.97734

Table 61 - Calculated energies for the β-pyridyl Magnus pathway with dispersion and solvation correction

Intermediate	Isomer	Entropy at 1 mol/dm3 (kJ/K/mol)	Electronic E gas (kJ/mol)	Electronic E+D gas (kJ/mol)	Electronic E CH2Cl2 (kJ/mol)	Electronic E+D CH2Cl2 (kJ/mol)
CP1	iso1	0.8498	0	0	0	0
CP2	iso1	0.8056	144	168	142	165
	iso2	0.8140	195	216	192	213
	iso3	0.8112	153	177	150	174
CP3	iso1	0.9325	94	49	92	47
	iso2	0.9098	67	26	67	25
	iso3	0.9145	113	71	114	72
TS34	iso1	0.8806	150	94	152	95
CP4	iso1	0.8696	96	26	93	23
CP5	iso1	0.9015	-39	-133	-43	-137
TS56	iso1	0.8955	42	-54	42	-54
CP6	iso1	0.9015	-39	-133	-43	-137
	iso3	0.9098	29	-60	26	-63
CP7	iso1	0.9294	-92	-207	-107	-223
	iso3	0.9506	-31	-147	-35	-151

Table 62- Calculated Gibbs energies for the β-pyridyl Magnus pathway with dispersion and solvation correction

		Gas Phase 298.15 K			COSMO CH2Cl2 298.15 K			DFT-D3 COSMO CH2Cl2 298.15 K			
Intermediate	**Isomer**	Rel H (kJ/mol)	Rel S (J/K/mol)	Rel G (kJ/mol)	Rel H (kJ/mol)	Rel S (J/K/mol)	Rel G (kJ/mol)	Rel H (kJ/mol)	Rel S (J/K/mol)	Rel G (kJ/mol)	Relative pathway energy to **CP2**
CP1	iso1	0	0	0	0	0	0	0	0	0	
CP2	iso1	138	127	100	135	127	97	159	127	121	0
	iso2	188	135	148	185	135	144	205	135	165	44
	iso3	146	133	107	144	133	104	168	133	128	8
CP3	iso1	93	-28	102	91	-28	99	46	-28	54	-66
	iso2	67	-50	82	67	-50	82	25	-50	40	-80
	iso3	112	-45	126	114	-45	127	72	-45	85	-36
TS34	iso1	148	-79	171	149	-79	172	93	-79	116	-4
CP4	iso1	98	-90	125	95	-90	122	22	-90	49	-71
CP5	iso1	-28	-230	41	-32	-230	37	-125	-230	-57	-178
TS56	iso1	49	-236	119	49	-236	119	-47	-236	24	-97
CP6	iso1	-28	-230	41	-32	-230	37	-125	-230	-57	-178
	iso3	39	-222	105	36	-222	102	-53	-222	13	-108
CP7	iso1	-73	-373	38	-89	-373	23	-204	-373	-93	-214
	iso3	-15	-352	90	-19	-352	86	-135	-352	-30	-151

Calculation results for the Magnus mechanism to give **140α** (α-pyridyl Magnus pathway)

Table 63 - Calculation results (BP86/SV(P)) for the α-pyridyl Magnus pathway

Intermediate	Isomer	SCF (a.u.)	DFT-D3 corr. (a.u.)	COSMO (CH2Cl2) (a.u.)	ZPE (a.u.)	Chem. Pot. (kJ/mol)	Energy (kJ/mol)	Entropy (kJ/K/mol)
CP1	iso1	-4150.93328	-0.10949044	-4150.95	0.233016	434.67	693.52	0.8765
CP2	iso1	-4037.64826	-0.09993327	-4037.66	0.224579	419.91	665.59	0.83233
	iso2	-4037.62881	-0.10095795	-4037.64	0.224044	416.47	664.64	0.84069
	iso3	-4037.64507	-0.0997562	-4037.66	0.224468	418.11	665.45	0.83788
CP3	iso1	-4310.18737	-0.15154279	-4310.2	0.374775	793.48	1076.98	0.95915
	iso2	-4310.19764	-0.15023441	-4310.21	0.375497	801.16	1077.9	0.9365
	iso3	-4310.18028	-0.15038177	-4310.19	0.375045	799.16	1077.3	0.9412
TS34	iso2	-4310.16461	-0.15645728	-4310.18	0.375428	807.88	1074.65	0.90307
CP4	iso2	-4310.18349	-0.15902456	-4310.2	0.377401	813.38	1080.32	0.90363
CP5	iso2	-4423.45373	-0.17220608	-4423.47	0.386583	835.42	1109.81	0.92863
TS56	iso3	-4423.43454	-0.17076944	-4423.45	0.385931	833.97	1106.63	0.9228
CP6	iso2	-4423.47587	-0.16770407	-4423.49	0.387456	842.62	1108.6	0.90041
	iso4	-4423.43933	-0.16961977	-4423.45	0.386836	835	1109.75	0.92982
CP7	iso2	-4536.7191	-0.18127809	-4536.74	0.394758	847.41	1137.14	0.98006
	iso4	-4536.70306	-0.18223011	-4536.72	0.396487	859.48	1138.99	0.94579

Table 64 - Calculated energies for the α-pyridyl Magnus pathway with dispersion and solvation correction

Intermediate	Isomer	Entropy at 1 mol/dm3 (kJ/K/mol)	Electronic E gas (kJ/mol)	Electronic E+D gas (kJ/mol)	Electronic E CH2Cl2 (kJ/mol)	Electronic E+D CH2Cl2 (kJ/mol)
CP1	iso1	0.8498	0	0	0	0
CP2	iso1	0.8056	144	168	142	165
	iso2	0.8140	195	216	192	213
	iso3	0.8112	153	177	150	174
CP3	iso1	0.9325	94	49	92	47
	iso2	0.9098	67	26	67	25
	iso3	0.9145	113	71	114	72
TS34	iso2	0.8764	154	96	150	92
CP4	iso2	0.8769	104	40	99	35
CP5	iso2	0.9019	-1	-99	-1	-99
TS56	iso3	0.8961	49	-45	45	-49
CP6	iso2	0.8737	-59	-145	-67	-152
	iso4	0.9031	37	-54	36	-55
CP7	iso2	0.9534	-94	-214	-97	-217
	iso4	0.9191	-52	-174	-63	-185

Table 65 – Calculated Gibbs energies for the α-pyridyl Magnus pathway with dispersion and solvation correction

		Gas Phase 298.15 K			COSMO CH2Cl2 298.15 K			DFT-D3 COSMO CH2Cl2 298.15 K			
Intermediate	**Isomer**	Rel H (kJ/mol)	Rel S (J/K/mol)	Rel G (kJ/mol)	Rel H (kJ/mol)	Rel S (J/K/mol)	Rel G (kJ/mol)	Rel H (kJ/mol)	Rel S (J/K/mol)	Rel G (kJ/mol)	Relative pathway energy to **CP2**
CP1	iso1	0	0	0	0	0	0	0	0	0	
CP2	iso1	138	127	100	135	127	97	159	127	121	0
	iso2	188	135	148	185	135	144	205	135	165	44
	iso3	146	133	107	144	133	104	168	133	128	8
CP3	iso1	93	-28	102	91	-28	99	46	-28	54	-66
	iso2	67	-50	82	67	-50	82	25	-50	40	-80
	iso3	112	-45	126	114	-45	127	72	-45	85	-36
TS34	iso2	151	-84	176	147	-84	171	89	-84	114	-7
CP4	iso2	107	-83	132	102	-83	126	37	-83	61	-59
CP5	iso2	9	-229	78	9	-229	78	-89	-229	-21	-142
TS56	iso3	57	-235	127	52	-235	122	-42	-235	28	-93
CP6	iso2	-50	-258	27	-57	-258	19	-143	-258	-66	-187
	iso4	47	-228	115	46	-228	114	-45	-228	23	-97
CP7	iso2	-78	-349	27	-80	-349	24	-200	-349	-96	-217
	iso4	-34	-383	81	-44	-383	70	-167	-383	-52	-173

Appendix 7: TR^{M}PS difference spectra

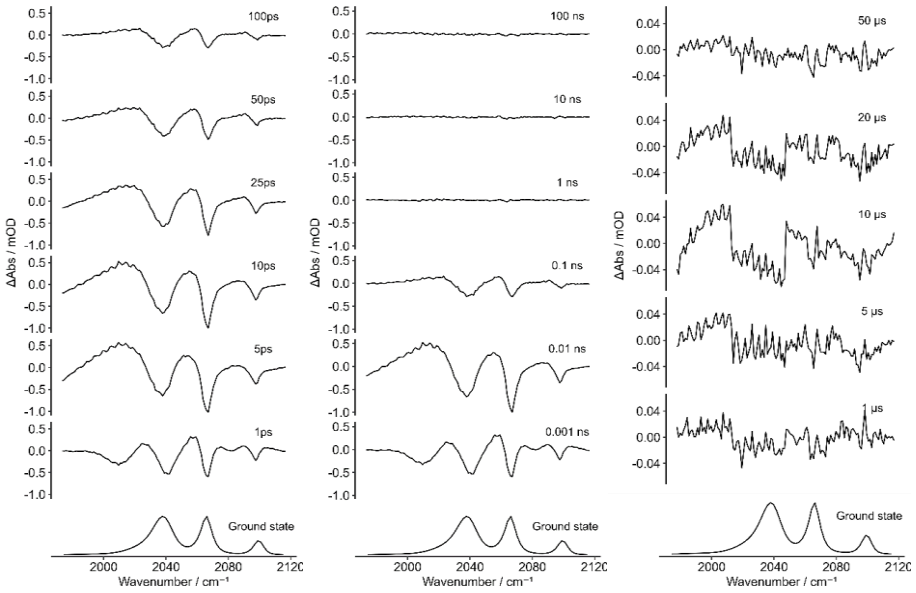

*Figure 137 – TR^{M}PS difference spectra at selected times for the excitation of **141** following excitation at 400nm*

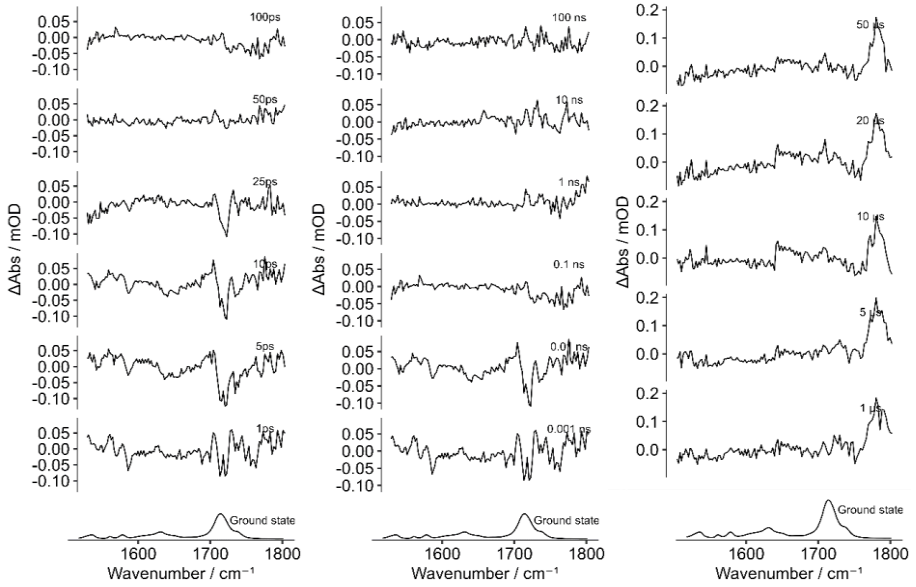

*Figure 138 - TR^{M}PS difference spectra at selected times for the excitation of **141** following excitation at 400nm*

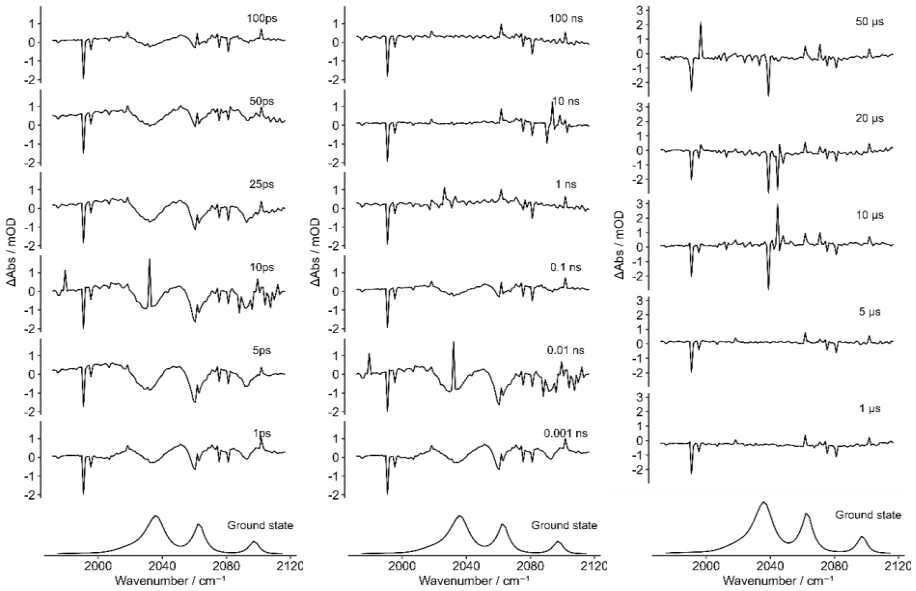

*Figure 139 - TR^{M}PS difference spectra at selected times for the excitation of **146** following excitation at 400nm*

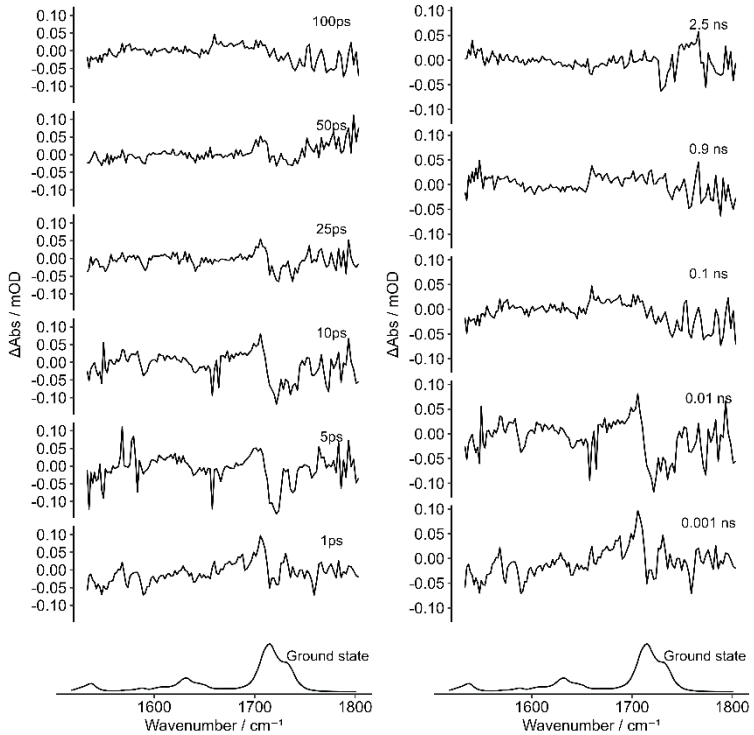

*Figure 140 - TR^{M}PS difference spectra at selected times for the excitation of **146** following excitation at 400nm*

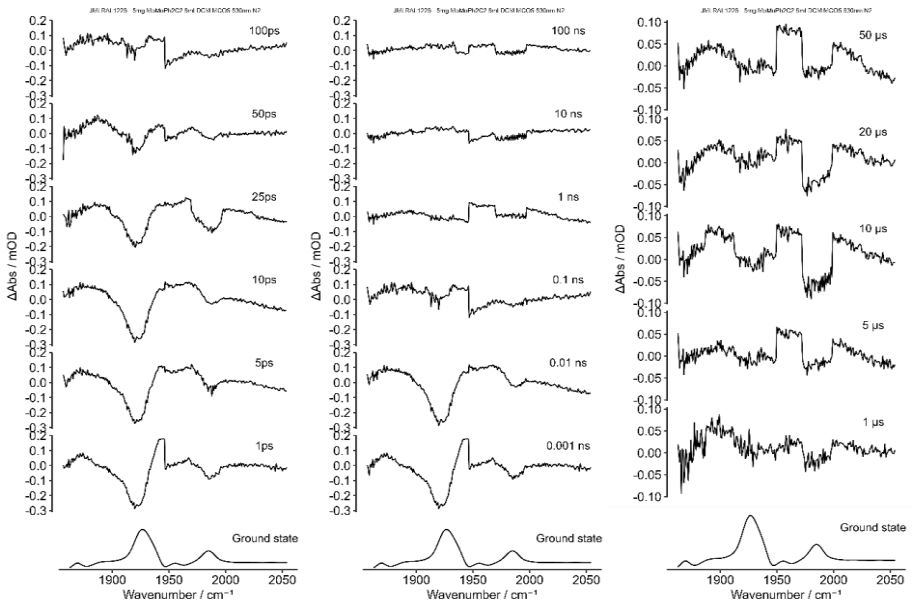

*Figure 141 – TR^{M}PS difference spectra of **157** following excitation at 530nm*

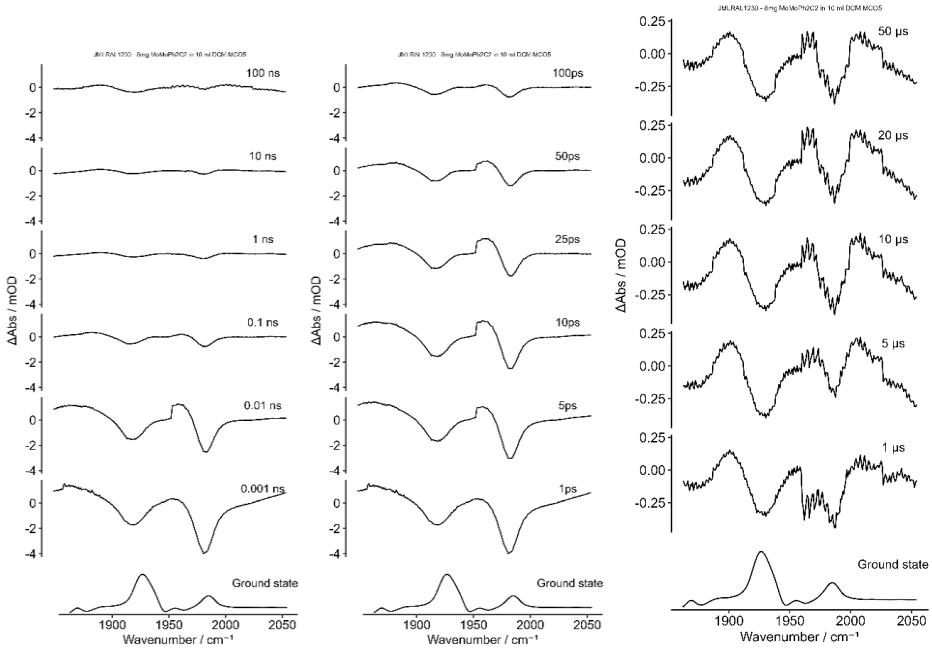

*Figure 142 - TR^{M}PS difference spectra of **157** following excitation at 355nm*

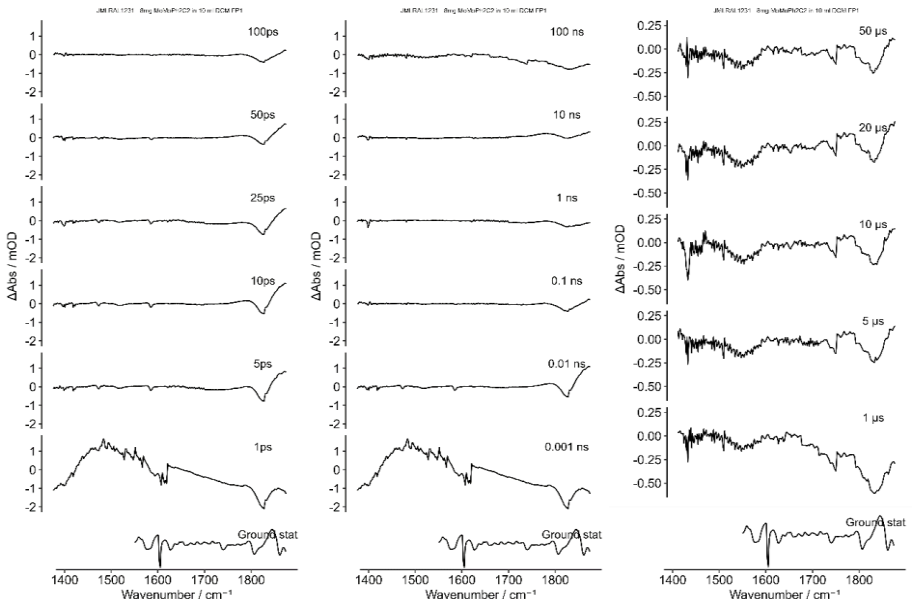

*Figure 143 - TR^{M}PS difference spectra of **157** following excitation at 355nm*

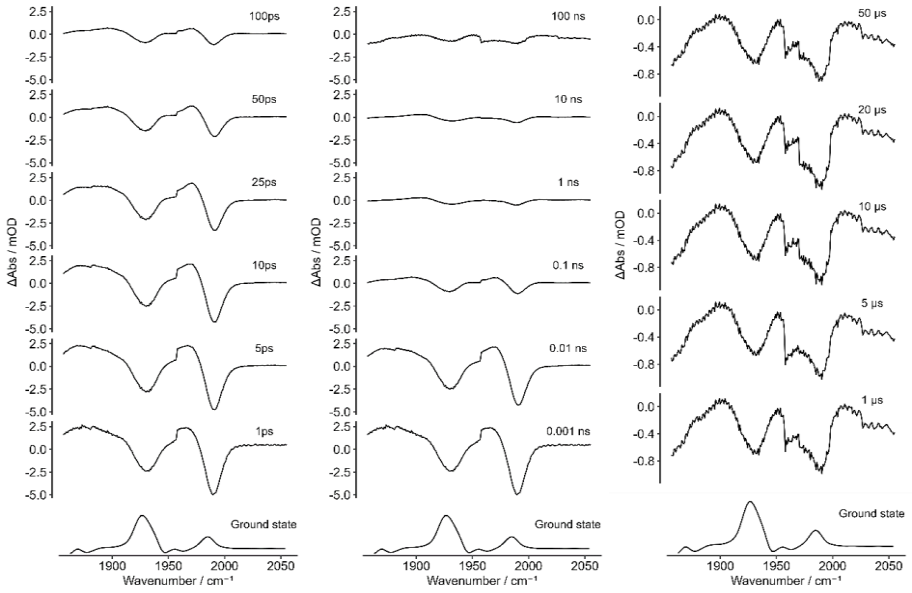

*Figure 144 - TR^{M}PS difference spectra of **157** following excitation at 355nm with an excess of acetonitrile*

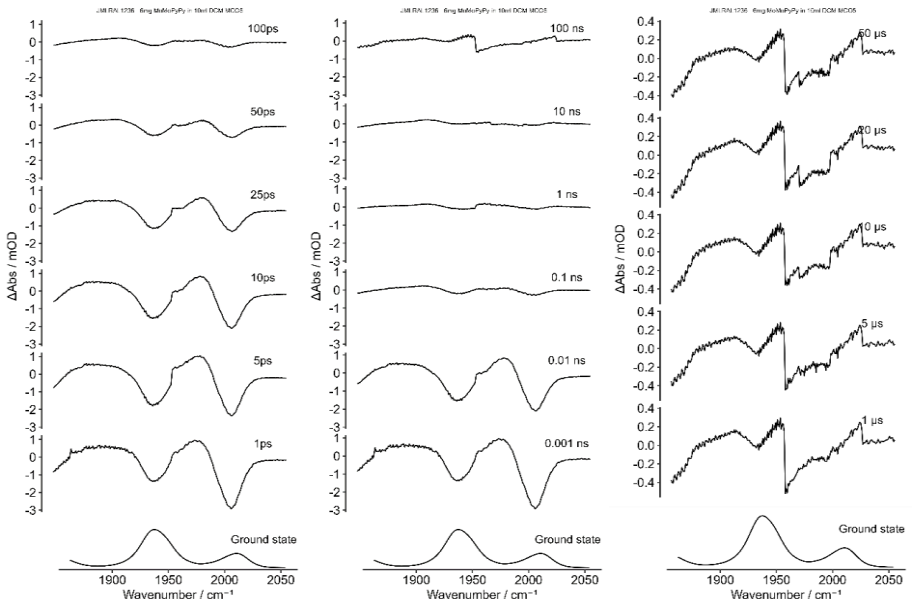

*Figure 145 - TR^{M}PS difference spectra of **158** following excitation at 355nm*

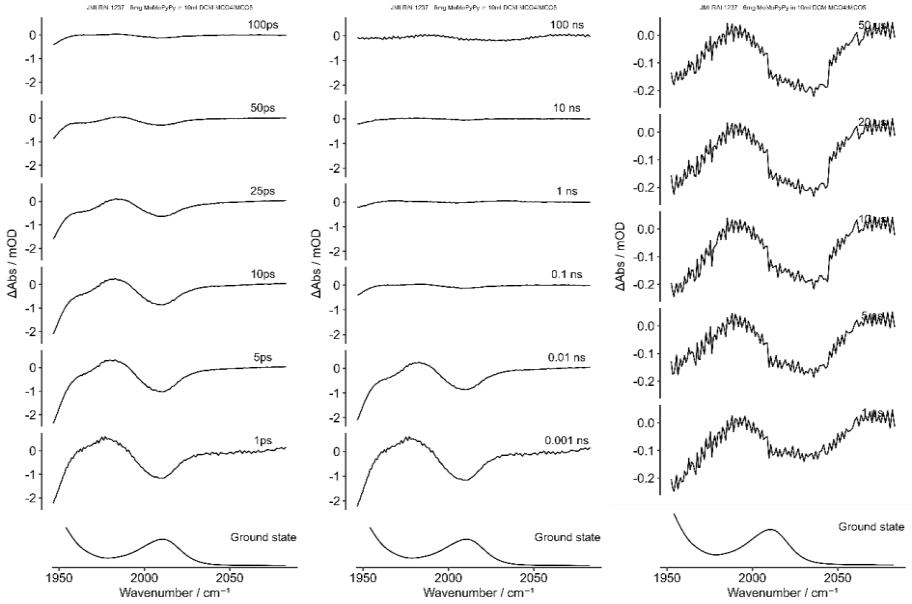

*Figure 146 - TR^{M}PS difference spectra of **158** following excitation at 355nm*

Appendix 8: Abbreviations

Abs	absorption
alphaprop	α product proportion
atm	atmosphere
ATR	attenuated total reflectance
ax	axial
BINAP	2,2′-bis(diphenylphosphino)-1,1′-binaphthyl
Bu	butyl
C	Celsius
cal	calorie
calcd	calculated
CID	collision-induced dissociation
Cp	cyclopentadienyl
Cy	cyclohexyl
DABCO	1,4-diazabicyclo[2.2. 2]octane
DAD	diazadiene
DCE	dichlorethane
DCM	dichlormethane
deltaC1C4	Charge difference across substituent carbons
deltaR	Difference between pi donations from substituents
DFT	density functional theory
DiffSec	Difference in substituent cone volume
DME	dimethoxyethane
DoE	design of experiments
DPA	diphenylacetylene
DPPM	bis(diphenylphosphino)methane
ee	enantiomeric excess
eq	equatorial
ESI	electrospray ionisation

Et	ethyl
FTIR	Fourier transform infrared
HOMO	highest occupied molecular orbital
hr	hour
Hz	Hertz
^{i}Pr	isopropyl
IR	Infrared
iso	isomer
k	rate constant
L	ligand
LOOCV	leave-one-out cross validation
LUMO	lowest unoccupied molecular orbital
m/z	mass-to-charge ratio
Me	methyl
MeCN	acetonitrile
ML	machine learning
MLCT	metal-ligand charge transfer
MO	molecular orbital
MS	Mass Spectrometry
Mw	Molecular Weight
MW	microwave
NBD	norbornadiene
NBE	norbornene
NBO	natural bond orbital
NDI	naphthyridine-diimine
NMO	n-methylmorpholine N oxide
NMO	n-methylmorpholine N oxide
NMR	nuclear magnetic resonance
OD	optical density
OOB	out-of-bag
OVAT	one variable at a time
PCA	principal component analysis
PES	potential energy surface

Ph	phenyl
PKR	Pauson-Khand Reaction
pp	photoproduct
ppm	parts per million
psax	pseudoaxial
pseq	pseudoequatorial
Q-Q	quartile-quartile
R	substituent
RF	random forest
RMSE	root-mean-squared error
RT	room temperature
SCXRD	single-crystal X-ray diffraction
TD-DFT	time-dependent density functional theory
TEMPO	2,2,6,6-tetramethylpiperidine N-oxide
TEP	Tolman electronic parameter
tert-	tertiary
THF	tetrahydrofuran
TMAO/TMANO	trimethylamine N-oxide
TRIR	time-resolved infrared
$TR^{M}PS$	time-resolved multiple probe spectroscopy
Ts	tosyl
TS	transition state
UV-Vis	UV-Visible spectroscopy
XRD	X-ray diffraction

References

1 I. U. Khand, G. R. Knox, P. L. Pauson and W. E. Watts, *J. Chem. Soc. - Ser. Chem. Commun.*, 1971, **1**, 36.
2 G. R. Knox and P. L. Pauson, *J Chem Soc Perkin Trans*, 1973, **1**, 977–981.
3 N. E. Schore and M. C. Croudace, *J. Org. Chem.*, 1981, **46**, 5436–5438.
4 C. Exon and P. Magnus, *J. Am. Chem. Soc.*, 1983, **105**, 2477–2478.
5 P. Magnus and L. M. Principe, *Tetrahedron Lett.*, 1985, **26**, 4851–4854.
6 M. E. Krafft, *J. Am. Chem. Soc.*, 1988, **110**, 968–970.
7 M. E. Krafft and C. A. Juliano, *J. Org. Chem.*, 1992, **57**, 5106–5115.
8 M. E. Krafft, *Tetrahedron Lett.*, 1988, **29**, 999–1002.
9 M. E. Krafft, C. A. Juliano, I. L. Scott, C. Wright and M. D. McEachin, *J. Am. Chem. Soc.*, 1991, **113**, 1693–1703.
10 M. Yamanaka and E. Nakamura, *J. Am. Chem. Soc.*, 2001, **123**, 1703–1708.
11 M. A. Pericàs, J. Balsells, J. Castro, I. Marchueta, A. Moyano, A. Riera, J. Vázquez and X. Verdaguer, *Pure Appl. Chem.*, 2002, **74**, 167–174.
12 J. Balsells, J. Vázquez, A. Moyano, M. A. Pericàs and A. Riera, *J. Org. Chem.*, 2000, **65**, 7291–7302.
13 Y. Gimbert, D. Lesage, A. Milet, F. Fournier, A. E. Greene and J. C. Tabet, *Org. Lett.*, 2003, **5**, 4073–4075.
14 V. Derdau, S. Laschat, I. Dix and P. G. Jones, *Organometallics*, 1999, **18**, 3859–3864.
15 E. V. Banide, H. Müller-Bunz, A. R. Manning, P. Evans and M. J. McGlinchey, *Angew. Chem. - Int. Ed.*, 2007, **46**, 2907–2910.
16 D. Lesage, A. Milet, A. Memboeuf, J. Blu, A. E. Greene, J.-C. Tabet and Y. Gimbert, *Angew. Chem. Int. Ed.*, 2014, **53**, 1939–1942.
17 M. A. Henderson, J. Luo, A. Oliver and J. S. McIndoe, *Organometallics*, 2011, **30**, 5471–5479.
18 A. M. Rodriguez and P. Prieto, *Tetrahedron*, 2016, **72**, 7443–7448.
19 D. R. Hartline, M. Zeller and C. Uyeda, *Angew. Chem. Int. Ed.*, 2016, **55**, 6084–6087.
20 T. J. M. De Bruin, A. Milet, A. E. Greene and Y. Gimbert, *J. Org. Chem.*, 2004, **69**, 1075–1080.
21 W. A. Smit, A. S. Gybin, A. S. Shashkov, Y. T. Strychkov, L. G. Kyz'mina, G. S. Mikaelian, R. Caple and E. D. Swanson, *Tetrahedron Lett.*, 1986, **27**, 1241–1244.
22 S. O. Simonian, W. A. Smit, A. S. Gybin, A. S. Shashkov, G. S. Mikaelian, V. A. Tarasov, I. I. Ibragimov, R. Caple and D. E. Froen, *Tetrahedron Lett.*, 1986, **27**, 1245–1248.
23 D. C. Billington, I. Malcolm Helps, P. L. Pauson, W. Thomson and D. Willison, *J. Organomet. Chem.*, 1988, **354**, 233–242.
24 N. Jeong, Y. K. Chung, B. Y. Lee, S. H. Lee and S.-E. Yoo, *Synlett*, 1991, **1991**, 204–206.
25 W. J. Kerr, D. M. Lindsay, W. J. Kerr and D. M. Lindsay, *Chem. Commun.*, 1999, 2551–2552.
26 T. Sugihara, *Chem. - Eur. J.*, 2001, **7**, 1589–1595.
27 B. L. Pagenkopf, T. Livinghouse, M. State and V. Uni, 1996, 2285–2286.
28 A. G. Gallagher, H. Tian, O. A. Torres-Herrera, S. Yin, A. Xie, D. M. Lange, J. K. Wilson, L. G. Mueller, M. R. Gau, P. J. Carroll and D. Martinez-Solorio, *Org. Lett.*, 2019, **21**, 8646–8651.
29 S. E. MacWhorter, V. Sampath, M. M. Olmstead and N. E. Schore, *J. Org. Chem.*, 1988, **53**, 203–205.
30 D. C. Billington, W. J. Kerr, P. L. Pauson and C. F. Farnocchi, *J. Organomet. Chem.*, 1988, **356**, 213–219.

31 D. C. Billington, W. J. Kerr, P. L. Pauson and C. F. Farnocchi, *J. Organomet. Chem.*, 1988, **356**, 213–219.
32 P. Magnus, L. M. Principe and M. J. Slater, *J. Org. Chem.*, 1987, **52**, 1483–1486.
33 D. C. Billington, *Tetrahedron Lett.*, 1983, **24**, 2905–2908.
34 S. E. Gibson (née Thomas) and A. Stevenazzi, *Angew. Chem. Int. Ed.*, 2003, **42**, 1800–1810.
35 V. Rautenstrauch, P. Mégard, J. Conesa and W. Küster, *Angew. Chem. Int. Ed. Engl.*, 1990, **29**, 1413–1416.
36 A. C. Comely, S. E. Gibson, A. Stevenazzi and N. J. Hales, *Tetrahedron Lett.*, 2001, **42**, 1183–1185.
37 S. E. Gibson, C. Johnstone and A. Stevenazzi, *Tetrahedron*, 2002, **58**, 4937–4942.
38 J. L. Arias, A. Cabrera, P. Sharma, N. Rosas and R. Sampere, *J. Mol. Catal. Chem.*, 2006, **246**, 237–241.
39 A. C. Comely, S. E. Gibson, N. J. Hales, C. Johnstone and A. Stevenazzi, *Org. Biomol. Chem.*, 2003, **1**, 1959–1968.
40 S.-W. Kim, S. U. Son, S. I. Lee, T. Hyeon and Y. K. Chung, *J. Am. Chem. Soc.*, 2000, **122**, 1550–1551.
41 S.-W. Kim, S. U. Son, S. S. Lee, T. Hyeon and Y. K. Chung, *Chem. Commun.*, 2001, 2212–2213.
42 J.-L. Muller, J. Klankermayer and W. Leitner, *Chem. Commun.*, 2007, 1939–1941.
43 J.-L. Muller, A. Rickers and W. Leitner, *Adv. Synth. Catal.*, 2007, **349**, 287–291.
44 B. Y. Lee, Y. K. Chung, N. Jeong, Y. Lee and S. H. Hwang, *J. Am. Chem. Soc.*, 1994, **116**, 8793–8794.
45 K. Hiroi, T. Watanabe, R. Kawagishi and I. Abe, *Tetrahedron Lett.*, 2000, **41**, 891–895.
46 S. E. Gibson, K. A. C. Kaufmann, J. A. Loch, J. W. Steed and A. J. P. White, *Chem. – Eur. J.*, 2005, **11**, 2566–2576.
47 S. E. Gibson, D. J. Hardick, P. R. Haycock, K. A. C. Kaufmann, A. Miyazaki, M. J. Tozer and A. J. P. White, *Chem. – Eur. J.*, 2007, **13**, 7099–7109.
48 S. E. Gibson, K. A. C. Kaufmann, P. R. Haycock, A. J. P. White, D. J. Hardick and M. J. Tozer, *Organometallics*, 2007, **26**, 1578–1580.
49 H. Lee and F. Kwong, *Eur. J. Org. Chem.*, 2010, **2010**, 789–811.
50 S. P. Simeonov, J. P. M. Nunes, K. Guerra, V. B. Kurteva and C. A. M. Afonso, *Chem. Rev.*, 2016, **116**, 5744–5893.
51 X. Verdaguer, A. Moyano, M. A. Pericàs, A. Riera, M. A. Maestro and J. Mahía, *J. Am. Chem. Soc.*, 2000, **122**, 10242–10243.
52 J. Solà, A. Riera, X. Verdaguer and M. A. Maestro, *J. Am. Chem. Soc.*, 2005, **127**, 13629–13633.
53 W. J. Kerr, G. G. Kirk and D. Middlemiss, *Synlett*, 1995, **1995**, 1085–1086.
54 N. E. Carpenter and K. M. Nicholas, *Polyhedron*, 1999, **18**, 2027–2034.
55 V. Derdau and S. Laschat, *J. Organomet. Chem.*, 2002, **642**, 131–136.
56 T. Fjermestad, M. A. Pericàs and F. Maseras, *Chem. - Eur. J.*, 2011, **17**, 10050–10057.
57 S. C. Berk, R. B. Grossman, S. L. Buchwald and R. B. Grossman, *J. Am. Chem. Soc.*, 1993, **115**, 4912–4913.
58 F. A. Hicks, N. M. Kablaoui and S. L. Buchwald, *J. Am. Chem. Soc.*, 1996, **118**, 9450–9451.
59 F. A. Hicks and S. L. Buchwald, *J. Am. Chem. Soc.*, 1996, **118**, 11688–11689.
60 F. A. Hicks and S. L. Buchwald, *J. Am. Chem. Soc.*, 1999, **121**, 7026–7033.
61 M. Zhang and S. L. Buchwald, *J. Org. Chem.*, 1996, **61**, 4498–4499.
62 T. Kondo, N. Suzuki, T. Okada and T. Mitsudo, *J. Am. Chem. Soc.*, 1997, **119**, 6187–6188.
63 T. Shibata and K. Takagi, *J. Am. Chem. Soc.*, 2000, **122**, 9852–9853.
64 N. Jeong, B. K. Sung and Y. K. Choi, *J. Am. Chem. Soc.*, 2000, **122**, 6771–6772.

65 Y. Tang, L. Deng, Y. Zhang, G. Dong, J. Chen and Z. Yang, *Org. Lett.*, 2005, **7**, 1657–1659.
66 M. M. Heravi and L. Mohammadi, *RSC Adv.*, 2021, **11**, 38325–38373.
67 Z. Yang, *Acc. Chem. Res.*, 2021, **54**, 556–568.
68 N. Jeong, S. H. Hwang, Y. Lee and Y. K. Chung, *J. Am. Chem. Soc.*, 1994, **116**, 3159–3160.
69 H. Wang, J. R. Sawyer, P. A. Evans and M. H. Baik, *Angew. Chem. - Int. Ed.*, 2008, **47**, 342–345.
70 L. C. Burrows, L. T. Jesikiewicz, P. Liu and K. M. Brummond, *ACS Catal.*, 2021, **11**, 323–336.
71 Y. Lan, L. Deng, J. Liu, C. Wang, O. Wiest, Z. Yang and Y.-D. Wu, *J. Org. Chem.*, 2009, **74**, 5049–5058.
72 Y. Tang, L. Deng, Y. Zhang, G. Dong, J. Chen and Z. Yang, *Org. Lett.*, 2005, **7**, 1657–1659.
73 L.-J. Deng, J. Liu, J.-Q. Huang, Y. Hu, M. Chen, Y. Lan, J.-H. Chen, A. Lei and Z. Yang, *Synthesis*, 2007, **2007**, 2565–2570.
74 C. A. Tolman, *Chem. Rev.*, 1977, **77**, 313–348.
75 L. P. Hammett, *Chem. Rev.*, 1935, **17**, 125–136.
76 L. P. Hammett, *J. Am. Chem. Soc.*, 1937, **59**, 96–103.
77 L. P. Hammett, *Trans. Faraday Soc.*, 1938, **34**, 156.
78 N. Fey, A. C. Tsipis, S. E. Harris, J. N. Harvey, A. G. Orpen and R. A. Mansson, *Chem. - Eur. J.*, 2005, **12**, 291–302.
79 N. Fey, S. E. Harris, J. N. Harvey and A. G. Orpen, *J. Chem. Inf. Model.*, 2006, **46**, 912–929.
80 R. A. Mansson, A. H. Welsh, N. Fey and A. G. Orpen, *J. Chem. Inf. Model.*, 2006, **46**, 2591–2600.
81 N. Fey, J. N. Harvey, G. C. Lloyd-Jones, P. Murray, A. G. Orpen, R. Osborne and M. Purdie, *Organometallics*, 2008, **27**, 1372–1383.
82 N. Fey, M. F. Haddow, J. N. Harvey, C. L. McMullin and A. G. Orpen, *Dalton Trans.*, 2009, 8183.
83 N. Fey, A. G. Orpen and J. N. Harvey, *Coord. Chem. Rev.*, 2009, **253**, 704–722.
84 J. Jover, N. Fey, J. N. Harvey, G. C. Lloyd-Jones, A. G. Orpen, G. J. J. Owen-Smith, P. Murray, D. R. J. Hose, R. Osborne and M. Purdie, *Organometallics*, 2010, **29**, 6245–6258.
85 J. Jover, N. Fey, M. Purdie, G. C. Lloyd-Jones and J. N. Harvey, *J. Mol. Catal. Chem.*, 2010, **324**, 39–47.
86 J. Jover, N. Fey, J. N. Harvey, G. C. Lloyd-Jones, A. G. Orpen, G. J. J. Owen-Smith, P. Murray, D. R. J. Hose, R. Osborne and M. Purdie, *Organometallics*, 2012, **31**, 5302–5306.
87 J. Jover and N. Fey, *Dalton Trans*, 2013, **42**, 172–181.
88 J. Jover and N. Fey, *Chem. - Asian J.*, 2014, **9**, 1714–1723.
89 N. Fey, *Chem. Cent. J.*, 2015, **9**, 1–10.
90 N. Fey, S. Papadouli, P. G. Pringle, A. Ficks, J. T. Fleming, L. J. Higham, J. F. Wallis, D. Carmichael, N. Mézailles and C. Müller, *Phosphorus Sulfur Silicon Relat. Elem.*, 2015, **190**, 706–714.
91 S. M. Mennen, C. Alhambra, C. L. Allen, M. Barberis, S. Berritt, T. A. Brandt, A. D. Campbell, J. Castañón, A. H. Cherney, M. Christensen, D. B. Damon, J. Eugenio de Diego, S. García-Cerrada, P. García-Losada, R. Haro, J. Janey, D. C. Leitch, L. Li, F. Liu, P. C. Lobben, D. W. C. MacMillan, J. Magano, E. McInturff, S. Monfette, R. J. Post, D. Schultz, B. J. Sitter, J. M. Stevens, I. I. Strambeanu, J. Twilton, K. Wang and M. A. Zajac, *Org. Process Res. Dev.*, 2019, **23**, 1213–1242.
92 L. Porwol, D. J. Kowalski, A. Henson, D. Long, N. L. Bell and L. Cronin, *Angew. Chem.*, 2020, **132**, 11352–11357.
93 Y. Shi, P. L. Prieto, T. Zepel, S. Grunert and J. E. Hein, *Acc. Chem. Res.*, 2021, **54**, 546–555.
94 C. B. Santiago, J.-Y. Guo and M. S. Sigman, *Chem. Sci.*, 2018, **9**, 2398–2412.
95 S. Yamaguchi, *Org. Biomol. Chem.*, 2022, **20**, 6057–6071.

96 D. M. Lustosa and A. Milo, *ACS Catal.*, 2022, **12**, 7886–7906.
97 P. M. Murray, F. Bellany, L. Benhamou, D.-K. Bučar, A. B. Tabor and T. D. Sheppard, *Org. Biomol. Chem.*, 2016, **14**, 2373–2384.
98 Y. Gil, M. Greaves, J. Hendler and H. Hirsh, *Science*, 2014, **346**, 171–172.
99 P. Raccuglia, K. C. Elbert, P. D. F. Adler, C. Falk, M. B. Wenny, A. Mollo, M. Zeller, S. A. Friedler, J. Schrier and A. J. Norquist, *Nature*, 2016, **533**, 73–76.
100 J. M. Granda, L. Donina, V. Dragone, D.-L. Long and L. Cronin, *Nature*, 2018, **559**, 377–381.
101 M. Foscato and V. R. Jensen, *ACS Catal.*, 2020, **10**, 2354–2377.
102 R. Gómez-Bombarelli, J. N. Wei, D. Duvenaud, J. M. Hernández-Lobato, B. Sánchez-Lengeling, D. Sheberla, J. Aguilera-Iparraguirre, T. D. Hirzel, R. P. Adams and A. Aspuru-Guzik, *ACS Cent. Sci.*, 2018, **4**, 268–276.
103 J. Burés and I. Larrosa, *Nature*, 2023, **613**, 689–695.
104 E. Caldeweyher, M. Elkin, G. Gheibi, M. Johansson, C. Sköld, P.-O. Norrby and J. F. Hartwig, *J. Am. Chem. Soc.*, 2023, jacs.3c04986.
105 M. Hassan, R. D. Brown, S. Varma-O'Brien and D. Rogers, *Mol. Divers.*, 2006, **10**, 283–299.
106 F. Robert, A. Milet, Y. Gimbert, D. Konya and A. E. Greene, *J. Am. Chem. Soc.*, 2001, **123**, 5396–5400.
107 J. H. Schulte, R. Gleiter and F. Rominger, *Org. Lett.*, 2002, **4**, 3301–3304.
108 T. J. M. De Bruin, A. Milet, F. Robert, Y. Gimbert and A. E. Greene, *J. Am. Chem. Soc.*, 2001, **123**, 7184–7185.
109 V. Derdau, S. Laschat and P. G. Jones, *Eur. J. Org. Chem.*, 2000, 681–689.
110 T. J. M. de Bruin, C. Michel, K. Vekey, A. E. Greene, Y. Gimbert and A. Milet, *J. Organomet. Chem.*, 2006, **691**, 4281–4288.
111 J. C. Kizirian, N. Aiguabella, A. Pesquer, S. Fustero, P. Bello, X. Verdaguer and A. Riera, *Org. Lett.*, 2010, **12**, 5620–5623.
112 B. E. Moulton, A. C. Whitwood, A. K. Duhme-Klair, J. M. Lynam and I. J. S. Fairlamb, *J. Org. Chem.*, 2011, **76**, 5320–5334.
113 E. Fager-Jokela, M. Muuronen, M. Patzschke and J. Helaja, *J. Org. Chem.*, 2012, **77**, 9134–9147.
114 N. P. Yahaya, PhD Thesis, University of York, 2015.
115 L. Milone, R. Rossetti and P. L. Stanghellini, .
116 E. D. Glendening, C. R. Landis and F. Weinhold, *J. Comput. Chem.*, 2019, **40**, 2234–2241.
117 F. Weinhold, C. R. Landis and E. D. Glendening, *Int. Rev. Phys. Chem.*, 2016, **35**, 399–440.
118 S. Liu and B. Luan, *Nanoscale*, 2022, **14**, 9466–9473.
119 K. Wu and A. G. Doyle, *Nat. Chem.*, 2017, **9**, 779–784.
120 K. Itami, K. Mitsudo and J. Yoshida, *Angew. Chem. Int. Ed.*, 2002, **41**, 3481–3484.
121 K. Itami, K. Mitsudo, K. Fujita, Y. Ohashi and J. Yoshida, *J. Am. Chem. Soc.*, 2004, **126**, 11058–11066.
122 A. Lagunas, A. M. I. Payeras, C. Jimeno and M. A. Pericàs, *Org. Lett.*, 2005, **7**, 3033–3036.
123 S. Shambayani, W. E. Crowe and S. L. Schreiber, *Tetrahedron Lett.*, 1990, **31**, 5289–5292.
124 Y. K. Chung, B. Y. Lee, N. Jeong, M. Hudecek and P. L. Pauson, *Organometallics*, 1993, **12**, 220–223.
125 R. Cabot, A. Lledó, M. Revés, A. Riera and X. Verdaguer, *Organometallics*, 2007, **26**, 1134–1142.
126 A. Lledó, J. Solà, X. Verdaguer, A. Riera and M. A. Maestro, *Adv. Synth. Catal.*, 2007, **349**, 2121–2128.
127 J. D. Ricker, V. Mohammadrezaei, T. J. Crippen, A. M. Zell and L. M. Geary, *Organometallics*, 2018, **37**, 4556–4559.

128 L. T. Mika, R. Tuba, I. Tóth, S. Pitter and I. T. Horváth, *Organometallics*, 2011, **30**, 4751–4764.
129 R. L. Hollingsworth, J. W. Beattie, A. Grass, P. D. Martin, S. Groysman and R. L. Lord, *Dalton Trans.*, 2018, **47**, 15353–15363.
130 M. S. Sigman, A. W. Fatland and B. E. Eaton, *J. Am. Chem. Soc.*, 1998, **120**, 5130–5131.
131 J. García-Lacuna, G. Domínguez, J. Blanco-Urgoiti and J. Pérez-Castells, *Org. Lett.*, 2018, **20**, 5219–5223.
132 R. J. Baxter, G. R. Knox, P. L. Pauson and M. D. Spicer, *Organometallics*, 1999, **18**, 197–205.
133 A. J. Atkin, S. Williams, P. Sawle, R. Motterlini, J. M. Lynam and I. J. S. Fairlamb, *Dalton Trans.*, 2009, 3653–3656.
134 G. M. Greetham, D. Sole, I. P. Clark, A. W. Parker, M. R. Pollard and M. Towrie, *Rev. Sci. Instrum.*, 2012, **83**, 103107.
135 J. J. Turner, M. W. George, M. Poliakoff and R. N. Perutz, *Chem. Soc. Rev.*, 2022, **51**, 5300–5329.
136 J. C. Anderson, B. F. Taylor, C. Viney and G. J. Wilson, *J. Organomet. Chem.*, 1996, **519**, 103–106.
137 S. M. Draper, C. Long and B. M. Myers, *J. Organomet. Chem.*, 1999, **588**, 195–199.
138 A. C. Coleman, C. Long, A. Meetsma, B. L. Feringa, W. R. Browne and M. T. Pryce, *Dalton Trans.*, 2009, **0**, 7885–7887.
139 K. Asano, Y. Uesugi and J. Yoshida, *Org. Lett.*, 2013, **15**, 2398–2401.
140 N. M. Boyle, A. C. Coleman, C. Long, K. L. Ronayne, W. R. Browne, B. L. Feringa and M. T. Pryce, *Inorg. Chem.*, 2010, **49**, 10214–10216.
141 C. M. Gordon, M. Kiszka, I. R. Dunkin, W. J. Kerr, J. S. Scott and J. Gebicki, *J. Organomet. Chem.*, 1998, **554**, 147–154.
142 J. A. Platts, G. J. S. Evans, M. P. Coogan and J. Overgaard, *Inorg. Chem.*, 2007, **46**, 6291–6298.
143 J. Overgaard, H. F. Clausen, J. A. Platts and B. B. Iversen, *J. Am. Chem. Soc.*, 2008, **130**, 3834–3843.
144 J. C. Manton, F. J. R. Cerpentier, E. C. Harvey, I. P. Clark, G. M. Greetham, C. Long and M. T. Pryce, *Dalton Trans.*, 2019, **48**, 14642–14652.
145 C. Mukai, M. Uchiyama and M. Hanaoka, *J. Chem. Soc. Chem. Commun.*, 1992, 1014–1015.
146 D. T. Rutherford and S. D. R. Christie, *Tetrahedron Lett.*, 1998, **39**, 9805–9808.
147 N. Gessner, A. K. Bäck, J. Knorr, C. Nagel, P. Marquetand, U. Schatzschneider, L. González and P. Nuernberger, *Phys. Chem. Chem. Phys.*, 2021, **23**, 24187–24199.
148 T. P. Dougherty and E. J. Heilweil, *Chem. Phys. Lett.*, 1994, **227**, 19–25.
149 D. M. Allen, A. Cox, T. J. Kemp, Q. Sultana and R. B. Pitts, *J. Chem. Soc. Dalton Trans.*, 1976, 1189.
150 J. C. Linehan, C. R. Yonker, R. S. Addleman, S. T. Autrey, J. T. Bays, T. E. Bitterwolf and J. L. Daschbach, *Organometallics*, 2001, **20**, 401–407.
151 H. Van Dam, D. J. Stufkens, A. Oskam, M. Doran and I. H. Hillier, *J. Electron Spectrosc. Relat. Phenom.*, 1980, **21**, 47–55.
152 D. M. Hoffman, R. Hoffmann and C. R. Fisel, *J. Am. Chem. Soc.*, 1982, **104**, 3858–3875.
153 R. L. DeKock, T. V. Lubben, J. Hwang and T. P. Fehlner, *Inorg. Chem.*, 1981, **20**, 1627–1628.
154 W. I. Bailey, M. H. Chisholm, F. A. Cotton and L. A. Rankel, *J. Am. Chem. Soc.*, 1978, **100**, 5764–5773.
155 M. D. C. Robert J. Klingler, William Butler, 1973, **827**, 3535–3536.
156 R. J. Klingler, W. M. Butler and M. D. Curtis, *J. Am. Chem. Soc.*, 1978, **100**, 5034–5039.

157 P. Bougeard, S. Peng, M. Mlekuz and M. J. McGlinchey, *J. Organomet. Chem.*, 1985, **296**, 383–391.
158 V. Krishnakumar, G. Keresztury, T. Sundius and R. Ramasamy, *J. Mol. Struct.*, 2004, **702**, 9–21.
159 M. K. Kesharwani, B. Brauer and J. M. L. Martin, *J. Phys. Chem. A*, 2015, **119**, 1701–1714.
160 Y. Bouteiller, J.-C. Gillet, G. Grégoire and J. P. Schermann, *J. Phys. Chem. A*, 2008, **112**, 11656–11660.
161 W. C. Still, M. Kahn and A. Mitra, *J. Org. Chem.*, 1978, **43**, 2923–2925.
162 O. V. Dolomanov, L. J. Bourhis, R. J. Gildea, J. a. K. Howard and H. Puschmann, *J. Appl. Crystallogr.*, 2009, **42**, 339–341.
163 G. M. Sheldrick, *Acta Crystallogr. Sect. Found. Adv.*, 2015, **71**, 3–8.
164 G. M. Sheldrick, *Acta Crystallogr. Sect. C Struct. Chem.*, 2015, **71**, 3–8.
165 L. Anders Hammarback, J. B. Eastwood, T. J. Burden, C. J. Pearce, I. P. Clark, M. Towrie, A. Robinson, I. J. S. Fairlamb and J. M. Lynam, *Chem. Sci.*, 2022, **13**, 9902–9913.
166 R. Ahlrichs, M. Bär, M. Häser, H. Horn and C. Kölmel, *Chem. Phys. Lett.*, 1989, **162**, 165–169.
167 S. Grimme, J. Antony, S. Ehrlich and H. Krieg, *J. Chem. Phys.*, 2010, **132**, 154104.
168 M.-T. Nolan, L. M. Pardo, A. M. Prendergast and G. P. McGlacken, *J. Org. Chem.*, 2015, **80**, 10904–10913.
169 B. E. Moulton, PhD Thesis, University of York, 2008.